Número: 400/2008

UNIVERSIDADE ESTADUAL DE CAMPINAS
INSTITUTO DE GEOCIÊNCIAS
PÓS-GRADUAÇÃO EM GEOCIÊNCIAS
ÁREA DE GEOLOGIA E RECURSOS NATURAIS

ODERSON ANTÔNIO DE SOUZA FILHO

DADOS AEROGEOFÍSICOS E GEOLÓGICOS APLICADOS À SELEÇÃO DE ÁREAS FAVORÁVEIS PARA ÁGUA SUBTERRÂNEA NO DOMÍNIO CRISTALINO DO CEARÁ, BRASIL

Tese apresentada ao Instituto de Geociências como parte dos requisitos para a obtenção do título de Doutor em Geociências.

Orientadora: Profa. Dra. Adalene Moreira Silva, IG-UnB/IG-UNICAMP
Co-orientadoras: Dra. Mônica Mazzini Perrotta, Serviço Geológico do Brasil – CPRM
M.Sc. Anne E. McCafferty, U.S. Geological Survey

CAMPINAS – SÃO PAULO

Agosto – 2008

Catalogação na Publicação elaborada pela Biblioteca do Instituto de Geociências/UNICAMP

Souza Filho, Oderson Antônio de.
So89d Dados aerogeofísicos e geológicos aplicados à seleção de áreas favoráveis para água subterrânea no domínio cristalino do Ceará, Brasil / Oderson Antônio de Souza Filho.-- Campinas,SP.: [s.n.], 2008.

Orientadores: Adalene Moreira Silva, Mônica Mazzini Perrotta, Anne E. McCafferty.
Tese (doutorado) Universidade Estadual de Campinas, Instituto de Geociências.

1. Geofísica – Processamento de dados. 2. Hidrogeologia.
4. Geofísica – Ceará (Estado). I. Silva, Adalene Moreira.
II. Perrotta, Mônica Mazzini. III. McCafferty, Anne E.
IV. Universidade Estadual de Campinas, Instituto de Geociências.
V. Título.

Título em inglês: Airborne geophysical and geological data applied to the selection of groundwater potential areas in crystalline rocks of Ceará, Brazil.

Keywords: - Geophysics – Data processing,
- Hydrogeology,
- Geophysics – Ceará (State),
Área de concentração: Geologia e Recursos Naturais
Titulação: Doutor em Ciências.
Banca examinadora: - Adalene Moreira Silva ,
- Sueli Yoshinaga Pereira,
- Carlos Roberto de Souza Filho,
- Michael J. Friedel,
- Francisco José Fonseca Ferreira.
Data da defesa: 29/08/2008
Programa: Geociências.

UNIVERSIDADE ESTADUAL DE CAMPINAS
INSTITUTO DE GEOCIÊNCIAS
PÓS-GRADUAÇÃO EM GEOCIÊNCIAS
ÁREA DE GEOLOGIA E RECURSOS NATURAIS

UNICAMP

AUTOR: ODERSON ANTÔNIO DE SOUZA FILHO

DADOS AEROGEOFÍSICOS E GEOLÓGICOS APLICADOS À SELEÇÃO DE ÁREAS FAVORÁVEIS PARA ÁGUA SUBTERRÂNEA NO DOMÍNIO CRISTALINO DO CEARÁ, BRASIL

ORIENTADORA: Profa. Dra. Adalene Moreira Silva
CO-ORIENTADORA: Profa. Dra. Mônica Mazzini Perrota
CO-ORIENTADORA: Profa. Dra. Anne Elizabeth McCafferty

Aprovada em: 29 / 08 / 2008

EXAMINADORES:

Profa. Dra. Adalene Moreira Silva Adalene Moreira Silva - Presidente
Profa. Dra. Sueli Yoshinaga Pereira
Prof. Dr. Francisco José Fonseca Ferreira Francisco José Fonseca Ferreira
Dr. Michael Jaimes Friedel Michael Friedel
Prof. Dr. Carlos Roberto de Souza Filho Carlos RS Filho

Campinas, 29 de agosto de 2008

DEDICATÓRIA

Dedico esta obra à minha esposa Jane e filha Isadora que muito me apoiaram nesta tarefa, e a meus pais pelo incentivo ao estudo e à prática do bem.

AGRADECIMENTOS

Expresso minha gratidão e reconhecimento a todas as pessoas e instituições que colaboraram para o desenvolvimento desta tese de doutorado. Agradeço também àqueles que não me atrapalharam (... parafraseando um geofísico).

À orientadora, a Profa. Adalene Moreira Silva, pelo incansável incentivo e ensinamentos sobre os métodos geofísicos e modelagens espaciais, bem como pela seriedade na orientação da tese, seguido por agradáveis conversas fora do expediente.

Às co-orientadoras Dra. Mônica Mazzini Perrotta/CPRM e Anne Elizabeth McCafferty/USGS cujos conhecimentos em sensoriamento remoto, modelagem espacial e geofísica, possibilitaram, junto com a orientadora, a aplicação de técnicas inovadoras na pesquisa hidrogeológica. O coleguismo também é uma característica dessas pessoas maravilhosas.

À CPRM, o Serviço Geológico do Brasil, em especial à Residência de Fortaleza, gerentes e amigos, sou grato pela confiança em mim depositada, coleguismo e pela disponibilização dos dados aerogeofísicos e hidrogeológicos utilizados nessa tese.

Ao Instituto de Geociências da Universidade Estadual de Campinas, pela excelente infra-estrutura e corpo docente que muito contribuíram para meu aprendizado. Aos amigos e colegas do Laboratório de Processamento de Informações Georreferenciadas e IG/UNICAMP pelas boas discussões e convivência.

Ao Serviço Geológico dos Estados Unidos (USGS), pelo apoio à realização de minhas atividades durante meu estágio nessa instituição, inclusive proporcionando atividades de campo e auxiliando na participação em importantes eventos científicos.

Ao Cientista-Chefe do *Crustal Imaging and Characterization Team*/USGS, Victor Labson, incentivador de minhas pesquisas durante ao período no USGS. Aos pesquisadores do USGS, pelas valorosas contribuições técnico-científicas ao meu trabalho, bem como pelos descontraídos momentos de interação durante minha estada naquele país.

À CAPES, pela concessão de bolsa de estudos através do seu Programa de Estágio Doutorando no Exterior (BEX-3688/05-4).

Pela Universidade de São Paulo, agradeço ao Prof. Dr. Carlos Mendonça do Instituto Astronomia e Geofísica e Ciências Atmosféricas pelo reconhecimento de meu trabalho e sugestões de aprimoramento e ao Instituto de Geociências, pelo apoio em algumas atividades laboratoriais e de campo.

UNIVERSIDADE ESTADUAL DE CAMPINAS
INSTITUTO DE GEOCIÊNCIAS
Pós-Graduação em Geociências
Área de Geologia e Recursos Naturais

Dados Aerogeofísicos e Geológicos Aplicados à Seleção de Áreas Favoráveis para Água Subterrânea no Domínio Cristalino do Ceará, Brasil

RESUMO

Tese de Doutorado
Oderson Antônio de Souza Filho

Os métodos usuais de locação de poços tubulares para água subterrânea no Nordeste do Brasil baseiam-se na identificação de estruturas permissivas através de fotointerpretações e caminhamentos geofísicos eletromagnéticos indutivos e eletrorresistivos em áreas de pouca extensão. Os resultados alcançados por esses métodos mostram uma grande variabilidade na produtividade de poços. Esta tese privilegia a utilização das geotecnologias, notadamente os levantamentos aerogeofísicos e modelagens espaciais para mapear regiões favoráveis para água subterrânea e a sua qualidade numa área do Estado do Ceará, Brasil. O conjunto de dados compreende levantamento aerogeofísico local e regional, imagens do sensor multiespectral ETM+/Landsat-7 e dados de campo. O desenvolvimento da tese teve três etapas: o processamento dos dados aerogeofísicos magnéticos, eletromagnéticos e radiométricos; a abordagem geoestatística objetivando o zoneamento da condutividade elétrica da água subterrânea e; a modelagem de propriedades geofísicas associadas a poços de alta e baixa vazão. O processamento aerogeofísico realçou estruturas compatíveis com a pesquisa hídrica até 250 m de profundidade. Gradientes magnéticos anômalos lineares e rasos, porém contínuos abaixo de 400 m, foram diferenciados das anomalias superficiais através da integração entre os aerolevantamentos. Inversões dos dados eletromagnéticos indicam que a camada de solo é bastante condutiva e o substrato rochoso é resistivo após 15 m de profundidade, dificultando a detecção de estruturas mais profundas. As técnicas de krigagem e simulação estocástica foram aplicadas às medidas de condutividade elétrica nos poços tubulares (variável principal) e aos dados aerogeofísicos de condutividade elétrica aparente do solo (variável externa) para gerar um mapa de condutividade elétrica da água subterrânea. A informação aerogeofísica de alta resolução auxiliou na simulação da variabilidade da condutividade elétrica da água. Testes de validação comparando valores calculados com medidas em novos poços confirmaram a competência destes modelos em caracterizar a qualidade das águas subterrâneas em rochas cristalinas. As técnicas de análise espacial por razão de probabilidades e pesos de evidências compararam valores de cada propriedade geofísica, lineamentos estruturais e dados multiespectrais a poços de diferentes vazões. Os modelos obtidos mostram que os poços mais produtivos estão associados ao substrato rochoso não-magnético, eletricamente condutivo, cortado por gradientes não-magnéticos WNW-ESE, lineamentos estruturais e por gradientes condutivos N-S. Dados de campo comprovaram a natureza rúptil extensional das estruturas WNW-ESE e N-S. As propriedades do solo, interpretadas através de dados radiométricos (teor de potássio maior do que urânio) e dos dados multiespectrais (conteúdo relativo de minerais de óxido de ferro e argilo-minerais) indicam uma associação de poços mais produtivos com solos de fração grosseira predominando sobre a componente mais fina e os argilo-minerais prevalecem como produtos de alteração em relação aos minerais de óxido de ferro.

UNIVERSIDADE ESTADUAL DE CAMPINAS
INSTITUTO DE GEOCIÊNCIAS
Pós-Graduação em Geociências
Área de Geologia e Recursos Naturais

Dados Aerogeofísicos e Geológicos Aplicados à Seleção de Áreas Favoráveis para Água Subterrânea no Domínio Cristalino do Ceará, Brazil

ABSTRACT

PhD Thesis

Oderson Antônio de Souza Filho

The location of water well in Northeast Brazil is usually based on the interpretation of structural lineaments in aerial-photographs and electromagnetic and electrical resistivity ground geophysics surveys. However, the success of these techniques is variable, and the small coverage area is another limitation. This Thesis favors a different approach, the use of airborne geophysical surveys and spatial modeling to map groundwater potential and quality in the State of Ceará, Brazil. The data sets comprise a local helicopter survey, a regional airborne survey as well as multispectral images from the Enhanced thematic Mapper sensor (ETM+)/Landsat-7 and field data. The thesis was developed in three stages: i) the processing of airborne magnetic, electromagnetic and radiometric data; ii) a geostatistical modeling to produce groundwater electrical conductivity maps, and; iii) groundwater favorability modeling based on the association of high- and low-yield wells and geophysical, structural and spectral properties. The magnetic anomaly data were filtered using the regional and local survey to enhance through-going structures whose gradients crosscut rocks below 400 m depth. The helicopter electromagnetic data (HEM) were processed so that shallow (up to 15 m depth) conductive structures and lithologic units were enhanced. Inversion modeling applied to electromagnetic data unveiled a conductive soil horizon over a resistive bedrock at depths greater than 15 m which restricts the detection of deeper conductive anomalies. The regional radiometric data together with ETM+ images characterized the soil texture and relative contents of Fe-oxide/clay-mineral/vegetation density ratios. Structural data were interpreted from aerial-photographs and from ETM+/Landsat-7 data. Kriging and stochastic simulation techniques were applied to electrical conductivity data from water-wells to generate a groundwater electrical conductivity map. The HEM data were used as an external variable to characterize the variability of groundwater electrical conductivity associated with crystalline aquifers. Validation tests comparing predicted values with measurements in new wells confirmed the competence of these models in locating fresh groundwater sources in bedrock. The probability ratio and weights of evidence techniques quantitatively described the association of each value of magnetization, electrical conductivity, geophysical gradients, structural lineaments, radiometric data and multiespectral data to different well yields. The groundwater favorability models imply the existence of structural lineaments in an E-W direction, with non-magnetic properties, which are pervasive below 250 m depth but conductive from up to 15 m below the surface. The E-W lineaments are cut by conductive N-S structures. Field data confirm that the geophysical trends are extensional brittle structures. High yield classes are more associated with coarse-grained soils (high potassium, medium thorium and uranium) where alteration minerals are predominantly clay-minerals as opposed to Fe-oxide minerals.

ÍNDICE

RESUMO .... **VI**

ABSTRACT .... **VII**

ÍNDICE .... **VIII**

LISTA DE FIGURAS E TABELAS .... **X**

LISTA DE MAPAS ANEXOS .... **XX**

1. Introdução **1**

1.1. Apresentação e Justificativas *1*

1.2. Objetivos *3*

1.3. Localização da Área de Estudo *4*

1.4. Bases de Dados *5*

Geológicos e Estruturais *5*
Hidrogeológicos *5*
Sensores Remotos *6*
Aerogeofísicos *6*

1.5 Estruturação da Tese de Doutorado *9*

1.6 Métodos *10*

1.6.1 Processamento e Resultados de Imagens do sensor ETM$^+$

do Satélite Landsat-7 .... *10*

O Método das Razões Orientadas de Bandas *11*
Análise por Principais Componentes – Método Crósta *13*

1.6.2 Processamento de Dados Aerogeofísicos *14*

1.6.3 Análise Geoestatística *14*
Krigagem e Simulação Estocástica com Deriva Externa *14*
Modelagem por Razões de Probabilidades *15*
Modelagem por Pesos de Evidência *15*

1.7 Problemática de Locação de Poços no Cristalino Semi-Árido *15*
Diferenças entre Domínios Hidrogeológicos *15*

2. **Área de Estudo** **21**

2.1 Aspectos Fisiográficos *22*

2.1.1 Geomorfologia *22*
2.1.2 Clima *22*
2.1.3 Vegetação *24*
2.1.4 Hidrografia *25*

2.2 Arcabouço Geológico *26*
2.3 Arcabouço Hidrogeológico *29*
2.3.1 Características de Poços na Área da Folha Irauçuba e do Juá *31*
3. Airborne Hydrogeophysics: an important tool to select target areas for groundwater exploration in the Crystalline Domain **34**
3.1. Introduction *35*
3.2. Regional Airborne Magnetic and Radiometric Data *37*
3.2.1. The Magnetic data *37*
3.2.2. The Radiometric Data *42*
3.3. High Resolution Helicopter Magnetic and Electromagnetic Data *45*
3.3.1. The Magnetic Data *45*
3.3.2. The Helicopter Electromagnetic (HEM) Data *52*
3.4. Sensitivity Analysis and Exploration Depth for Juá HEM Data *55*
3.4.1. HEM Depths of Investigation and their Hydrogeological Meaning *56*
3.5. Electromagnetic Anomalies: Analogy to Conductive Thin Plates *58*
3.5.1. Theory of Mutual Inductance *58*
3.5.2. Identification of HEM Anomalies and Their Hydrogeological Meaning *59*
3.6. Inversions and Modeling of Juá Electromagnetic Data *66*
3.7. Geophysical Properties Associated to Juá Rocks *69*
3.8. Conclusions *72*
4. Helicopter Electromagnetic Data as External Variable to Predict Groundwater Electrical Conductivity in the Crystalline Domain of Juá District, Ceará, Brazil **77**
4.1. Introduction *78*
4.2. Data Sets *78*
4.2.1. Helicopter Electromagnetic Data *78*
4.2.2. Water Well Data *79*
4.3. Geostatistical Analysis *82*
Electrical Conductivity-EC Analysis in Drilled Wells *83*
Preparing EC Water Data for Interpolation – The Primary Variable *84*
Helicopter Electromagnetic Data-HEM as the Secondary, Drift Variable *85*
4.3.1. Kriging Model with External Drift *88*
The Interpolation by Kriging with External Drift *88*
4.3.2. Stochastic Simulations *90*
Transforming the well water EC variable – De-clustering and Anamorphosis *90*
Simulation with External Drif *91*

4.4. Validation of the Methods *94*

4.5. Predicting Good Water-Quality Region *94*

4.6. Conclusions *96*

5. Data-Driven Spatial Analysis for Groundwater Exploration **98**

5.1. Introduction *99*

- *5.1.1. The Probability Ratio Method* *101*
- *5.1.2. The Weights of Evidences Method* *104*
- *5.1.3. Data Set Preparation* *107*

5.2. Predictive Groundwater Models Based on Probability Ratio Technique *109*

- *5.2.1. Training Sites* *109*
- *5.2.2. Evidential Themes in Probability Ratio Modeling* *112*
- *5.2.3. High-Yield Groundwater Favorability Models* *114*
- *5.2.4. Low-Yield Groundwater Favorability Models* *116*

5.3. Predictive Groundwater Models Based on Weights of Evidences Technique *118*

- *5.3.1. Training Sites* *118*
- *5.3.2. Evidential Themes* *118*
- *5.3.3. High-Yield Groundwater Favorability Models* *122*
- *5.3.4. Low-Yield Groundwater Favorability Models* *125*
- *5.3.5. Validity of Weights of Evidence Groundwater Favorability Models* *132*

5.4. Comparisons between Probability Ratio and Weights of Evidences Predictive Models *132*

- *5.4.1. What Is The Final Groundwater Predictive Model to Follow?* *135*

6. Discussões e Conclusões **139**

7. Referências Bibliográficas **143**

Anexo 1 – Conceitos Teóricos

Técnica de Terraceamento em Geofísica

Mapa Pseudo-Gravimétrico

Aquisição pelo Método eletromagnético-EM

Condutividade Elétrica Aparente

Profundidade de Investigação dos Sensores Eletromagnéticos

Deriva na Geoestatística

Annex 2 - Probability Ratio Maps of Geophysical, Structural and Alteration Mineral Evidences Associated with Groundwater Potential

Annex 3 - Geophysical, Structural and Alteration Mineral Evidences used for Groundwater Modeling with Weights of Evidences Technique

LISTA DE FIGURAS - CAPÍTULO 1

Figura 1.1 – Localização da área de estudo. Adicionalmente, o modelo digital de terreno da Folha Irauçuba (dados do sensor SRTM), destacando a área do Juá (Polígono vermelho)......... 4

Figura 1.2 – Localização dos aerolevantamentos na área de estudo: NUCLEBRAS/Itatira-B (polígono cinza); PROASNE no Estado do Ceará (quadrado preto). (Modificado de CPRM, 2007b e Lasa, 2001 7

Figura 1.3 – Plataforma utilizada no aerolevantamento do PROASNE. Detalhe do helicóptero e do *bird* que continha os sensores eletromagnético e magnético. O sensor VLF situava-se no cabo a meia distância entre a aeronave e o *bird* (Lasa, 2001)............................... 8

Figura 1.4 – Composição falsa-cor das razões de bandas para a cena do sensor ETM$^+$/Landsat-7 recortada para a área de estudo de Juá. Ordem: vermelho_R (3/1); verde_G (4/2); azul_B (5/7). Coordenadas UTM-SAD-69, zona 24-Sul. Drenagem em azul .. 11

Figura 1.5 – Imagem das combinações realizadas com as imagens filtradas por passa-baixa e reclassificadas das razões de bandas 3/1, 4/2 e 5/7 do sensor ETM$^+$/Landsat-7 para a área de Juá, referente ao conteúdo de minerais de óxido de ferro, vegetação e minerais com hidroxila. Tabela para identificação das cores. Coordenadas UTM-SAD-69, zona 24sul. Drenagem em azul... 12

Figura 1.6 - Localização de poços e a relação positiva da produtividade com baixo morfoestrutural no cristalino de São Paulo (Mandrucci, 2003) 18

Figura 1.7 - Modelos tectônicos em níveis crustais rasos para a região de João Câmara-RN e direções de abertura de fendas (Coriolano, 2002)... 18

Figura 1.8 - Poço não produtivo perfurado de acordo com anomalias condutivas eletromagnéticas aerogeofísicas e eletrorresistividade em Juá, Ceará (Souza Filho *et al.*, 2006)............. 20

LISTA DE FIGURAS - CAPÍTULO 2

Figura 2.1 – Caracterização morfológica da Folha Irauçuba e área de estudo de Juá (polígono vermelho), modificado de Brandão (2003a). Observa-se a área de estudo dentro de uma superfície moderadamente conservada.. 23

Figura 2.2 – Modelo de elevação topográfica da área do Juá (dados originários do levantamento aerogeofísico PROASNE, 2001). Drenagem em azul, tendo o riacho e açude São Gabriel ao centro e açude Cairú a Noroeste e estrada em linha marrom. Falsa iluminação com declinação 315^0 Az. e inclinação 45^0Az 24

Figura 2.3 – Subclimas e pluviometria na área da Folha Irauçuba e de Juá (polígono vermelho). Modificado de Ceará (1997 in Souza Filho, 1998).. 25

Figura 2.4 – Mapa geológico simplificado de Irauçuba com os seus principais traços estruturais. Área de Juá indicada pelo polígono em azul. Os poços estão indicados em azul e as fontes em vermelho. Modificado de Souza Filho (1998) e Veríssimo e Feitosa (2002) 27

Figura 2.5 - Mapa geológico simplificado da área de estudo de Juá, Irauçuba-CE. Modificado de Souza Filho (1998).. 28

Figura 2.6 - Carta hidrogeológica da Folha Irauçuba (Feitosa, 1999). Área de Juá indicada pelo polígono vermelho... 29

Figura 2.7 - Modelo hidrogeológico conceitual elaborado para a área de Juá, Irauçuba-CE (Modificado de Feitosa *et al.*, 2000, in Souza Filho et al, in press). As profundidades não estão em escala 30

Figura 2.8 - Sistemas hidrogeológicos na área de Juá, Irauçuba-CE. Critérios de classificação baseados no trabalho de Feitosa (2000). Os Poços identificados referem-se aos utilizados nas modelagens de favorabilidade para água subterrânea................................. 32

LISTA DE FIGURAS - CAPÍTULO 3

Figure 3.1 – The beginning of AEM systems and surveys. On to the left is the original schematic diagram (with the signature of the inventor) showing the transmitter coil (24), powered by an oscillator (26) and the towed receiver coil (27), connected to detector electronics (30, 31). On the right is the photo of the wood framed Anson aircraft showing the receiver bird below the fuselage (Fountain, 1998).. 35

Figure 3.2 – Maps of magnetic anomaly field of Itatira-B Survey: a) IGRF-reduced raw data; b) Microleveled data. Red polygon is the Juá study area 39

Figure 3.3 – Maps of magnetic anomaly field of Itatira-B Survey: a) Reduced to the magnetic north pole-RTP map; b) RTP-magnetic field filtered to sources between 2000 m and 400 m depth. Red polygon is the Juá study area 40

Figure 3.4 – Radially averaged amplitude spectrum of the gridded reduced-to-the-pole Itatira magnetic data 41

Figure 3.5 – RGB Color composite of Itatira-B radiometric data, with potassium in red, thorium in green and uranium in blue. Red polygon is the study area of Juá 42

Figure 3.6 – Itatira-B radiometric data resampled to 25-m cell-size grid and trimmed to Juá study-area. a) Potassium intensity in counts per second. b) Thorium intensity in counts per second. Drainage and reservoirs are indicated by blue lines... 43

Figure 3.7 – Itatira-B radiometric data resampled on 25-m cell-size grid and trimmed to Juá study-area. Uranium intensity in CPS. Drainage and reservoirs are indicated by blue lines 44

Figure 3.8 – Comparison of reductions to magnetic north pole filters applied on Juá magnetic residual field grid: a) good result using Phillips (1997) algorithm with amplitude correction of 79.11°; b) bad result using Oasis Montaj algorithm with amplitude correction of 70 ° plus a cosine low-pass filter at 130° Azimuth. Red traces mark artifacts with direction parallel to the geomagnectic declination, generated after the application of Oasis Montaj's algorithm.. 46

Figure 3.9 – Radially averaged amplitude spectrum of the gridded reduced-to-the-pole Juá magnetic data. 47

Figure 3.10 – Juá reduced-to-pole magnetic anomaly data filtered to depth ranges from: a) 20 m to 60 m and b) from 20 m to 270 m. Application of Phillips (1997)'s algorithm............. 48

Figure 3.11 – Juá high-resolution magnetic potential map applied to the magnetic anomaly grid of sources located within 60 m to 270 m depth 49

Figure 3.12 - Juá high-resolution magnetic data processed as: a) Terrace-magnetization map using the terracing technique of Cordell and McCafferty (1989), and b) High-resolution 2000-m-depth layer grid after the subtraction of the regional 2000-m-depth grid from higher-resolution anomaly grid. The dots represent locations of drilled water-wells. Note that in the map (b), the most productive wells (surrounded by a red circle) are in the border of an important negative gradient, oriented WNW-ESE (marked by a green ellipse)........................ 51

Figure 3.13 – Juá high-resolution magnetic data. Vertical derivative map (nT/m) calculated from the magnetic residual field filtered to 60-m-depth layer. Map shows high-frequency information, related to shallow sources and boundaries between geomagnetic units.................52

Figure 3.14 – Apparent conductivity (mS/m) maps gridded from the Juá helicopter electro-magnetic data-HEM: a) HEM – 33000 Hz, coplanar coil configuration, and it is more indicative of soil horizon conductivity; b) HEM – 4500 Hz, coaxial coil configuration, and is more related to rock and cross-cutting gradients conductivity; c) HEM – 900 Hz, coplanar coil configuration, which better depicts geoelectric units related to lithology........... 54

Figures 3.15 - Sensitivity of the HEM sensor for the Juá area, in respect to the basement resistivity based in one-layer model. Top layer with fixed resistivity of 33 ohm-m (30 mS/m) and 15 m thick. Note that the HEM sensor does not distinguish basement resistivity greater than 1000 ohm-m 55

Figure 3.16 - Map of the χ ratio (I/Q), calculated for the HEM-900 Hz frequency data: a) I/Q ratio for the coplanar configuration; b) I/Q ratio for the coaxial configuration. Note that N-S- oriented conductive gradients that have high χ ratio are few comparatively to the same calculation for the HEM-4500 Hz frequency data (Figure 3.17). A strip of low χ ratio, oriented parallel to flight line in the center of the area, is caused by spurious values within the data 61

Figure 3.17 - Map of the χ ratio, calculated for the HEM-4500 Hz data: a) Ip/q ratio for the coplanar configuration; b) Ip/q ratio for coaxial configuration. Gradients related to cross-cutting structures are better defined than in χ ratio map for 900 Hz data 62

Figure 3.18 - Map of the χ ratio, calculated for the HEM-33000 Hz coplanar data 63

Figure 3.19 – Variability map of χ ratio for the HEM-900 Hz data, calculated by the subtraction of coaxial and coplanar χ ratios: a) Total variability χ ratio for the HRM-900 Hz data; b) Enhancement of the variability higher than 10. The anomalous regions in the northern part of the area correlate with granites and migmatites units 64

Figure 3.20 – Variability map of χ ratio for the HEM-4500 Hz data, calculated by the subtraction of coaxial and coplanar χ ratios. The small difference of χ ratios means that the conductive properties are more homogenous at the exploration depth for these data (less than 24 m, according to anomaly depths of calculated by forward modeling and also interpreted from Lasa, 2001), than to the exploration depth related to the 900 Hz frequency data 65

Figure 3.21 - Apparent conductivity map from Coplanar 900 Hz data (mS/m) and the geology for Juá area. Black square is the subset area where inverse modeling was calculated 66

Figures 3.22 - Least-squares inversion model for the Juá central-area. One layer over the half-space basement using in-phase and quadrature data from the three coplanar frequencies. Black lines in (b) are NNE-SSW trends with less resistivity, and with correspondence in the top-layer. Drainage in blue lines 68

Figure 3.23 – Spatial association between lithology and the higher classes of the terrace of the HEM-4500 Hz frequency data calculated by the probability ratio technique. Terrace values are multiplied by 10. Undefined association (values < 2) of Pbgn and Pggn with conductive terrains, but positive association of Pcgm, Pxt and Pqt 70

Figure 3.24 – Spatial association between lithology and the lower classes of the terrace of the HEM-4500 Hz frequency data calculated by the probability ratio technique. Terrace values are multiplied by 10. Ngra is positively associated with low conductivity, whereas Pbgn and Pggn
are undefined 70

Figure 3.25 – Spatial association between lithology and the negative classes of the terrace of the magnetic data calculated by the probability ratio technique. Ngra and Pmig are positively associated with magnetic anomalies, whereas Pbgn is not.......................................71

Figure 3.26 – Spatial association between lithology and the positive classes of the terrace of the magnetic data calculated by the probability ratio technique. Pqt and Pxt are associated with non-magnetic anomalies 71

Figure 3.27 - Geologic map of Juá study-area, modified from Souza Filho *et al.* (2002). Black lines are structural lineaments. Note that lineament orientations do not match magnetic gradients of shallow source in Figure 3.22, but lithology has good correspondence to geomagnetic units of Figure 3.28... 72

Figure 3.28 - Juá airborne filtered magnetic data to 60 m depth. Shallow magnetic gradients: non-magnetic in white and highly magnetic in red (ridges). Shaded relief illumination at 45^o inclination and, declined to 315 azimuth. Drainage is in blue. Gradients do not match lineament orientation in Figure 3.27. Circles mark geomagnetic units off-sets due to WNW-ESE and NE-SW gradients...73

Figure 3.29 - Comparison between Juá geologic map and the vertical derivative of 60 m-filtered magnetic anomalies. Note the good correspondence between them. Black contours are geomagnetic units extracted from horizontal gradient amplitude 74

Figure 3.30 - Reclassified filtered 60 m-depth magnetic data (nT) overlaid by the geologic map of Juá. Note the correspondence of migmatite (Pmig) with alternate high- and low-magnetic anomaly classes, and the calc-silicate gneiss with moderate magnetic classes.......... 75

LISTA DE FIGURAS - CAPÍTULO 4

Figure 4.1 – The Juá area: a) Simplified geologic map, modified from Souza Filho (1998); b) Apparent electrical conductivity map calculated from HEM-4500 Hz frequency at coaxial mode (after Lasa 2001). Locations of water wells are shown in dots (drilled before year 2000) and crosses (drilled after year 2000) and identified by numbers as described in Tables 4.1 and 4.2. 80

Figure 4.2 – Classes of electrical conductivity (mS/m) for Juá water well data: Min. = 117 mS/m; max. = 1104 mS/m; mean = 480.2 mS/m; standard deviation = 306 83

Figure 4.3 - Relation between groundwater salinity-TDS and electrical conductivity for Juá water data 84

Figure 4.4 – Comparison of electrical conductivity measured in well data and calculated from HEM-4500 Hz data. Data are ordered according increasing values of HEM data. No direct relationship is apparent present between HEM data and electrical conductivity in wells 86

Figure 4.5 – Spatial variability of electrical conductivity of Juá well data: a) experimental semivariograms calculated at different directions; b) modeled semivariogram resulted from combination of: i) spherical model, with a nugget = 0, range = 3,500 m, and sill = 8500); ii) nugget model = 25000; iii) spherical model, with range = 10000 m, sill = 9000) 87

Figure 4.6 – Histogram for HEM data at 4500 Hz frequency: minimum = 0.2 mS/m; maximum = 145.4 mS/m; mean = 10.36 mS/m; standard deviation = 9.89 mS/m 87

Figure 4.7 – Groundwater EC distribution in the Juá area: a) Map resulted from the use of Kriging with HEM data as an external drift variable. Values in mS/m, black squares indicate locations of drilled wells; b) Histogram of kriged data, min. 127 mS/m, max. 2084 mS/m, mean 475 mS/m, standard deviation = 147 89

Figure 4.8– Cumulative frequency for original Juá EC water data. Anamorphosis function (dot curve) applied onto the original data (step function) 90

Figure 4.9 – Probability scenarios for groundwater electrical conductivity (mS/m) in the Juá area: a) 25% probability map; b) 75% probability map. Black squares refer to drilled wells and red dots are the new wells used for validation and the red dots are the new drilled wells used for validation. Less saline groundwater were mapped in the central-south region 92

Figure 4.10 – Variability of groundwater EC after 100 simulations with external drift for the Juá area: a) standard deviation; b) inter-quartile range. Black squares refer to locations of conditioning drilled wells. More uncertainties where there is no well information 93

Figure 4.11 – Comparisons among groundwater EC (mS/m) measured in the 2005 campaign and the simulations/interpolations with 2000 data: a) new drilled wells; b) new dug wells. The bars indicate standard deviation for 100 electrical conductivity simulations. 96

Figure 4.12 – Probability cut-off map for 200 mS/m conductivity for Juá groundwater after 100 simulations with HEM external drift. Values in percentage, black squares refer to conditioning drilled wells. The central region has the most potential for this cut-off, varying from yellow to red colors 97

LISTA DE FIGURAS - CAPÍTULO 5

Figure 5.1 - Flowchart of the probability ratio modeling to produce groundwater predictive maps for the Juá area 103

Figure 5.2 - Sequential procedures adopted in Weights-of-Evidence modeling (Modified from Masetti *et al.*, 2007) 104

Figure 5.3 – Location of wells classified by water yield in the Juá area. The information was used in predictive groundwater modeling using the probability ratio mapping technique 111

Figures 5.4 – Predictive groundwater models calculated from the sum of positive values for all data probability ratios: a) high yield favorability model; b) low-yield favorability model 115

Figure 5.5 – Locations of yield-well classes in relation to classes of high-yield groundwater favorability model. The success of the model is determined by the clear separation between locations of low- and high-yield wells in the least favorable and most favorable model classes 116

Figure 5.6 – Locations of yield-well classes in relation to classes of low-yield groundwater favorability model. The predominance of low-yield wells in the least favorable class is an indication the model was not successful to low-groundwater favorability. Yet high-yield wells predominated in non-expected classes of medium favorability 117

Figure 5.7 - High-yield groundwater *Model A1* for Juá area: a) Cumulative distribution of the posterior probabilities; b) Map representation of the posterior probabilities. Post-probability ranges: 0 – 0.05 –Gray; 0.051 – 0.5 –Blue; 0.51 – 0.8 –Green; 0.81 – 0.95 –Orange; 0.951 – 1.0 –Red 127

Figure 5.8 - High-yield groundwater *Model A2* for Juá area: a) Cumulative distribution of the posterior probabilities; b) Map representation of the posterior probabilities. Post-probability ranges: 0 – 0.05 –Gray; 0.051 – 0.5 –Blue; 0.51 – 0.8 –Green; 0.81 – 0.95 –Orange; 0.951 – 1.0 –Red 128

Figure 5.9 - High-yield groundwater *Model A3* for Juá area: a) Cumulative distribution of the posterior probabilities; b) Map representation of the posterior probabilities. Post-probability ranges: 0 – 0.05 –Gray; 0.051 – 0.5 –Blue; 0.51 – 0.8 –Green; 0.81 – 0.95 –Orange; 0.951 – 1.0 –Red 129

Figure 5.10 - Low-yield groundwater *Model B1* for Juá area: a) Cumulative distribution of the posterior probabilities; b) Map representation of the posterior probabilities. Post-probability ranges: 0 – 0.05 –Gray; 0.051 – 0.5 –Blue; 0.51 – 0.8 –Green; 0.81 – 0.95 –Orange; 0.951 – 1.0 –Red 130

Figure 5.11 - Low-yield groundwater *Model B2* for Juá area: a) Cumulative distribution of the posterior probabilities; b) Map representation of the posterior probabilities. Post-probability ranges: 0 – 0.05 –Gray; 0.051 – 0.5 –Blue; 0.51 – 0.8 –Green; 0.81 – 0.95 –Orange; 0.951 – 1.0 –Red 131

Figure 5.12 – Representation of lithologic units and the groundwater favorability models: a) Groundwater model A1 based on the weights-of-evidence technique; b) Groundwater model based on the probability ratio technique 134

Figure 5.13 - Combinations of high-yield and low-yield groundwater favorability models, provided by the WofE technique, respectively models A1, A2 and A3 and models B1 and B2 137

Figure 5.14 - Combined map between the five favorability classes of WofE model A2 and the yield class 4-Pr model, according to the conditional operator of Either Pr-WofE IF Pr>WofE ELSE WofE. Regions not mapped as favorable in WofE model (e.g. northwestern area) were better ranked 138

LISTA DE TABELAS

Tabela 1.1 – Coordenadas da área do Juá. Datum *South America*-1969, zona 24-sul 4

Tabela 1.2 - Características de produtividade entre províncias hidrogeológicas do Nordeste e Sudeste do Brasil 17

Tabela 2.1 – Características construtivas e hidrodinâmicas de 20 poços em Juá, Irauçuba-CE. Modificado de Veríssimo e Feitosa (2002) e Souza Filho et al. (2002) 33

Table 3.1 – Estimated depth to the top of magnetic sources based on a half-layer model from the Itatira airborne survey calculated with the matched filtering technique (Syberg, 1972). Depth values are rounded to the nearest 10s of meters 41

Table 3.2 – Estimated depth for wavelength intervals of magnetic sources from Juá helicopter survey calculated with the matched filtering technique (Syberg, 1972). Depth values are rounded to the nearest 10s of meters 48

Table 3.3 – Skin depth estimates for the Juá HEM data, based on equation in Telford *et al.* (1984). Note the differences in signal penetration due to acquisition frequency and conductivity variation 57

Table 4.1 – Juá well data from year 2000 campaign: EC = electrical conductivity (mS/m); W. Level = water level (m); Suberm. Pump = submersible pump (Modified from Veríssimo and Feitosa 2002) 81

Table 4.2 – Juá well data from 2005 campaign.. 82

Table 4.3 – Comparisons between water electrical conductivity (EC) measured in wells and calculated from HEM-4500 Hz data. Both measurements are in mS/m 85

Table 5.1 - Cross-tabulation of training points and binary evidential theme (present or absent). N_{pix} indicates the number of pixels (Mathew *et al.*, 2007) 105

Table 5.2a – Well data used in Probability Ratio modeling 110

Table 5.2b - Yield classes for Juá area 110

Table 5.3 - Data sets used in Probability Ratio modeling and their association with water wells productivity. Fe(OH) = iron-oxide or iron–hydroxide mineral 113

Table 5.4 – Juá well data: Yield (m^3/h); EC = electrical conductivity (mS/m): a) high-yield wells class; b) low-yield wells class. (Adapted from Veríssimo and Feitosa, 2002 and own data) 119

Table 5.5 - Themes used for modeling high-yield groundwater favorability. SD = standard deviation 120

Table 5.6 - Themes and parameters used to model low-yield groundwater favorability......... 121

Table 5.7 - Posterior-probability values for model A1, classified according to arbitrary divisions. The presence of high- and low- yield wells was quantified for each class............. 122

Table 5.8 - Tests of conditional independence-CI among two or more evidences calculated for model A1. Training points n = 8; Expected Points, T = 5.8; Difference T-n = -2.2; Standard Deviation of T, Tsd = 2.73 123

Table 5.9 - Post-probability values for *Model A2*, classified according to arbitrary divisions. The presence of high- and low- yield wells was quantified for each class............. 123

Table 5.10 - Conditional independence tests calculated for model model A2. Training points n = 8; Expected points T = 6,0; Difference T-n = -2,0; Standard deviation of T, TSD = 2,622 124

Table 5.11 - Probability classes for model A3, regarding high-yield wells. The presence of high- and low- yield wells was quantified for each class 124

Table 5.12 - Conditional independence tests calculated for model model A3. Training points n = 8; Expected points T = 6.1; Difference T-n = -1.9; Standard deviation of T, TSD = 2.733 124

Table 5.13 - Probability classes for model B1, regarding low-yield wells. The presence of high- and low- yield wells was quantified for each class 125

Table 5.14 - Conditional independence tests applied to model B1 regarding low-yield favorability, according to Bonham-Carter (1994) CI-ratio and the Agterberg and Cheng (2002) CI-test. Training points n = 12; Expected points T = 6.7; Difference T-n = -53; Standard Deviation of T, TSD = 1.612 125

Table 5.15 - Probability classes for model B2, regarding low-yield wells. The presence of high- and low- yield wells was quantified for each class 126

Table 5.16 - Conditional independence tests according Bonham-Carter (1994) CI-ratio and the Agterberg e Cheng (2002) CI-test applied to model B2 regarding low-yield favorability. Training points n = 12; Expected training points T = 6.8; Difference, T-n = -5.2; Standard Deviation of T, TSD = 2.102..126

LISTA DE MAPAS ANEXOS

MAPAS DO ANEXO - 2

Annex 2.1 – Weights of probability ratio referred to the spatial association between magnetic the field down to 60 m –depth and well yield classes for the Juá area: a) Full-range values of probability ratio as a chart representation; b) Map representation of reclassified values of probability ratio relative to the yield class 4. Negative values are the reciprocal negative of original values range from 0 to 0.99.

Annex 2.2 – Weights of probability ratio referred to the spatial association between the terracing of magnetic data and well yield classes for the Juá area.

Annex 2.3 – Weights of probability ratio referred to the spatial association between the terracing of electrical conductivity and well yield classes for the Juá area.

Annex 2.4 – Weights of probability ratio referred to the spatial association between the electrical conductivity from HEM-33000 HZ data and well yield classes for the Juá area.

Annex 2.5 – Weights of probability ratio referred to the spatial association between the electrical conductivity from HEM-4500 HZ data and well yield classes for the Juá area.

Annex 2.6 – Weights of probability ratio referred to the spatial association between the electrical conductivity from HEM-900 HZ data and well yields classes for the Juá area.

Annex 2.7 – Weights of probability ratio referred to the spatial association between the electrical conductivity from the subtraction of HEM-4500 – HEM-900 HZ data and well yield classes for the Juá area.

Annex 2.8 – Weights of probability ratio referred to the spatial association between the map of relative contents of Fe-(OH) oxide minerals, vegetation and clay-minerals (a composite-band ratio product of ETM+/Landsat-7 data) and well yield classes for the Juá area.

Annex 2.9 – Weights of probability ratio referred to the spatial association between potassium content and well yield classes for the Juá area.

Annex 2.10 – Weights of probability ratio referred to the spatial association between uranium content and well yield classes for the Juá area.

Annex 2.11 – Weights of probability ratio referred to the spatial association between thorium content and well yield classes for the Juá area.

Annex 2.12 – Weights of probability ratio referred to the spatial association between non-magnetic gradients and well yields classes for the Juá area.

Annex 2.13 – Weights of probability ratio referred to the spatial association between magnetic gradients and well yields classes for the Juá area.

Annex 2.14 – Weights of probability ratio referred to the spatial association between non-electrically conductive gradients and well yield classes for the Juá area.

Annex 2.15 – Weights of probability ratio referred to the spatial association between electrically conductive gradients and well yield classes for the Juá area.

Annex 2.16 – Weights of probability ratio referred to the spatial association between structural lineaments and well yield classes for the Juá area.

MAPAS DO ANEXO - 3

Annex 3.1 - Map of the magnetic residual field at 60 m depth of Juá study area.

Annex 3.2 - Terracing from magnetic field (nT) filtered down to 270 m depth of Juá study area.

Annex 3.3 - Apparent electrical conductivity map from HEM 900 Hz data (mS/m) of Juá study area.

Annex 3.4 - Apparent electrical conductivity map from HEM 33000 Hz data (mS/m) of Juá study area.

Annex 3.5 - Map of interpreted magnetic gradients at 60 m depth of Juá study area.

Annex 3.6 - Map of non-magnetic gradients at 60 m depth of Juá study area.

Annex 3.7 - Map of electrically conductive gradients of Juá study area.

Annex 3.8 - Map of electrically non-conductive gradients of Juá study area.

Annex 3.9 - Map of potassium content (counting per second-CPS) of Juá study area.

Annex 3.10 - Map of thorium content (counting per second-CPS) of Juá study area.

Annex 3.11 - Map of Fe-oxide (goethite) mineral content, plus Al-hydroxide mineral (kaolinite-smectite) content of Juá study area.

Annex 3.12 - Map of Al-hydroxide mineral (kaolinite-smectite) content of Juá study area.

Annex 3.13 - Map of proximity zones of 100 m from structural lineaments depicted from the digital elevation model of SRTM, ETM+/Landsat images and aerial-photographs of Juá study area.

Annex 3.14 - Map of multiple proximity zones from structural lineaments depicted from Landsat images and aerial-photographs for Juá study area.

Annex 3.15 - Map of slope aspect (Azimuth) depicted from the digital elevation model of SRTM images for Juá study area.

Annex 3.16 - Map of apparent electrical conductivity (mS/m) from the difference between HEM 4500 Hz and HEM 900 Hz data of Juá study area.

1 - INTRODUÇÃO

1.1 – Apresentação e Justificativas

O nordeste do Brasil possui mais da metade do seu território sobre rochas do embasamento cristalino de natureza granito-gnaisse-migmatítica. Os solos são pouco espessos, os são rios intermitentes, a vegetação é do tipo caatinga e as chuvas ocorrem sazonalmente, concentradas nos quatro primeiros meses do ano. Nestes terrenos, a água subterrânea é salina e rara. No Ceará, os processos de desertificação constituem-se outro agravante.

Estas características naturais posicionam o semi-árido brasileiro (um dos mais populosos do planeta, com aproximadamente 45 milhões de habitantes - dados CPRM, 2007a) numa situação desfavorável ao abastecimento de água. No interior do estado do Ceará, a ocupação territorial é difusa, onde lugarejos (com cinco a trinta casas) estão separados por dezenas de quilômetros.

Tais fatos, aliados à conjuntura socioeconômica da região, dificultam o fornecimento de água pelo poder público no modo tradicional, ou seja, pelo sistema reservatório-adutora, como existem para as cidades. A solução encontrada provém da perfuração de poços, do armazenamento da água da chuva, de carros-pipa e, mais recentemente, da construção de barragens submersas em aluviões de drenagens intermitentes.

O programa de cadastramento de fontes de água subterrânea no semi-árido nordestino executado pela CPRM desde 1998 contabilizou pouco mais de 87 mil poços. No Estado do Ceará foram cadastrados 11.889 poços, sendo 1.642 (15%) abandonados e, em termos de qualidade, 4.636 (39%) eram salgados (> 1500 mg/l de sais dissolvidos). Até 1990, as principais razões para a não-instalação de poços no Nordeste eram a baixa produtividade e água salgada. Atualmente, os programas governamentais de convivência com a seca incorporaram inovações tecnológicas como bombas injetoras e submersas, que se adequam às baixas vazões entre 300 e 500 l/h e o uso de sistemas dessalinizadores de pequeno e médio porte.

As técnicas de locação mais utilizadas baseiam-se na interpretação de estruturas rúpteis e da morfologia (ex.: Neves, 2005) ou adicionando estudos de geofísica terrestre através dos métodos eletromagnético indutivo e de eletrorresistividade, a exemplo de Pinéo (2005). No entanto, ainda há dificuldades para locação devido à restrita área de pesquisa (técnicas de caminhamento geofísico), potência de sinal captado no caso do *Very Low Frequency*-VLF, ruídos antrópicos e naturais que interferem na penetração do sinal (camada argilosa espessa ou cercas de fazendas no caso do eletromagnético e solos secos no caso de eletrorresistividade).

Considerando-se o volume de recursos disponibilizados nos programas emergenciais contra a seca e perspectivas de perfuração de algumas centenas de poços ao ano (ao custo unitário estimado em R$ 2.500,00 por perfuração e R$ 1.500,00 por instalação), evidencia-se a importância da melhoria de técnicas de locação, pois ainda não garantem alta produtividade em terrenos cristalinos.

Por outro lado, a integração de dados em Sistemas de Informações Geográficas para o estudo de favorabilidade para água subterrânea é relativamente recente no Brasil e não existe uma técnica consensual. Poucos trabalhos integraram dados aerogeofísicos aos geológicos e cadastros de poços, tal como Mandrucci *et al.* (2003) em São Paulo, Coriolano (2002) no Rio Grande do Norte e Pinéo (2005) no Ceará.

No exterior, há considerável número de trabalhos publicados, inclusive séries especiais de revistas especializadas como no *Hydrogeology Journal* (2007). Simpósios são organizados exclusivamente para divulgar a aplicação de aerogeofísica em estudos ambientais e hidrogeológicos como o SAGEEP, organizado pela *Engineering and Environmental Geophysical Society-EEGS* (2007). A aerogeofísica aplicada a estudos ambientais e hídricos (hidrogeofísica aérea, Paine and Minty, 2005) compõe programas governamentais que prevêem levantamentos magnéticos, radiométricos, eletromagnéticos e gravimétricos detalhados como na Austrália (Wilkinson *et al.,* 2005; Coppa *et al.*, 1998), na China (Meng *et al.*, 2006), na América do Norte (Smith *et al.*, 2000; Pine e Minty, 2005) e na Suécia (SGU, 2007). No Brasil, a maioria dos trabalhos de integração geológica-aerogeofísica está voltada para a área da exploração mineral com o uso de levantamentos magnético, radiométrico e eletromagnético em detalhe (Silva, 1999; Fuck, 2000, dentre outros) e magnéticos e radiométricos em escala regional (CPRM, 2007b).

O levantamento aerogeofísico disponível para o desenvolvimento desta tese destaca-se pela alta resolução espacial, variedade de fontes de dados e freqüências amostradas. O mesmo pode ser afirmado sobre os detalhes de informações hidrogeológicas dos recentes trabalhos do Serviço Geológico do Brasil – CPRM na região.

Apesar do processamento e interpretação inicial dos dados realizados pela CPRM (Oliveira *et al.*, 2002; Souza Filho *et al.*; 2003 e Souza Filho *et al.*, 2006a), estes trabalhos não utilizaram todo o estado da arte disponível para o processamento, a modelagem e a integração destes dados. O refinamento dos dados e a aplicação de ferramentas de análise espacial permitiram a seleção das variáveis geofísicas relacionadas ao arcabouço hidrogeológico, bem como a geração de novos critérios para a integração de dados nesta área do conhecimento.

Cabe reforçar que a utilização de aerolevantamento geofísico e, posteriormente a aplicação de análise espacial para gerar mapas de favorabilidade hidrogeológica têm um grande potencial no Brasil, principalmente no semi-árido. No entanto, as áreas-piloto devem ser consideradas como o primeiro passo para a discussão sobre o uso destas ferramentas e somente então, recomendar ou não a sua aplicação como um dos requisitos para compor as políticas públicas nesta região tão carente do nosso país.

1.2 - Objetivos

O objetivo desta tese é identificar técnicas de processamento de dados aerogeofísicos adequadas à prospecção hídrica e integrar os produtos derivados com dados geológicos e hidrogeológicos através da utilização de análise espacial para mapear condições favoráveis de armazenamento e salinidade da água subterrânea em terrenos cristalinos.

Os **objetivos específicos** incluem:

(a) Mapear estruturas regionais e locais, utilizando dados de magnetometria e de sensores remotos de alta resolução espacial, com o intuito de se definir o arcabouço estrutural associado com a água subterrânea;

(b) Identificar regiões eletricamente condutoras, associadas à presença de água subterrânea, bem como ao grau de salinidade;

(c) Uso de técnicas geoestatísticas de interpolação e simulação estocástica para estimar a variabilidade da salinidade, a partir do estudo da condutividade elétrica da água subterrânea medida em poços e a condutividade elétrica do solo (informação aerogeofísica);

(d) Aplicar as técnicas de análise espacial por razões de probabilidade e pesos de evidências com o intuito de produzir mapas de favorabilidade convenientes para a interpretação geológica e análise do potencial hidrogeológico na área de estudo.

1.3 – Localização da Área de Estudo

A área de estudo localiza-se no Distrito de Juá (Tabela 1.1), no município de Irauçuba, norte do Estado do Ceará e está compreendida na Folha SA.24-Y-D-V, Irauçuba (Figura 1.1). A partir da capital Fortaleza (distante 160 km a leste), o acesso à região é feito pela BR-222 e por estradas não pavimentadas.

Tabela 1.1 – Coordenadas da área do Juá. Datum *South America*-1969, zona 24-sul.

PONTOS LIMITES	LAT. SUL	LONG. OESTE	UTM Y	UTM X
SUPERIOR ESQUERDO	-3^{o} 48` 59”,86	-39^{o} 54’ 29”,33	9578087.50	399487.50
INFERIOR DIREITO	-3^{o} 56’ 39”, 42	-39^{o} 47’ 50”,23	9563987.50	411487.50

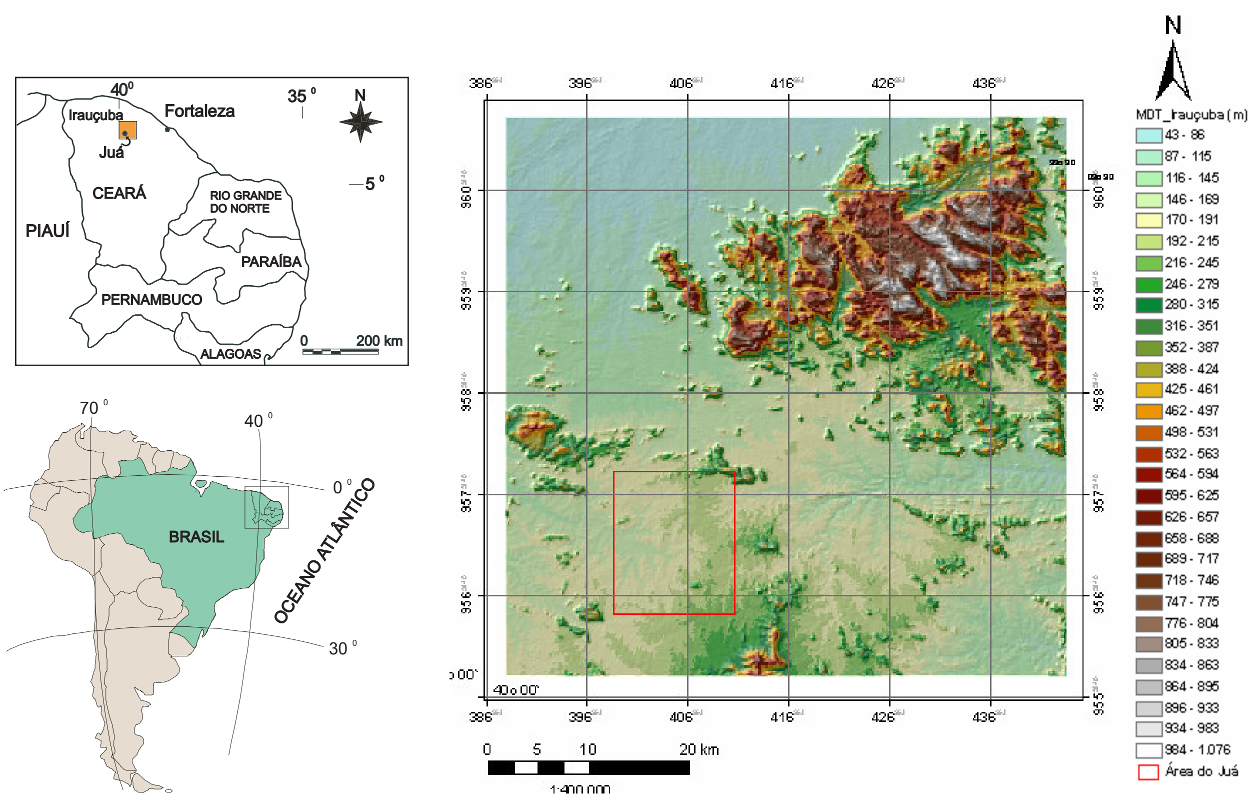

Figura 1.1 – Localização da área de estudo e o modelo digital de terreno da Folha Irauçuba (dados do sensor SRTM), destacando a área do Juá (polígono vermelho).

1.4 – Bases de Dados

O desenvolvimento desta tese envolveu uma série de métodos objetivando o processamento, integração e interpretação dos dados adquiridos ou disponíveis de projetos anteriores (Souza Filho, 1998; Souza Filho *et al.*, 2003 e Souza Filho *et al.*, 2006a, entre outros).

Do volume de informações contidas nesses projetos, destacam-se os dados eletromagnéticos e magnéticos aéreos de alta resolução, destinados a conduzir futuras campanhas de locação de poços e que foi o objeto principal deste trabalho. Todos os dados apresentados nesta tese estão referenciados para o Datum *South America*-1969, Projeção Universal de Mercartor-UTM, zona 24-sul.

Geológicos e Estruturais

Levantamentos geológico-estruturais foram executados em várias etapas:

a) durante o desenvolvimento da Dissertação de Mestrado de Souza Filho (1998) na área em questão;

b) através de projetos da CPRM - Residência de Fortaleza e da Cooperação Brasil-Canadá (PROASNE, 2007) entre 1999 e 2004 (Souza Filho, 2000; Souza Filho et al., 2003).

As campanhas de campo objetivaram o mapeamento geológico, o reconhecimento de estruturas rúpteis e a caracterização geotécnica de maciços rochosos no auxílio ao cadastro de poços de água, levantamentos geofísicos terrestres e perfuração de poços. As escalas de trabalho variaram desde 1: 100.000 até 1: 2.000, com visitas a mais de 300 afloramentos. Os resultados e informações originadas compõem parte das referências bibliográficas desta tese.

Hidrogeológicos

As informações hidrogeológicas são oriundas principalmente de pesquisas da CPRM de Fortaleza e da Cooperação Brasil-Canadá. Ressaltamos as contribuições de Souza Filho (2000), Veríssimo e Feitosa (2002), Souza Filho *et al.* (2003) e Souza Filho *et al.* (2004). Esses trabalhos proporcionaram a caracterização de produtividade e salinidade dos poços, bem como hidroquímica das águas subterrâneas na área da Folha Irauçuba e do Juá.

Sensores Remotos

Os dados ópticos multiespectrais utilizados correspondem à cena de órbita 217 e ponto 063 do sensor ETM$^+$ a bordo do satélite Landsat-7, com data de passagem em 7 de outubro de 1999. Tais cenas foram adquiridas através do Global Landcover Facility (GLCF, 2003). Os dados multiespectrais possuem resolução espacial de 30 m, posicionadas no intervalo visível (Bandas 1, 2 e 3), infravermelho próximo (Banda 4) e infravermelho de ondas curtas (Bandas 5 e 7) do espectro eletromagnético. O sensor também possui uma banda pancromática que inclui o intervalo do visível, com 15 m de resolução e uma banda no faixa do termal, com 60 m de resolução. Estes dados são adequados para o mapeamento de solos, rochas e cobertura vegetal, além da identificação de feições lineares e morfológicas.

Modelos Digitais SRTM - O sistema radar interferométrico da missão *Shuttle Radar Topography Mission*/ SRTM proporciona modelos digitais de terreno, disponíveis para o Brasil, com resolução de 90 m (Rabus *et al.*, 2003). Tais produtos auxiliaram no mapeamento de estruturas regionais na área de estudo. Os dados foram importados das páginas eletrônicas da NASA (www2.jpl.nasa.gov/srtm/).

Aerogeofísicos

Duas bases de dados com resoluções diferentes foram processadas nesse trabalho de tese.

O Projeto Itatira/Bloco-B é um levantamento aerogeofísico regional encomendado pela NUCLEBRAS à LASA em 1977 (Lasa, 1978 e CPRM, 2007b, Figura 1.2). Para o levantamento, utilizou-se a aeronave Islander, com linhas de vôo orientadas N-S e 500 m de espaçamento e linhas de controle com direção E-W e espaçadas de 20.000 m. Os sensores aerotransportados foram:

a) Aerogamespectrômetro, modelo EXPLORANIUM DIGRS-3001, com cristais de iodeto de sódio ativado a tálio, perfazendo um volume de 1017,87 polegadas cúbicas, posicionado no interior da aeronave;

b) Magnetômetro de prótons, modelo G-803 GEOMETRICS, montado na cauda da aeronave (*stinger*).

A amostragem foi realizada no intervalo de 1 s, equivalente a uma leitura aproximadamente cada 55 m, posto que a velocidade média da aeronave foi de 200 km/h a 150 m de altura. Trata-se de um levantamento regional, cujos dados magnéticos auxiliaram na caracterização de estruturas profundas e os radiométricos na caracterização da composição do solo superficial.

O Projeto PROASNE/Bloco Juá foi executado pela LASA em 2001. Trata-se de um aerolevantamento de detalhe (PROASNE, 2007 e Lasa, 2001). A aquisição foi por helicóptero voando a 60 m de altura e velocidade média de 140 km/h, com linhas de vôo (produção) E-W separadas de 100 m e linhas de controle N-S com 500 m de espaçamento. O sensor eletromagnético (HEM) e o magnetométrico estavam num *bird* rebocado por um cabo a 30 m do solo *(towed bird*) e o sensor VLF-*Very Low Frequency* foi rebocado a 45 m do solo. (Figura 1.3).

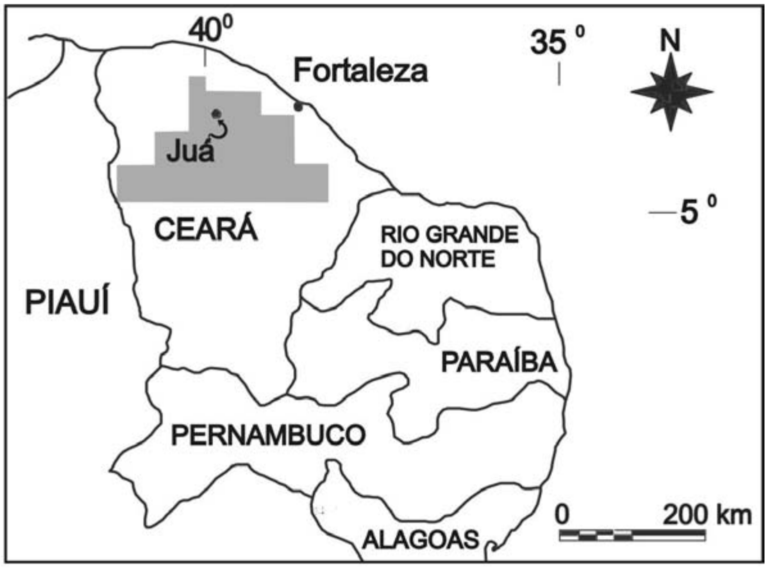

Figura 1.2 – Localização dos aerolevantamentos na área de estudo: NUCLEBRAS/Itatira-B (polígono cinza); PROASNE no Estado do Ceará (quadrado preto). (Modificado de CPRM, 2007b e Lasa, 2001).

Os sistemas possuem as seguintes características (Lasa, 2001):

a) Sistema eletromagnetométrico Aerodat DSP 99, domínio da freqüência. O conjunto de dados compreende aquisições através dois arranjos de bobinas com cinco freqüências: três pares de bobinas horizontais coplanares (CP1-874,3 Hz; CP2-4.865 Hz; CP3-33.645 Hz) e dois pares de bobinas verticais (CX1-918,5 Hz; CX2-4.443 Hz).;

b) Sistema aeromagnetométrico de vapor de césio, Geometrics G-822;

c) Sistema VLF, Totem Hertz, modelo 2A, de dois canais, realizando medições do campo VLF em fase e quadratura nas seguintes estações: NAA - 24,0 kHz (Cutler, Maine, EUA) e NLK - 24,8 kHz (Seattle, Washington, EUA).

Para simplificação da nomenclatura, nos textos seguintes, trataremos as cinco freqüências de aquisição HEM por indicadores nominais: a baixa freqüência nominal de 900 Hz que compreenderá as freqüências do arranjo coplanar-CP1 e do arranjo coaxial-CX1; a média freqüência nominal 4500 Hz que reunirá as freqüências do arranjo coplanar-CP2 e do arranjo coaxial-CX2 e a alta freqüência nominal 33.000 Hz referindo-se ao arranjo coplanar-CP3.

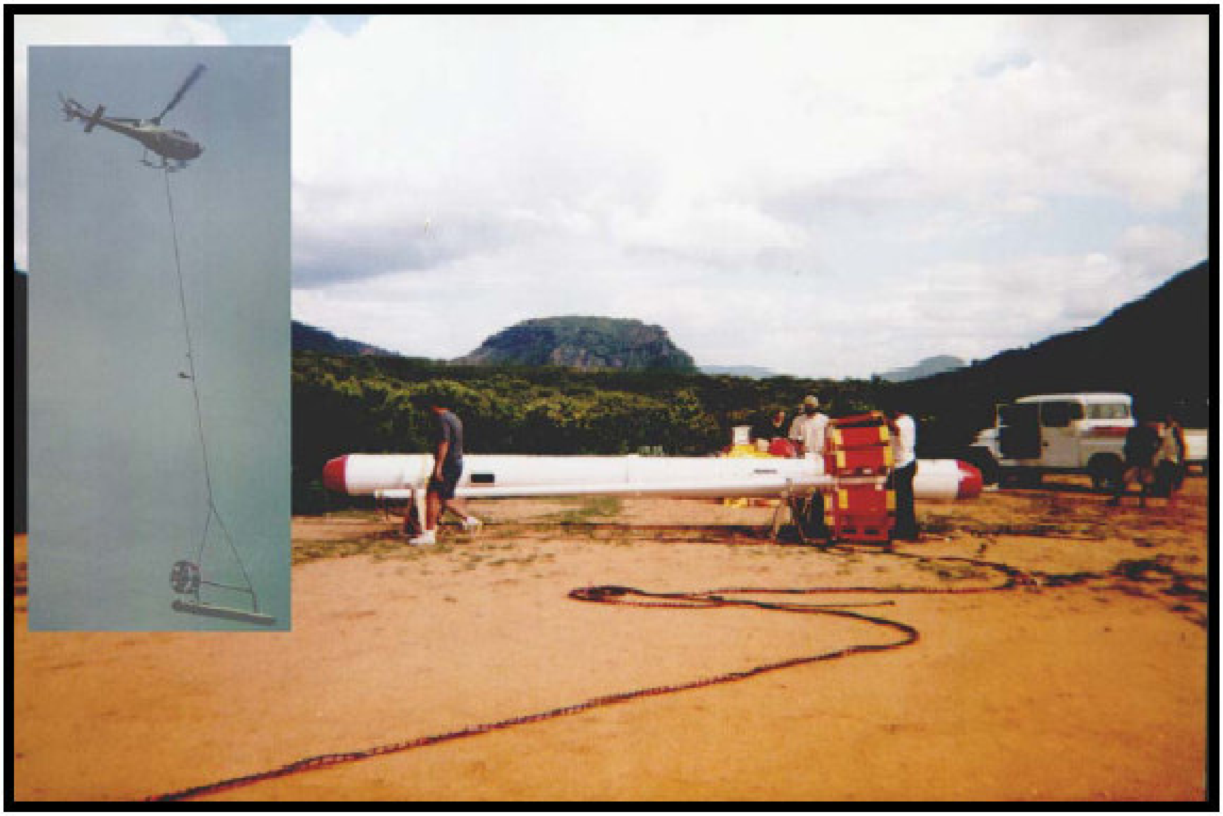

Figura 1.3 – Plataforma utilizada no aerolevantamento do PROASNE. Detalhe do helicóptero e do *bird* que contém os sensores eletromagnético e magnético. O sensor VLF (no detalhe da foto) situava-se preso ao cabo à meia distância entre a aeronave e o *bird*. (Lasa, 2001).

As taxas de amostragem dos sensores magnético e HEM eram de 10 Hz, equivalente a uma leitura a cada 4 m no terreno, considerando-se a velocidade do helicóptero. Dados oriundos do sensor VLF não foram estudados nessa tese e a própria Lasa os referiu como adquiridos com baixa qualidade de sinal com relação às distâncias às estações emissoras.

1.5 – Estruturação da Tese de Doutorado

Este trabalho reflete a participação do autor no Programa de Pós-Graduação em Geociências da UNICAMP e às interações mantidas com especialistas do USGS, IG/UnB e IAG/USP no decorrer destes três anos e meio de trabalho. O volume da Tese foi estruturado considerando as seguintes etapas de trabalho:

a) Escolha do zoneamento de favorabilidade e de salinidade de água subterrânea como temáticas a serem abordadas dentre os objetos de estudo da hidrogeologia em domínio cristalino;

b) Definição da área de estudo, dos objetivos específicos e da abordagem de estudo, como sendo baseada no processamento de dados aerogeofísicos e na modelagem espacial, utilizando sistemas especialistas;

c) Escolha e estruturação das bases de dados disponíveis, incluindo-se trabalhos de campo;

d) Preparação dos dados para serem utilizados nos processamentos de imagens como a definição dos limites para a modelagem dentro da área de estudo, a utilização de sistema único de referência espacial e conversão para mesma unidade de medida para dados equivalentes, quando necessário;

e) Processamento de dados com foco nos objetivos específicos, e posterior inserção das imagens resultantes nos modelamentos espaciais. Durante essa fase, destaca-se o tempo dispendido no aprendizado sobre métodos geofísicos, de sensoriamento remoto e suas aplicações, mormente em hidrogeologia;

f) Modelagens dos dados processados através da simulação estocástica e determinística (krigagem) para o zoneamento de salinidade da água subterrânea e da análise “Bayesiana”, com as técnicas de Razão de Probabilidades e Pesos de Evidências, resultando em mapas de favorabilidade hídrica;

g) Discussões sobre os resultados alcançados e deficiências encontradas.

A parte introdutória desta tese encontra-se nos capítulos 1 e 2. O capítulo 1 trata dos itens a, b e c, supracitados e no capítulo 2 é descrito o arcabouço geológico e hidrogeológico da área de estudo. O capítulo 3 trata do processamento e preparação dos dados aerogeofísicos segundo os objetivos específicos e escolha das imagens que participarão das modelagens espaciais. Como resultados preliminares destacamos a identificação das propriedades físicas magnéticas e eletromagnéticas associadas às diversas rochas da área de estudo.

No capítulo 4 encontram-se os resultados da modelagem estocástica e determinística do zoneamento de salinidade executado a partir dos dados de condutividade elétrica da água amostrada em poços e da condutividade elétrica do terreno, medida pela aerogeofísica, como variável secundária. A boa aproximação entre os valores simulados e as medidas em poços não utilizados nas modelagens validou as técnicas utilizadas.

As modelagens “bayesianas” por Razão de Probabilidades e por Pesos de Evidências são apresentadas no capítulo 5. São baseadas nos conceitos de probabilidades à *priori* e a *posteriori*, onde se identificam os valores de cada evidência geofísica, espectral e estrutural associados às classes de poços muito produtivos e pouco produtivos. Áreas potenciais para água subterrânea são selecionadas e comparadas entre os dois modelos. Os mapas finais são validados com relação às diferentes classes de poços.

Ao final, no capítulo 6 apresentamos uma análise crítica dos resultados alcançados e restrições verificadas, seguidas de recomendações sobre a aplicabilidade das geotecnologias na prospecção hidrogeológica em domínio cristalino.

Optou-se por escrever os capítulos principais em inglês, pois estão sendo submetidos para revistas internacionais indexadas, e para que fosse possível incorporar as sugestões dos parceiros do Serviço Geológico Americano (USGS).

1.6 - Métodos

A metodologia utilizada deverá ser passível de replicação em outras áreas de clima semi-árido, e, indiretamente, favorecer as locações de poços e inclui:

1.6.1 - Processamento e Resultados de Imagens do sensor ETM$^+$ do Satélite Landsat-7

Regiões intensamente fraturadas favorecem a percolação de água e conseqüentemente, a alteração de minerais presentes na rocha ou solo. Nesse processo intempérico, físico-químico, a água e os sais minerais dissolvidos são os principais agentes. O sensor ETM$^+$ é útil na identificação de minerais de alteração com hidróxido e óxido de ferro e argilo-minerais (Sabins, 1997) e no mapeamento de rochas e estruturas. Nesta tese foram aplicadas as técnicas de razão de bandas (Sabins, 1997) e análise das principais componentes (Método Crósta – Loughlin, 1991).

O Método das Razões Orientadas de Bandas (Sabins, 1997)

Para as razões de bandas foram adotados os seguintes procedimentos:

a) Recorte na área de interesse: Latitude 3º49' a 3º57' S; Longitude 39º48' a 39º 55' W;

b) Correção atmosférica pelo método baseado nos pixels escuros presentes na banda 7 (Sabine, 1999);

c) Aplicação de razões entre bandas na seqüência: 3/1, 4/2, 5/7;

d) Composição falsa-cor das razões na ordem: vermelho_R (3/1); verde_G (4/2); azul_B (5/7), visualizada na Figura 1.4;

e) Aplicação de filtro digital de passa baixa, kernel 17X17 para eliminação de valores anômalos e homogeneização da informação seguido de reescalonamento dos intervalos de valores para o intervalo 0-255 com função de normalização dos dados. (RGB=3/1, 4/2, 5/7);

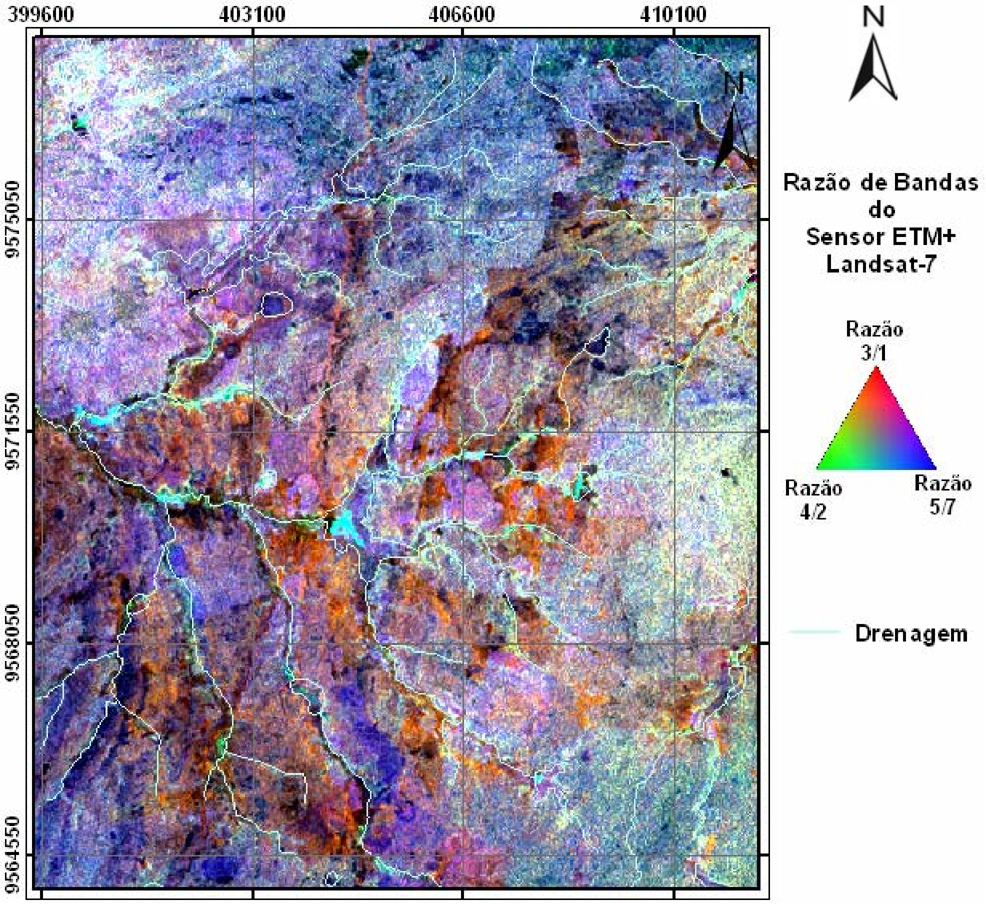

Figura 1.4 – Composição falsa-cor das razões de bandas para a cena do sensor ETM$^+$/Landsat-7 recortada para a área de estudo de Juá. Ordem: vermelho_R (3/1); verde_G (4/2); azul_B (5/7). Coordenadas UTM-SAD-69, zona 24-Sul. Drenagem em azul.

f) Reclassificação de cada uma das imagens razão em 3 intervalos iguais de valores: 0 a 84, 85 a 169 e 170 a 255, que representariam relativamente conteúdos baixos, médios e altos em óxidos, cobertura vegetal e hidróxidos respectivamente. Em termos de porcentagem de pixels nas imagens estes intervalos representam:

3/1: B=9%, M=60% e A=31%

4/2: B=39%, M=55% e A=6%

5/7: B=9%, M=70% e A=20%

g) Combinação das três imagens numa única do tipo *unique conditions* gerando-se uma imagem com 18 classes, conforme as combinações encontradas no procedimento (Figura 1.5).

Classe/razão	3/1	4/2	5/7	legenda
1	A	A	A	⬜
2	A	A	M	🟨
3	A	M	A	🟪
4	A	B	M	🟥
5	A	B	B	🟥
6	M	B	B	🟫
7	A	M	M	🟧
8	M	B	M	🟪
9	B	B	M	🟦
10	M	M	A	🟦
11	B	M	A	🟦
12	B	M	M	🟩
13	M	A	M	🟩
14	M	M	M	⬛
15	B	B	B	⬛
16	A	B	A	🟪
17	M	A	A	🟦
18	M	B	A	🟦

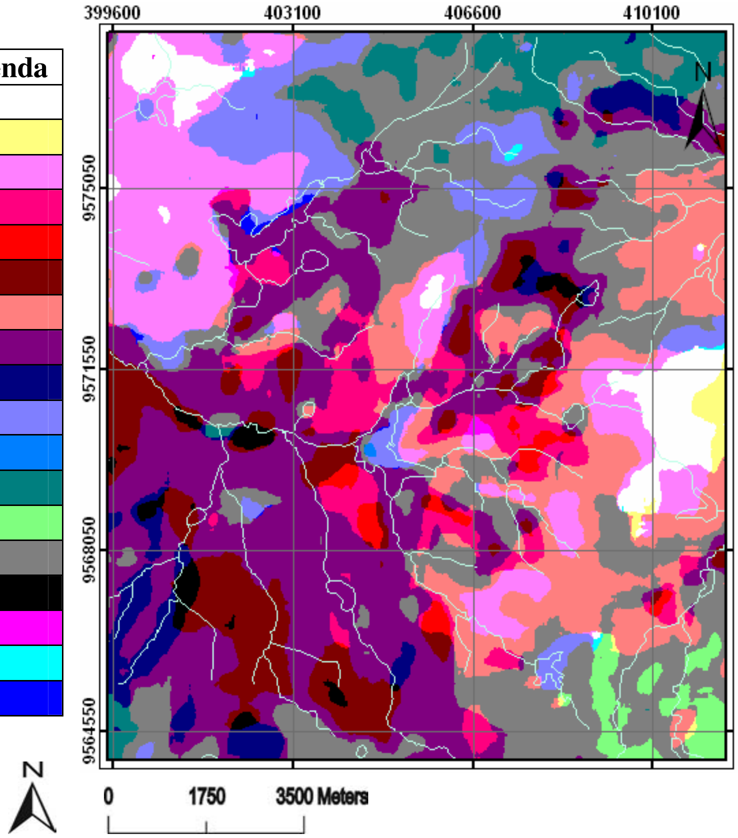

Figura 1.5 – Imagem das combinações realizadas com as imagens filtradas por passa-baixa e reclassificadas das razões de bandas 3/1, 4/2 e 5/7 do sensor ETM$^+$/Landsat-7 para a área de Juá, referente ao conteúdo de minerais de óxido de ferro, vegetação e minerais com hidroxila. Tabela para identificação das cores. Coordenadas UTM-SAD-69, zona 24sul. Drenagem em azul.

Análise por Principais Componentes - Método Crósta

O método Crósta (Loughlin, 1991) é um direcionamento da técnica desenvolvida por Crósta e Moore (1989) para a análise das principais componentes orientadas por feições espectrais que discriminam minerais com óxidos de ferro com hidroxila e teve o seguinte desenvolvimento:

a) Análises de Principais Componentes orientadas à discriminação de óxidos (bandas 1, 3, 4 e 5) e hidroxilas (bandas 1, 4, 5 e 7);
b) Seleção das componentes representativas de óxidos (PC4) e hidroxilas (PC3) nos conjuntos de bandas analisadas através da análise da matriz de autovetores;
c) Multiplicação da PC3 das hidroxilas por -1 para inverter a contribuição das bandas 5 e 7;
d) Aplicação de filtro digital de passa baixa, kernel 11x 11 para eliminação de valores anômalos e homogeneização da informação (caracteristicamente de alta freqüência);
e) Reescalonamento do intervalo de valores obtido em cada imagem a partir do valor 0 (presença de óxidos ou hidroxilas) até o valor que representa acumuladamente 99.9% de pixels (5 para a imagem óxidos e 9,7 para a imagem hidroxilas), para o intervalo entre 0 e 5;
f) Adição das imagens óxido e hidróxido obtidas no item (e) para a geração da imagem óxidos+hidroxilas;
g) Reclassificação das imagens óxido, hidroxila e óxidos+hidroxilas em 3 classes com quebras em: 0; média; média + 1 desvio padrão; valor máximo;

A aplicação das técnicas de razão de bandas (Sabins, 1997) e análise das principais componentes (Método Crósta – Loughlin, 1991) foi capaz de identificar regiões com predominância de argilo-minerais, minerais de óxido de ferro e presença de vegetação. Para cada parâmetro individualizaram-se as classes de abundância relativa (alta, média e baixa), que, combinadas entre si, produziram um mapa de classes espectrais integradas. As imagens foram processadas com apoio do programa Envi v. 4.3 e os resultados estão apresentados no Capítulo 5.

1.6.2 - Processamento de Dados Aerogeofísicos

O processamento dos dados aerogeofísicos foi efetuado na UNICAMP e no United States Geological Survey-USGS no Colorado. As informações magnéticas foram processadas com o programa Oasis-Montaj v. 6.3 da Geosoft e com as rotinas escritas por Phillips (1997) e Phillips et al. (2003) do USGS. Os dados eletromagnéticos foram tratados nos programas Oasis-Montaj e EMIGMA v. 7.8, esse especialmente para a inversão dos dados eletromagnéticos. As etapas do processamento, os objetivos e os produtos estão descritos a seguir:

a) correção de dados magnéticos espúrios pela técnica de micronivelamento, correção do posicionamento das anomalias sobre as fontes causadoras através da redução ao pólo e ao equador magnético, conversão para mapa pseudogravimétrico (definição no Anexo), cálculo dos gradientes horizontal total e vertical do campo magnético e integração com dados regionais através de álgebra de grids e filtragens diversas para realce das anomalias magnéticas rasas (60 m e 270 m) e profundas (400 e 2000 m);

b) Aplicação da técnica de Terraceamento (*Terrace)*, desenvolvida por Cordell e McCafferty (1989) do USGS (definição no Anexo), aos dados aerogeofísicos magnéticos e eletromagnéticos. Os mapas de propriedades físicas de magnetização e condutividade elétrica gerados realçaram propriedades geofísicas das rochas resultantes de mudanças de litológicas ou tectonismo;

c) Correção de dados eletromagnéticos espúrios, inversões de dados a partir do modelo de camadas horizontais, calculando-se a profundidade de fontes condutoras, e associando-as com elementos litológicos e estruturais. O objetivo foi identificar corpos condutores fraturados contendo água e discriminá-los de corpos condutores argilosos.

1.6.3 - Análise Geoestatística

Krigagem e Simulação Estocástica com Deriva Externa

As técnicas, determinística de krigagem e a probabilística por simulação estocástica, utilizadas nessa tese, tiveram como objetivo modelar a salinidade da água subterrânea a partir de medidas de condutividade elétrica da água subterrânea em poços e no solo (dados aerogeofísicos eletromagnéticos-HEM) com o auxílio do programa ISATIS (Bleines *et al.*, 2000). A heterogeneidade do sistema condutor fraturado foi outro fator determinante para a utilização dos dados aerogeofísicos como variável secundária ou externa (conceituação no Anexo). As aplicações desses dois processos geoestatísticos estão detalhadas no Capítulo 4.

Modelagem por Razões de Probabilidade

A técnica de Razão de Probabilidades foi desenvolvida por colaboradores do USGS em 1999 (Lee *et al.*, 2001) para aplicação ambiental e utilizada por Silva (1999) e McCafferty *et al.* (1999) para aplicação mineral. É a primeira vez que é aplicada para estudos hidrogeológicos no Brasil, aproveitando-se dos dados geofísicos (magnéticos, eletromagnéticos e radiométricos), geológicos (litologia e lineamentos), morfológicos (aspecto e declividade) e espectrais do sensor ETM$^+$/Landsat-7. Com o auxílio dos programas ArcMap v. 9.1 e Imagine v. 9.2 os dados foram convertidos para o formato *raster* e computadas as estatísticas destes com relação às classes de poços. Os métodos e resultados estão apresentados no Capítulo 6.

O objetivo é contabilizar o quão característicos (ou não) as feições oriundas dos temas geofísicos, espectrais, litológicos e estruturais podem ser das classes de vazões. Outros detalhes sobre o método e aplicações podem ser encontrados em McCafferty *et al.* (1999) e Silva (1999).

Modelagem por Pesos de Evidência

À semelhança do método de razão de probabilidades, pesos de evidência também é uma técnica baseada no princípio Baysiano de probabilidades à priori e a posterior, porém, com maior envolvimento estatístico. O grau de associação entre uma evidência e a classe teste é contabilizado através do cálculo, em ordem cumulativa crescente ou decrescente, dos pesos positivos e negativos da ocorrência de pontos de treinamento em cada classe da evidência e o seu desvio padrão. Limites de confiança são estabelecidos para que definir qual classe da evidência participará na construção do modelo. Esta técnica está descrita no item 5.1 e o desenvolvimento dos modelos de favorabilidade para água subterrânea estão apresentados no item 5.3.

1.7 - Problemática da Locação de Poços no Cristalino Semi-Árido

Diferenças entre Domínios Hidrogeológicos

Para melhor compreender as dificuldades de locação em terrenos cristalinos do Nordeste e a metodologia adotada nessa tese, é apresentado neste capítulo uma compilação dos resultados de diversos autores aplicando técnicas diferentes e em épocas distintas. Ao final, comparou-se as características de poços em várias regiões do Brasil com poços na região de Irauçuba e do Juá.

Diferentemente de terrenos cristalinos em áreas tropicais úmidas brasileiras, poços no semi-árido nordestino são de menor profundidade, menor produtividade e mais salinos. A Tabela 1.2 apresenta dados tabulados por Manoel Filho (1996) para poços no cristalino do Rio Grande do Norte, Paraíba e São Paulo e para os basaltos da Bacia do Paraná, bem como poços do cristalino de Irauçuba e Juá, apresentados por Veríssimo e Feitosa (2002), Souza Filho *et al.* (2003) e com informações obtidas nesse trabalho. Percebe-se que as diferenças entre parâmetros hidrodinâmicos e construtivos para os diversos ambientes são de duas ordens de grandeza para a capacidade específica (que quantifica a produtividade de um poço) e até três vezes para os demais parâmetros.

De maneira sistemática, as características produtivas e a qualidade da água são explicadas pela interação de vários fatores ao longo do tempo:

i) A diferença e a regularidade da precipitação influenciam tanto na produtividade como na salinidade, a exemplo dos poços situados na zona tropical úmida do Sudeste e no semi-árido do Nordeste (Tabela 1.2);

ii) A espessura do manto de intemperismo ou de cobertura elúvio-coluvionar atua como aqüífero poroso, impedindo a rápida evaporação e transferindo a água superficial para o aqüífero cristalino;

iii) A presença de porosidade primária além da secundária (fraturas) contribui para maior produtividade, a exemplo dos metacarbonatos dos Grupos Bambuí/Salitre, da Província São Francisco (Manoel Filho, 1996);

iv) As classes morfoestruturais baixas a intermediárias (Figura 1.6) estão associadas a poços mais produtivos no caso de São Paulo (Mandrucci, 2003,);

v) A tectônica rúptil favorece na geração de estruturas abertas e intemperismo localizado (Souza Filho, 2002; Souza Filho et al., 2007), nesse contexto, a neotectônica (Figura 1.7) assume maior importância (Coriolano, 2002; Neves, 2005).

Tabela 1.2 - Características de produtividade entre províncias hidrogeológicas do Nordeste e Sudeste do Brasil.

Províncias Hidro-geológicas	**PARÂMETROS HIDRODINÂMICOS E DE CONSTRUÇÃO**															
	NE (m)		**ND (m)**		**Q (m^3/h)**		**Resíduo Seco (mg/l)**		**MCI (m)**		**FMP (m)**		**Profundidade (m)**		**Cap. Espec. (m^3/h.m)**	
	M	**Max**	**M**	**Max**	**M**	**Max**	**M**	**Max**	**Max**	**Max**	**M**	**Max**	**M**	**Max**	**M**	**Max**
Carbonatos SF (33 poços)[1]	**11,6**	**31,0**	**31,5**	**64,0**	**14,2**	**36,0**	-	-	-	-	-	-	-	-	-	-
Cristalino RN e PB (814 poços)[1]	**4,9**	**31,0**	**19,7**	**64,0**	**3,1**	**36,0**	**3161**	**31125**	**3,18**	**23,7**	**26,5**	**98,0**	**< 80**	-	-	-
Cristalino SP (85poços)[1]	**12,2**	**55,0**	**72,9**	**200,0**	**19,5**	**150**	-	-	**37,4**	**120**	**106,5**	**220,0**	**133,9**	**240,00**	-	-
Serra Geral (198 poços)[1]	-	-	-	-	**26,6**	**221**	-	-	-	-	**71,4**	**165,0**	**123,2**	**234,0**	**36,7**	**120**
Irauçuba, CE (220)[2]	**7,2**	**26,0**	**34,5**	**87,0**	**2,5**	**15,0**	**3361**	**13392**	-	**5**	-	**52**	**60,3**	**100,0**	**0,3**	**1,5**
Juá, Irauçuba (20poços)[3]	**6,2**	**12**	**7,7**	**9,0**	**3,2**	**6,0**	**2778**	**6845**	-	**3**	-	-	**55,3**	**75,0**	**0,7**	**1,0**

Fonte: [1] adaptado de Manoel Filho (1996); [2] adaptado de Veríssimo e Feitosa (2002) e Souza Filho et al. (2003), [3] adaptado de Veríssimo e Feitosa (2002) e dados próprios. **NE** = nível estático, **ND** = nível dinâmico, **Q** = vazão, **MCI** = manto de cobertura individualizada, **FMP** = fenda produtora mais profunda, **Cap. Espec.** = capacidade específica, relaciona a vazão e rebaixamento, Q/s_w (m^3/h), **Rebaixamento (s_w)** = diferença entre o nível estático e dinâmico da água no poço durante o bombeamento (m).

A alta variabilidade dos parâmetros hidrogeológicos em terrenos cristalinos limita as aplicações de regionalizações de parâmetros quando se trata de locação de poços. No Nordeste semi-árido, na escala de poço, distâncias de poucos metros são suficientes para se registrar diferenças de vazão, salinidade e profundidade das fendas produtoras.

Os fatores responsáveis pela produtividade de um do poço podem ser os mesmos que os estudados em escala regional para o sistema fraturado, ou seja, podemos admitir um padrão fractal (repetição em diferentes escalas) para as variáveis de fraturamento. O conceito de fractais foi utilizado por Manoel Filho para aprimorar testes de produtividade de poços em diferentes domínios cristalinos. Todavia, as abordagens de estudo necessariamente incluirão diferentes métodos de prospecção geofísica (ressonância magnética, perfilagem de poço, caminhamento geofísico multimétodos) para auxiliar no entendimento dos resultados da perfuração.

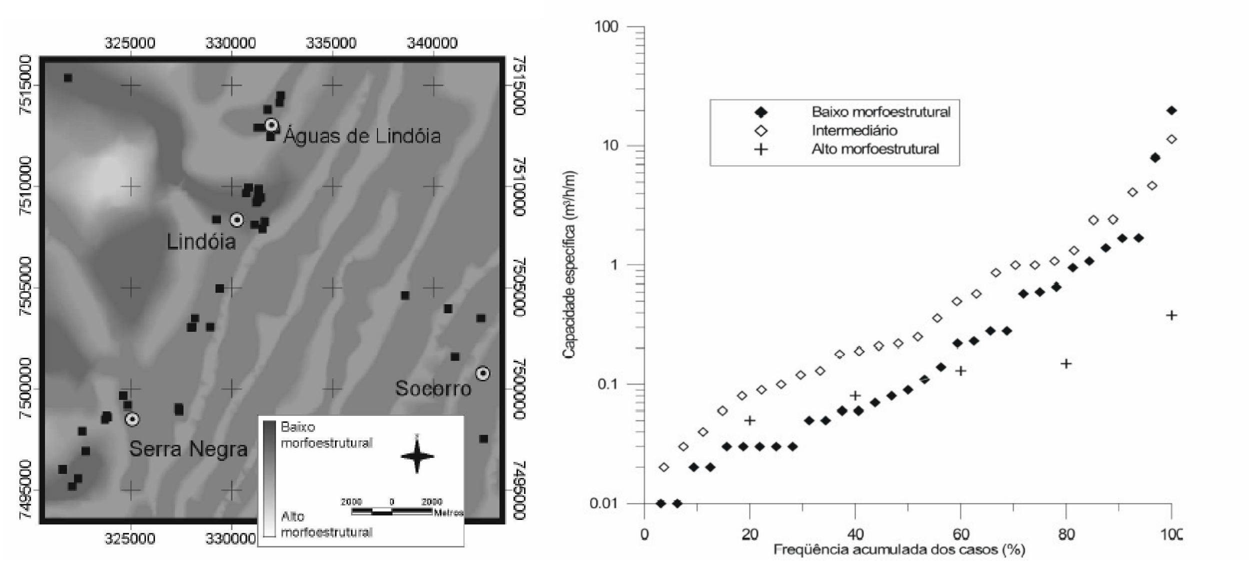

Figura 1.6 - Localização de poços e a relação positiva da produtividade com baixo morfoestrutural no cristalino de São Paulo (Mandrucci, 2003).

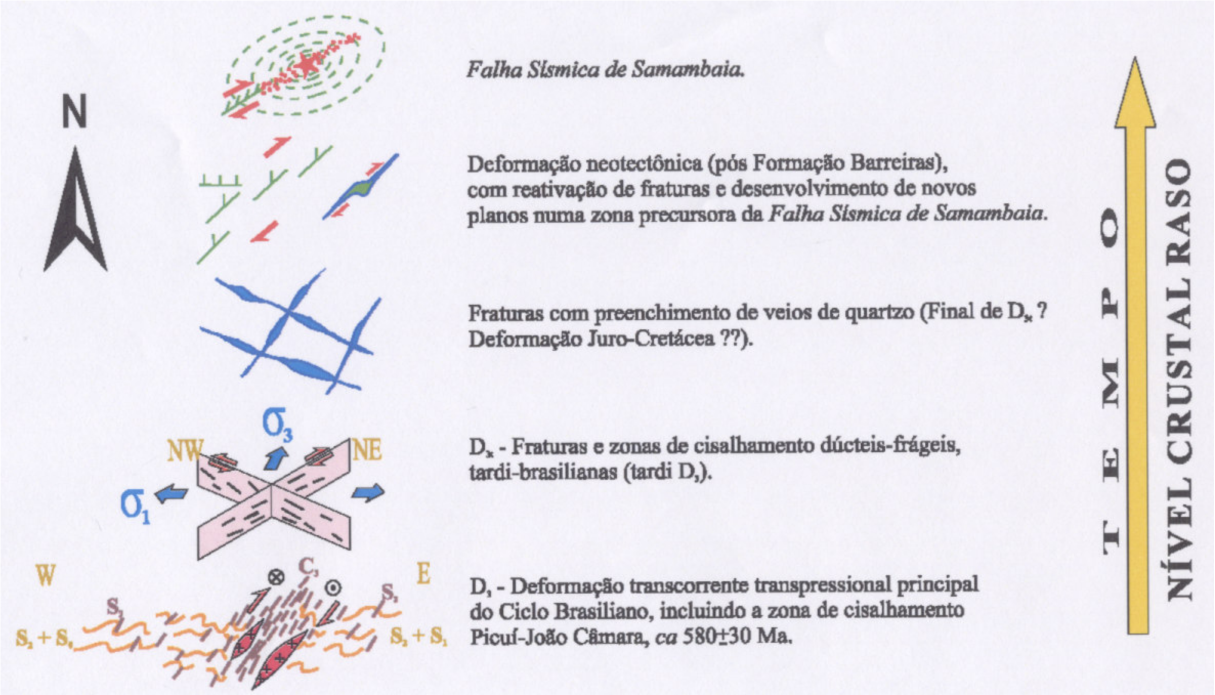

Figura 1.7 - Modelos tectônicos em níveis crustais rasos para a região de João Câmara-RN e direções de abertura de fendas (Coriolano, 2002).

Durante dezoito anos estudou-se o nível d'água no manto de intemperismo sobre rochas cristalinas na Suécia (Olofsson, 1994, *in* Manoel Filho, 1996). Mediram-se 30 variáveis geológicas, topográficas, de construção civil e de poços dentro de um túnel e distantes até 1 km. Esperava-se um declínio do nível freático por causa do túnel ao longo do tempo e os resultados estatísticos foram "decepcionantes" porque apenas 15% do declínio podia ser explicado através das variáveis selecionadas. O autor afirma que a falta de informações no contato elúvio-rocha foi a principal razão para o pouco entendimento e que o fluxo de água do solo para a rocha só ocorrer em pontos específicos, onde existe uma combinação favorável de condições.

As primeiras modelagens espaciais sobre a favorabilidade de água subterrânea para a área da Folha Irauçuba foram construídas por Brandão (2003b) e Gomes *et al.* (2004). Os autores compararam os poços produtivos ($Q > 1\ m^3/h$) e pouco produtivos ($Q < 1\ m^3/h$) com 10 variáveis que pudessem influenciar a ocorrência e circulação da água subterrânea (precipitação, azimutes – freqüência - interseção de lineamentos, litologia, declividade, orientação de encosta, proximidade de drenagem e índice de vegetação). Pelos resultados, tanto o modelo baseado nos dados quanto o modelo baseado no conhecimento não representaram, consistentemente, o fenômeno de acumulação de água em rochas fraturadas. As variáveis teoricamente mais influentes (ocorrência, freqüência e densidade de lineamentos e distância de drenagem) não foram determinantes do modelo, pois muitos poços estavam em área de cobertura que impossibilitava o reconhecimento de lineamentos.

Gomes *et al.* (2004) reconheceram que parte da limitação de seus resultados deveu-se à falta de resolução espacial dos dados disponíveis, não adequada ao tema tratado (exemplo da cartografia de estruturas em regiões com coberturas) e à própria variabilidade da vazão em terrenos cristalinos. Também sugeriu a mudança de foco, com estudos geológicos, estruturais e geofísicos terrestres no entorno dos poços, objetivando uma caracterização 3-D do ambiente.

Outro exemplo da dificuldade de locação de poços está relatado em Souza Filho *et al.* (2006) na própria área do Juá. O processamento de dados aerogeofísicos eletromagnéticos e do levantamento terrestre eletromagnético e de eletrorresistividade foram as principais técnicas utilizadas para a locação de poços, baseando-se na identificação de anomalias eletromagnéticas (Figura 1.8) que tivessem associação com fendas produtoras abaixo do manto intemperizado. Todavia, dos três poços perfurados (profundidades até 80 m), apenas um foi produtivo ($Q = 1{,}25\ m^3/h$) e dois improdutivos, considerando o critério de fendas produtoras, apesar de que um deles atravessou um depósito eluvio-coluvionar produtivo (Q = 2 m^3/h). Como os poços tiveram sua locação sobre anomalias mais condutivas, essas pareceram discriminar a extrema salinidade das águas e não a quantidade de água armazenada.

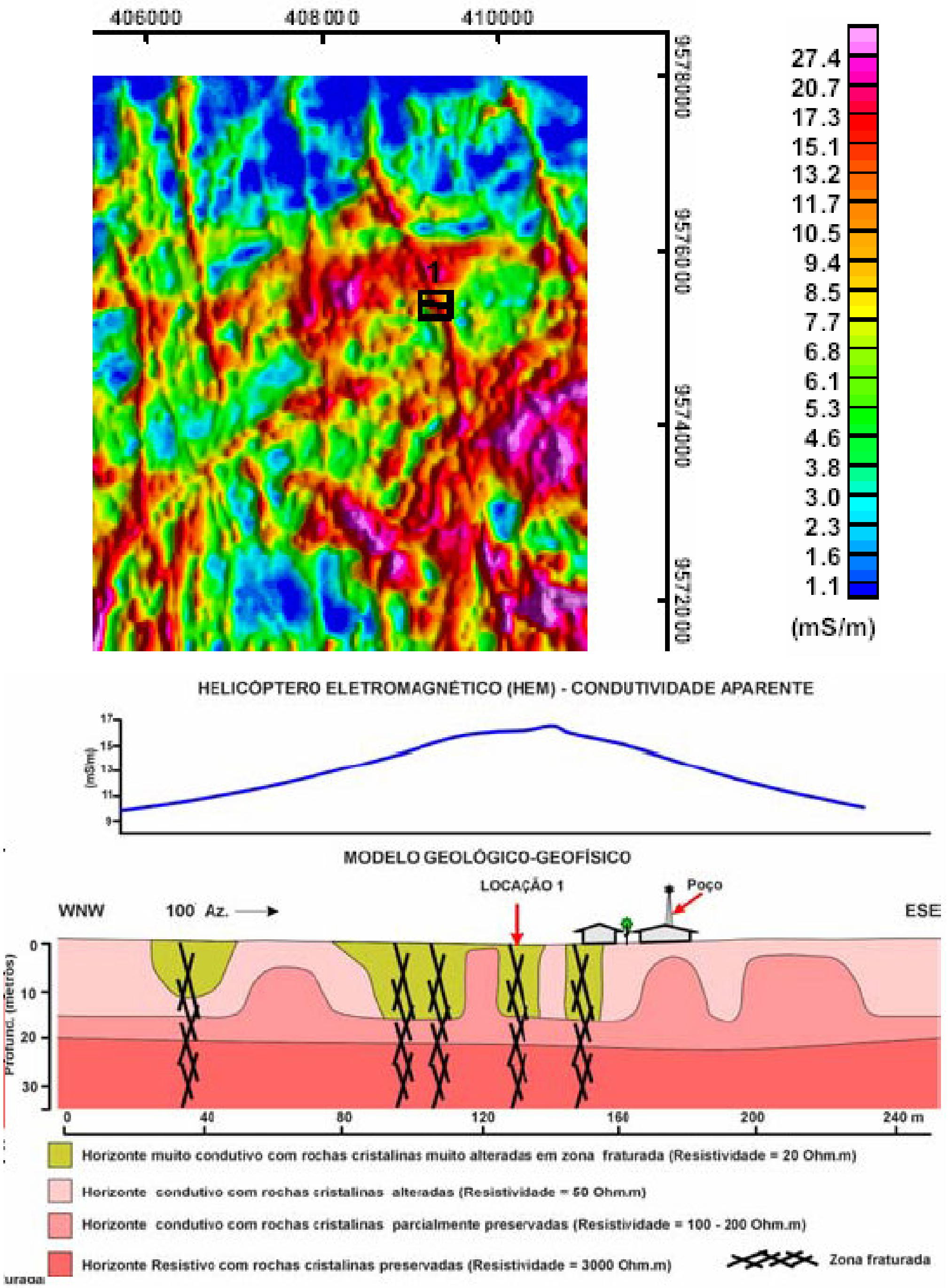

Figura 1.8 - Poço não produtivo perfurado de acordo com anomalias condutivas eletromagnéticas aerogeofísicas e eletrorresistividade em Juá, Ceará (Souza Filho *et al*., 2006).

2 – ÁREA DE ESTUDO

2 – ÁREA DE ESTUDO

Neste capítulo serão descritas as características fisiográficas e hidrogeológicas da área de estudo de Juá.

2.1 – Aspectos Fisiográficos

2.1.1 - Geomorfologia

A área de Juá (Figuras 2.1 e 2.2) caracteriza-se por um relevo plano a ondulado, com altitudes entre 155m e 170m, acima do nível do mar, limitado a leste por colinas e cristas do sopé da Serra da Santa Lucia (240 m) e a norte o serrote do Mandacaru (380 m). Brandão (2003a) adaptou a compartimentação regional do Estado do Ceará estudada por Souza (1994, 2000) à região de Irauçuba (Figura 2.1). Os relevos plano-ondulados representam o compartimento Depressões Sertanejas, com superfícies moderadamente dissecadas, que foram submetidas a pediplanização em biotita-gnaisses, lentes calciossilicatadas e anfibolitos, após o Plioceno, a partir dos relevos residuais e são inclinadas em direção aos vales fluviais. Os serrotes e cristas representam seções mais resistentes aos processos erosivos, sustentadas por quartzitos, gnaisses-graníticos ou outra litologia cujo conteúdo de quartzo e feldspato supera os anfibólios e minerais micáceos.

Ao longo do riacho São Gabriel está presente a única planície fluvial, com altitude entre 140 e 150m. Contém depósitos colúvio-aluvionares menores do que 1 m de espessura nas partes mais elevadas a leste, progredindo para oeste com seções exclusivamente aluvionares, de até 2,5 m de espessura e vales com largura de 50 m.

2.1.2 – Clima

Segundo Brandão (2003a), a porção nordeste do Brasil apresenta uma caracterização climático-meteorológica, definida basicamente por três sistemas geradores de precipitações, que são os vórtices clônicos, as frentes frias e, principalmente, as zonas de convergência intertropical. A gênese dos vórtices clônicos ocorre no oceano Atlântico-Sul, geralmente nos meses de setembro e abril, sendo mais intensamente atuante no período de verão, no mês de janeiro.

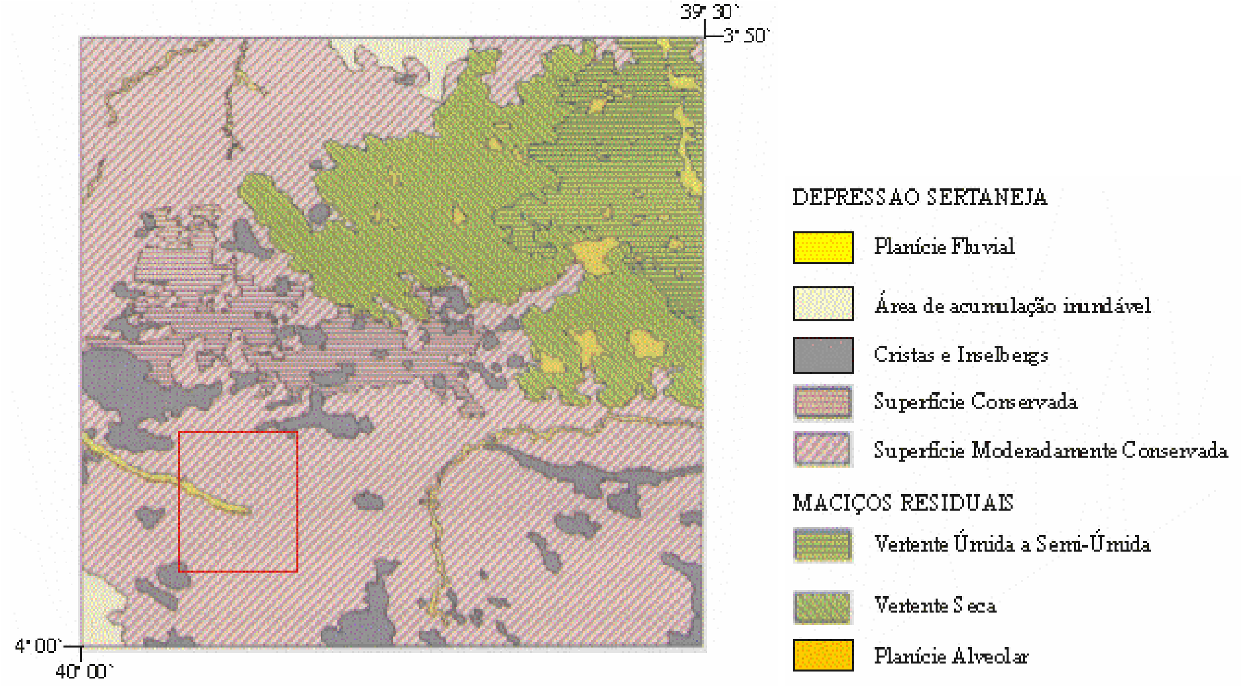

Figura 2.1 – Caracterização morfológica da Folha Irauçuba e área de estudo de Juá (polígono vermelho), modificado de Brandão (2003a). Observa-se a área de estudo dentro de uma superfície moderadamente conservada.

O ciclo das frentes frias tem origem no continente Antártico e interfere diretamente no regime de chuvas na porção norte do nordeste brasileiro. A formação e deslocamento das Zonas de Convergência Intertropical, é diretamente influenciada pela temperatura das águas do oceano Atlântico e responde pelo estabelecimento da “quadra chuvosa”, que concentra quase 90% das chuvas, mormente de fevereiro a maio. A estiagem estende-se de setembro a novembro.

A área em estudo fica totalmente inserida no denominado "Polígono das Secas", onde o índice de probabilidade de secas ultrapassa 80%.

O Juá e toda a porção sul da Folha Irauçuba (Figura 2.3) encontram-se na chamada zona de sombra da Serra de Uburetama, caracterizada por um clima semi-árido com precipitações anuais abaixo de 650 mm. Todavia, a menos de 50 km a norte, na Serra de Uruburetama, existem subclimas mais úmidos, entre 850-950 mm. A temperatura média anual é de 28°C, enquanto que a média das máximas alcança 34°C, não obstante, o autor já mediu temperaturas próximas de 45 °C.

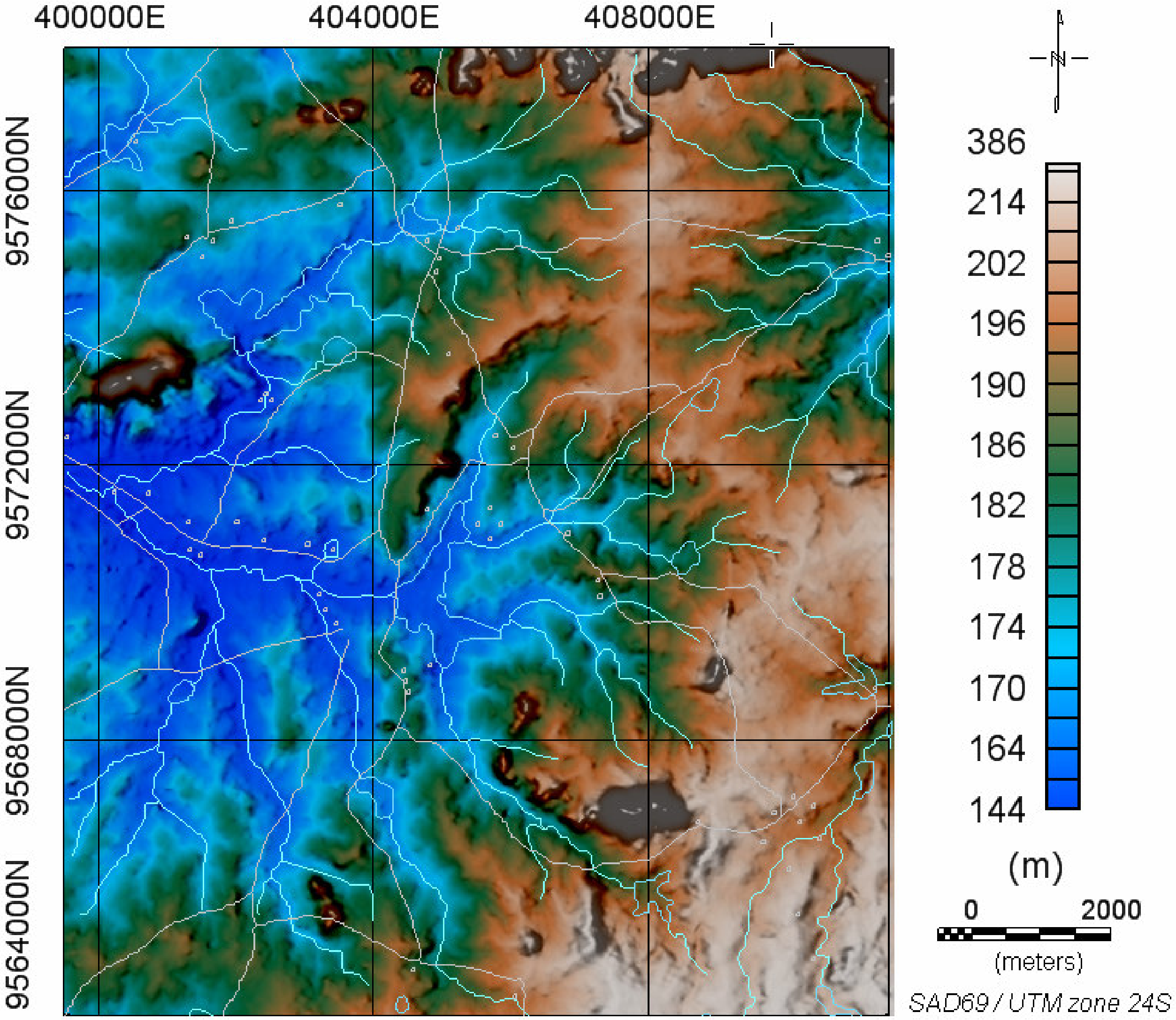

Figura 2.2 – Modelo de elevação topográfica da área de Juá (dados originários do levantamento aerogeofísico PROASNE, 2001). Drenagem em azul, tendo o riacho e açude São Gabriel ao centro e açude Cairú a Noroeste e estrada em linha marrom. Falsa iluminação com declinação 315^0 Az. e inclinação 45^0 Az.

2.1.3 - Vegetação

Na área de estudo, a vegetação predominante é a caatinga de médio porte, do tipo arbustiva-arbórea, e tem influência do relevo, solo e umidade. Os representantes mais comuns são: juá, catingueira, umburana, pau branco, pereiro, marmeleiro, angico e aroeira. Nas porções mais áridas são abundantes as juremas e cactos, enquanto que nas regiões mais úmidas e margens dos riachos a associação é menos xerofítica, com oiticica, carnaubeira e mufumbo.

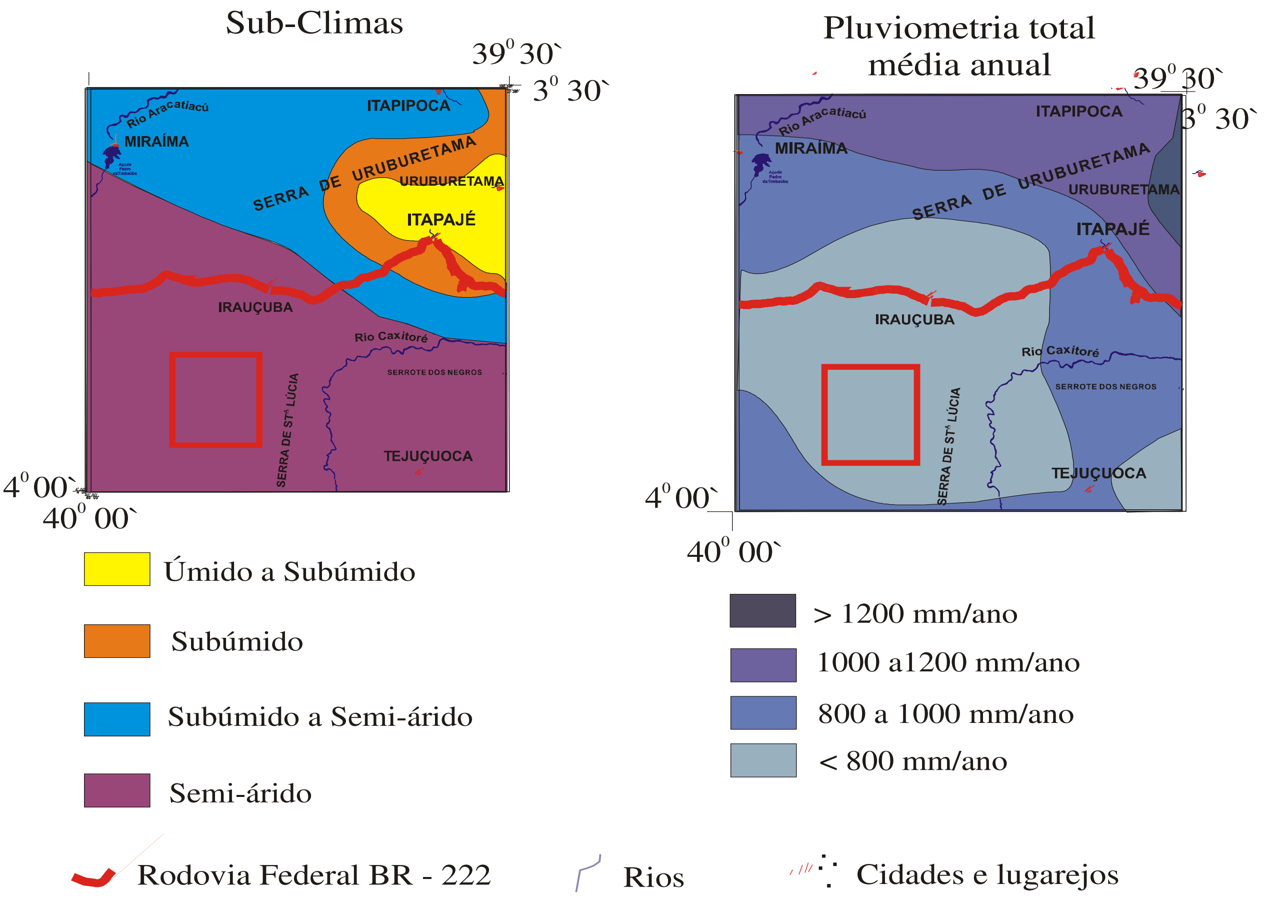

Figura 2.3 – Subclimas e pluviometria na área da Folha Irauçuba e de Juá (polígono vermelho). Modificado de Ceará (1997 in Souza Filho, 1998).

2.1.4 - Hidrografia

A rede hidrográfica é determinada pelas condições climáticas da região e características lito-estruturais. Toda a drenagem é intermitente e nos períodos de estiagem há expressivo rebaixamento do nível freático. No período das chuvas, surgem lagoas temporárias (com extensões decamétricas) em depressões no terreno sobre rochas carbonáticas. Os pequenos açudes, como o São Gabriel e Cairu (Figura 2.2), formam reservatórios de significativa importância para o abastecimento animal, apoio na agricultura e, secundariamente, para o abastecimento humano.

O padrão de drenagem mostra-se fortemente estruturado por contatos litológicos na porção central, por zonas de cisalhamento e falhamentos nas porções norte e oeste. O padrão subradial é encontrado na parte nordeste da área de Juá.

2.2 - Arcabouço Geológico

Em termos regionais a área de trabalho está inserida na Província Estrutural da Borborema (Almeida *et al.,* 1977), dentro da Folha Irauçuba. Souza Filho (1998) identificou três unidades pré-cambrianas (Figura 2.4), a saber: quatro seqüências supracrustais a sul e a noroeste, referentes ao Complexo Ceará de idade mesoproterozóica (Arthaud *et al.* 1998); terrenos ortognáissicos e migmatíticos a norte e oeste e os terrenos granitóides de dimensões batolíticas a nordeste. Essas duas últimas unidades são correlacionáveis ao arco magmático neoproterozóico de Santa Quitéria descrito por Fetter *et al.* (2003). Os diques de basalto são correlacionados ao evento de abertura do Oceano Atlântico no Mesozóico.

As coberturas cenozóicas estão representadas por depósitos aluvionares, originados de rios intermitentes mais importantes e coluvionares nas regiões montanhosas, porém não cartografáveis.

A área de detalhe de Juá situa-se no sudoeste da folha em epígrafe, compreendendo uma unidade supracrustal pelito-carbonática (Souza Filho, 1998). Nessa unidade afloram silimanita-biotita gnaisses e granitos deformados, associados a lentes de gnaisses calciossilicáticos e mármores (Figura 2.4 e 2.5). A unidade é correlata ao Complexo Ceará de Arthaud *et al.* (1998) e à unidade Canindé apresentada no Mapa Geológico do Ceará (CPRM, 2003).

Rasos depósitos coluvionares e aluvionares (menores do que 2 m de espessura) foram individualizados, através da análise de regiões uniformes com alta condutividade elétrica aparente (dado HEM-33000 Hz), coincidentes com calhas de drenagens ou regiões de morfologia suave e textura lisa nas imagens ETM+/Landsat-7 e com alto conteúdo de minerais de hidroxila ou óxidos de ferro (Figura 2.5).

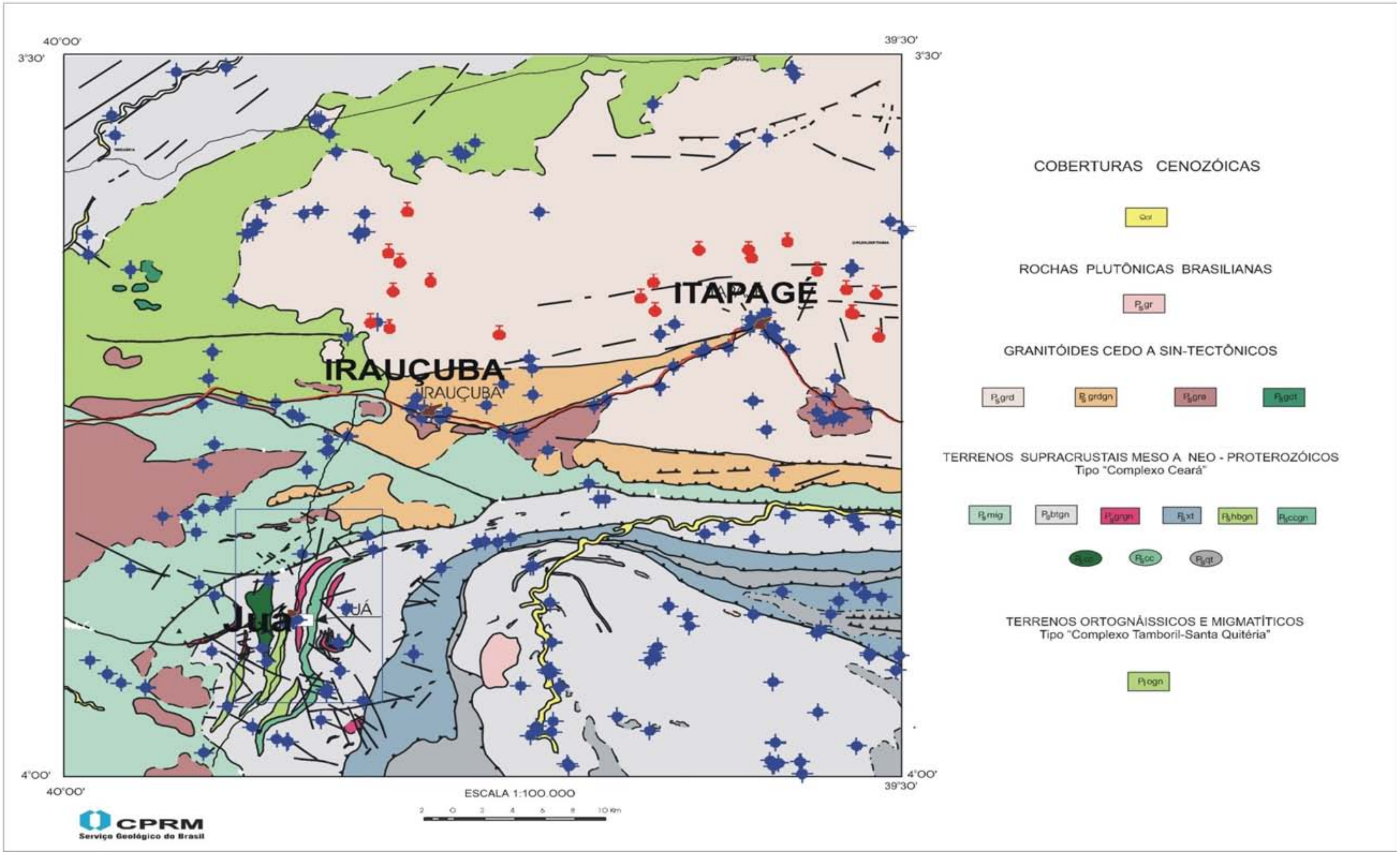

Figura 2.4 – Mapa geológico simplificado de Irauçuba com os seus principais traços estruturais. Área de Juá indicada pelo polígono em azul. Os poços estão indicados em azul e as fontes em vermelho. Modificado de Souza Filho (1998) e Veríssimo e Feitosa (2002).

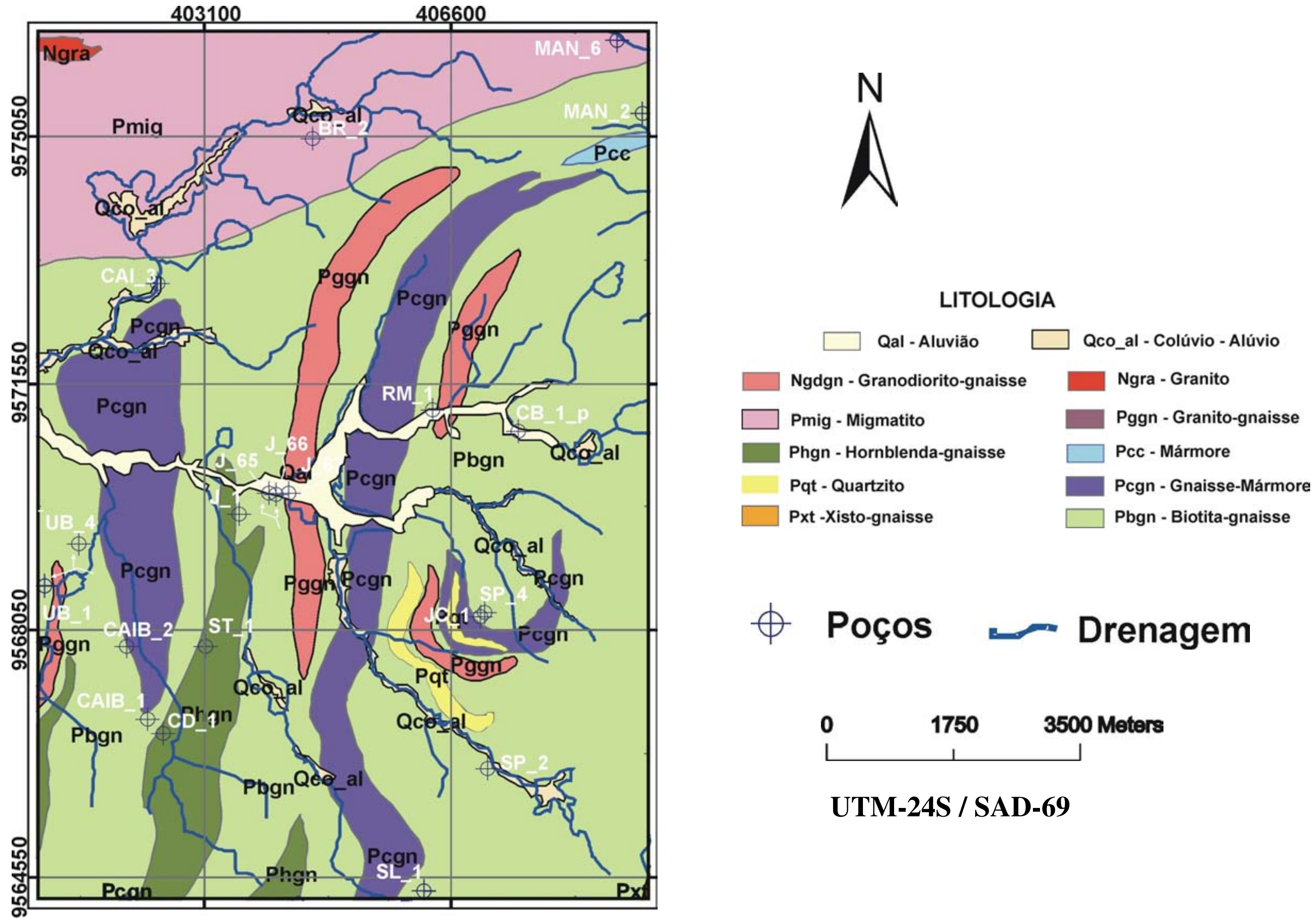

Figura 2.5 - Mapa geológico simplificado da área de estudo de Juá, Irauçuba-CE. Modificado de Souza Filho (1998).

2.3 - Arcabouço Hidrogeológico

A área da Folha Irauçuba está inserida no domínio de rochas cristalinas e os restritos depósitos aluvionares são as únicas coberturas sedimentares mapeáveis em escala regional. Assim sendo, Feitosa (1999) discriminou as unidades hidrogeológicas na área da Folha Irauçuba, em escala 1: 100.000 (Figura 2.6), segundo as potencialidades definidas através de parâmetros intrínsecos ou mensuráveis das condições de armazenamento (rochas sedimentares e cristalinas) e de recarga (grau de fraturamento e o posicionamento morfológico e condições climático-pluviométricas). Aluvião possui importância hidrogeológica alta e as rochas cristalinas possuem importância local média, quando em regiões montanhosas, com alta pluviosidade, ou baixa importância no resto da área, incluso a região de Juá.

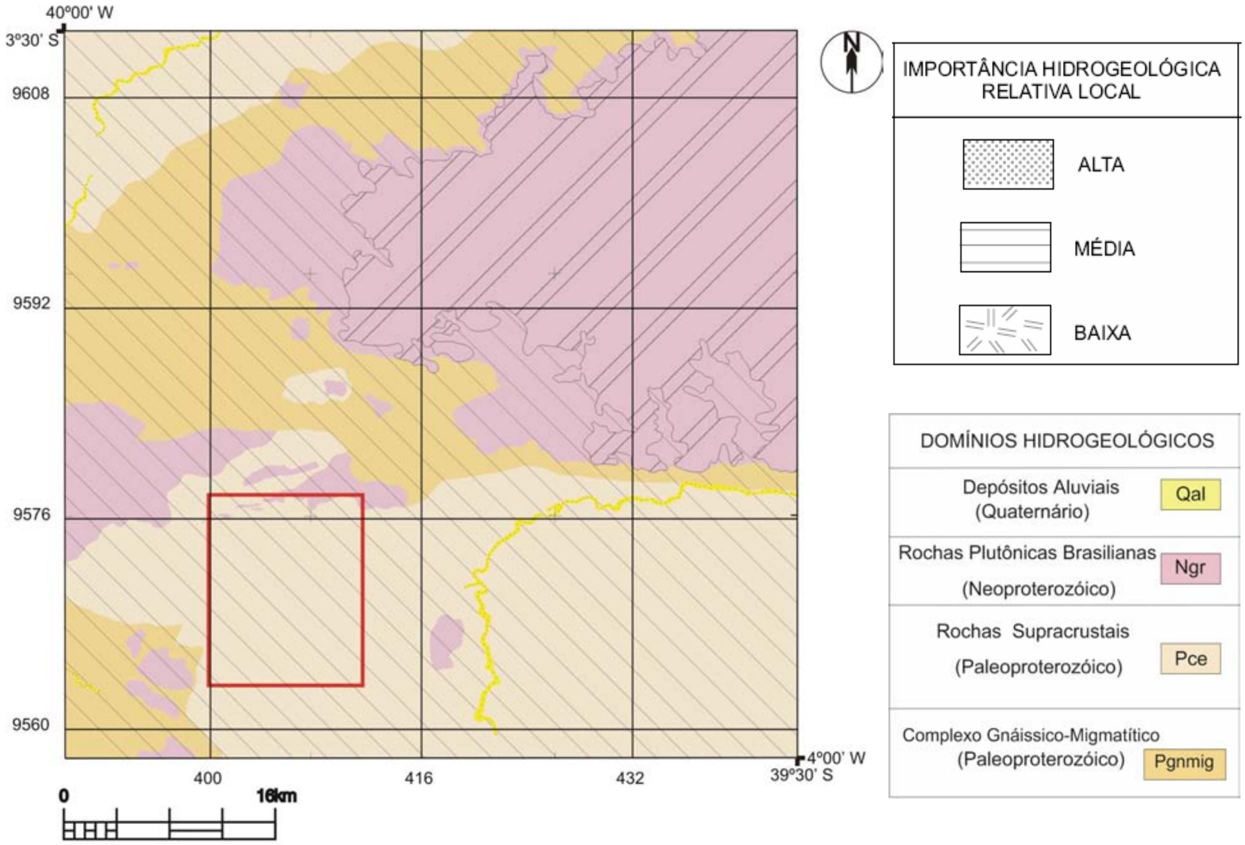

Figura 2.6 - Carta hidrogeológica da Folha Irauçuba (Feitosa, 1999). Área de Juá indicada pelo polígono vermelho.

Na escala 1: 70.000 ou maior, o modelo hidrogeológico para a área de estudo de Juá (Figura 2.7) é representado por um substrato aflorante de rochas cristalinas, onde a ocorrência de água subterrânea está nos bolsões de intemperismo e é favorecida pelo acúmulo de condutores hidráulicos (juntas e foliação). Localmente, aluviões e mantos de regolito (< 2 m de espessura) facilitam a drenança da água superficial para os bolsões. Porções de Regolito e rocha alterada podem se prolongar até 20 m da superfície, conforme as descobertas durante as perfurações da CPRM na região, que se basearam nas anomalias HEM-4500 Hz lineares condutivas, embora não tenham, necessariamente, encontrado água em grandes quantidades (Souza Filho *et al.*, 2006).

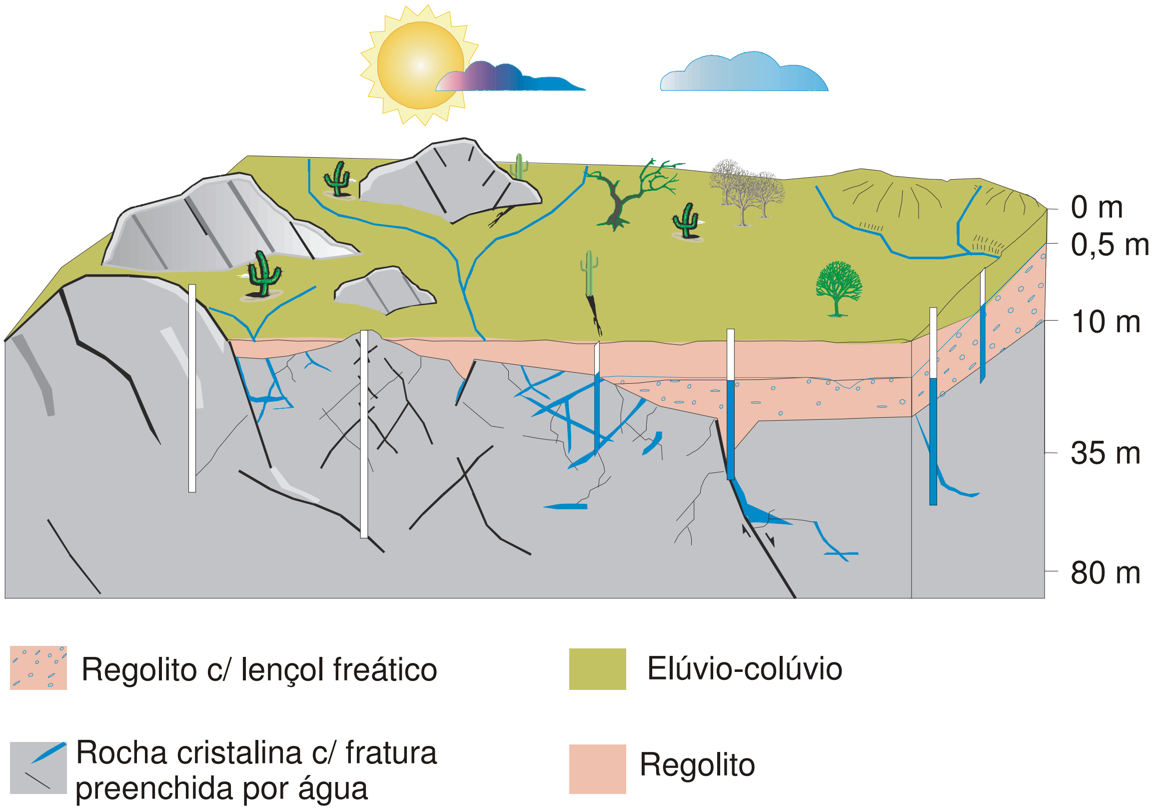

Figura 2.7 - Modelo hidrogeológico conceitual elaborado para a área de Juá, Irauçuba-CE (Modificado de Feitosa *et al.*, 2000). As profundidades não estão em escala.

Baseado no modelo hidrogeológico conceitual, três sistemas hidrogeológicos (importância relativa local) podem ser individualizados na área de Juá (Figura 2.8), à semelhança dos critérios de Feitosa (1999): i) Sistema aluvionar-cristalino-S_{ac} com favorabilidade hídrica relativamente alta, representado por coberturas aluvionares com espessura entre 1 e 2 m, sobrepostas a rochas cristalinas intensamente fraturadas - a exemplo da região ao longo do riacho São Gabriel; ii) Sistema colúvio-cristalino-S_{cc} , com favorabilidade relativa média a baixa, definido por coberturas colúvio-eluvionares com 0,5 m de espessura, sobrepostas a rochas cristalinas fraturadas ou não – situação das fazendas Mandacaru e Situação; iii) Sistema cristalino-S_c, mais abrangente e com relativa baixa favorabilidade, correspondendo às regiões sem cobertura, cujo substrato pode estar fraturado – exemplificado pelos poços pouco produtores nas cercanias da vila de Juá e no extremo sul da área.

Tais sistemas servem meramente como guias gerais para campanhas de locação de poços, haja vista que poços de alta produtividade são encontrados em sistemas de baixa importância hidrogeológica. Mesmo fora da área de Juá foram encontrados poços de alta produtividade inseridos no mesmo contexto, cujos dados de resistividade indicaram porções de bolsões de intemperismo dentro da rocha sã (Ribeiro *et al.*, 2003).

Os mapas de favorabilidade hídrica elaborados nessa tese (Capítulos 4 e 5) são criteriosos no que tange o número de parâmetros (as evidências geofísicas, lito-estruturais e espectrais) e ao tratamento matemático envolvido.

2.3.1 - Características de Poços na Área da Folha Irauçuba e de Juá

O cadastro de poços da Folha de Irauçuba é constituído por 220 pontos, 21 fontes e 113 análises físico-químicas estudadas por Veríssimo e Feitosa (2002), cujas características principais são: profundidade de poços com média de 60 m; nível estático a 26 m. O nível dinâmico possui maior freqüência entre 33,1 m e 42 m. A vazão mediana dos poços é 2,0 m^3/h, com máxima de 15 m^3/h. O potencial de exploração é muito baixo se comparado às regiões cristalinas do sudeste do país. A capacidade específica em 33 poços apresenta valores até 1,5 m^3/h/m.

Análises no período seco (novembro/2000) e após o período das chuvas (julho/2001) identificaram alterações sazonais na composição química das águas subterrâneas. A relação iônica entre ânions e cátions é $rCl^{--} > rHCO_3^{--} > rSO_4^{++}$ e $rNa^{+} > rMg^{++} > rCa^{++}$, com uma predominância das águas cloretadas sódicas. Poços localizados em quartzitos, mármores e ortognaisses produzem águas salobras. Nas rochas paragnáissicas e granitóides as águas são mais diferenciadas.

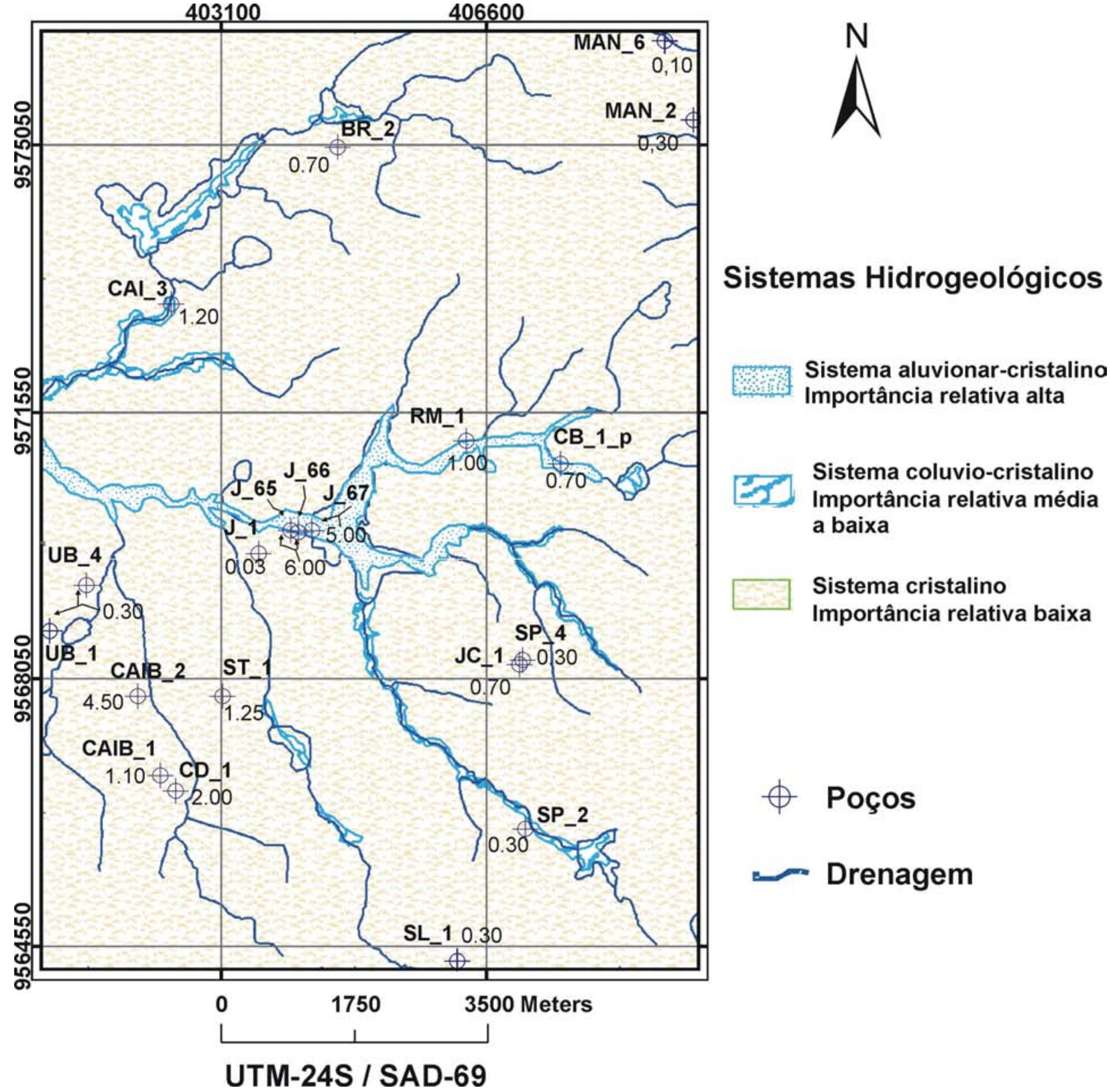

Figura 2.8 - Sistemas hidrogeológicos na área de Juá, Irauçuba-CE. Critérios de classificação baseados no trabalho de Feitosa (2000). Os Poços identificados referem-se aos utilizados nas modelagens de favorabilidade para água subterrânea.

As Tabelas 1.2 e 2.1 apresentam as características dos poços na área de Juá. Nota-se que os valores são semelhantes aos da Folha Irauçuba. Com relação ao uso dessas águas para irrigação, segundo a classificação do U.S. Salinity Laboratory (1954 in Souza Filho *et al.*, 2003), as classes C_4-S_2 e C_5-S_3 indicam que elas possuem elevada condutividade-C e médio a alto conteúdo de sódio-S, significando que são impróprias para irrigação tradicional. Ademais, o conteúdo elevado de sódio pode causar salinização do solo. Apenas plantas bastante resistentes ao conteúdo salino poderiam ser irrigadas.

Tabela 2.1 – Características construtivas e hidrodinâmicas de 20 poços em Juá, Irauçuba-CE. Modificado de Veríssimo e Feitosa (2002) e Souza Filho et al. (2002).

Prof. (m)	**NE (m)**	**ND (m)**	**Q (m3/h)**	**Y(m3/h/m)**	**STD (mg/l)**	**pH**	**Relações Iônicas**	**Potabilidade**	**Irrigação**
55,3 **7 a 75**	**6,2** **2,0 a 12,0**	**7,7** **6,6 a 9,0**	**3,2** **0,7 a 6,0**	**0,70** **0,03 a 1,01**	**2.778** **725 a 6.845**	**7,6** **6,7 a 7,9**	**Cloretada Sódica**	**Variável**	**C_4-S_2** **E** **C_5-S_3**

Siglas: Prof., profundidade; NE, nível estático; ND, nível dinâmico; Q, vazão; Y, vazão específica; STD, sólidos totais dissolvidos.

3 - Airborne Hydrogeophysics: an important tool to select target areas for groundwater exploration in the Crystalline Domain

(Parte do capítulo foi apresentado como um resumo expandido no X Congresso Internacional da Sociedade Brasileira de Geofísica - Souza Filho *et al.*, 2007b)

3 – AIRBORNE HYDROGEOPHYSICS

3.1 – Introduction

The history of airborne geophysical exploration began in 1944 when the USGS used a modified Magnetic Airborne Detector-MAD developed by U.S. Navy to detect submarines and, to fly the first magnetic survey over a petroleum reserve in Alaska (Hildebrand *et al.*, 1987). Airborne electromagnetic (AEM) exploration began soon after 1948 in Canada with test flights by Nickel Company using a fixed-wing system (Figure 3.1). The catalyst for the development of AEM geophysics in Canada was due to the discovery of Heath Steele deposit in News Brunswick, in 1954, and the Kidd Creek massive sulfide deposit in 1959, in Ontario. Airborne and helicopter-borne systems were responsible for the latter discovery. Several cost-effective national airborne programs for mineral exploration were then conducted world-wide using magnetics, radiometrics, electromagnetics and occasionally gravity. Countries involved in these efforts included the United States, Finland, Canada, the former U.S.S.R., China, Australia, Liberia, and Zimbabwe (Hildenbrand *et al.*, 1987), nevertheless minor areas were surveyed throughout the world.

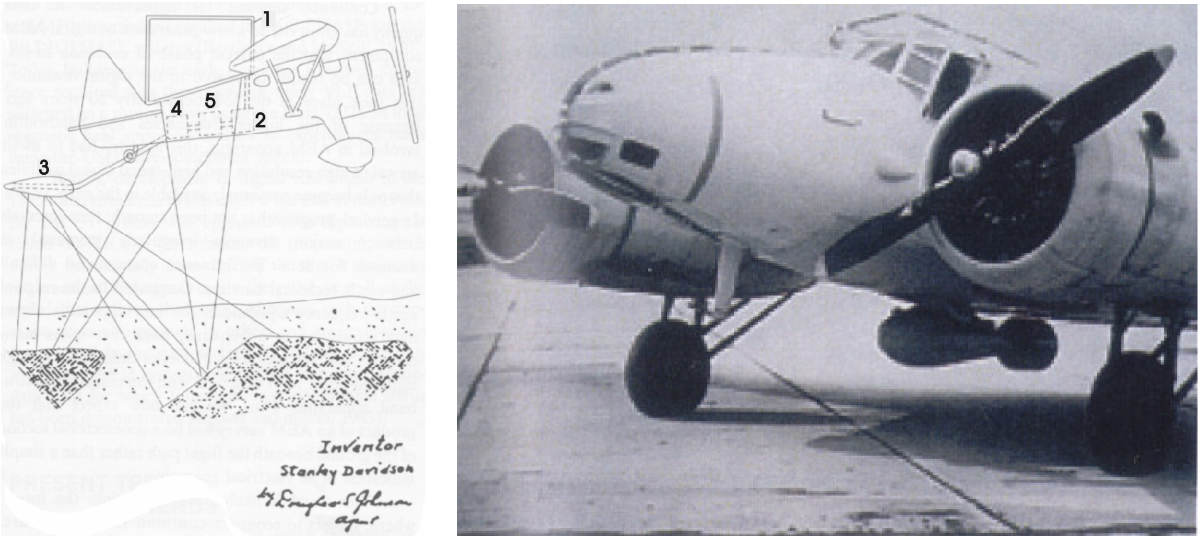

Figure 3.1 – The beginning of AEM systems and surveys. On to the left is the original schematic diagram (with the signature of the inventor) showing the transmitter coil (24), powered by an oscillator (26) and the towed receiver coil (27), connected to detector electronics (30, 31). On the right is the photo of the wood framed Anson aircraft showing the receiver bird below the fuselage (Fountain, 1998).

Hydrogeophysics has developed in recent years to investigate the potential that geophysical methods hold for providing quantitative information about subsurface hydrogeological parameters and processes (Hubbard and Rubin, 2005). Hydrogeophysical investigations seek further than the indication of geophysical “anomalies” but provide information that can be used in groundwater flow and occurrence models as examples.

The availability of airborne hydrogeophysics provides a unique tool to guide governmental management of ground-water resources and well drilling and it is used in many governmental programs such as in Australia (Coppa *et al.*, 1998) and in China (Meng *et al.*, 2006). Hildenbrand *et al.* (1987), Becker, *et al.* (1987) and Fountain (1998) provide the history of airborne geophysics development. Agencies stated the need to better-developed approaches to characterize, monitor, and investigate hydrogeological processes in shallow subsurface at relevant spatial resolution and with minor invasion (e.g., the National Research Council, 2000 and U.S. Global Change Research Program, 2001, in Hubbard and Rubin, 2005). Hydrogeophysics has evolved from the need to couple hydrogeological and geophysical studies to better provide quantitative information about environmental and hydrogeological issues.

The use of helicopter electromagnetic (HEM) surveys in hydrological applications date from the 1980`s, as described by Palacky (1986), Paterson and Reford (1986 in Becker *et al.,* 1987). The HEM data have been used to map geologic features that identify probable water bearing structures and lithologies (Sattel and Kgotlhand, 2003; Pine and Minty, 2005), and support water quality studies (Smith *et al.*, 1997; Coppa *et al.,* 1998; Meng *et al.*, 2006).

In Brazil, airborne geophysics has been used since mid 1950`s when government initiatives through the Nuclear Company (NUCLEBRAS); the Oil-and-Gas Company (PETROBRAS), National Department of Mining Production (DNPM); and the Brazilian Geological Survey (CPRM) incorporated regional magnetic and radiometric surveys on fixed-wing aircraft as prospect tools for uranium, oil, gas and metallic ore. New airborne surveys programs re-started after 2004 by CPRM. Collaborative efforts between private and state companies provided high-resolution magnetic and electromagnetic helicopter-borne surveys to explore for metallic ore bodies, specifically in Iron-Quadrangle Mineral Province in Minas Gerais State, Carajás Mineral Province in the State of Pará, and at the State of Goiás.

There were several surveys for mineral prospecting, none have focused on groundwater exploration in Brazil, despite the successful case histories known in other countries to foster the management of water salinity in farm lands or the development of water supplying alternatives. One reason is that the ground electromagnetic induction and direct current resistivity surveys have lower costs; therefore, they have traditionally been the choice during government drilling programs using equipments such as EM-34-3XL-Geonics Limited and electrical resistivimeters.

The Juá area, including Serrinha, in Rio Grande do Norte State and Samambaia in Pernambuco State was chosen for testing airborne geophysical (electromagnetic and magnetic) surveys aimed at hydrogeological exploration in Brazil. Funding was provided by an initiative of CPRM and the Geological Survey of Canada (PROASNE, 2007). In addition, the lower spatial resolution Itatira-B airborne magnetic and radiometric surveys were acquired by NUCLEBRAS (Lasa, 1978) and available from CPRM (2007b). The technical specifications of these surveys were presented in Section 1.4.

3.2 – Regional Airborne Magnetic and Radiometric Data

3.2.1 – The Magnetic Data

The Itatira-B survey consists of magnetic and radiometric data sets (Lasa, 1978). The magnetic data were provided in grid form as values of total magnetic anomaly field (nT), that were subtracted from the International Geomagnetic Reference Field (IGRF - adjusted to the date of acquisition) to enhance residual (local) field anomalies (Figure 3a). The IGRF is a theoretical higher order polynomial surface representing the geomagnetic field strength in a given area. The IGRF is specific to the local geomagnetic inclination and declination based on the date the data were collected, latitude, longitude, and elevation of the observation point (Blakely, 1995 in Silva, 1999; Millingan and Gunn, 1997).

The magnetic data along flight lines were interpolated to a grid with cell-size of 250 m. The data were corrected for spikes, using the test of 4th-difference that enhances random noise so they can be deleted. Then, the data were microleveled to avoid random values along flight-line direction due to instrumental noise or variations in flight height (Figure 3.2b). The microleveling procedure is defined Minty (1991) and in Blum (1999) and it consisted of subtracting the original grid from an error grid. The error grid is calculated in four steps: i) low-pass filtering of the original grid in the line direction to produce low-pass grid (Lp); ii) application of a high-pass filter to the original grid in the direction of the control line to produce high pass (Hp) grid; iii) creation of error grid (error) by subtraction the high-pass grid from the low-pass grid; iv) microleveling the original grid by subtracting the error grid from it. The microleveling operation can be applied more than once if the interpreter believes it is needed; however, increased application of the procedure may result in a very smooth grid and might remove geologic-related anomalies of interest. It was used the interpolation algorithm available in Oasis Montaj software.

To correct for the distortion of anomaly position and shape due to the low geomagnetic latitude of the study area, the magnetic anomaly data were reduced to the magnetic north pole (RTP, Figure 3.3a), using the algorithm of Phillips (1997) with an azimuthal filter in the frequency domain to minimize the directional noise caused by the low geomagnetic latitude. This algorithm is found in the Potential Field, a set of DOS-based algorithms organized by Phillips (1997), and lately up-graded as USGS geosoft executables in Oasis Montaj software (Phillips et al., 2003). Nowadays, the Fortran codes of USGS executables are available in Phillips (2007).

The reduction-to-magnetic pole calculation was applied to the residual magnetic anomaly grid, using the latitude and longitude channels of the regional data base and the geomagnetic parameters found in the high-resolution Juá survey (inclination of – 10.89 and declination of – 21.53, with amplitude correction of 79.11). Phillips's algorithm proved very effective in that it did not introduce noise that is often the case with similar reduction to the pole at low latitude algorithms. These declination-direction oriented artifacts are discussed in section 3.3.1.

In general, magnetic anomaly fields are produced by sources spanning a range of depths within the Earth crust. The interpreter usually wants to separate the effect of anomalies by depth according to the study's objectives. A matched filtering algorithm (Syberg, 1972) found in Potential Field software provided a way of separating the top of magnetic anomalies associated with shallow sources from anomalies associated with top of deeper magnetic sources. The technique, which assumes simple magnetic source models (half-layer, dipole-layer or density-alyer) uses frequency domain filters (Syberg, 1972) to interactively design wavelength filters based on segmentation of the power spectrum of the regional data (Figure 3.4), adjusted to the chosen source models. The fourier transformation enables the application of the designed filters to the data in the frequency domain then the data are transformed back into the space domain and re-gridded.

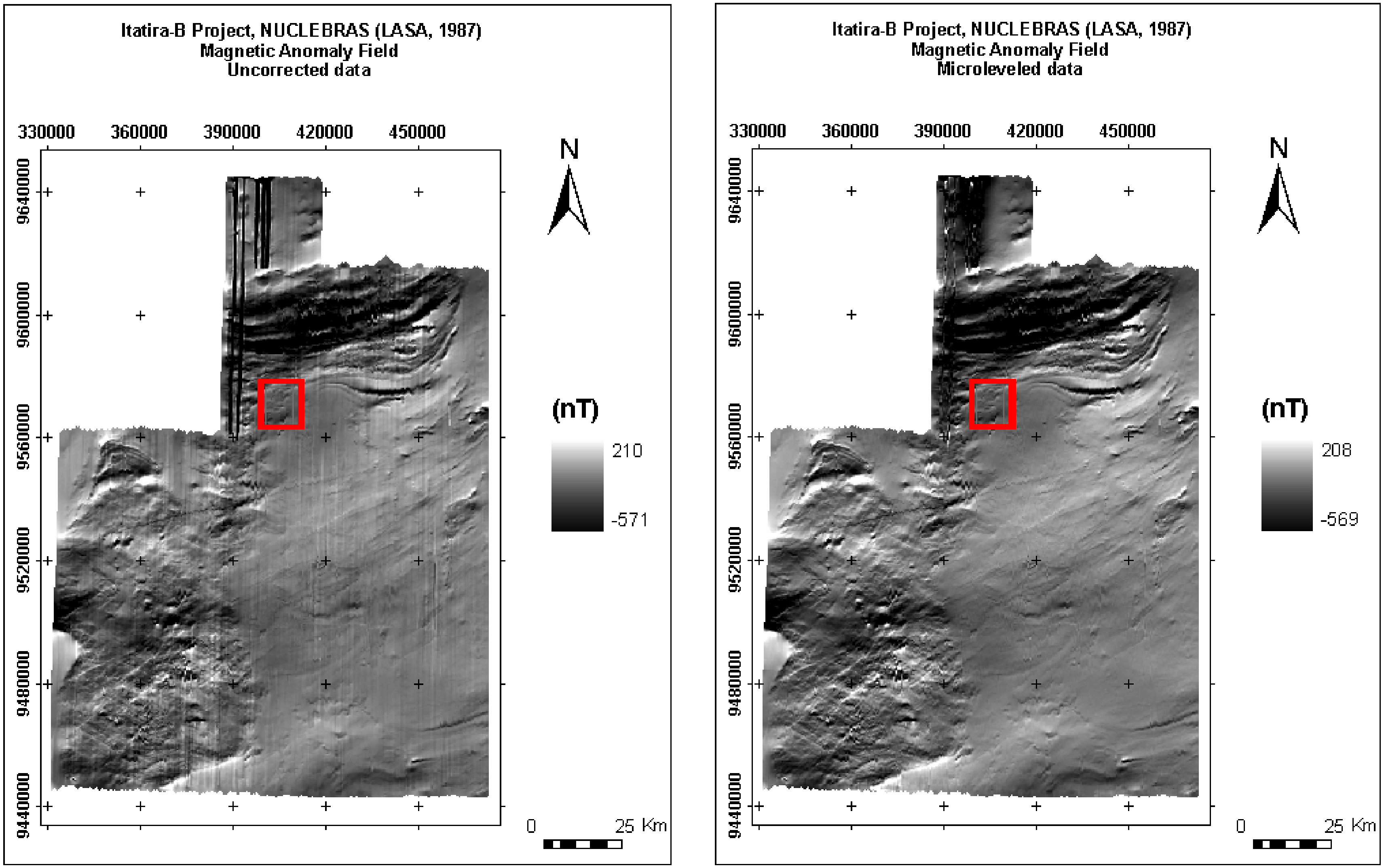

a)

b)

Figure 3.2 – Maps of magnetic anomaly field of Itatira-B Survey: a) IGRF-reduced raw data; b) Microleveled data. Red polygon is the Juá study area.

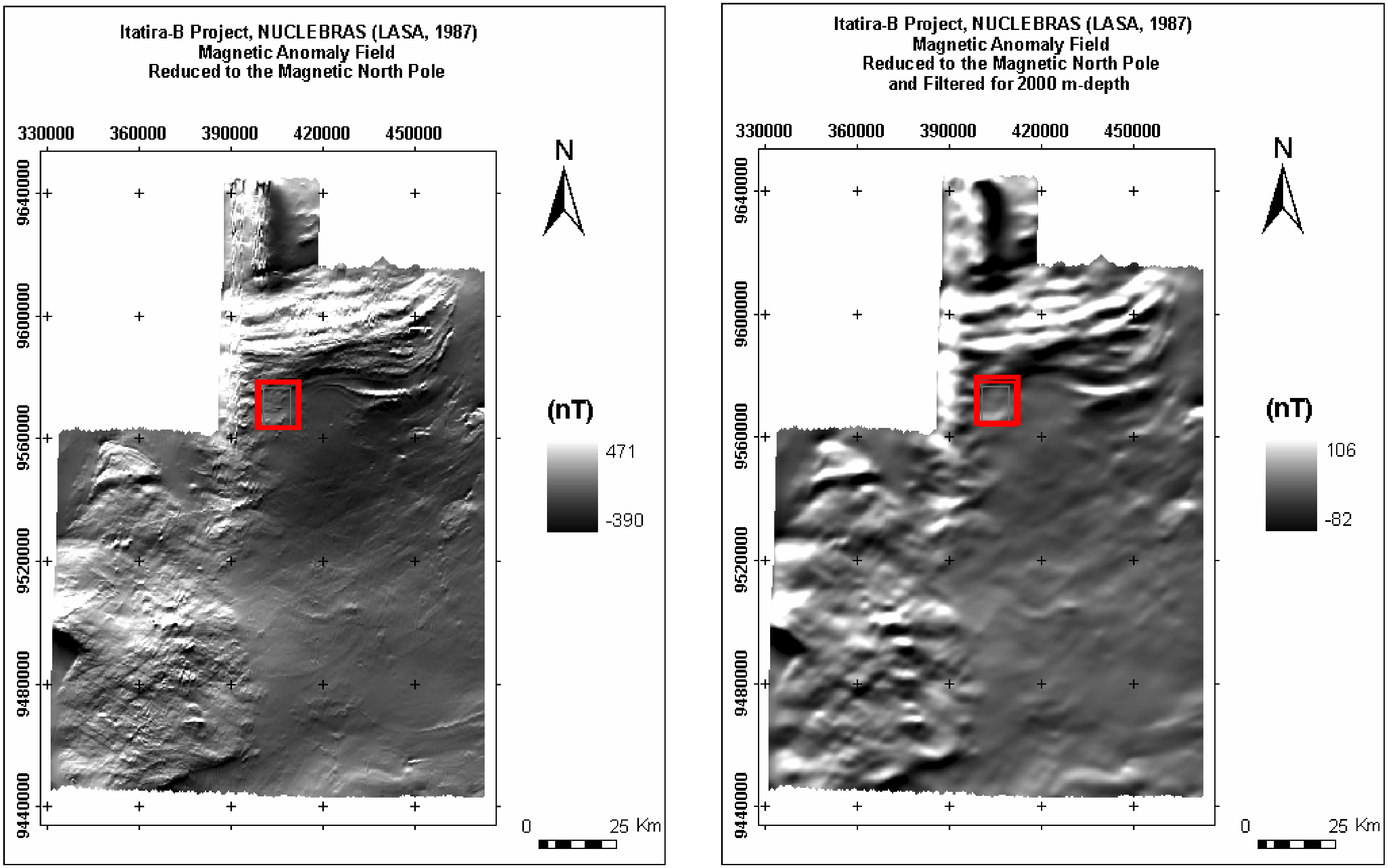

a) b)

Figure 3.3 – Maps of magnetic anomaly field of Itatira-B Survey: a) Reduced to the magnetic north pole-RTP map; b) RTP-magnetic field filtered to sources between 2000 m and 400 m depth. Red polygon is the Juá study area.

Thus, the main contributions of higher, mid, and lower frequencies can be distinguished within the data and separated into depth intervals. Three magnetic layers associated with the following depth ranges (0 - 50, 50 - 400 and 400 - 2000 meters) were determined for the Itatira data (Table 3.1). Wavelengths related to the first layer were fit considering a magnetic dipole model to represent the high-frequency variation of surface small sources. The wavelengths of next layers were adjusted as half-layer source models, more indicative of uniform geomagnetic units. The adjusted spectrum combines linear, concave upward and concave downward behavior.

The data whose wavelengths correspond to anomalies between 400 m and 2000 m depth were gridded (Figure 3.3b). This grid was subtracted from the grid of reduced-to-pole magnetic anomalies of Juá airborne data to emphasize deep anomalies within the study area (section 3.3.1).

Table 3.1 – Estimated depth to the top of magnetic sources based on a half-layer model from the Itatira airborne survey calculated with the matched filtering technique (Syberg, 1972). Depth values are rounded to the nearest 10s of meters.

Depth (m)	Magnetic Model	Minimum Wavelength	Maximum Wavelength
Less than 50	Magnetic dipole	501.0	567.4
400 to 2000	Half-layer	567.4	10430
More than 2000	Half-layer	10430	26670

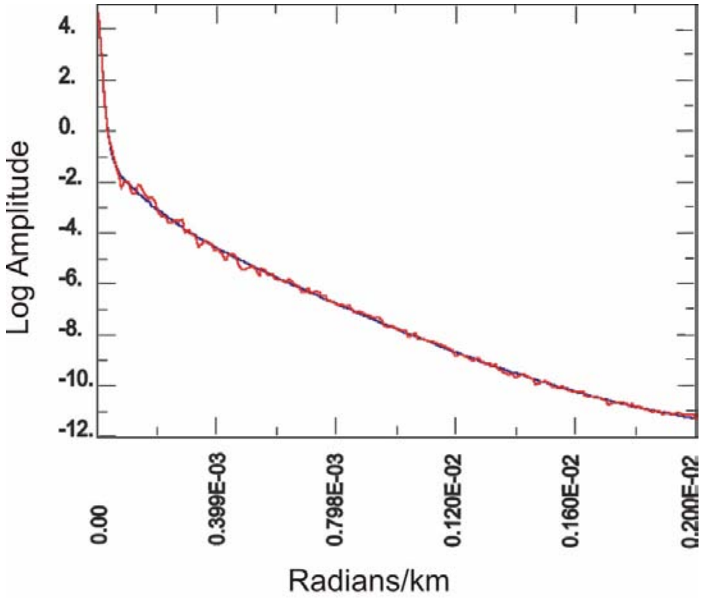

Figure 3.4 – Radially averaged amplitude spectrum of the gridded reduced-to-the-pole Itatira-B magnetic data.

3.2.2 – The Radiometric Data

The radiometric data base provided by CPRM consists of potassium, thorium and uranium channels as counts per second (cps) (Figure 3.5). Each radiometric channel was microleveled with the same technique as for the magnetic data. Then, they were interpolated by minimum curvature technique (algorithms available in Oasis Montaj software) and resampled onto a 25-m cell over the Juá study area (Figures 3.6a,b and 3.7). This resampling parameter was chosen to match the higher spatial resolution of the helicopter-borne survey, and the unit cell of the groundwater modeling procedures.

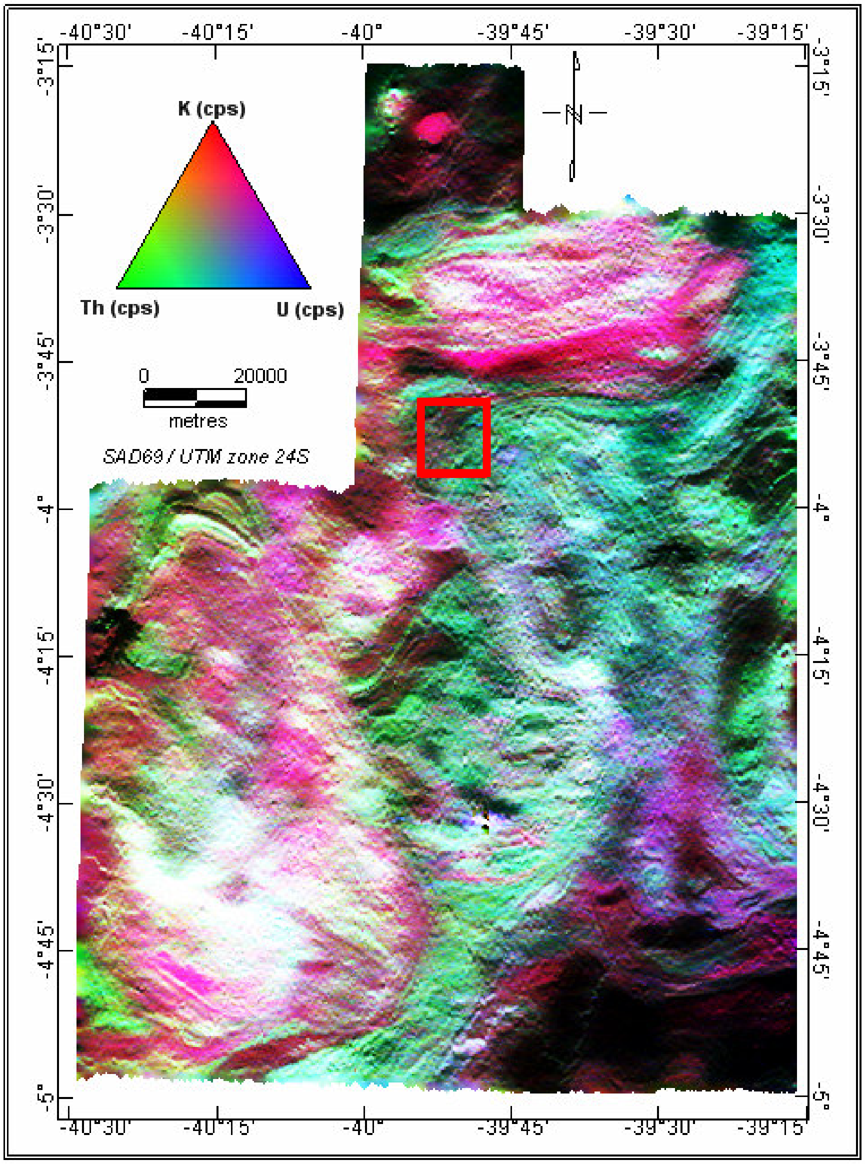

Figure 3.5 – RGB Color composite of Itatira-B radiometric data, with potassium in red, thorium in green and uranium in blue. Red polygon is the study area of Juá.

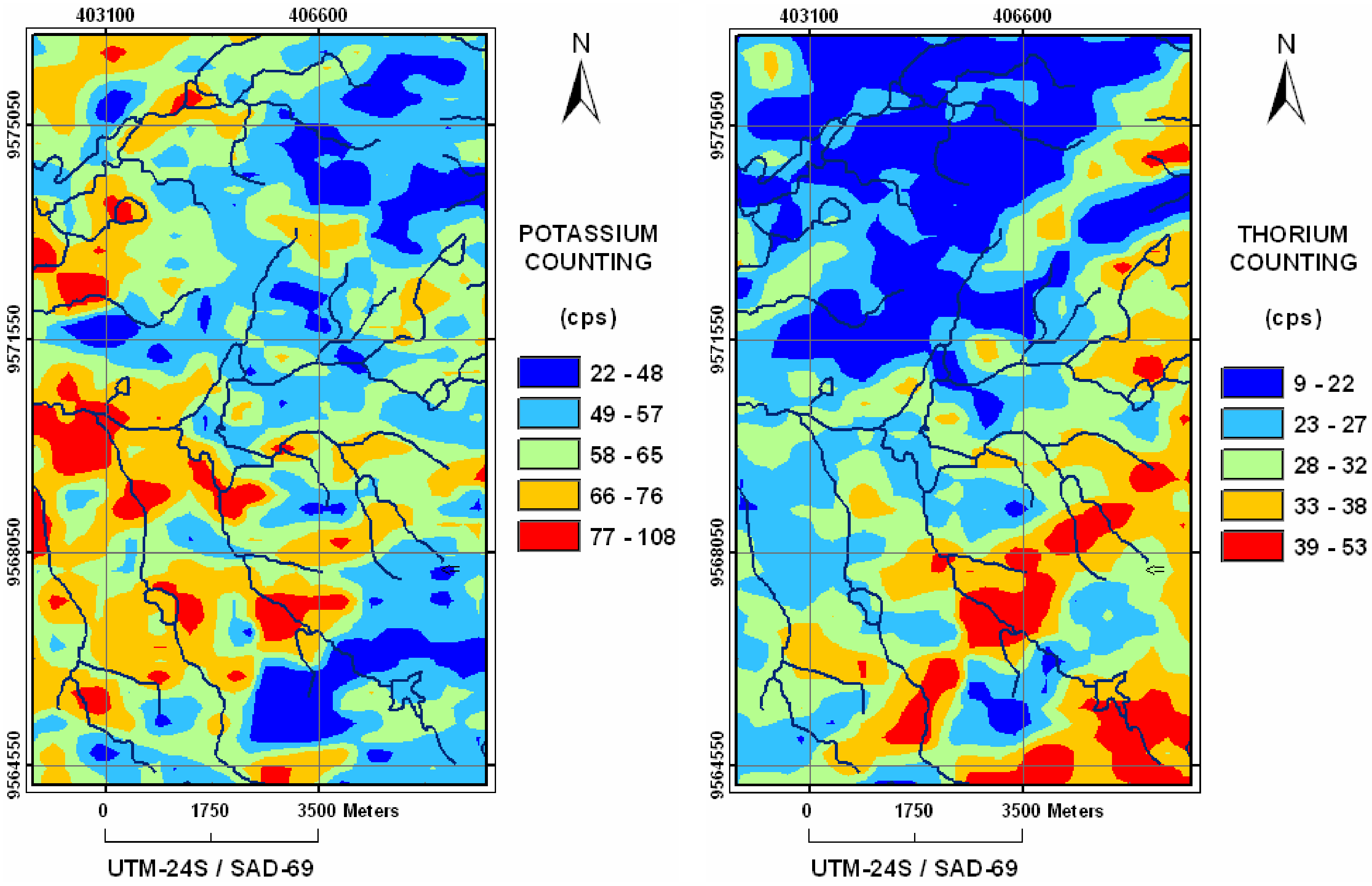

a) b)

Figure 3.6 – Itatira-B radiometric data resampled to 25-m cell-size grid and trimmed to Juá study-area. a) Potassium intensity in counts per second. b) Thorium intensity in counts per second. Drainage and reservoirs are indicated by blue lines.

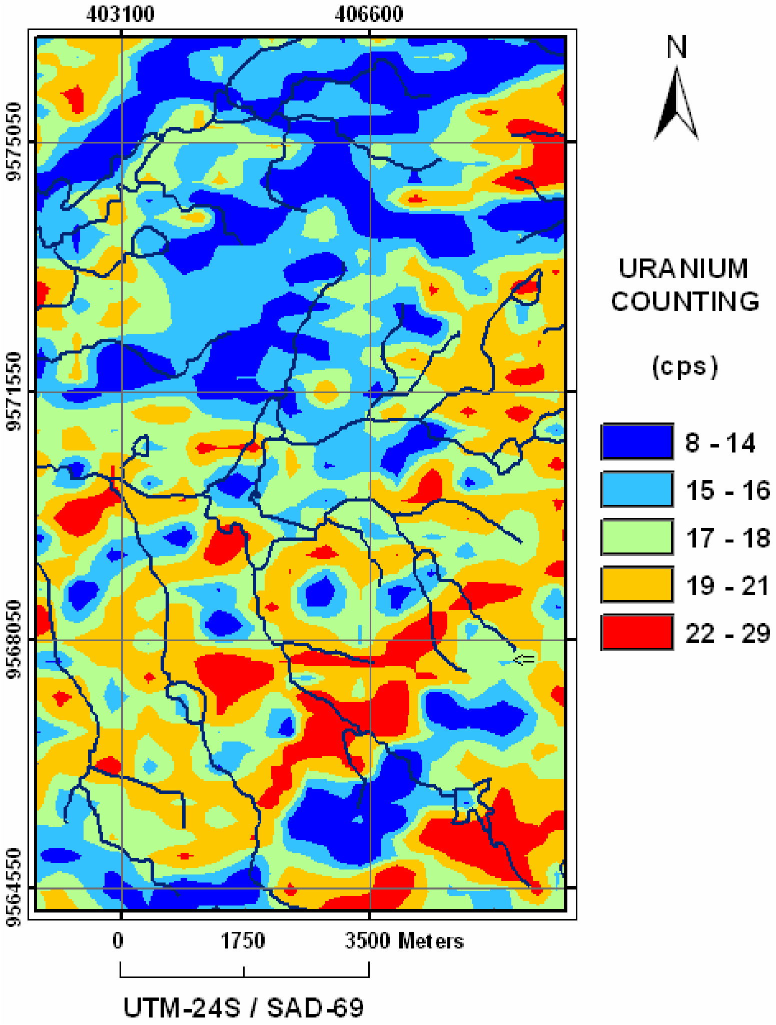

Figure 3.7 – Itatira-B radiometric data resampled on 25-m cell-size grid and trimmed to Juá study-area. Uranium intensity in CPS. Drainage and reservoirs are indicated by blue lines.

3.3 –High Resolution Helicopter Magnetic and Electromagnetic Data

3.3.1 - The Magnetic Data

The high resolution magnetic data were provided by the contractor as values of total magnetic field (nT). The magnetic data recorded along flight lines were interpolated using a minimum curvature algorithm (available in Oasis Montaj) to a regular 25-m cell-size grid, corrected for spikes, and microleveled (using the same technique applied to Itatira-B magnetic data). The corrected total field magnetic data was subtracted from the Definitive International Geomagnetic Reference Field-DGRF (referred to the acquisition date) to enhance the residual (local) field anomalies associated with the earth's crust. The following local geomagnetic parameters were used: inclination -10.89°, declination of -21.53° and an elevation represented by the barometric height of the magnetic sensor.

The magnetic residual field data were reduced to the magnetic north pole (RTP grid) using the methodology of Phillips (1997) based on the geomagnetic parameters described above, the latitude, the longitude, and the altitude channels from the data base. An azimuthal filter was applied to reduce artifacts created in the direction of magnetic field declination, a common problem for data acquired at low geomagnetic latitudes (Figure 3.8a,b).

The RTP data were filtered using the methodology of Syberg (1972) in Potential Field software (Phillips, 1997) to separate shallow and deep magnetic sources as previously discussed (Figure 3.9). The results indicate tops of very shallow sources at depths about 20 m, tops of shallow magnetic sources with depth about 60 m and deep magnetic sources at 270 m below ground surface (Table 3.2). For this groundwater study, the regions of interest extends to 200 m from the surface, so data related to the magnetic layers with tops at 60 m and 270 m are important.

The data with wavenumber intervals associated to depths ranging from 20 m to 60 m were gridded to comprise a map of shallow magnetic anomalies (60m-layer magnetic map, Figure 3.10a). This map corresponds to geomagnetic units and gradients located within depths of water-wells in the Juá area (mean depth of 55 m, Section 2.3), and it was one of the geophysical information used for spatial characterization of the physical properties associated with lithology (Section 3.5) and groundwater modeling (Chapter 5).

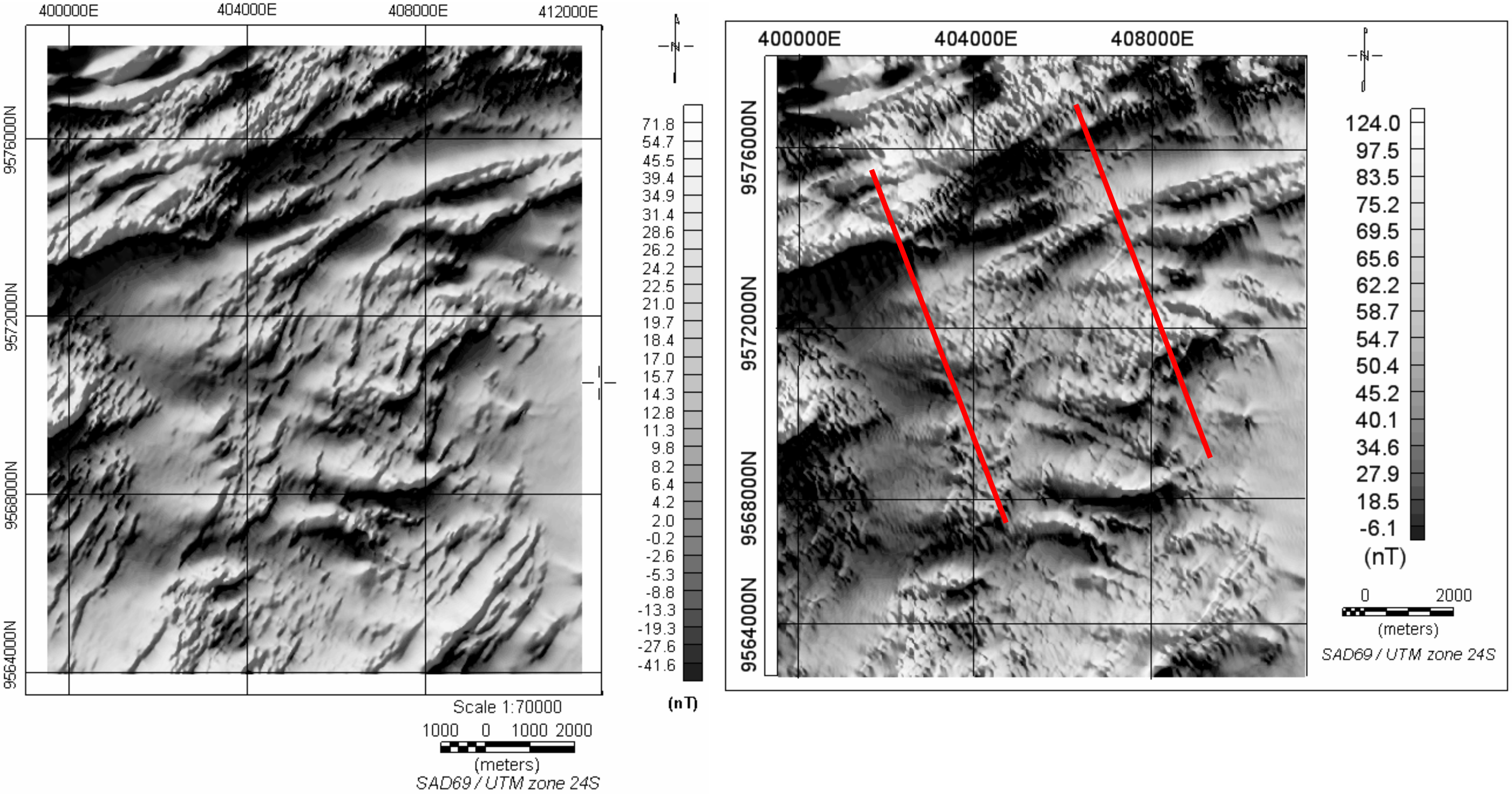

a) b)

Figure 3.8 – Comparison of reductions to magnetic north pole filters applied on Juá magnetic residual field grid: a) good result using Phillips (1997) algorithm with amplitude correction of 79.11°; b) bad result using Oasis Montaj algorithm with amplitude correction of 70 ° plus a cosine low-pass filter at 130° Azimuth. Red traces mark artifacts with direction parallel to the geomagnectic declination, generated after the application of Oasis Montaj's algorithm.

Table 3.2 – Estimated depth for wavelength intervals of magnetic sources from Juá survey data calculated with the matched filtering technique (Philipps, 1997). Depth values are rounded to the nearest 10s of meters.

Depth (m)	Magnetic Model	Minimum Wavelength	Maximum Wavelength
Less than 20	Magnetic dipole	50.4	73.0
60 to 270	Half-layer	73.0	482.1
More than 270	Half-layer	482.1	1.7 x 10^{-6}

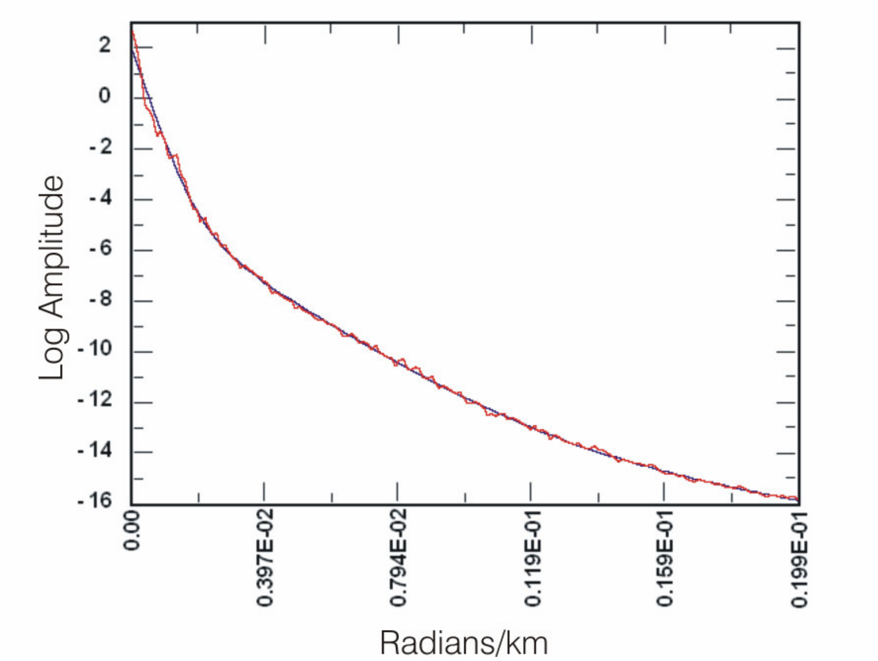

Figure 3.9 – Radially averaged amplitude spectrum of the gridded reduced-to-the-pole Juá magnetic data.

Gridded data from the mid and deep magnetic layers were combined to produce a mid-layer grid (MLgrid) that contains anomalies related to shallower sources (correlated to fractures, joints, and geologic units under the influence of weathering processes) and the longer wavelength of deeper sources at 270 m (geologic units and boundaries).

The MLgrid grid were converted to a magnetic potential grid (PsGgrid map) using methodology by Baranov (1957) and algorithm of Phillips (1997) (Figures 3.11; definition in Annex) to improve the location of magnetic source boundaries associated with edges of geologic units or to map geologic structures.

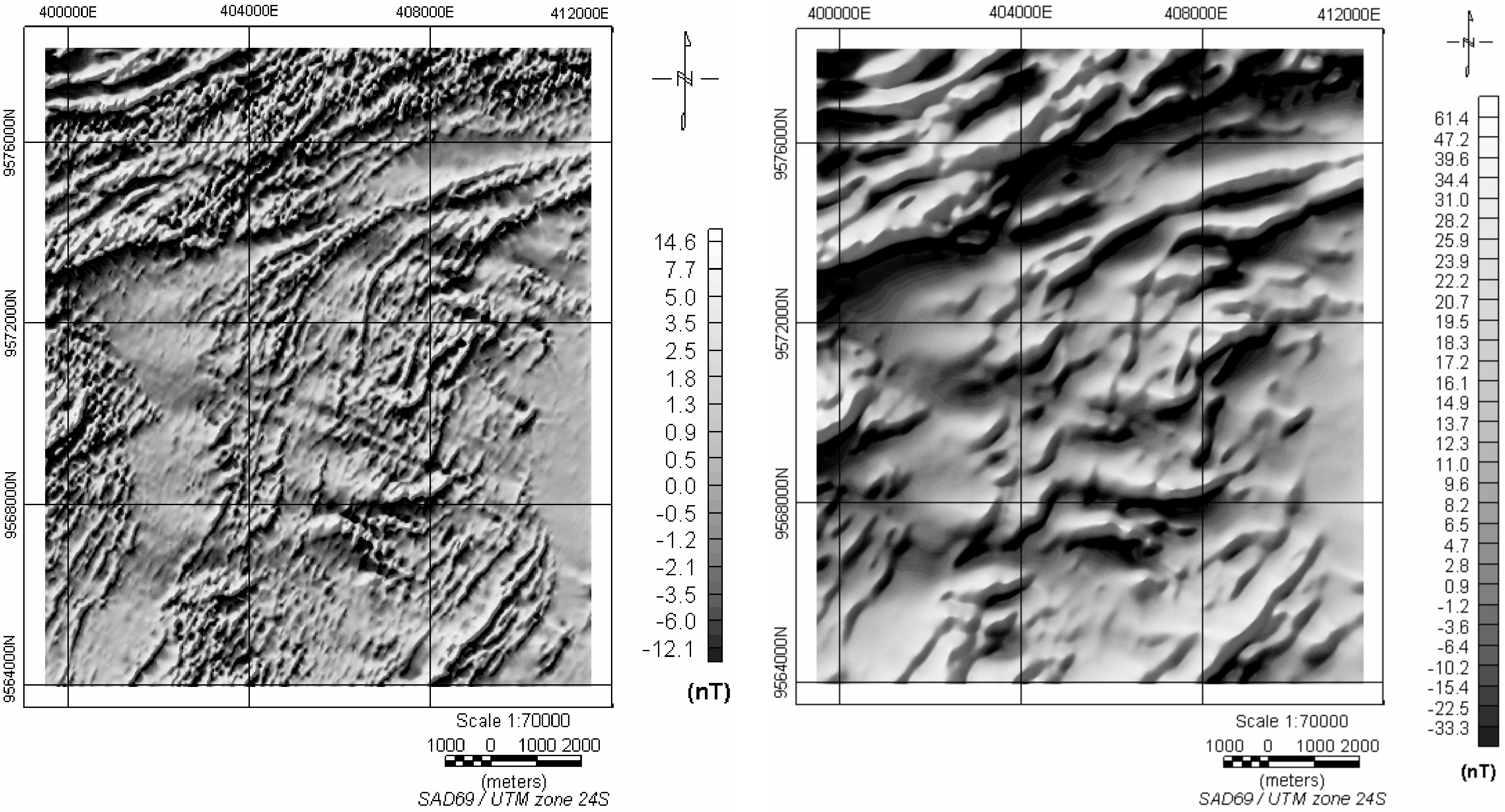

a) b)

Figure 3.10 – Juá reduced-to-pole magnetic anomaly data filtered to depth ranges from: a) 20 m to 60 m and b) from 20 m to 270 m. Application of Phillips (1997)'s algorithm.

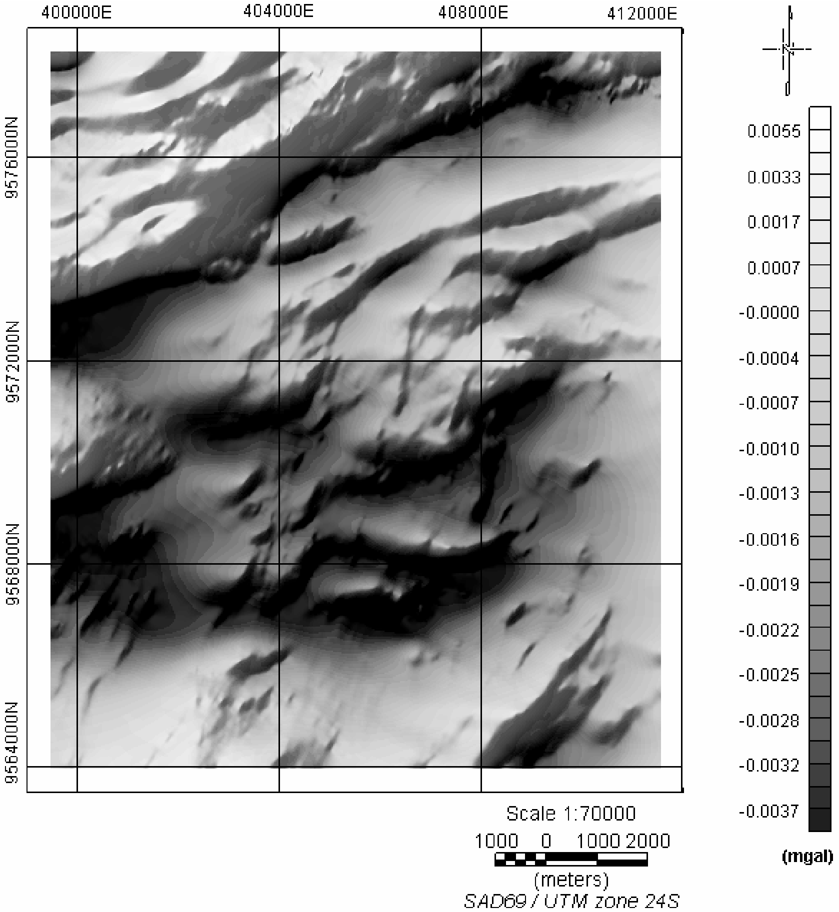

Figure 3.11 – Juá high-resolution magnetic potential map applied to the magnetic anomaly grid of sources located within 60 m to 270 m depth.

To delineate the edges of magnetic sources, the horizontal gradient of the magnetic potential was calculated (Blakely and Simpson, 1986). Linear gradients also were extracted from the vertical derivatives of magnetic anomalies filtered to 60 m depth and from the map of residual field.

The magnetic potential grid served as input to a terracing operator (Cordell and McCafferty, 1989), which generates a geologic-like map of magnetic sources (TerMgrid). The terracing technique enhances zones of similar magnetization and sharply delineates the edges between geologic units with different magnetic properties. These edges often enhance magnetization contrast caused by shear zones and geologic fault boundaries (Figure 3.12a). This terrace map was used in modeling of groundwater favorability, and the recognition of geophysical parameters associated with mapped lithology.

The longer wavelength magnetic field calculated from the regional magnetic anomaly grid was resampled to 25-m cell size grid and trimmed to the Juá area. This grid was subtracted from the local RTP-magnetic of the Juá survey (Figure 3.12b) and provided information about magnetic sources and structures that extend down to 2000 m depth.

The information about deep-crust gradients could not be obtained by only processing the local data because the longest possible mapped wavelength is limited to the survey extent, therefore the regional survey can better represent the longer wavelength anomalies than the local Juá survey (Figure 3.9 and Table 3.2).

Vertical derivatives were calculated from both 270 m-depth layer and the 60 m-depth layer (Figure 3.13) to help the physical characterization of geologic units. The calculus of vertical derivative quantifies the rate of change in the magnetic field in the vertical direction, and works as a high-pass filter, enhancing information related to shallow sources. Magnetic and non-magnetic gradients were extracted from these maps and then transformed to raster images to provide additional information to be used for spatial groundwater modeling.

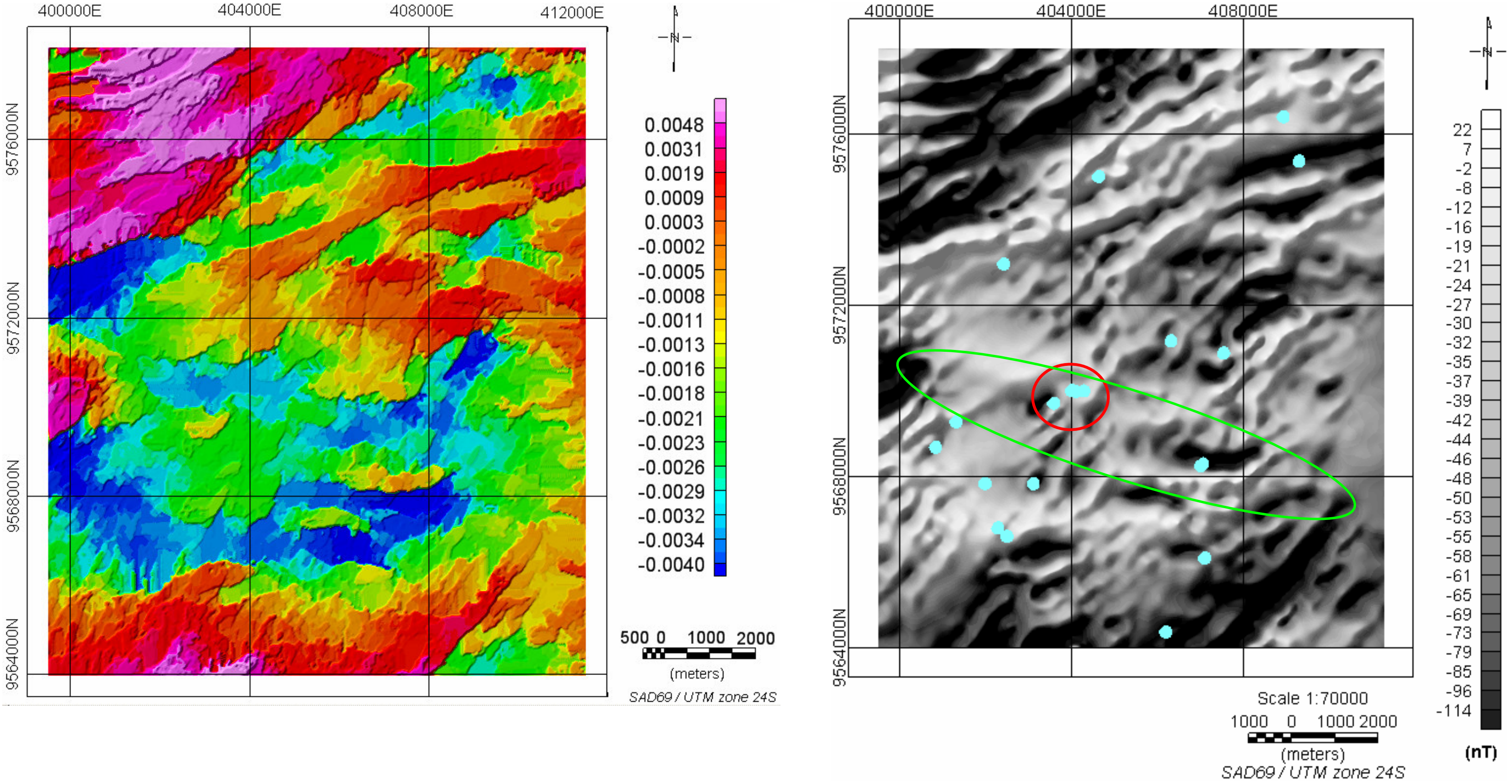

a) b)

Figure 3.12 - Juá high-resolution magnetic data processed as: a) Terrace-magnetization map using the terracing technique of Cordell and McCafferty (1989), and b) High-resolution 2000-m-depth layer grid after the subtraction of the regional 2000-m-depth grid from higher-resolution anomaly grid. The dots represent locations of drilled water-wells. Note that in the map (b), the most productive wells (surrounded by a red circle) are in the border of an important negative gradient, oriented WNW-ESE (marked by a green ellipse).

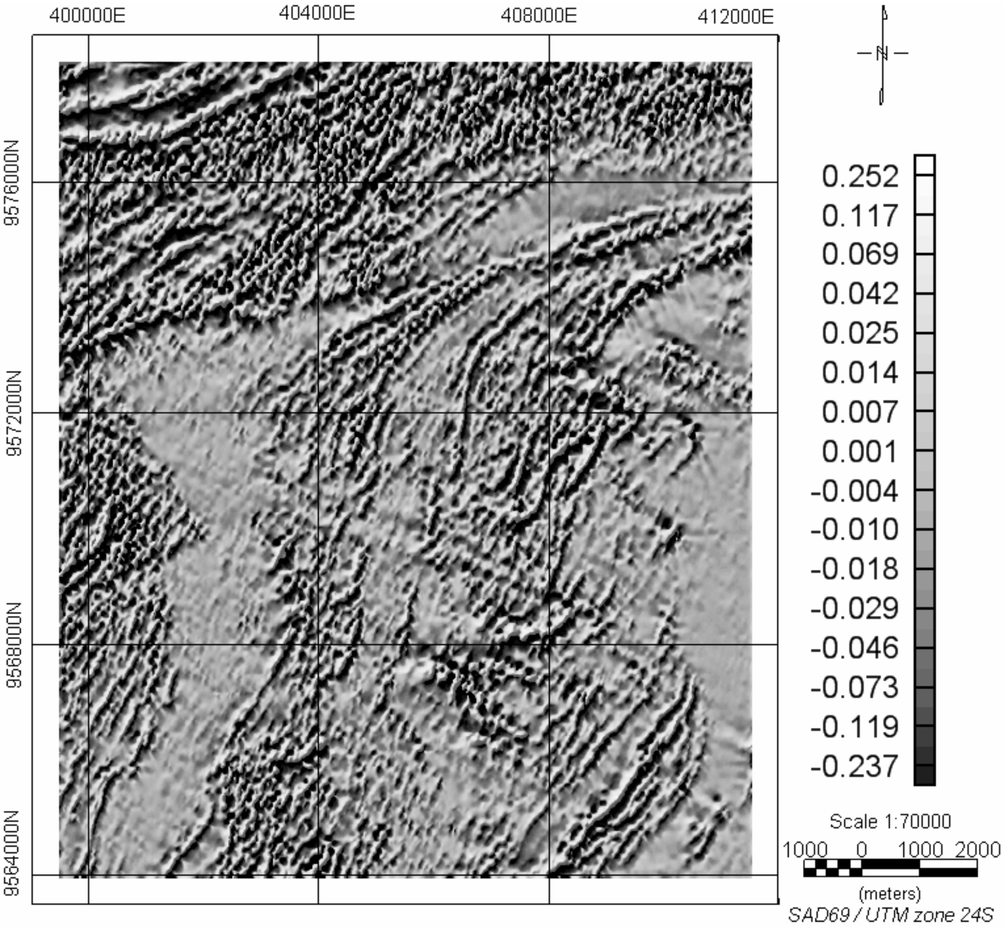

Figure 3.13 – Juá high-resolution magnetic data. Vertical derivative map (nT/m) calculated from the magnetic residual field filtered to 60-m-depth layer. Map shows high-frequency information, related to shallow sources and boundaries between geomagnetic units.

3.3.2 - The Helicopter Electromagnetic (HEM) Data

Of all the data sets, the airborne electromagnetic data required the most processing to correct for variations in flight height and instrumental noise along the flight lines. Some incoherent values (noise) remained in the channels of the 900 Hz and 33000 Hz frequencies (apparent electrical conductivity values), however they did not interfered with the quality of information. Further microleveling might have removed high frequency geological information of interest such as conductive linear features.

The microleveled data were interpolated to grids of 25-m cell-size using a minimum curvature method available in the Oasis Montaj software. Figures 3.14 (a,b,c) show the apparent conductivity maps for the three frequencies measured. Due to frequency and coil configurations, similarities regarding the main conductive boundaries are evident among them, nevertheless, each one provides different information with respect to depth and type of source. These characteristics shall be discussed in Sections 3.4 with regard to correspondence with depths of exploration and in Section 3.5 with regard to characterization of geophysical properties of rocks at the Juá area.

The grid of the apparent conductivity data at the 4500 Hz frequency (HEM-4500) was transformed to physical property map of conductivity using the terracing technique (Cordell and McCafferty, 1989). The terrace operator was applied to the conductivity data to produce uniform conductivity domains separated by abrupt boundaries. This map has been used in the spatial groundwater modeling and in the characterization of geophysical properties of Juá rocks. Details of this technique are presented in the Annex.

Conductive and non-conductive gradients were interpreted from several HEM grids and transformed into vector files. Proximity zones of 50 m apart from lineaments were calculated for each lineaments vector file and then, transformed in to raster of proximity zones of lineaments to participate in groundwater modeling.

The conductivity data were also inverted for depth assuming horizontal half-layer models with EMIGMA v. 7.8 software (Petros Eikon Inc.). The resulting models were correlated with known lithology and mapped tectonic structures. Details of the inversion and results are described in Section 3.5 of this chapter.

Another kind of data available in HEM data base are the quadrature (Q) and in-phase (I) channels which represent the direct measurement of the components of the secondary electromagnetic field generated by conductive bodies in the ground. These maps were used investigate the variations of electrical properties with depth, as described in Section 3.5.

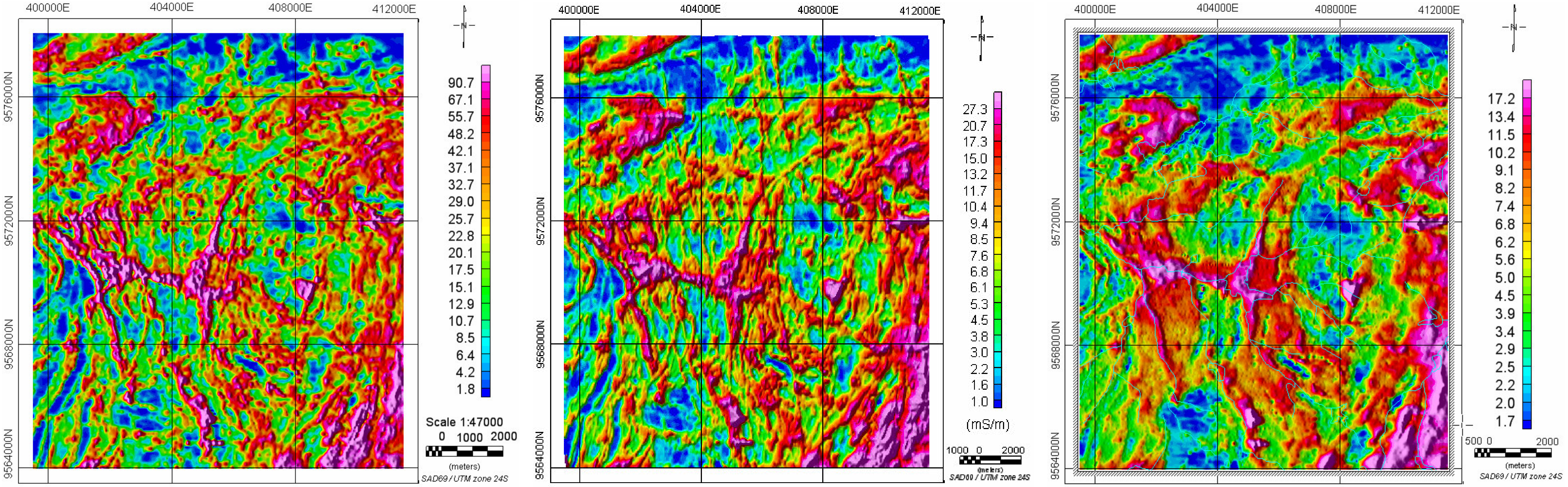

a) b) c)

Figure 3.14 – Apparent conductivity (mS/m) maps gridded from the Juá helicopter electromagnetic data-HEM: a) HEM – 33000 Hz, coplanar coil configuration, and it is more indicative of soil horizon conductivity; b) HEM – 4500 Hz, coaxial coil configuration, and is more related to rock and cross-cutting gradients conductivity; c) HEM – 900 Hz, coplanar coil configuration, which better depicts geoeletric units related to lithology.

3.4 - Sensitivity Analysis and Exploration Depth for Juá HEM Data

The detection of electromagnetic anomalies depends on the attenuation of the emitted (primary) electromagnetic field with depth (skin depth), and the sensor sensitivity compared to the secondary field generated by current induced in the conductive target. Sensitivity means the minimum signal above the noise level that can be measured. Other attenuation factors include the increasing of the operational frequency transmitted by the sensor, high ground conductivity, the height of the sensor, and as well as artificial and geologic noise levels. (See the annex for details).

The HEM sensor used in the Juá survey, Aerodat-DSP-99, has a sensitivity of about 5 ppm with respect the primary field (Lasa, 2001). Sensitivity analysis was done by forward modeling (in EMIGMA software) where it was calculated what would be the value of the secondary field components (ppm) at a given frequency, regarding a fixed top layer thickness and resistivity, and varying the half-space basement resistivity (Figure 3.15 a,b).

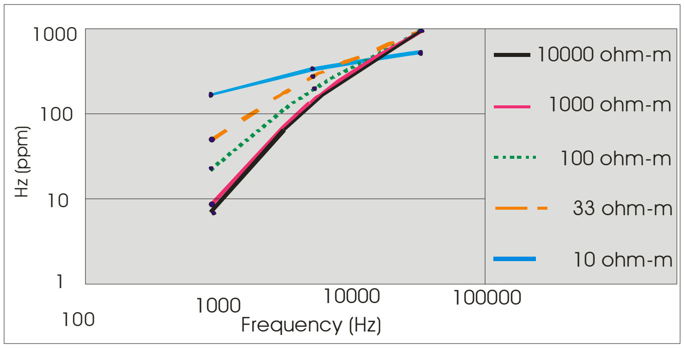

a) In-phase sensitivity to basement resistivity.

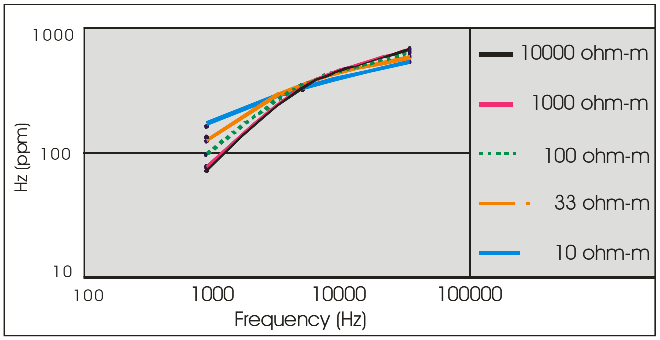

b) Quadrature sensitivity to basement resistivity.

Figures 3.15 - Sensitivity of the HEM sensor for the Juá area, in respect to the basement resistivity based in one-layer model. Top layer with fixed resistivity of 33 ohm-m (30 mS/m) and

15 m thick. Note that the HEM sensor does not distinguish basement resistivity greater than 1000 ohm-m.

From Figures 3.15 a,b it is known that the system can resolve the basement resistivity if it is less than 1000 ohm-m (or greater than 1 mS/m apparent conductivity). Therefore, for basement resistivities above 1000 ohm-m, the HEM response is too small to distinguish higher values of resistivity (apparent conductivity less than 0.1 mS/m).

Skin depth refers to the electrical attenuation of an electromagnetic plane-wave that was generated in infinite source (e.g. magnetotelluric field). In practical terms, this is considered the depth at which the primary field strength is reduced by about 37% from the original value according to the Equation 3.1 (Telford *et al.*, 1984; Pine and Minty, 2005), and assuming that the field strength on the surface is 1.

$$\delta = 503\sqrt{\rho / f} \quad \text{or} \quad 15910\sqrt{1/\sigma f} \;, \qquad \text{Equation 3.1}$$

where, δ = *skin depth (m)*; ρ = electrical resistivity (ohm-m); σ = electrical conductivity (mS/m); f = operational frequency of electromagnetic sensor (hertz)

The formula has been used in the airborne and ground electromagnetic surveys as a first approximation of the depth of signal penetration (e.g. McNeill, 1980; Stewart, 1987; Peltoniemi, 1998; Pine and Minty, 2005 among others).

3.4.1 - HEM Depths of Investigation of and Their Hydrogeological Meaning

The skin depth values for the Juá HEM data are presented in Table 3.3. Based on measured values of apparent conductivity, a moderately conductive and a more conductive ground are represented by the mean and mean + standard deviation, respectively, for each acquisition frequency. Values compiled in this manner should be considered as a guide for exploration depths because the penetration of the signal can be affected by other factors as previously mentioned.

The Juá HEM survey was planned to investigate to depths of 40 m below the surface (Lasa, 2001 and personal communications by PROASNE managers), and a variety of geologic information is distinguished for each acquisition frequency (Figure 3.14 a,b,c) and related exploration depth.

Table 3.3 – Skin depth estimates for the Juá HEM data, based on equation in Telford *et al.* (1984). Note the differences in signal penetration due to acquisition frequency and conductivity variation.

	Estimated Depth of Investigation					
	HEM 900 Hz σ (mS/m)	Skin Depth (m)	HEM 4500 Hz σ (mS/m)	Skin Depth (m)	HEM 33000 Hz σ (mS/m)	Skin Depth (m)
Mean	7	200	10	75	31	16
Mean + Standard Deviation	13	147	21	52	64	11

As can be seen from Table 3.3 and from the forward calculations for the central area (Section 3.6, Figure 3.24) the HEM-33000 Hz high-frequency survey only penetrates the first 10 m of subsurface, therefore it provides information about surface cover but contains high frequency noise however. The measured secondary field at this frequency is only sensible from the first meters of soil due to contrast between highly conductive surface cover above resistive bedrock (Figure 3.15), while lower acquisition frequencies penetrate farther (tens to hundred of meters). Based on forward calculations for HEM-4500 Hz data, using a model of conductive vertical thin plate (Lasa, 2001), 95 % of anomaly depths are above 24 m depth, and that explains why this intermediary frequency channel provided information on both gradients and surface cover. The 900-Hz frequency channel can penetrate farther than 24 m, so rock units are more visible than gradients or surface cover in these data.

Consequently, two situations are found: i) the more resistive bedrock does not generate a secondary EM field that is strong enough to be detected by the sensors (i.e. the anomalies are beyond the sensitivity limit of 5 ppm); and ii) the conductivity of water-filled fractures in bedrock are low enough to be detected. Nevertheless, the contrast between the conductive regolith and the resistive bedrock allows estimation of depth to the bedrock.

The N-S and ESE-WNW orientations (Figures 3.14 b,c) correspond to coherent electrically conductive gradients, which field data and others like Souza Filho (1998) confirm an extensive brittle-tectonic origin, therefore, they are favorable to groundwater occurrence.

According to Palacky (1991), the conductivity of granite-derived saprolites ranges from 15 mS/m to 4.5 mS/m, whereas schist- and gneiss-derived saprolites begin around 7.6 mS/m. Such values are compatible with those found in table 3.3 and in the apparent conductivity maps for the three acquisition frequencies used to study the Juá area. Laboratory measurements (Telford *et al.,* 1984) with 3% volume water content in crystalline rocks produces an apparent electrical conductivity mean of $2.3\text{x}10^{-1}$ mS/m. This value is very representative of the Juá apparent conductivity maps (see Figures 3.14 ab,c).

3.5 – Electromagnetic Anomalies: Analogy to Conductive Thin Plates

This section discusses the interpretation of Juá electromagnetic anomalies in the context of tabular vertical conductors. This analysis is based on the principle of mutual inductance of electromagnetic fields generated by elongated 2-D conductors. The identification of these vertical anomalies is useful for mapping permeable brittle structures in a crystalline domain (E.g.: Palacky, 1991; McNeill, 19991; Feitosa, 2000; Everett and Meju 2005).

For this study, the leveled 25-m cell size grids of the inphase (Ip), the quadrature (Q) and the apparent electrical conductivity channels were used. The Ip and Q response channels, which are reported as parts per million (ppm) of the primary electromagnetic field, are generated by conductive targets in the subsurface. The corresponding apparent electrical conductivity maps were provided in Figures 3.14 a,b,c (Section 3.3). See Annex for further definitions of HEM data measurements.

3.5.1 – Theory of Mutual Inductance

When a conductive geological target is excited by the primary electromagnetic field, a secondary induced field is generated. The characteristics of this induced field are dependent on the intensity and geometry of the primary field, and the inductance of the target itself (Telford *et al.*, 1984). Consequently, these dependencies review the quality of the target being a strong or weak conductor. The conductivity of the host rock and soil are the main causes of induced field attenuation, as they restrain the detection capability of the HEM sensor.

The majority of the signal generated by a tabular vertical conductor comes from its upper-most portion. As a first approximation, its response is equivalent to that generated by a current travelling through a line conductor. This allows the signature of a planar source of simple geometry to be approximated. For such a conductor, the measured signal S is a complex quantity given by Equation 3.2.

$$S = -\frac{k_{CR} k_{TC}}{k_{TR}} \frac{\chi^2 + i\chi}{1 + \chi^2} \qquad \text{Equation 3.2,}$$

k_{CR}, k_{TC} and k_{TR} are mutual coupling parameters that depend on the configuration and distance of the sensors (T = Transmitter coil; R = Receiver coil) in relation to the conductive target (C); $i = \sqrt{-1}$ the unit imaginary number.

The term χ is such that (Equation 3.3):

$$\chi = \omega \frac{L_C}{r_C}, \qquad \text{Equation 3.3,}$$

where ω is the wavenumber, $\omega = 2\pi f$ (f is the transmitter frequency), L_C and r_C are the inductance and resistance of target, respectively. Defining I/Q as the ratio of the real to the imaginary part of S, thus $I/Q = \chi$. This ratio assumes a constant value as $\omega L_C / r_C$ consequently it must depend on the inductance and the resistance of the conductor as well as measurement frequency. If this ratio is not constant (in practical terms: between a range defined by the experimental error) it may indicate that the conductor in question can not be represented by a linear feature of homogeneous characteristic. Assuming that a fracture zone can be represented by a linear feature in 2-D maps one test of consistency might be the verification that the I/Q ratio is constant over all profiles traversing the feature.

3.5.2 – Identification of HEM Anomalies and Their Hydrogeological Meaning

Experiments done at the Institute of Astronomy, Geophysics and Atmospheric Science/University of São Paulo indicated that the Geonics EM-38 ground-conductivity meter could discriminate between iron and aluminum bars buried few a centimeters in the soil. The measurements were taken as transverse profiles across the bars. The χ ratio was calculated for each line data (Mendonça, personal communication). The χ ratio was similar for measurements over individual bars.

The χ ratio for the Juá HEM data also was calculated for the three frequencies and coil arrangements: $\chi^{900}{}_{\text{coaxial, coplanar}}$ (Figure 3.15a,b), $\chi^{4500}{}_{\text{coaxial, coplanar}}$ (Figure 3.16a,b) and $\chi^{33000}{}_{coplanar}$ (Figure 3.17). Since each frequency gives information over a different range of depths, the $\chi_{coaxial}$ and $\chi_{coplanar}$ grids were subtracted from each other for the HEM-4500Hz and HEM-900 Hz data sets as shown in Equations 3.4a, b**.** These calculations were done to quantify the apparent variation of the χ ratio with depth, and consequently, the relative intensity of the anomalies.

For HEM-4500 Hz data; $\chi^{4500}sub = \chi_{coaxial} - \chi_{coplanar}$ Equation 3.4a

For HEM-900 Hz; $\chi^{900}sub = \chi_{coaxial} - \chi_{coplanar}$ Equation 3.4b

As results, some linear anomalies shown in the apparent conductivity maps were enhanced in the intensity χ ratio maps. Large variations in anomaly inductances were found in the χ^{900} ratio map (Figure 3.18a,b) and can be explained by the complexity of structures at depths greater than that explored by the HEM-4500 Hz configuration (i.e. 24 m). The closing of fracture is an example of that complexity, which has influence on the amount of conductive material that can be any one of or a mixture of conductive soil moisture, clay, metal/sulfide concentration, or pore water.

The χ ratio difference for HEM-4500 Hz data does not vary significantly; in fact it is almost null (Figure 3.19). This suggests that gradients at depths of less than 24 m behave as simple structures whose anomaly intensity are homogeneous along their lengths, otherwise the shallow bedrock is very homogeneous in terms of conductivity. Both assumptions are corroborated by the ground resistivity investigations carried out by Oliveira et al, (2002), and Pineo (2005). They interpreted the presence of a conductive regolith 8 m in depth, which occasionally reaches 20 m in depth, as detected by CPRM drillings (Souza Filho *et al.*, 2004).

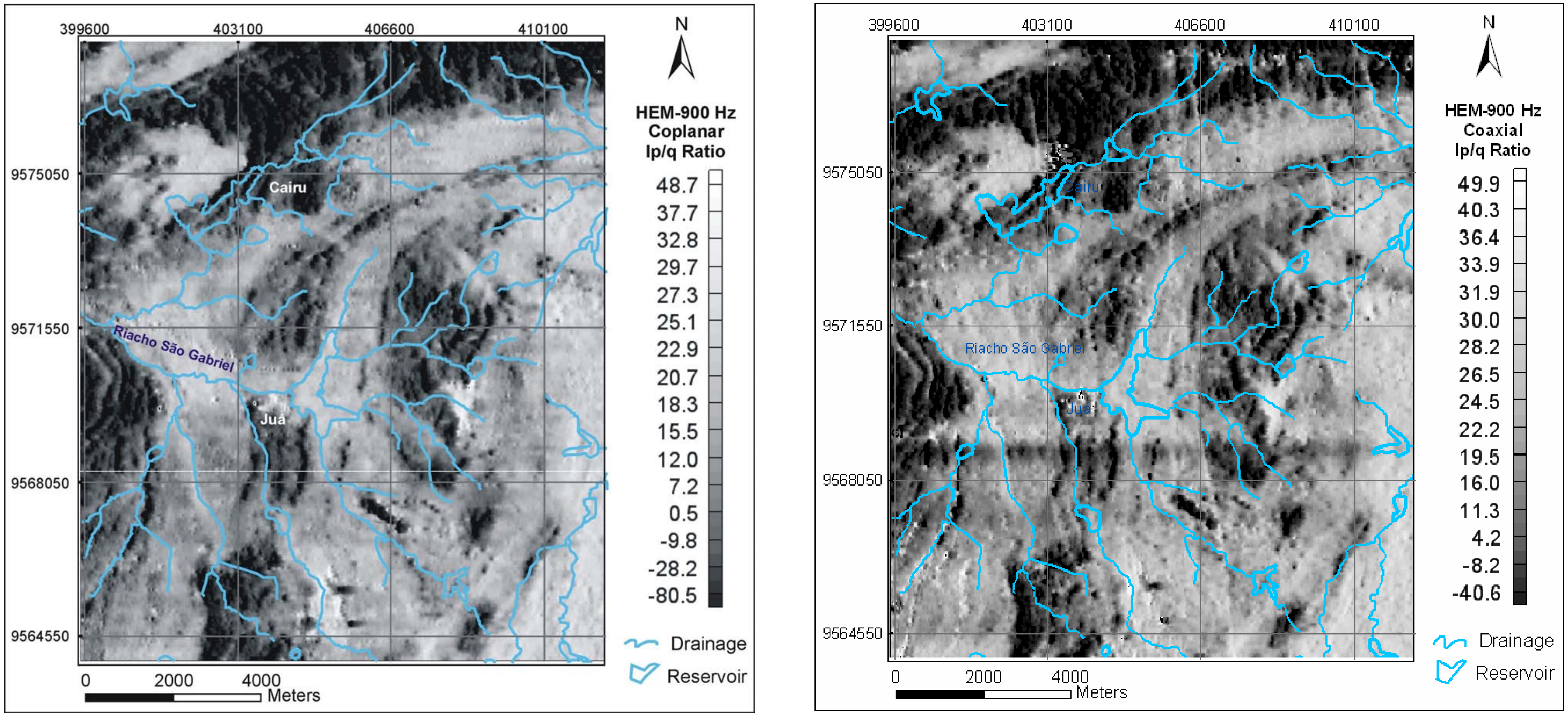

a)

b)

Figure 3.16 - Map of the χ ratio (I/Q), calculated for the HEM-900 Hz frequency data: a) I/Q ratio for the coplanar configuration; b) I/Q ratio for the coaxial configuration. Note that N-S- oriented conductive gradients that have high χ ratio are few comparatively to the same calculation for the HEM-4500 Hz frequency data (Figure 3.17). A strip of low χ ratio, oriented parallel to flight line in the center of the area, is caused by spurious values within the data.

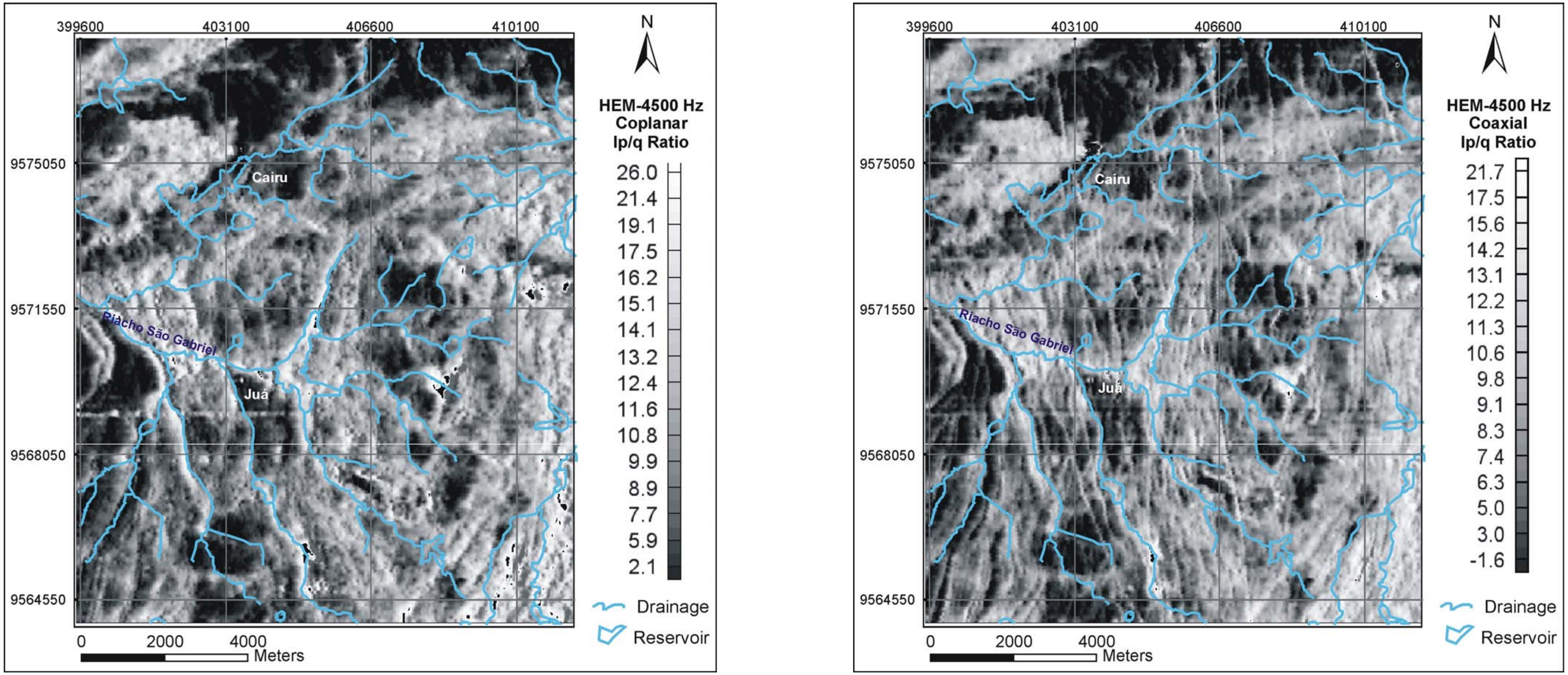

a) b)

Figure 3.17 - Map of the χ ratio, calculated for the HEM-4500 Hz data: a) Ip/q ratio for the coplanar configuration; b) Ip/q ratio for coaxial configuration. Gradients related to cross-cutting structures are better defined than in χ ratio map for 900 Hz data.

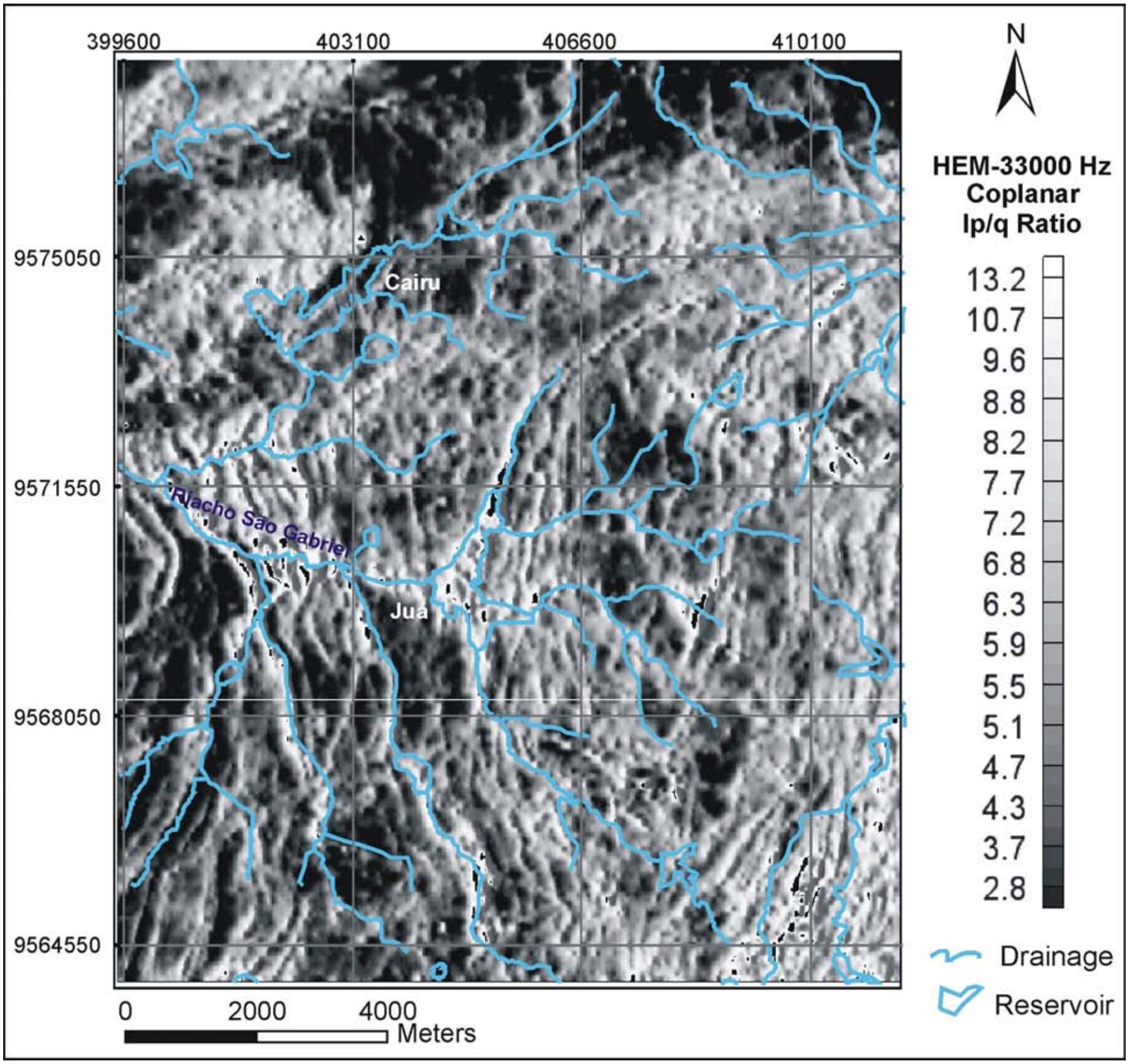

Figure 3.18- Map of the χ ratio, calculated for the HEM-33000 Hz coplanar data.

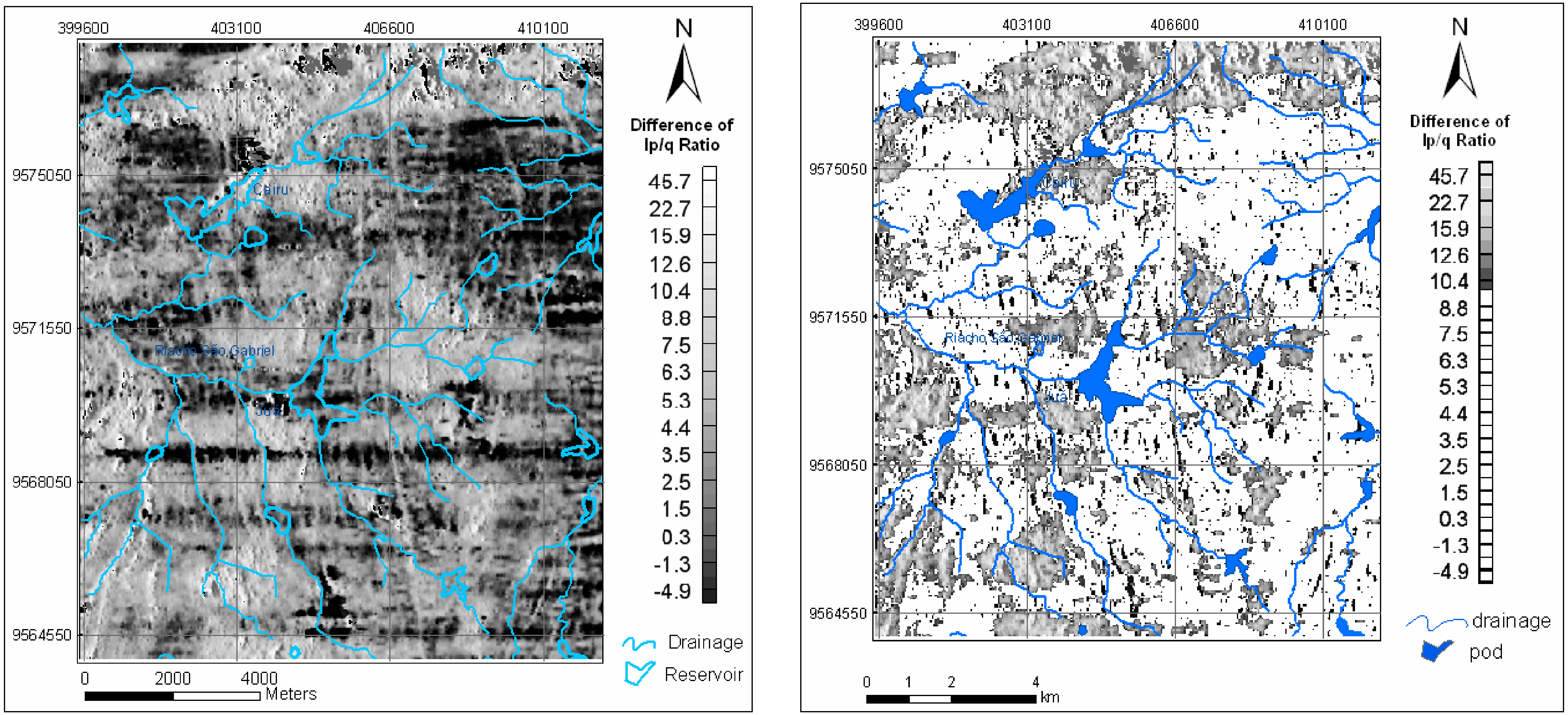

a)

b)

Figure 3.19 – Variability map of χ ratio for the HEM-900 Hz data, calculated by the subtraction of coaxial and coplanar χ ratios: a) Total variability χ ratio for the HRM-900 Hz data; b) Enhancement of the variability higher than 10. The anomalous regions in the northern part of the area correlate with granites and migmatites units.

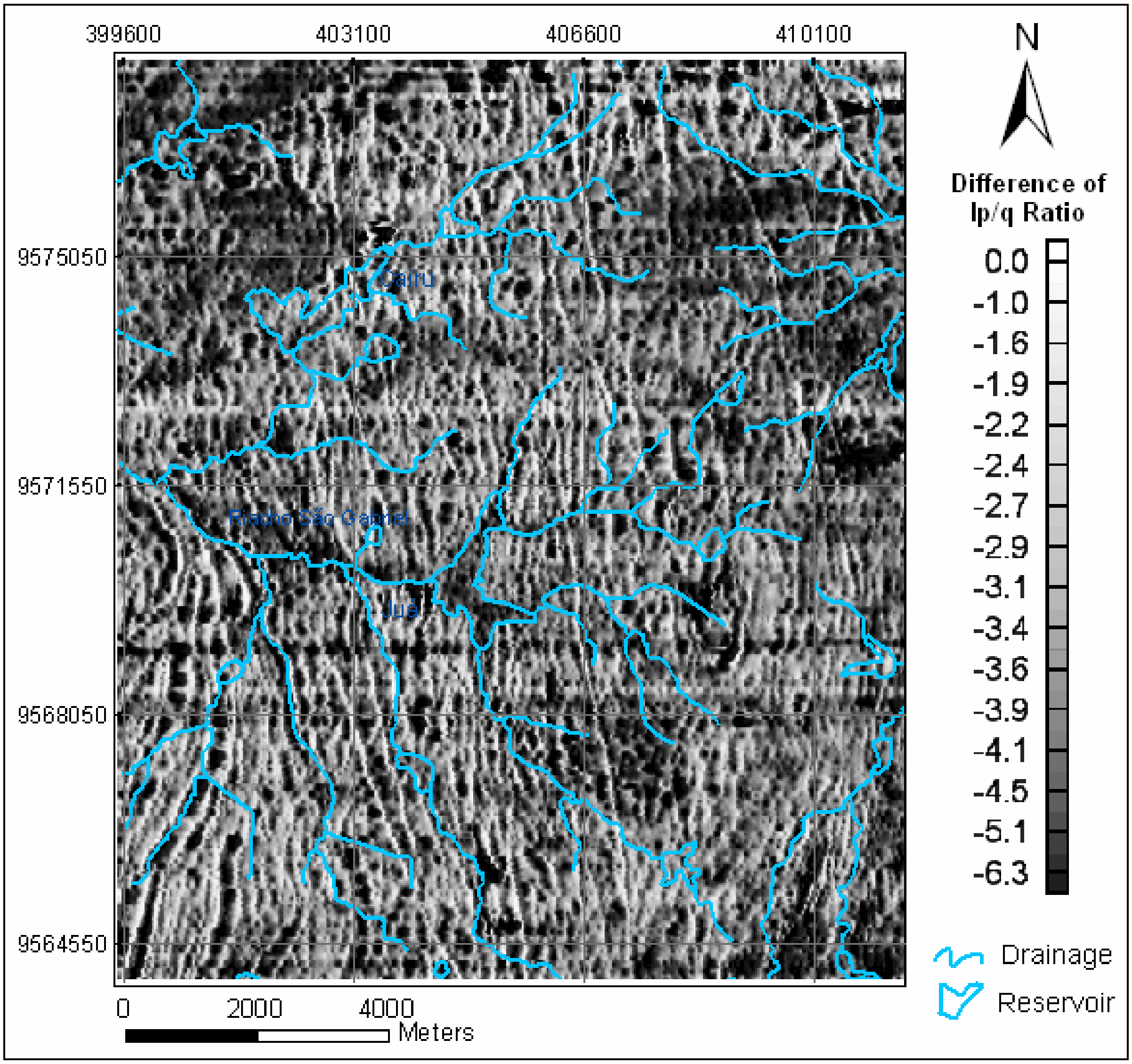

Figure 3.20 – Variability map of χ ratio for the HEM-4500 Hz data, calculated by the subtraction of coaxial and coplanar χ ratios. The small difference of χ ratios means that the conductive properties are more homogenous at the exploration depth for these data (less than 24 m, according to anomaly depths of calculated by forward modeling and also interpreted from Lasa, 2001), than to the exploration depth related to the 900 Hz frequency data.

3.6 – Inversions and Modeling of Juá Electromagnetic Data

Inversion models are usually generated to characterize anomaly properties and associate them with lithology, structures and depth of occurrence. Lasa (2001) provided apparent conductivity maps from the three measurement frequencies (Figures 3.14a,b,c). These maps were calculated according the Fraser (1978) model of a single resistive layer over the conductive half-layer. Although they look similar, the map from the 4,500-Hz coaxial vertical coil was the most remarkable because of the major NNW-SSE electromagnetic anomalies that cut cross the entire area. The 900 Hz data shows that the Pcgn unit appears more conductive than unit Pbgn meanwhile marbles/Pcc are always non-conductive (Figure 3.21).

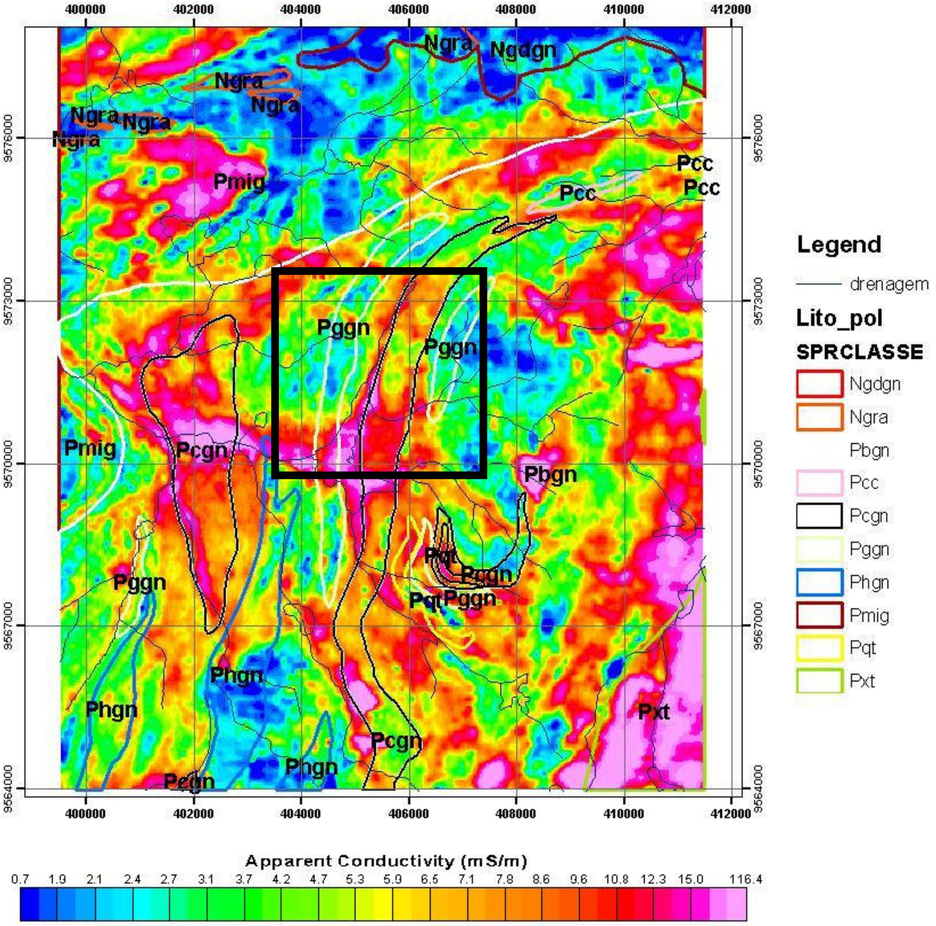

Figure 3.21 - Apparent conductivity map from Coplanar 900 Hz data (mS/m) and the geology for Juá area. Black square is the subset area where inverse modeling was calculated.

The apparent conductivity data were also inverted for depth assuming horizontal layer models, and using a subset located in the central area, containing biotite-gneiss, and the main creek valley comprised within the important WNW-ESE gradient. The purpose was to estimate depth of geoelectric properties and associate them with lithology and structures. Two inversion methods were used: a variable layer thickness least-squares (Marquardt, 1963) and Occam inversion (Constable *et al.*, 1987), both methods are available in EMIGMA v. 7.8 software (Petros Eikon Inc). For least-squares inversion, the real and quadrature components of the three coplanar frequencies (33,000, 4,500 and 900 Hz) were used. For Occam inversion the quadrature signals were used because the results from this signal appeared less noisy when grided. These results provided general information about the bulk electromagnetic properties for the central area.

The least-squares model consisted of a single layer over the half-space basement. The algorithm inverted for the resistivities of the top and bottom layer and the layer thickness (Figures 3.22 a,b,c). The resistivity of the top layer is between 4 and 130 ohm-m (250 and 7.6 mS/m apparent conductivity) and the layer is between 7 and 38 m thick. The layer is the most conductive in the river valley (E-W and, N-S trends in the center), where it is also the thinnest – about 7 m thick. The basement resistivity is very high – between 960 and 1100 ohm-m (1.04 and, 0.9 mS/m apparent conductivity). In the basement, at the center of the map there are NNE-SSW linear resistivity lows (still very high, above 900 ohm-m) that are not clearly correlated with the top layer resistivity. The left gradient is shallower: note the linear trend in the thickness map over this lower resistivity region.

Occam inversion creates the smoothest model that fits the data to a reference model. The thicknesses of the reference layers are fixed and chosen at the start of inversion. Layer thicknesses were of 2, 3, 4, 5, 5, 5, 5, 5, 5 and, 5 m, putting the top of the half-space at a depth of 44 m. The uppermost 2 m in Occam inversion is noisy and susceptible to the data errors. The 5-9 m depth slice is conductive (12-107 ohm or 83 to 9.3 mS/m), while the 34-39 m depth slice is resistive, (above 1000 ohm-m). Resuming, both Occam and least-squares inversions show similar features – thin, top-conductive layer, and a very resistive bottom-layer, and this conductive layer usually extends down to 10 m.

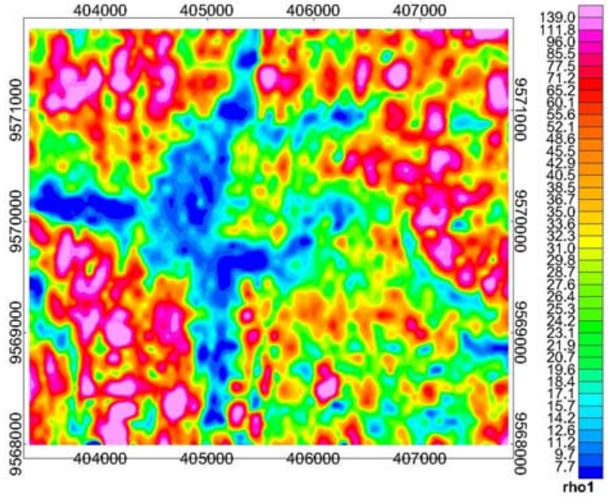

a) Top-layer resistivity (ohm-m)

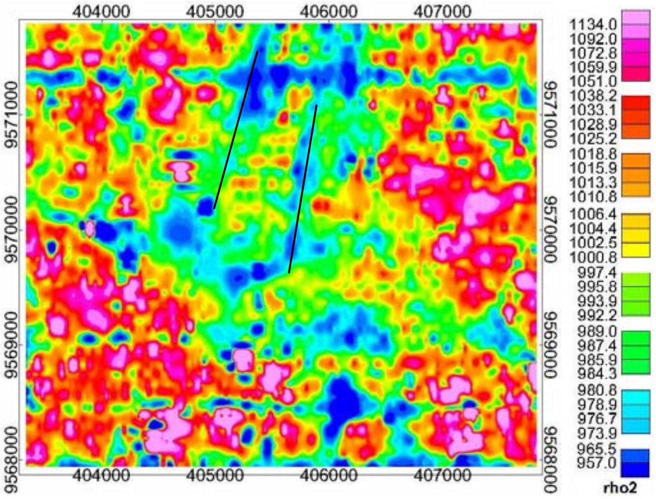

b) Bottom-layer resistivity (ohm-m)

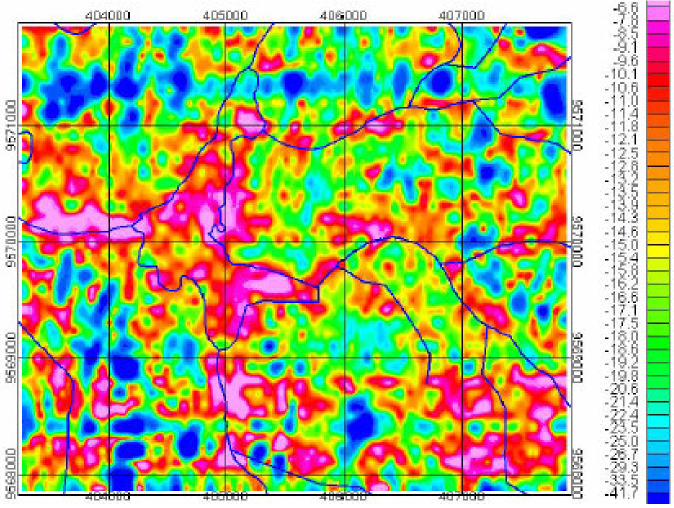

c) Top-layer thickness (m)

Figures 3.22 - Least-squares inversion model for the Juá central-area. One layer over the half-space basement using in-phase and quadrature data from the three coplanar frequencies. Black lines in (b) are NNE-SSW trends with less resistivity, and with correspondence in the top-layer. Drainage in blue lines.

3.7 - Geophysical Properties Associated to Juá Rocks

To quantify how characteristic (or not) the geophysical data are of mapped lithologies, the predictive methodology of Lee *et al.* (2001, known as Probability Ratio-PR) was applied to the grids of magnetic data filtered to 60 m-depth, to the terrace of the magnetic layer filtered to 270 m-depth and to the conductivity data of all acquisition frequencies. The approach describes the statistical likelihood of a class of a particular evidential layer having a spatial association with a given prototype area. For this study, the evidential layers are the geophysical data described above and the prototype areas are lithologies. The technique is exemplified in Equation 3.5, and more details are given in Chapter 5.

$$PR = \frac{(\text{Pixels}_{\text{gneiss} \cap \text{mag } 30}\ \text{I}\ \text{Pixels}_{\text{mag } 30})}{(\text{Pixels}_{\text{gneiss}}\ /\ \text{Pixels}_{\text{Study area}})}\quad, \qquad \text{Equation 3.5}$$

which is interpreted as: given the prior odds of a gneiss to occur in the study area (denominator), what would be the odds that this gneiss to be found if related to an geophysical evidence (numerator).

Results of the Probability Ratio (PR) technique applied to the terrace of electromagnetic data, at 4500 Hz frequency, showed that biotite-granites/Ngra, hornblende-gneisses/Phbgn, migmatites /Pmig and, marbles/Pcc are most likely to be non-conductive (0.3 – 2.1 mS/m) and are least likely to be associated with conductivities higher than 101 mS/m. The area comprised by schistose gneisses/Pxt and, quartzites/Pqt have strong likelihood for high conductivities (32.1 – 52.6 mS/m. Biotite-gneiss/Pbgn and, granite-gneiss/Pggn does not have distinct HEM signature (Figures 3.23 and 3.24).

Related to magnetic properties, the PR method revealed that granites/Ngra are associated with high magnetic anomalies (values 90-140 nT have PR up to 17). Migmatites/Pmig have weak positive association with both high-and-low magnetic field. Marbles, as would be expected, is non-magnetic but, some areas have weak association with low residual fields of 50 to 70 nT. Biotite-gneisses have dual behavior with respect to magnetic properties, presenting weak association as both non-magnetic and high magnetic unit (Figures 3.25 and 3.26).

Granite-gneisses /Pggn have similar dual behavior as Pbgn; there is a negative association with magnetic anomalies and, with non-magnetic anomalies. Hornblende-gneisses have strong association only with the higher magnetic classes (PR = 2 to 11 for residual filed from 117 to 214 nT) and, are negatively associated as non-magnetic unit. Calc-silicate gneisses/Pcgn and schist-gneisses/Pxt have strong negative associations as non-magnetic and as magnetic units. Quartzites/Pqt have the strongest association as both non-magnetic and as a magnetic unit (Figures 3.25 and 3.26).

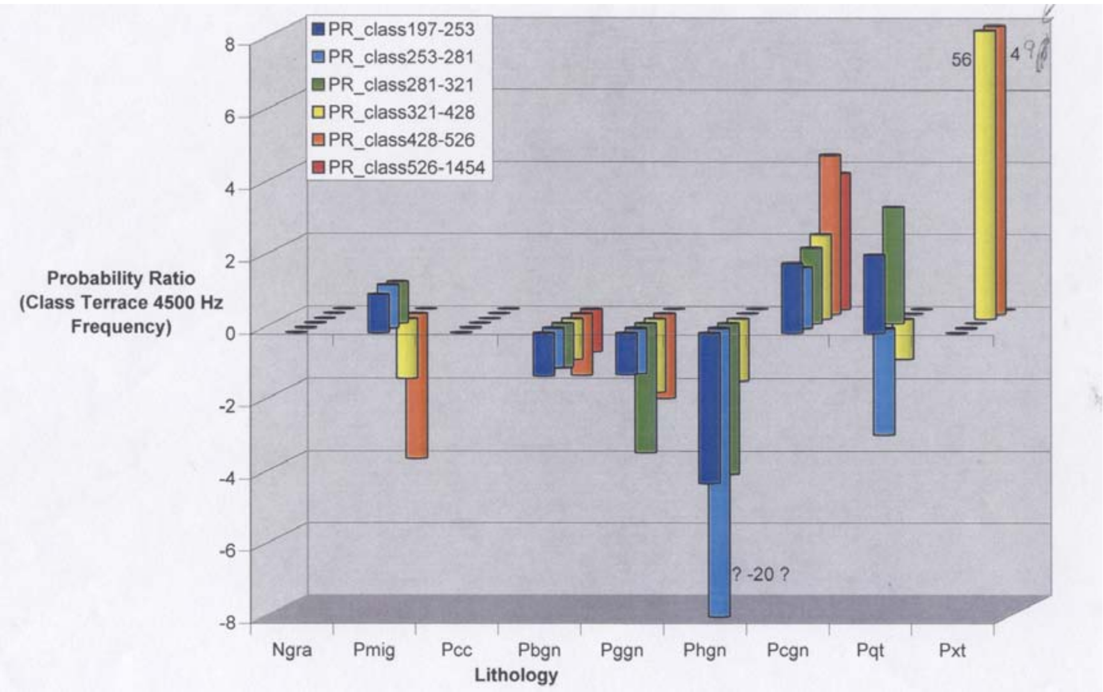

Figure 3.23 – Spatial association between lithology and the higher classes of the terrace of the HEM-4500 Hz frequency data calculated by the probability ratio technique. Terrace values are multiplied by 10. Undefined association (values < 2) of Pbgn and Pggn with conductive terrains, but positive association of Pcgm, Pxt and Pq.

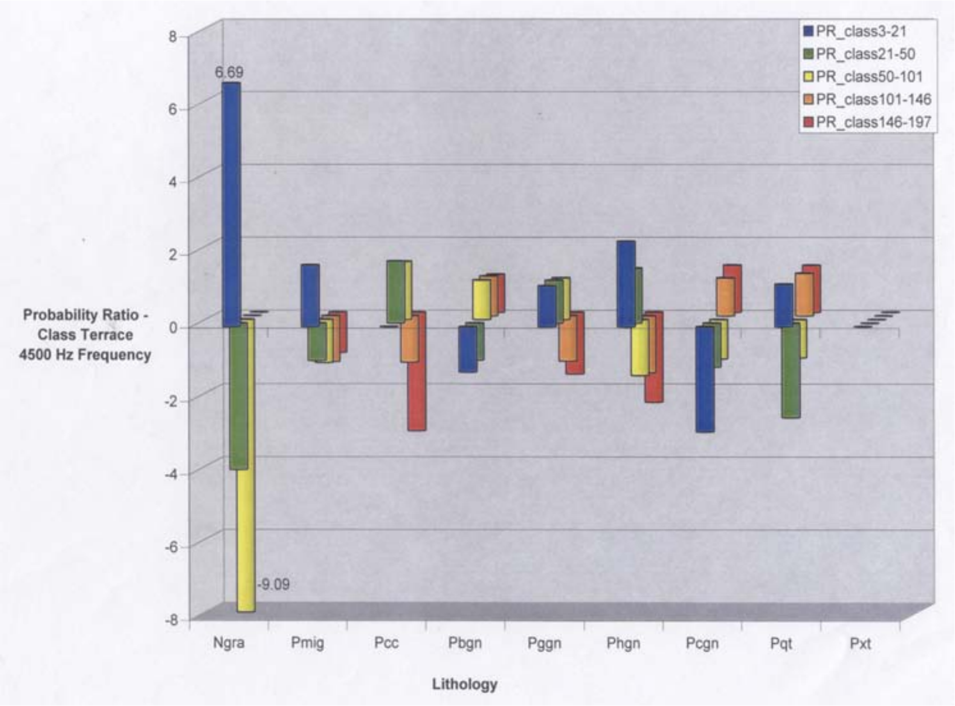

Figure 3.24 – Spatial association between lithology and the lower classes of the terrace of the HEM-4500 Hz frequency data calculated by the probability ratio technique. Terrace values are multiplied by 10. Ngra is positively associated with low conductivity, whereas Pbgn and Pggn are undefined.

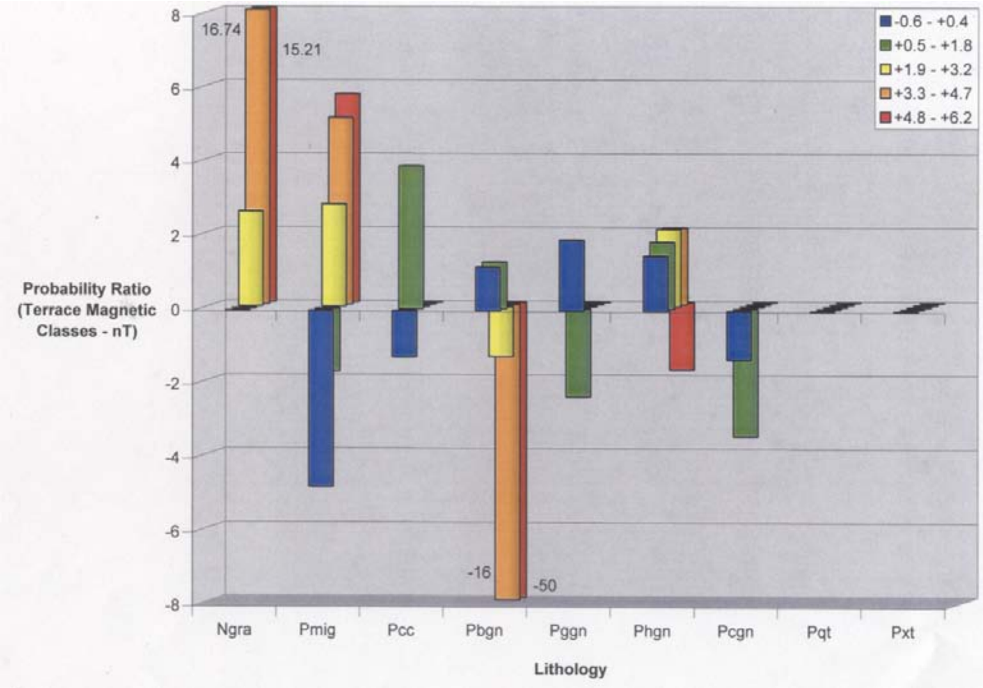

Figure 3.25 – Spatial association between lithology and the negative classes of the terrace of the magnetic data calculated by the probability ratio technique. Ngra and Pmig are positively associated with magnetic anomalies, whereas Pbgn is not.

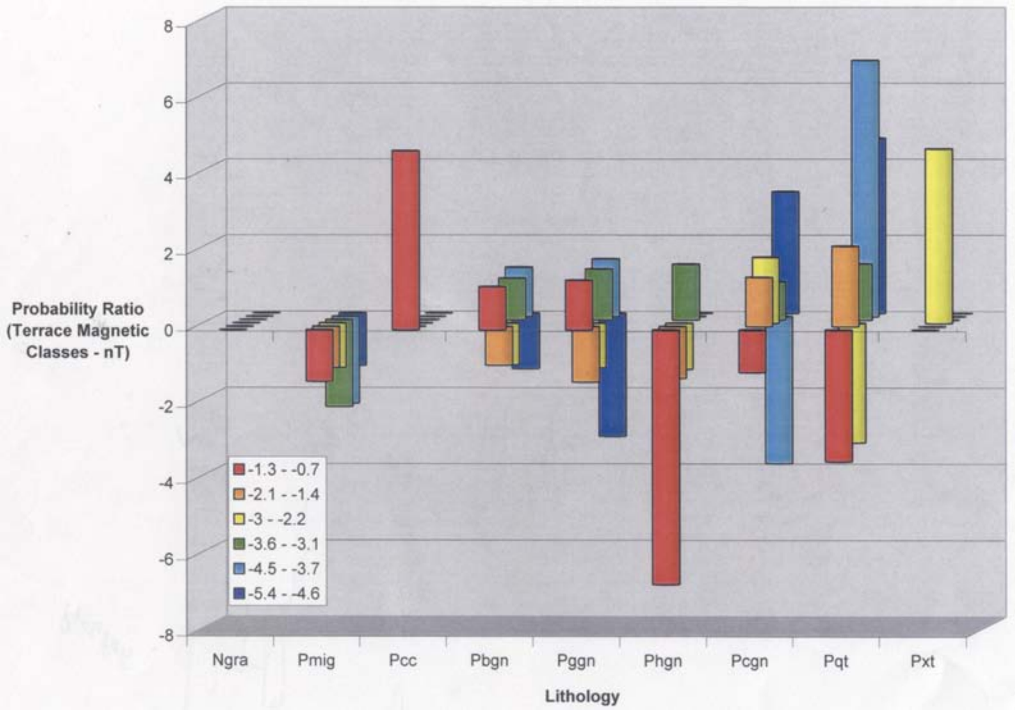

Figure 3.26 – Spatial association between lithology and the positive classes of the terrace of the magnetic data calculated by the probability ratio technique. Pqt and Pxt are associated with non-magnetic anomalies.

3.8 - Conclusions

In this chapter, the magnetic and electromagnetic properties of Pre-Cambrian rocks and structures within the Juá region (Figure 3.27) were characterized. Matched filtering allowed separation of anomalies by relative depth (deep versus shallow) magnetic sources and allowed ready mapping of surface geologic structures that likely extend into deeper crust.

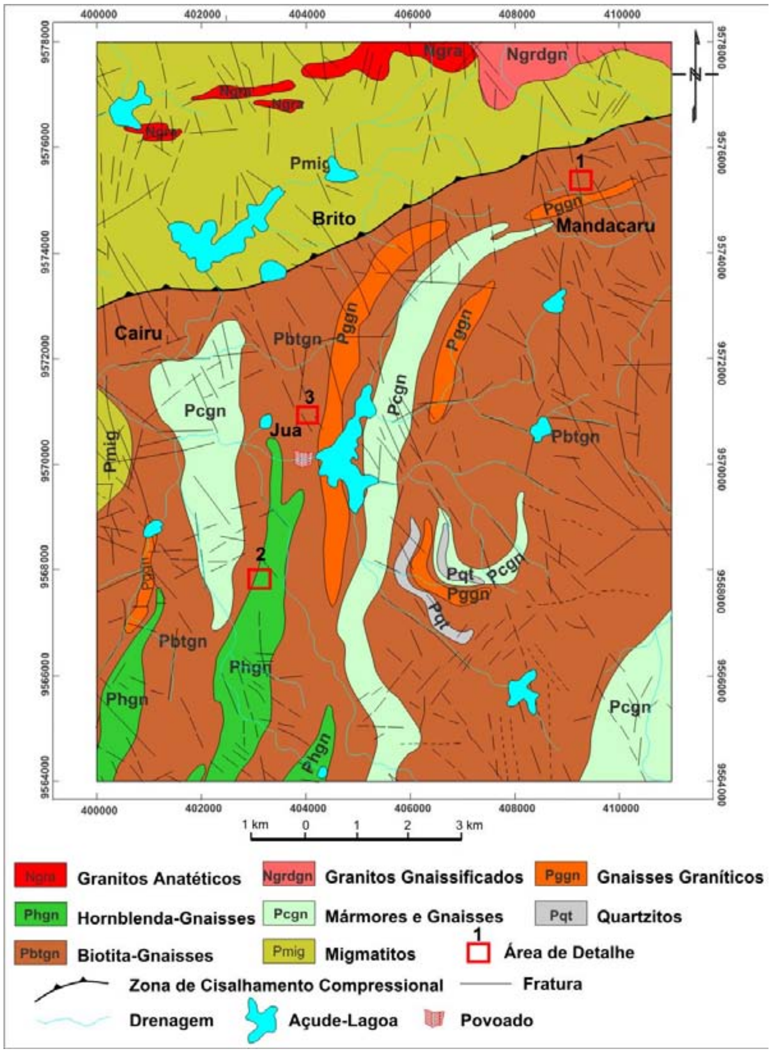

Figure 3.27 - Geologic map of Juá study-area, modified from Souza Filho *et al*. (2002). Black lines are structural lineaments. Note that lineament orientations do not match magnetic gradients of shallow source in Figure 3.22, but lithology has good correspondence to geomagnetic units of Figure 3.28.

Magnetic units and boundaries were extracted from the combined analysis of the horizontal gradient map of the residual field (that was transformed to magnetic potential data) and, from the 60 m-filtered vertical derivative map. The gradients were extracted from the shallow magnetic sources within the upper 60 m (Figures 3.28). This data set is compatible with well depths found in the area of study and were integrated in the groundwater favorability models.

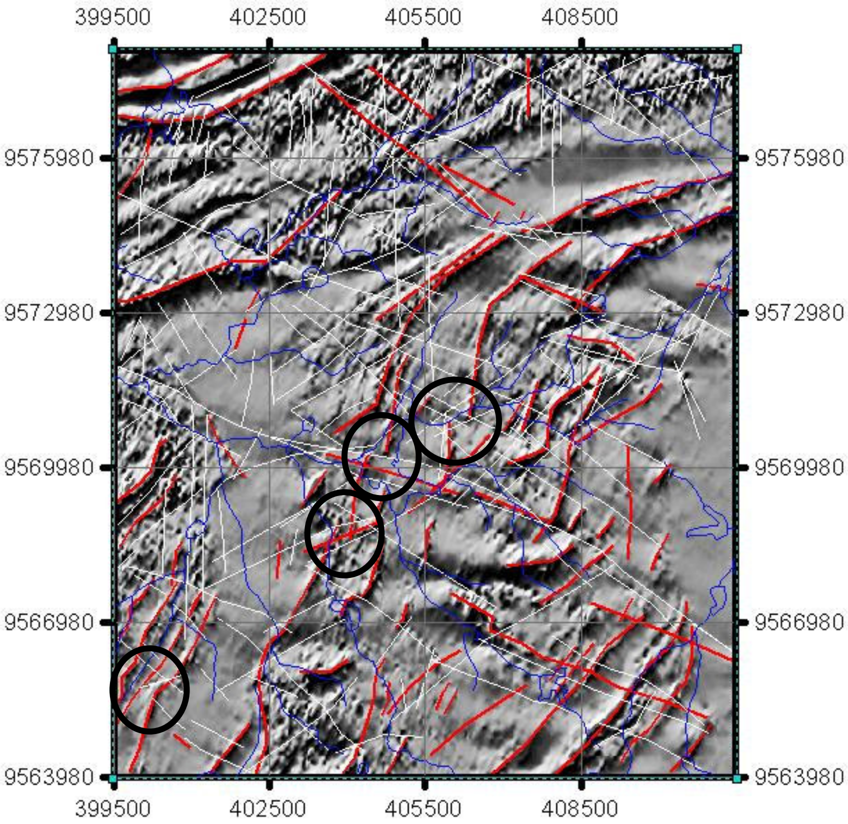

Figure 3.28 - Juá airborne filtered magnetic data to 60 m depth. Shallow magnetic gradients: non-magnetic in white and highly magnetic in red (ridges). Shaded relief illumination at 45^{o} inclination and, declined to 315 azimuth. Drainage is in blue. Gradients do not match lineament orientation in Figure 3.27. Circles mark geomagnetic units off-sets due to WNW-ESE and NE-SW gradients.

The integration of the regional and local magnetic data provided information about magnetic sources and structures that are visible as shallow sources but extend down to 2000 m depth (3.12b). As expected, this map shows the regional NE-SW and WSW-ENE magnetic gradients related to geologic sequences. It also revealed the presence of major WNW-ESE non-magnetic gradients in the center of the area (along the São Gabriel creek) that cross-cut NE-SW gradients and geomagnetic structures. The WNW-ESE gradients were identified in the maps of shallower magnetic anomalies (60-m-layer depth), and were confirmed in field as important geologic structures.

These WNW-ESE geomagnetic structures that likely extend into deeper crustal levels are coincident with co-linear conductive anomalies. We interpret the conductive anomalies to be due to weathering and higher moisture content because of groundwater occurrence. In contrast, the N-S conductive anomalies are likely not associated with deep crustally-extensive fractures as they do not appear as gradients in the magnetic products or in the EM inversions deeper than a 10 m depth.

Non-magnetic gradients were found to correlate with conjugate shear-faults oriented N60W and N60E (Figure 3.28). The later was interpreted as dextral fault, with 200 m horizontal offset. A secondary set of gradients is oriented north-south. Magnetic gradients have primary directions to NE-SW and coincide with magnetic boundaries and rock limits. Minor linear anomalies with same orientation do not correspond to geologically mapped features and are explained by buried sources. See the different orientations of structural and magnetic gradients displayed in Figures 3.27 and 3.28.

Magnetic units were closely related to the geologic map. The distinct magnetic properties (represented in map by texture and gray-shading) revealed non-mapped mineralogic/lithologic differences in the western Pcgn, Pmig and, at the shear zone that limits Pmig and Pbgn (Figure 3.29).

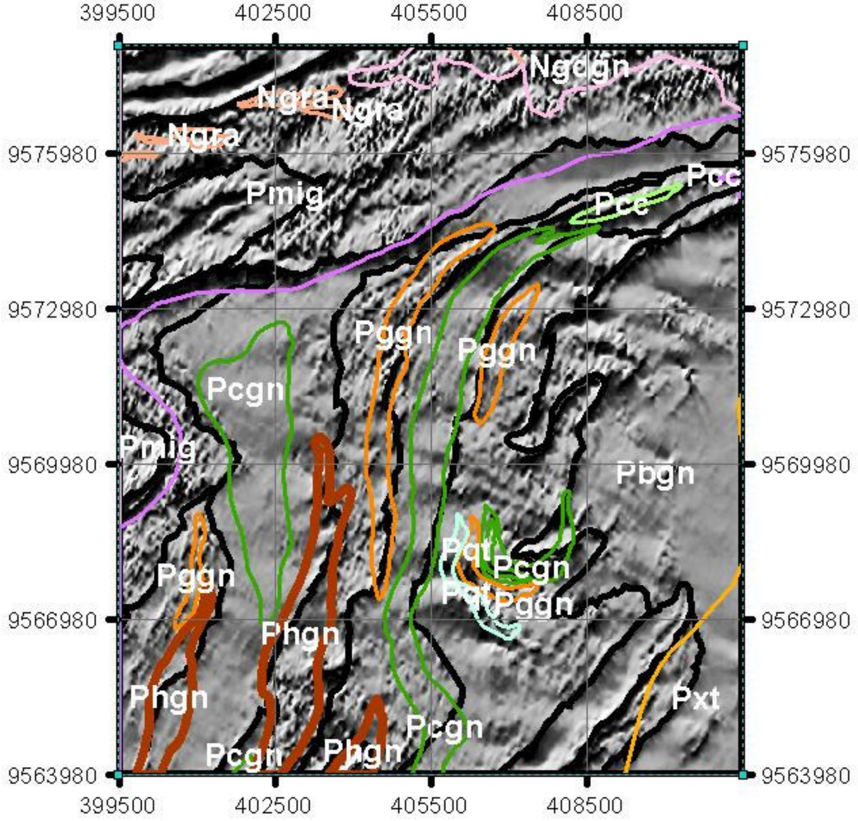

Figure 3.29 - Comparison between Juá geologic map and the vertical derivative of 60 m-filtered magnetic anomalies. Note the good correspondence between them. Black contours are geomagnetic units extracted from horizontal gradient amplitude.

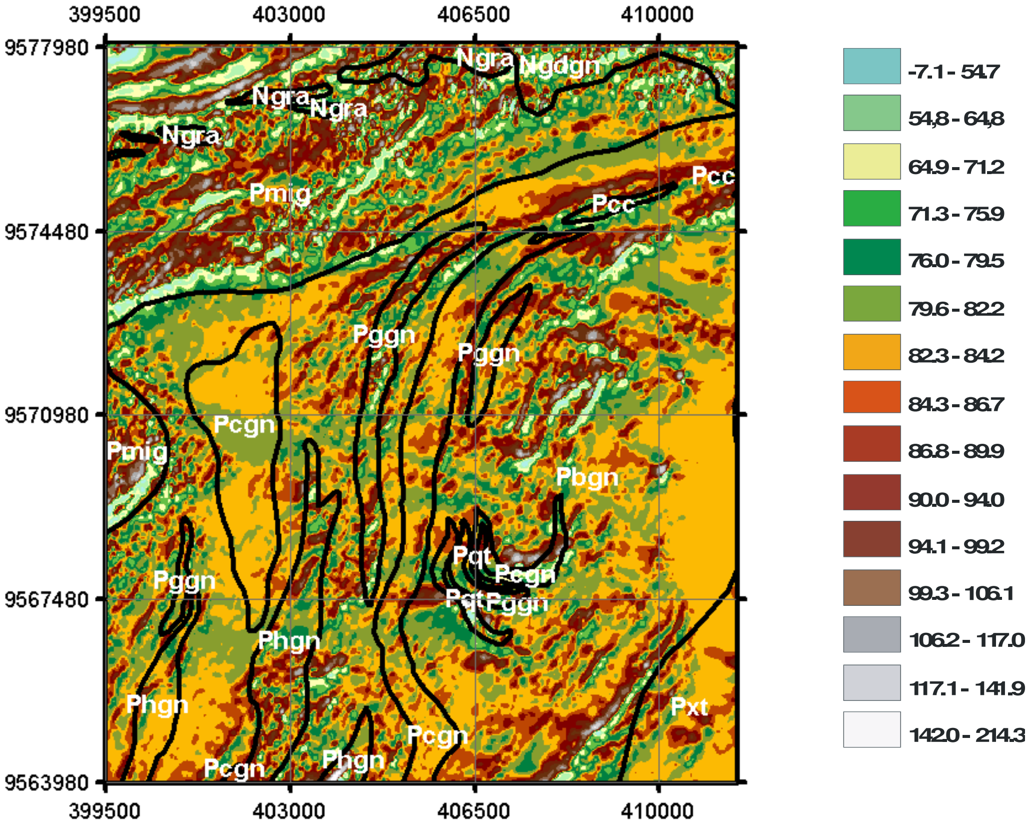

Figure 3.30 - Reclassified filtered 60 m-depth magnetic data (nT) overlaid by the geologic map of Juá. Note the correspondence of migmatite (Pmig) with alternate high- and low- magnetic anomaly classes, and the calc-silicate gneiss with moderate magnetic classes.

The magnetic-terrace map enhanced the NE-SW shear zone between the highly and less magnetic migmatites within the migmatite-Pmig (Figures 3.27 and 3.12a). Good correlation exists between boundaries and areas influenced by the shear zones to the north. Other lithologies are very well enhanced in the 60 m –filtered magnetic maps, presented as its vertical derivative or reclassified by natural breaks/jenks, as seen in Figures 3.13, 3.29 and 3.30, respectively.

Marbles are most often characterized as non-magnetic and are electrically resistive. Biotite-granites and migmatites, considered to be part of the Santa Quitéria Magmatic Arc, are non-conductive and strongly magnetic. The high magnetic properties of both corroborate Souza Filho (1998) field data that the granite is of anatetic origin and, the migmatites might one of the parental rocks. By the HGA and vertical derivative magnetic products, the granite limits might be more important than the few areas mapped. The granite-gneisses within the paraderivated sequences have distinct properties from granites within the magmatic arc, being non-magnetic with a smoother magnetic texture (little magnetic contrast).

The spatial correlation between rocks and the magnetic and electromagnetic properties has showed distinct characteristics useful for re-evaluation of the geologic map. Non-mapped but generalized colluvium covers and, regolith development may explain the inconsistent conductivity properties of quartzites and schist-gneisses (thought to be resistive, see about apparent conductivity in Annex 1). This electromagnetic characteristic may indicate where more weathering-susceptible lithologies occur. These rocks are also non-magnetic. From the inversions and field observations we understand that the clay content (layers with 0.2 m thick) is the main responsible for the extreme conductive values measured over in major creeks and reservoirs. Although there are opened fractures in surrounding outcrops, they do not seem to be conductive below 10 m.

Dual behavior related to magnetic properties of most gneissic units (Pbgn, Pcgn, Pxt) and migmatites/Pmig can be explained by either: a) these units comprise rock associations with wide variation in mineralogical assemblages and thus variation in geophysical properties; b) migmatization has locally modified the magnetic properties as occurred with granite-gneisses; c) necessity to revise mapped units and, boundaries. Dual behavior of hornblende-gneisses with high-and-low magnetic properties may discriminate para-and-ortho derivation of the rocks since, Souza Filho (1998) has identified (but not mapped) both types of amphibolites in thin-sections and, field data.

The HEM data are strongly influenced by electrical properties of the alluvium and colluvium, moisture content, and mineralogy. Bedrock is too resistive in the central area to be resolved by the 33,000 Hz frequency used for the HEM survey, which means that all information are related to the first meters of subsurface.

Based on ground surveys using electromagnetic induction (EM-34) and electrical resistivity (dipole-dipole) methods across some of N-S conductive anomalies, Pinéo (2005) attributed most of them to noises due to data interpolation along helicopter survey control-lines (oriented in the same direction). Our studies disagree with Pinéo (2005). According to our inversions these anomalies are real although not pervasive below 10 m from the surface. These features are coeval with: lineaments seen in aerial photographs in the northern part of the area; segments of creeks in the southern part; and with N-S joints, some quartz-filled. All of these features were identified by Pinéo (2005) proving their existence.

4 - Use of Helicopter Electromagnetic Data as an External Variable to Predict Groundwater Electrical Conductivity in Crystalline Bedrock, Northeastern Brazil

(O Capítulo foi reformulado para a forma de artigo e submetido à revista Hydrogeology Journal em 23 de julho de 2008, sendo que os resultados preliminares foram apresentados no 2006 Hydrogeophysics Symposium, Vancouver, organizado pela Society of Exploration Geophysicists, Tulsa., abstracts, 2006, Souza Filho *et al.* , 2006b)

4.1 - Introduction

In this study, the HEM data are used as an external variable to help characterize the variability of groundwater electrical conductivity associated with crystalline aquifers, and therefore water quality. The study area of Juá has about 2000 inhabitants and familiar farming and ranching are the principal economic activities in the study area and suitable water is a major issue in local development and settlement.

The availability of airborne data, specially the electromagnetics, provides a unique source of information that may be used to guide government actions with respect to regional groundwater management. The HEM survey has been found to be useful in groundwater exploration in other countries such as Australia (e.g. Coppa *et al.* 1998) and China (e.g. Meng *et al.* 2006).

Although the HEM data do not directly measure the presence or absence of water, modeling of these data can be used to produce maps and depths sections from which geologic water bearing structures and or salinity distribution may be identified (e.g. Sattel and Kgotlhand 2003; Pine and Minty 2005; Smith *et al.* 1997; Coppa *et al.* 1998; Meng *et al.* 2006).

4.2 – Data Sets

The data sets used in this study comprise a helicopter geophysical survey, hydrogeological information from water wells (Figure 4.1a) and outcrops. The adopted coordinate system is the Universal Transverse Mercator-UTM, zone 24, South American Datum of 1969.

4.2.1 - Helicopter Electromagnetic Data

The Juá helicopter electromagnetic (HEM) data set is considered to be a high-resolution geophysical survey because sampling rate is 0.1 s, or the equivalent to one measurement per 4 m on the ground. In this study the 4500 Hz frequency data in the coaxial mode was chosen as the secondary variable because it was found useful in identifying both conductive gradients that electromagnetic anomalies potentially map geologic structures and hydrogeologic units.

Electrical conductivity was calculated as the reciprocal of the 4500 Hz frequency resistivity data by Lasa (2001) according to a model (Fraser, 1978) of a resistive layer over a resistive half-space. After the derived conductivity data were corrected for noise and helicopter leveling, they were interpolated and onto a regular grid with a 25 m cell size (Figure 4.1 b). Further information about the HEM data acquisition system and processing can be found in sections 1.4 and 3.3.2.

Electrical conductivity characterizes the ability of an electric current to be transmitted through a substance. In water, the transmission of a current is due to the molecular interaction of dissolved salts that allow the movement. In general, the acidic igneous rocks and their derived soils found in northeastern Brazil have large amounts of quartz and feldspar that resist the flow of electric current, except in the presence of clay minerals, moisture, or water within rock discontinuities. Basic rocks and related soils or metasedimentary rocks are considered to be better conductors because they may have large amount of metals, sulfides, clay minerals or graphite within matrix or discontinuities. See Telford *et al.* (1976) and Palacky (1991) for comparative values of conductivity for different rocks and minerals.

4.2.2 - Water Well Data

Aqueous electrical conductivity measured in groundwater (EC) is the primary variable in this study. The EC was measured at fifteen of the twenty drilled wells in the Juá area (Table 4.1) during the dry period of November 2000. In November 2005, the EC also was measured in these same wells plus five newly drilled wells and three dug wells (Table 4.2). Their locations are indicated in Figure 4.1a. November is the middle of the dry period, where evaporation and salt concentration is higher in soil and water, which means that the modelings will represent the worst scenario of groundwater salinity and maximum of variability.

Both water EC measurements (µS/cm) and HEM data (mS/m) are provided in units of electric conductance per distance, relating to their ability to conduct electric current. So, to better work with this information, the water EC was transformed to the same unit system as the HEM data.

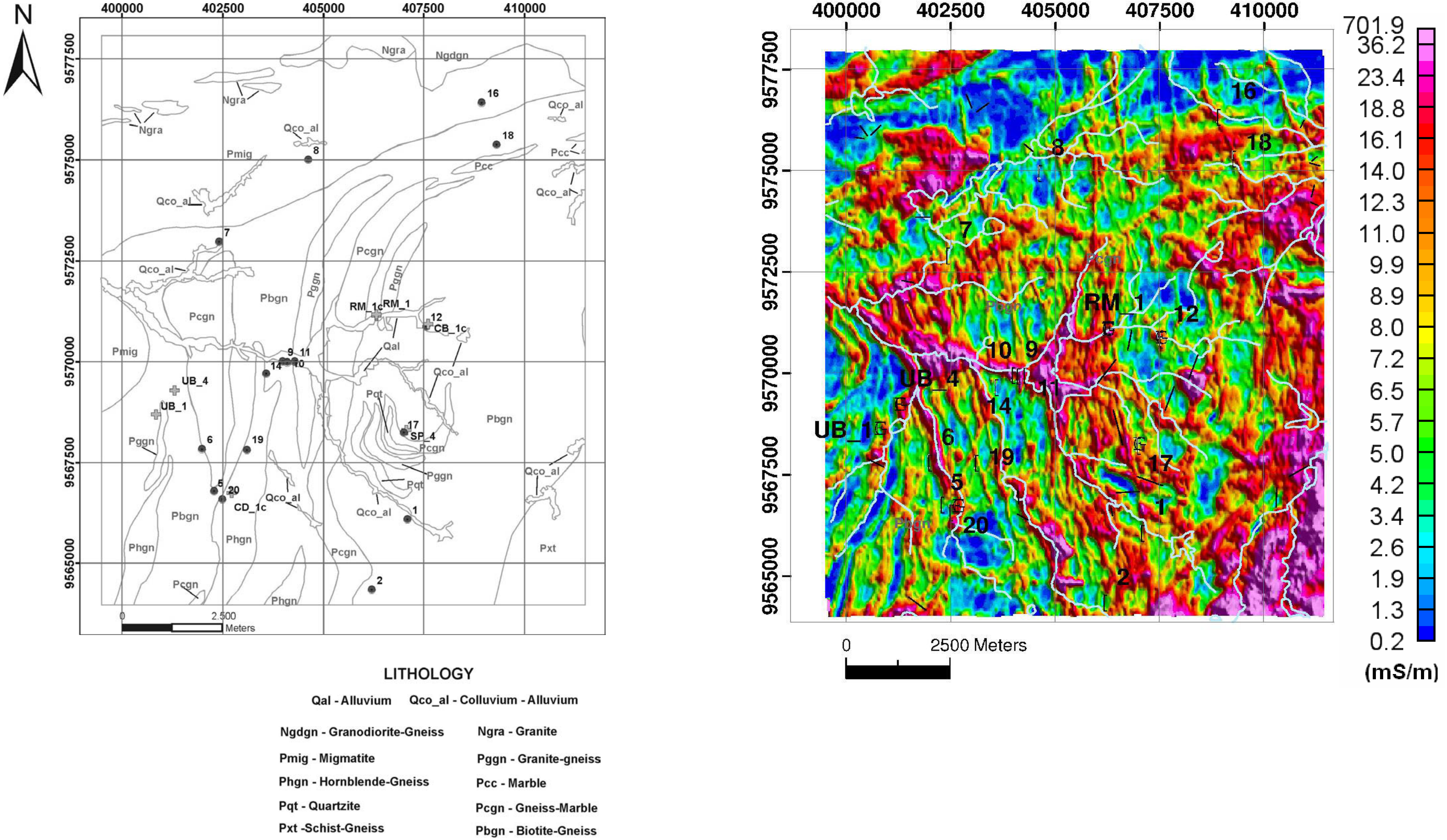

a)

b)

Figure 4.1 – The Juá area: a) Simplified geologic map, modified from Souza Filho (1998); b) Apparent electrical conductivity map calculated from HEM-4500 Hz frequency at coaxial mode (after Lasa 2001). Locations of water wells are shown in dots (drilled before year 2000) and crosses (drilled after year 2000) and identified by numbers as described in Tables 4.1 and 4.2.

Table 4.1 – Juá well data from year 2000 campaign: EC = electrical conductivity (mS/m); W. Level = water level (m); Suberm. Pump = submersible pump (Modified from Veríssimo and Feitosa 2002).

Well	Depth (m)	Yield (m^3/h)	W. level (m)	EC (mS/m)	Water Entrance depth (m)	Operating Status	Pump System	Rock
1	7	-	-	234	-	Operational	Pump	Paragneiss
2	60	-	12.40	200	-	Operational	-	Marble/Paragneiss
3	-	-	-	-	-	Abandoned	-	Marble/Paragneiss
4	-	-	-	-	-	Abandoned	-	Marble/Paragneiss
5	60	1.10	10.50	415	-	Operational	Windmill	Paragneiss
6	60	4.50	9.00	558	-	Operational	Suberm. Pump	Paragneiss
7	60	1.20	-	203	-	Abandoned	-	Paragneiss
8	72	0.70	-	-	-	Abandoned	-	Paragneiss
9	48	6.00	3.10	274	8	Not-installed	-	Paragneiss
10	54	6.00	4.05	603	11	Operational	Pump	Paragneiss
11	42	5.00	3.54	117	-	Operational	Pump	Paragneiss
12	60	0.70	3.50	1104	-	Operational	-	Paragneiss
13	56	-	2.00	768	-	Operational	Windmill	Marble/Paragneiss
14	-	-	-	-	-	Operational	Windmill	Paragneiss
15	60	-	-	-	-	Operational	-	Paragneiss
16	60	0.10	9.00	750	-	Not-installed	-	Paragneiss
17	75	0.38	5.00	150	44, 56, 60, 66	Not-installed	-	Paragneiss
18	80	0.03	-	417	-	Not-installed	-	Marble/Paragneiss
19	78	1.25	16.00	360	19, 23 to 25, 63	Not-installed	-	Paragneiss
20	72	2.00	4.50	1050	5, 27	Not-installed	-	Gneiss

Table 4.2 – Juá well data from 2005 campaign.

Well	Depth (m)	Yield (m^3/h)	W. level (m)	EC (mS/m)	Operating Status	Pump System	Rock
RM_1/drilled	60	1.5	4.70	184.0	Deactivated	Pump	Paragneiss
UB_1/ drilled	-	0.3	12.31	858.0	Non Operational	Not installed	Paragneiss
UB_4 /drilled	-	< 0.3	5.73	810.0	Not-installed	Not installed	Marble/Gneiss
J_1 /drilled	63	< 0.3	6.43	290.0	Abandoned	Windmill	Paragneiss
SL_4 / drilled	-	< 0.3	13.15	321.0	Abandoned	Not installed	Paragneiss
SP_4 /drilled	-	< 0.5	-	151.2	Operational	Windmill	Paragneiss
CD_1c / dug	-	-	7.70	261.0	Operational	Manual	Gneiss/Migmatite
CB_1c / dug	-	-	-	231.0	Operational	Manual	Paragneiss
RM_1c / dug	-	-	3.7	140.4	Operational	Manual	Paragneiss
SP_2 /drilled	7	< 0.5	4.00	219.0	Operational	Manual	Gneiss/Amphibolite

4.3 - Geostatistical Analysis

The electrical conductivity measured in 15 drilled wells was spatially interpolated using both kriging and stochastic methods to generate groundwater electrical conductivity maps. These interpolation procedures were done using the ISATIS software (Bleines et al 2000).To better reproduce the variability of groundwater electrical properties within the crystalline bedrock, the more densely spaced HEM data were incorporated to augment the relatively sparse well data. The interpolations followed two geostatistic concepts: 1) values of a variable may be determined using a secondary, external and, independent variable and 2) the variability of a primary variable is not similar in every direction (the non-stationary concept). This study examines both of these concepts with respect to groundwater EC behavior.

Additional field work in November 2005 provided measurements of EC at all 15 of the existing wells and some new ones. These EC data were later used to test the validity of the previously interpolated EC.

Electrical Conductivity-EC Analysis in Drilled Wells

Groundwater electrical conductivities (EC) measured in 2000 are displayed in Figure 4.2. The spatial distribution of sampled wells has a NE-SW trend with clusters located near the mid-west portion. Inspection of these data reveals a high anomalous EC value (EC > 1000 mS/m) at the center part (an outlier of this variable). Silva *et al.* (2001 e 2003) and Veríssimo and Feitosa (2002) discuss the high seasonal variability of water electrical conductivity observed in wells and reservoirs since 1999. One finding is that these EC values can increase by a factor of two in the dry season.

The EC values measured in 2000 (Figure 4.2) have an approximately log-normal distribution, in which 40% of the samples are associated with the first class (100 < EC < 250). There is a gap in the histogram between the two highest value classes, separating the anomalous values (those greater than 1000 mS/m) from the rest of the sample population. Other studies also found the lognormal distribution suitable for characterizing EC data for the Irauçuba area (Veríssimo and Feitosa 2002; Souza Filho *et al.* 2004) and other crystalline bedrock regions in Northeast Brazil (Manoel Filho 1996).

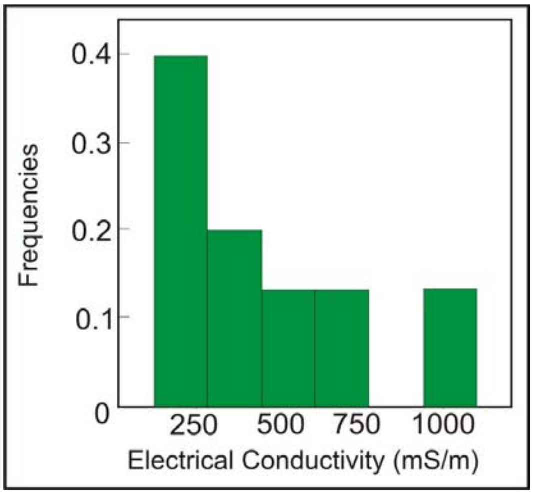

Figure 4.2 – Classes of electrical conductivity (mS/m) for Juá water well data: Min. = 117 mS/m; max. = 1104 mS/m; mean = 480.2 mS/m; standard deviation = 306

The salinity of groundwater is a measure of the amount of total dissolved solids (TDS in mg/l) and, it has a highly positive correlation with EC. For this reason, the EC can be used to estimate the groundwater salinity and thereby, water potability by a conversion factor that is typically between 0.55 and 0.75 (Santos 2000). For the Juá groundwater EC data, this conversion factor was determined to be 0.62 (Figure 4.3).

In Brazil, the potability standards (Ministério da Saúde, 2005) state that the maximum acceptable TDS limit for human consumption is 1000 mg/l. which after applying the conversion factor corresponds to an EC value of about 160 mS/m. Inspection of the results reveals that only two locations in the Juá area have an EC value that is below 160 mS/m. Wells in which water EC is greater than 5000 mg/l are unsuitable even for agricultural activities or animals when (Souza Filho *et al.*, 2003).

<u>Preparing EC Water Data for Interpolation – The Primary Variable</u>

Before the interpolation, it is important to know if the prediction variable has directional dependence (anisotropy). This can be assessed through variogram modeling. In variogram modeling, the semivariogram is computed as a measure of the squared difference between values as a function of distance. This analysis consists of two steps: i) an experimental semivariogram is computed from measured data (this includes multiple directions to identify anisotropy), and ii) an analytical model is fit to the discrete experimental variogram values. The reader is referred to Clark (1979) for a review of variogram modeling.

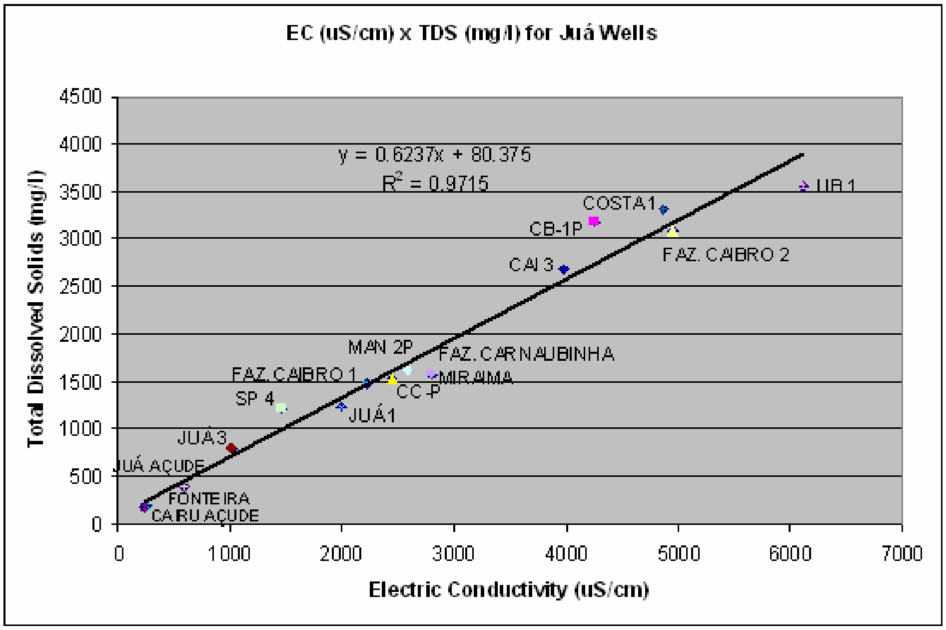

Figure 4.3 - Relation between groundwater salinity-TDS and electrical conductivity for Juá water data.

The ISATIS software was used to model the EC experimental semivariogram (Figure 4.5a). Initially, the calculated isotropic semivariogram resulted from the following parameters: pass range = 1200 m; pass number = 7. The pass indicated the degree to which the EC data are self-related and the presence of anisotropy. At the Juá site, the presence of EC could be described using the following combination of principal models: i) spherical model, with a nugget = 0, range = 3,500 m, and sill = 8500); ii) nugget model = 25000; iii) spherical model, with range = 10000 m, sill = 9000). The resulted isotropic model is shown in Figure 4.5b.

Helicopter Electromagnetic Data-HEM as the Secondary, Drift Variable

The HEM data were found to exhibit a log-normal distribution (Figure 4.6). The distribution is asymmetric with 60 % of the values within the first quartile (from 0 – 13 mS/m), a behavior that is characteristically similar to the histogram of groundwater EC (Figure 4.2). Comparisons of the values of groundwater EC and conductivity derived from helicopter data-HEM at the same locations (15 samples) might not be enough to determine a relationship between them. The impossibility of a correlation (Table 4.3 and Figure 4.4) serves to invalidate the use of methods like Collocated Co-Kriging (Wackernagel 1995).

Table 4.3 – Comparisons between water electrical conductivity (EC) measured in wells and calculated from HEM-4500 Hz data. Both measurements are in mS/m.

Well	EC_2000 Data	EC_2005 Data	HEM Data
1	234.0	219,0	9.0
2	200	143.2	4.0
3	-	-	-
4	-	-	-
5	415.0	261.0	7.0
6	558.2	526.0	8.0
7	203.0	422.0	4.0
8	-	-	-
9	274.4	200.0	21.0
10	603	-	26.0
11	117.0	101.0	16.0
12	1104.1	634.0	12.0
13	-	-	-
14	-	290.0	1.0

Table 4.3 – Comparisons between water electrical conductivity (EC) measured in wells and calculated from HEM-4500 Hz data. Both measurements are in mS/m (continuation).

15	-	-	-
16	750.0	-	15.0
17	150.0	204.0	6.0
Well	EC_2000 Data	EC_2005 Data	HEM Data
18	416.5	252.0	15.0
19	360.0	38.1	10.0
20	1050	-	5.0
RM_1/drilled	-	184.0	15.0
UB_1/ drilled	-	858.0	10.0
UB_4 /drilled	-	810.0	12.0
J_1 /drilled	-	290.0	1.0
SL_4 / drilled	-	321.0	-
SP_4 /drilled	-	151.2	6.0
CD_1c / dug	-	261.0	13.0
CB_1c / dug	-	231.0	12.0
RM_1c / dug	-	140.0	16.0
SP_2 /drilled	234.0	219.0	9.0

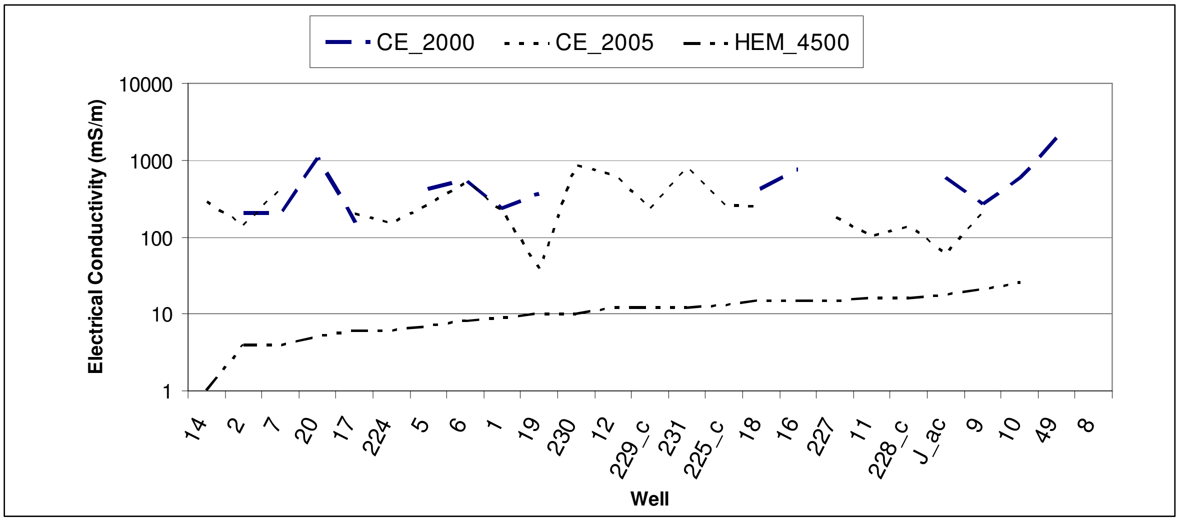

Figure 4.4 – Comparison of electrical conductivity measured in well data and calculated from HEM-4500 Hz data. Data are ordered according increasing values of HEM data. No direct relationship is apparent present between HEM data and electrical conductivity in wells.

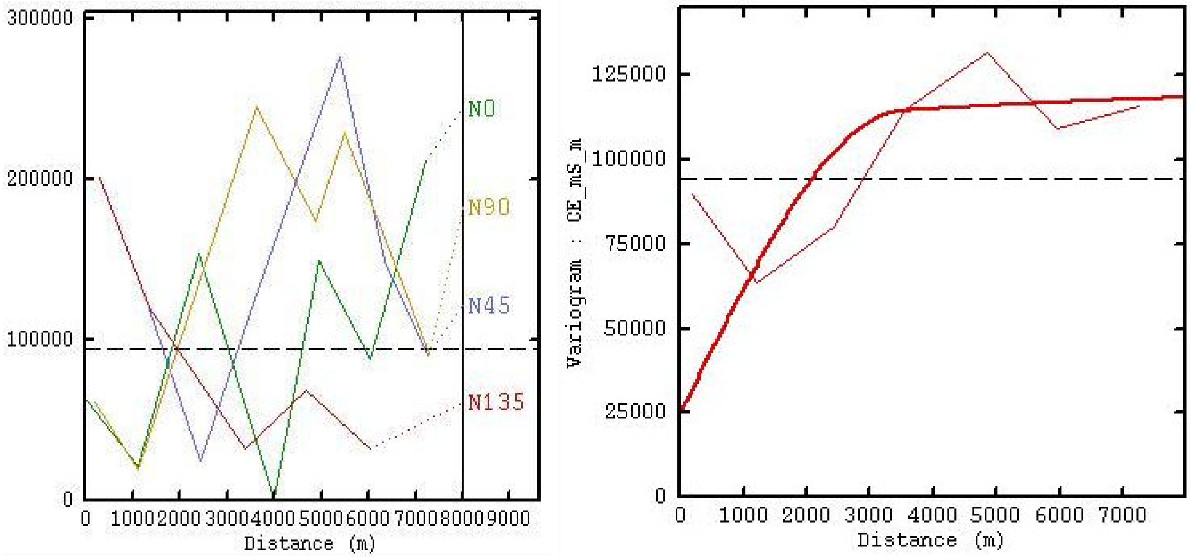

a) b)

Figure 4.5 – Spatial variability of electrical conductivity of Juá well data: a) experimental semivariograms calculated at different directions; b) modeled semivariogram resulted from combination of: i) spherical model, with a nugget = 0, range = 3,500 m, and sill = 8500); ii) nugget model = 25000; iii) spherical model, with range = 10000 m, sill = 9000).

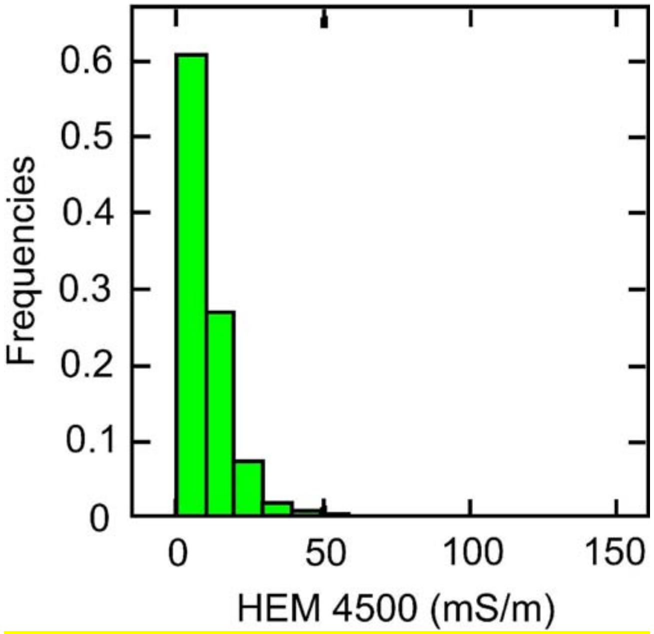

Figure 4.6 – Histogram for HEM data at 4500 Hz frequency: minimum = 0.2 mS/m; maximum = 145.4 mS/m; mean = 10.36 mS/m; standard deviation = 9.89 mS/m.

4.3.1 - Kriging Model with External Drift

When two variables reflect the same phenomena that are physically related in nature, but the spatial distributions of variable measurements differ, the distributions of one variable can be used to predictively enhance the distribution of the other variable (Wackernagel 1995; Oliveira 1997). This variable, known as an external drift variable, can be derived based on the spatial statistical parameters of the other variable and serves as a surrogate data set to estimate values for the variable of primary interest in areas where principal variable data are sparse or absent.

Kriging with External Drift (KED) is an extension of the Universal Kriging method. This Kriging method integrates one or more external drift functions measured in the same spatial domain as the primary variable. Drift functions must be known in all positions of the grid, inclusive from where primary variable data are located.

The variability of a primary variable is implicitly defined at each location through the drift of the secondary variable (Deutsch and Journel, 1992 in Oliveira, 1997). The KED method has an advantage over Co-Kriging, which also uses secondary variables but it does not require knowledge of the cross correlation between the variables. However, both the variables must be related to the same natural phenomenon.

The Interpolation by Kriging with External Drift

Considering the modeled semivariogram (Figure 4.5), the processed grid area for KED was the same as the grid of the external HEM drift data (481 rows by 564 columns or 270,327 squared cells of 25 m). The map of expected groundwater conductivity for the Juá area according to the KED method is shown in Figure 4.7a. Where groundwater information is absent from wells, the KED method gives more weight to the external HEM variable as seen in the southeastern and northwestern part of the map.

The interpolation histogram (Figure 4.7b) shows a Gaussian pattern (expected for Kriging method results) in contrast to the original log-normal distribution for water EC (Figure 4.2). Also, the KED model has extrapolated expected EC values to be greater than the original EC data, as predicted values, for example, between the range of 400 and 700 mS/m were valued produced.

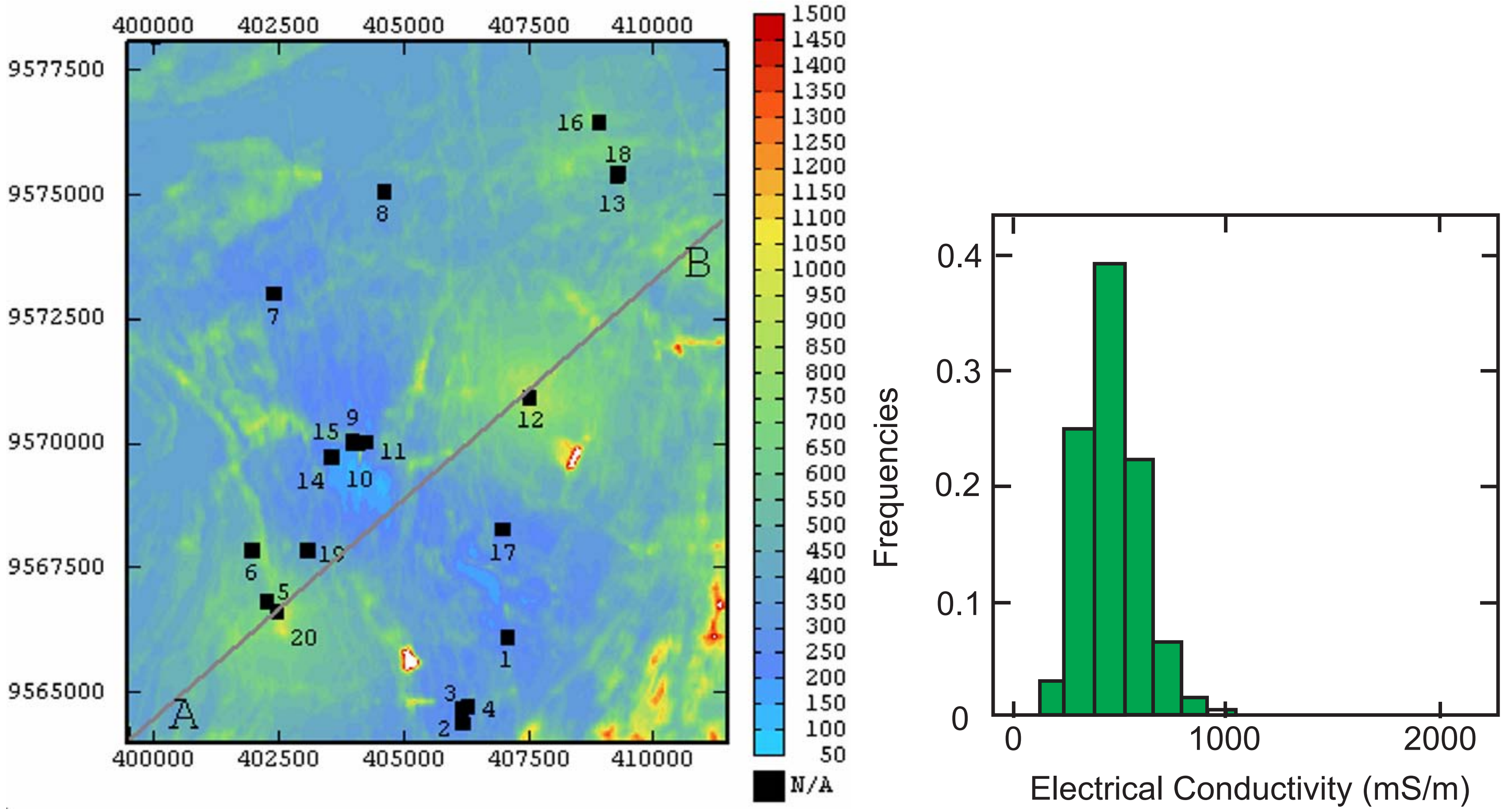

a) b)

Figure 4.7 – Groundwater EC distribution in the Juá area: a) Map resulted from the use of Kriging with HEM data as an external drift variable. Values in mS/m, black squares indicate locations of drilled wells; b) Histogram of kriged data, min. 127 mS/m, max. 2084 mS/m, mean 475 mS/m, standard deviation = 147.

4.3.2 – Stochastic Simulations

Groundwater Electrical conductivity in crystalline rocks is one kind of natural phenomena that has such a variation that prevents the use of standard interpolation techniques to estimate values in un-sampled locations. Alternatively, stochastic simulation technique can be used to quantify the effect of variability on prediction uncertainty by generating random realizations that are constrained by the statistical nature of the variables beings simulated. Because stochastic simulation is a random process the statistics and probable occurrence for a variable of extreme variability like EC can be computed.

<u>Transforming the well water EC variable</u> – <u>De-clustering and</u> <u>Anamorphosis</u>

To maintain the variability of EC for use in a stochastic simulator, groundwater data in the central-western part of the study area (Figure 4.1a) were de-clustered using the Mean-Kriging method (Deutsch 1993). The de-clustering weights determined for each of the 15 points were then applied during the simulation processes.

Because the stochastic simulation method requires the variable to have a Gaussian distribution, an anamorphosis process was applied to ensure that the variable has a mean value of about 0 and variance of about 1. The Gaussian transformation of Juá groundwater EC data yield a satisfactory variable (Figure 4.8), with: minimum = -1.58; maximum = 1.56; mean = 0.007; variance = 0.994; standard deviation = 0.997.

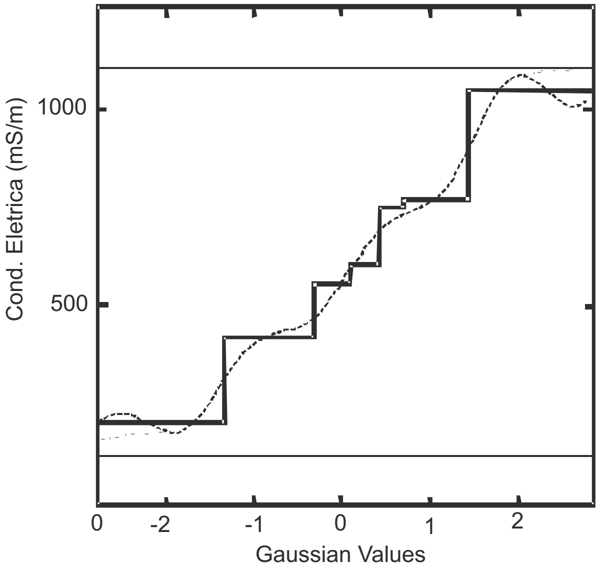

Figure 4.8– Cumulative frequency for original Juá EC water data. Anamorphosis function (dot curve) applied onto the original data (step function).

Simulation with External Drift

Simulation with an external drift comprises the following steps: i) the new gaussian variable is use to interpolates the groundwater EC data, according to the modeled variogram; ii) the external drift distribution function (HEM data) is used to predict the primary EC Gaussian variable; and iii) inversion of the results to the original distribution function.

Repetitions of the process occurred until 100 simulations were completed. The simulations of probable EC at all of the grid cells were evaluated in terms of probability scenarios, probability cut-off value maps and related accuracy.

Probability scenarios are equally probable spatial distributions of the simulated variable related to each cell of the grid. Among many frequency maps the 25% and 75% likelihoods were selected (Figures 4.9a,b) to represent the conservative measure of groundwater EC and possibly resembling the variability during dry season, when the EC greatly increases (Veríssimo an Feitosa 2002). These maps review that the southern and central parts of the study area are the most likely to have minimum groundwater EC and therefore best water quality. These EC values are just above 160 mS/m, indicating that water may be suitable for human consumption with minor actions (as mixing rain water). A 90% probability map depicts a more pessimistic scenario, where the EC values exceed up to 9 times the potability limit at more than half of the Juá area.

The variability associated with 100 simulations is characterized statistically by measures such as the standard deviation and the inter-quartile range of the predicted values for each cell (Figures 4.10a,b). Although the inter-quartile range is less than the standard deviation (because outlier values are not included) both measures indicate that simulated values for the central region have least variability of the Juá area. This suggests that possible new drilled wells would likely have EC similar to that estimated by the simulation model. In contrast, the northern and southwestern portions of the study area show more variability and interpretations in these regions are less reliable.

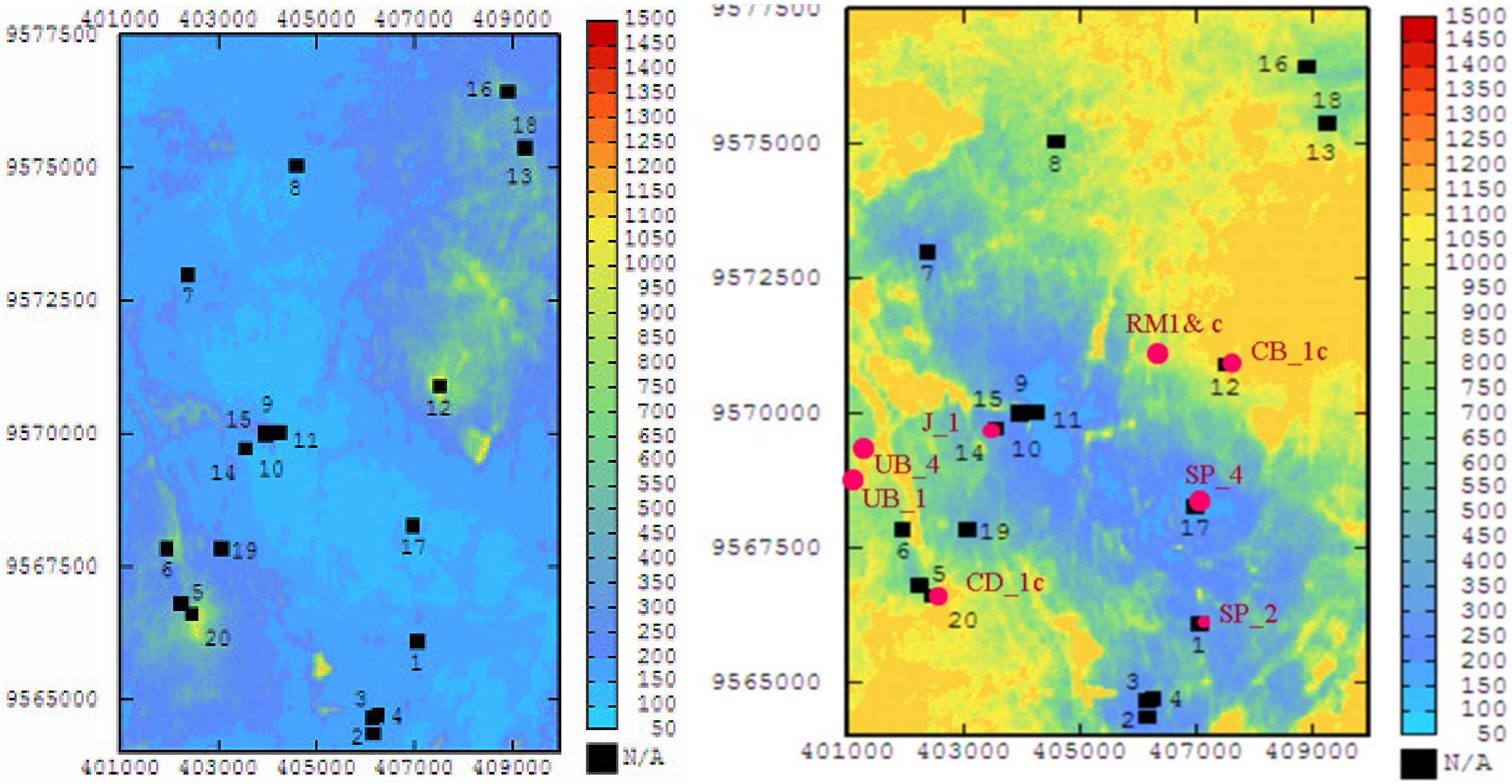

a)

b)

Figure 4.9 – Probability scenarios for groundwater electrical conductivity (mS/m) in the Juá area: a) 25% probability map; b) 75% probability map. Black squares refer to drilled wells and red dots are the new wells used for validation and the red dots are the new drilled wells used for validation. Less saline groundwater were mapped in the central-south region.

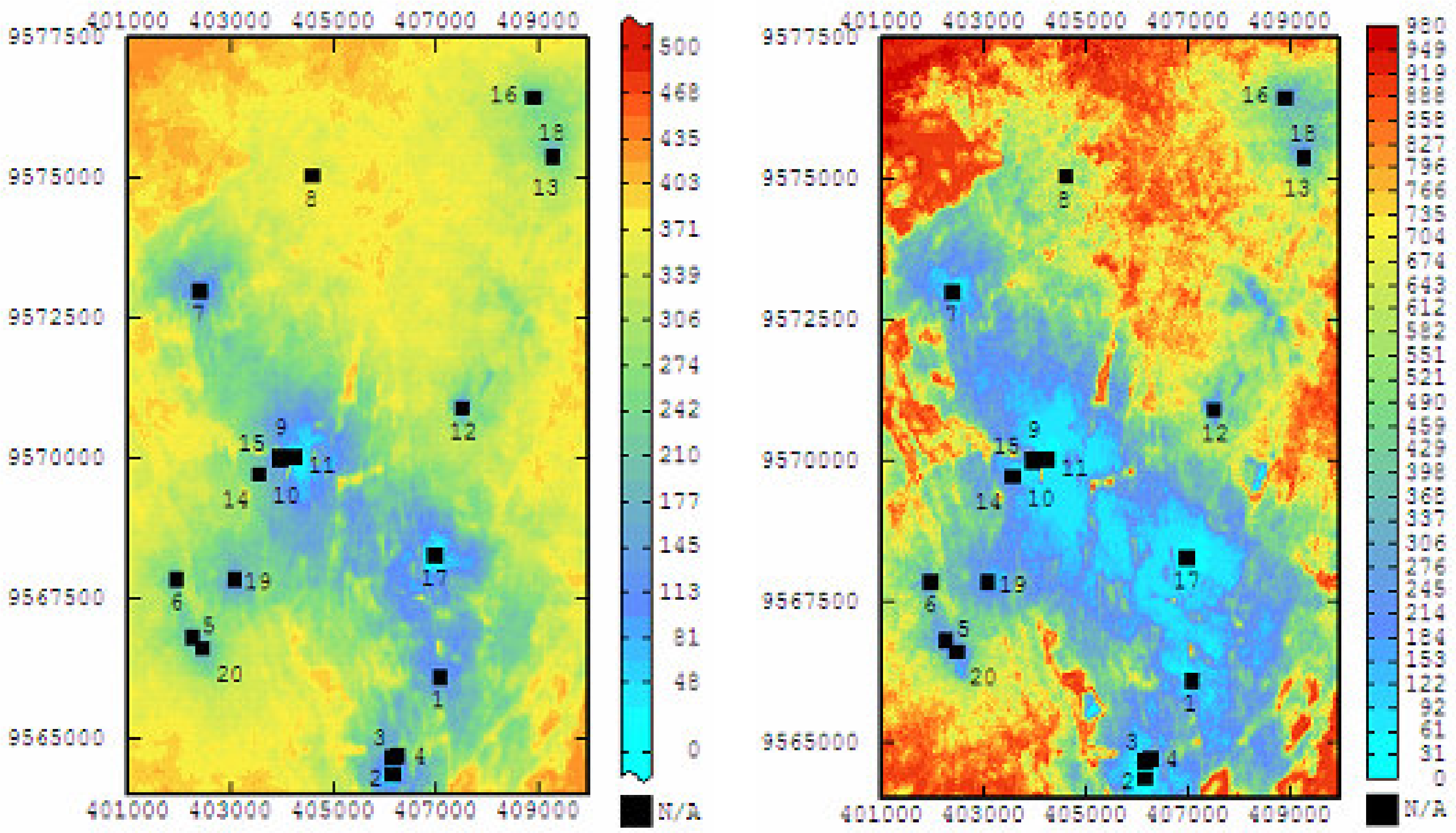

a)

b)

Figure 4.10 – Variability of groundwater EC after 100 simulations with external drift for the Juá area: a) standard deviation; b) inter-quartile range. Black squares refer to locations of conditioning drilled wells. More uncertainties where there is no well information.

4.4 – Validation of the Methods

Validation of the model results was attempted following the groundwater sampling campaign of November, 2005. Measurements from 10 new wells (4 new drilled wells, 2 non-operational wells, and 4 dug wells, Table 4.2) were compared with KED and stochastic model values of the 75% probability scenario. Simulated and interpolated values were observed in each cell that contained a well as shown in Table 4.3.

Electrical conductivity values from new drilled wells compared very favorably with those from simulations, and, with the exception of well RM_1, they were within a standard deviation of the mean of 100 simulations. Well RM_1 is located in a zone of high EC variability in which the measured value was overestimated by the simulation model (Figure 4.11a). This deviation is due to well #12, the highest conductive (Table 4.1), whose conductivity had dropped by 43% between 2000 and 2005. If the EC measured in 2005 were used for well #12, the model would have simulated a closer value for the RM_1 well position.

Values of groundwater EC in dug wells were also compared to simulated values. Because none of the measured EC values were within the range of one standard deviation from the simulated value (Figure 4.11b) this suggests that the EC models that incorporated HEM data do not characterize shallow groundwater system.

4.5 - Predicting Good Water-Quality Regions

An attempt to predict regions with good water quality in the Juá area was carried out with the construction of a cut-off map of groundwater EC. As demonstrated earlier, salinity, therefore water quality, is proportional to EC. A cut-off EC value of 200 mS/m was imposed for two reasons: i) Juá groundwater are already above the correspondent Brazillian potability limit (160 mS/m); ii) the cut-off is a more realistic lower limit to the groundwater EC in the study area since 80 % of all wells have EC above this cut-off.

Probability maps produced by the several realizations of stochastic analysis allowed us to define regions in which groundwater conductivities were consistently at or below the imposed cut-off value of 200 mS/m. The results are given in probability of a cell in the grid to have a value below the cut-off limit. As shown in Figure 4.12, the central region is the only one with high probability for this situation.

Table 4.3 – Comparison between groundwater EC measured in well data and calculated from simulation and interpolation with external drift techniques. Values are in mS/m.

Well (map code)	**EC year 2000**	**EC year 2005**	**Kriging Ext. Drift**	**Q75% Sml Ext. Drift**	**Q75% - 25% Sml Ext. Drift**	**Std Dvt Sml Ext. Drift**
CAIB_1 (5)	415.0	261.0	593.21	414.1	6.42	25.82
CAIB_2 (6)	558.2	526.0	514.9	543.29	24.57	59.34
SL_1 (2)	200.0	143.2	223.17	190.97	3.76	18.75
SP_2 (1)	234.0	219.0	269.87	244.14	4.25	28.81
SP_4	-	151.2	221.1	168.55	29.14	21.02
JC_1 (17)	150.0	204.0	213.08	154.96	1.48	9.18
ST_1 (19)	360.0	38.1	428.58	352.1	7.12	26.45
CD_1 (20)	1050.0	-	749.4	961.26	60.54	83.52
CD_1_c	-	261.0	817.8	1104.1	372.81	239.16
CAI_3 (7)	203.0	422.0	251.32	205.76	2.91	18.01
RM_1	-	184.0	715.69	1081.24	832.68	367.75
RM_1_c	-	140.4	716.25	1019.28	775.29	361.81
CB_1_p (12)	1104.1	634.0	959.94	1079.84	19.66	58.19
CB1_c	-	231.0	962.65	1104.1	45.96	83.95
UB_1	-	858.0	484.21	1053.21	834.56	369.26
UB_4	-	810.0	467.35	861.48	657.87	356.72
J_1 (14)	-	290.0	159.71	302.38	167.48	199.12
MAN_2 (13)	416.5	252.0	604.89	555.67	8.94	33.61
MAN_4 (16)	890.0	-	-	-	-	-
J_65	274.4	200.0	336.34	316.16	37.24	38.04
J-66	603.0	-	412.13	584.85	25.68	65.09
J_67	117.0	101.0	314.17	124.1	5.69	7.13

EC = electrical conductivity measured in 2000 and 2005; Q75% Sml Ext. Drift = simulated value within 75% probability out of 100 interactions; Q75% - Q25% Sml ext. Drift = Difference between 75% probability and 25% probability values after 100 interactions (the Inter-quartile difference) during the simulation with external drift; Std Dvt Sml Ext. Drift = standard deviation from all 100 interactions during simulation.

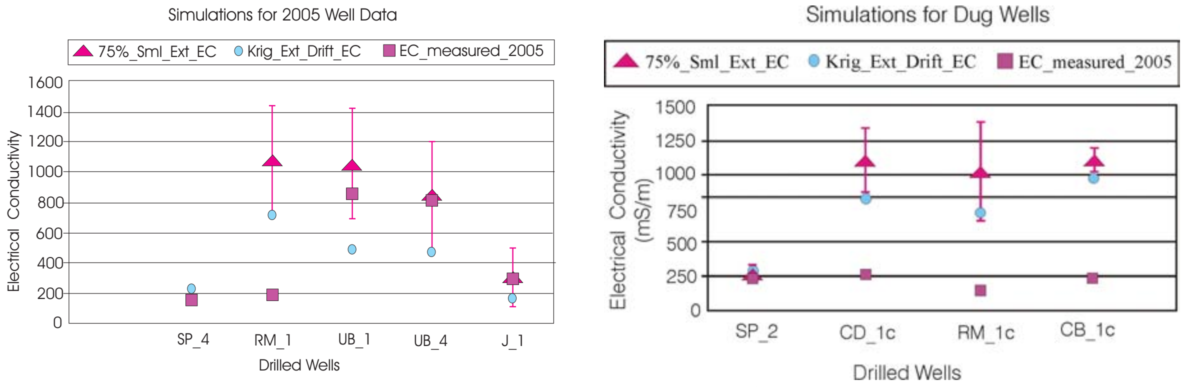

a) b)

Figure 4.11 – Comparisons among groundwater EC (mS/m) measured in the 2005 campaign and the simulations/interpolations with 2000 data: a) new drilled wells; b) new dug wells. The bars indicate standard deviation for 100 electrical conductivity simulations.

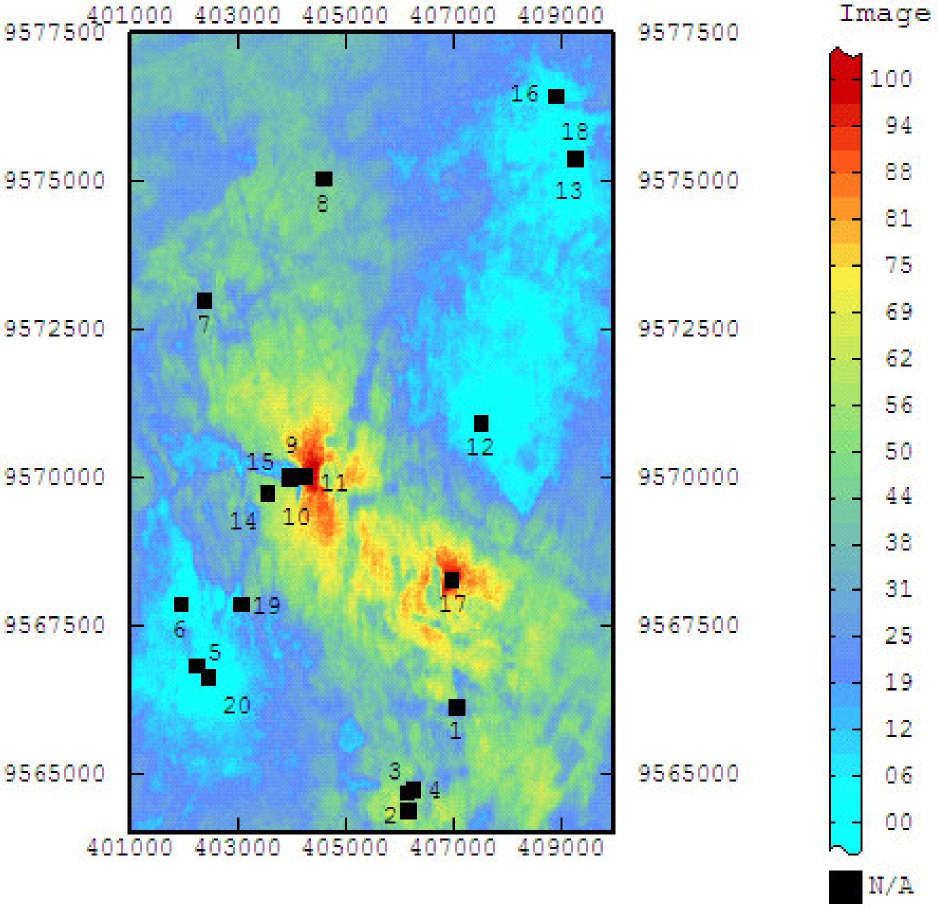

Figure 4.12 – Probability cut-off map for 200 mS/m conductivity for Juá groundwater after 100 simulations with HEM external drift. Values in percentage, black squares refer to conditioning drilled wells. The central region has the most potential for this cut-off, varying from yellow to red colors.

4.6 – Conclusions

Kriging and stochastic simulation methods with an external drift provided a means to predict groundwater EC from which probability maps were constructed. These probability maps were useful for differentiating both spatial and temporal changes in EC. Using an EC-salinity relation, this information was transformed to maps and helped locating regions of better groundwater quality for future use, even considering the high seasonal salinity variability.

The central region of the Juá area was found to be that with the best perspective for good groundwater quality (Figure 4.12). Mainly in the Kriging model, it is remarkably the influence of HEM data where well information is absent (edges of the area), and interpretation in this region shall be taken with caution. Therefore, where both well and helicopter-borne data exist, electrically conductive regions are assumed to be more realistically modeled by the stochastic technique.

The results are encouraging to assess the variability of groundwater EC in crystalline rocks, however, there are some limitations. Both the Kriging and stochastic models do not account for groundwater and salinity mixture that may exist due to distinct hydraulic systems (fractures) within the well, since the electrical conductivity could not be measured for each water-productive fracture. Due to their crystalline structure, clay minerals are not only very conductive but interfere in HEM signal propagation, owing to overestimation of electrical conductivity from underneath rock, therefore groundwater modeling shall be overestimated as well. That might be the case why measured and modeled conductivities for wells 12 and RM were so dissimilar.

The applied methods were not successful to estimate EC of dug wells and a possible explanation is because dug wells were used for validation only and the four samples were not representative of the EC variation for these wells. Also, the models were built with drilled well data, so they were more biased to hydrogeological systems deeper and different from those of surface systems that are explored by dug wells.

5 - Data-Driven Spatial Analysis for Groundwater Exploration

5 – Data-Driven Spatial Analysis for Groundwater Exploration

5.1 – Introduction

Airborne geophysical surveys provide data suitable for groundwater exploration, if one or more physical properties can be measured appropriately. Geophysical data interpretation typically involves many processing methodologies, assessment of other geologic and hydrologic information, and integration of all information into meaningful products.

This chapter presents the chosen approaches to determine how productivities of wells are related to variables of airborne geophysical data, spectral characteristics extracted from ETM^+/Landsat-7 images, and hydrogeological field measurements from the Juá region. Another goal is to examine and quantify the relationships between the airborne geophysical data and other variables related to groundwater. Because groundwater occurrence in the Juá area is controlled by fracturing and weathering (See Figure 2.6, Section 2.3), the geophysical and spectral signatures of groundwater zones may be different from the host rock. For this reason, probabilistic modeling with Probability Ratio (Lee *et al.*, 2000; Silva, 1999) and Weights-of-Evidence (WofE) (Bonham-Carter *et al.*, 1989) techniques are used to determine a relation for locating regions of groundwater favorability.

Although magnetic and electromagnetic data do not measure the presence or absence of water directly, the data have the ability to enhance and map geologic features that can be used to identify probable water-bearing structures and lithologies in crystalline rocks. As discussed in Chapter 3, there are three main points that also illustrate the usefulness of airborne geophysics to map favorable hydrogeological conditions in the Juá area:

a) Magnetic anomaly gradients refer to boundaries between geomagnetic units and define shear zones. Non magnetic anomaly gradients may be interpreted as brittle-related tectonic discontinuities;

b) Electrically conductive anomaly gradients may be water-filled discontinuities, moisture, salt-rich soil, clay-mineral or graphite content in rock. Non conductive anomaly gradients may represent quartz-filled discontinuities (a hydrological barrier) or non water-filled structures;

c) Structural lineaments interpreted from remote sensing techniques may be correlated to any of the above geophysical features and they are important for groundwater storage and flow.

Although spatial data integration methods are being used increasingly for mineral resource assessments (Bonham-Carter *et al*. 1989, Bonham-Carter 1994, Agterberg *et al*. 1990, 1990, Wrigth and Bonham-Carter, 1996, Silva 1999; Teixeira, 2003 and others), the application of statistical approaches for groundwater modeling represents a new way of a research area called hydrogeophysics. In some mineral and environmental modeling applications, the parameters are well-constrained. In hydrogeological studies there are few directly-related evidences such as electromagnetic induction, direct current resistivity, magnetic and the resonance soundings (Lubczynski and Roy, 2004).

To assess groundwater favorability, well yield-classes were used as the related parameter and their locations were the training sites. It is worth to say that yield (Q, m^3/h) is not the most appropriate hydrogeological parameter of well productivity because it does not account for the drawdown (s, in meters) within the well. Therefore, yield varies also with the installed pump system. The appropriate parameter that reflects the real capacity of the aquifer system to provide water at the required yield is the specific capacity Q/s ((m3/h)/m)) (E.g.: Manoel Filho, 1996; Mandrucci, 203; Fernandes *et al*., 2005; Perrotta and Salvador, 2006). We work with yield and electrical conductivity, because they were the most available parameter in the Juá well data that could be statistically defined or estimated by the installed pump system.

The geology of the Juá region is comprised by migmatites and granites bodies to the north, separated from a sequence with gneisses, amphibolites, granite sheetings and marbles to the south by a ductile shear zone of ENE-WSW orientation. Quaternary soil cover is limited in thickness to about 2 m near the main creek and about 0.5 m of combined alluvium-colluvium cover across the region (Figure 2.5).

5.1.1 – The Probability Ratio Method

The Probability Ratio Method uses a ratio of probabilities (Pr) to describe the statistical likelihood for a class of evidential layers having some spatial association with a given prototype area. These associations are defined according to the mathematical basis described below (Lee *et al.*, 2000).

1) The probability ratio of the percentage of the prototype area occupied by the candidate to the percentage of the study area occupied by the candidate is given by Equation 5.1:

$$Pr = [100(Aref \cap Atest)/Aref] \,/\, [100(Atest/A_{sa})] \Rightarrow \qquad \text{Equation 5.1}$$

$$PR = [(Aref \cap Atest)/Aref] \,/\, [(Atest/A_{sa})] = [(Aref \cap Atest)(A_{sa})] \,/\, [(Aref)(Atest)],$$

where: Pr – is the probability ratio, Aref – is the area occupied by the prototype, Atest – is the area occupied by the tested class, A_{sa}– is the study area, Aref∩Atest – is the area within the prototype area occupied by tested class [= area occupied by both the prototype and by the tested class (overlap area)].

2) The ratio of the percentage of the tested class area occupied by the prototype to the percentage of the study area occupied by the prototype. This calculation is given by:

$$Pr = [100(Atest \cap Aref)/(Atest)] \,/\, [100(Aref/A_{sa})] \Rightarrow \qquad \text{Equation 5.2}$$

$$Pr = [(Atest \cap Aref)/(Atest)] \,/\, [(Aref)/(A_{sa})] = [(Atest \cap Aref)(A_{sa})] \,/\, [(Aref)(Atest)],$$

where Aref ∩Atest is the area within the prototype area occupied by tested class (area occupied by both the prototype and by the tested class (overlap area).

Because Atest ∩ Aref = Aref ∩ Atest, the expressions (5.1) and (5.2) are equivalent. Following some algebraic manipulation, the above expressions can be simplified to

$$Pr_{\text{Weights}} = \frac{(\text{Pixels}_{\text{overlap}} / \text{Pixel}_{\text{evid}})}{(\text{Pixels}_{\text{classe}\,\iota} / \text{Pixels}_{\text{study area}})} \qquad \text{Equation 5.3}$$

Where:

- *Pr = probability ratio;*
- *$Pixels_{overlap}$ = area of overlap between an evidential layer and a prototype yield class;*
- *$Pixels_{evid}$ = area that an evidence layer class occupies in the overall study area; $Pixels_{classe\ \iota}$ = area occupied by a prototype yield class,*
- *$Pixels_{study\ area}$ = total area of study.*

The evidential layers (or test classes) for this equation are the prepared data sets, and the prototype areas are the proximity zone of wells within the four yield classes (Table 5.2, Section 5.2.1).

Weights from Pr are real positive numbers. To better evaluate strong (values > 2) and weak (0 < Pr < 1) associations among evidential layers and prototype yield classes, the Pr results characterized by less than 1 (one) were transformed to their reciprocal negative as follows (Equation 5.4).

$Pr_{final} = (1/Pr_{orig}) * (-1)$, e.g. $Pr = 0.25 \Rightarrow Pr_{final} = -4$ Equation 5.4

Where Pr_{final} is now in real number format, meaning that n positive Pr are n^{th} times most likely to occur and –n negative Pr are n^{th} times least likely to occur. Pr Weights fall into three categories that describe the spatial associations between evidential data layers and yield classes:

Positive association if $Pr > 1$

Negative association if $Pr < -1$

Random association if $-1 < Pr < 1$

Therefore, only probability ratios indicating a positive spatial association with values greater than 2 were considered for this study, because this number represents twice the odds that a test class is found within an evidence class.

This method requires equal spatial coverage for the maps that are being compared. This equal spatial was considered as the extent of yield class, so the modeling area became smaller than the original coverage of the evidential layers. The processing steps for this technique were completed using ERDAS® IMAGINE v. 9.1 and ERMapper software. The final modeling results presented are of favorability maps for high productivity wells - yield class 4, and low productivity wells - yield class 2. The spatial distribution of well-yield classes are showed in Figure 5.3, Section 5.2.

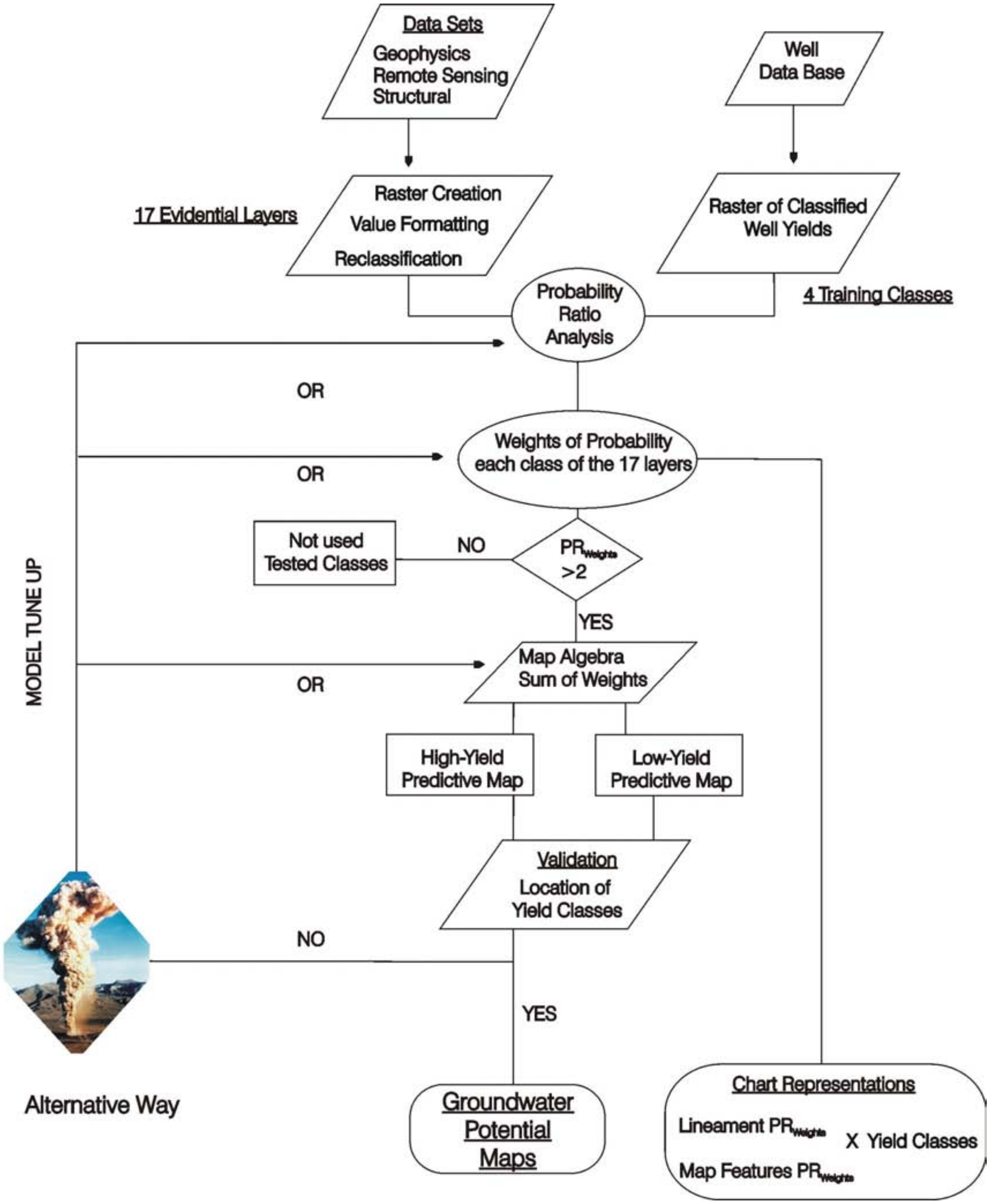

Figure 5.1 - Flowchart of the probability ratio modeling to produce groundwater predictive maps for the Juá area.

5.1.2 – Weights of Evidences Method

The weights of evidence (WofE) method (Bonham-Carter *et al.*, 1989) is a data-driven modeling approach that uses the spatial distribution of known occurrences as training sites to create multi-map signatures from weighted multi-classes or categorical input evidence layers (Bonham-Carter *et al.*, 1989; Masetti *et al.*, 2007). In this study, the training sites consist of water well locations classified by yield, and the evidence layers are the geophysical, the ETM$^+$/Landsat-7 images and the structural geologic data.

The model is based on the idea of prior and posterior probability. The former is the probability that a yield class to occur in the study area, or before considering any existing predictor variables. The latter is an improved response of the prior probability, taking into account distribution patterns from other evidences such as geophysical, spectral, and structural products. The posterior-probability results are then employed to map ground-water favorability according to the sequence shown in Figure 5.2.

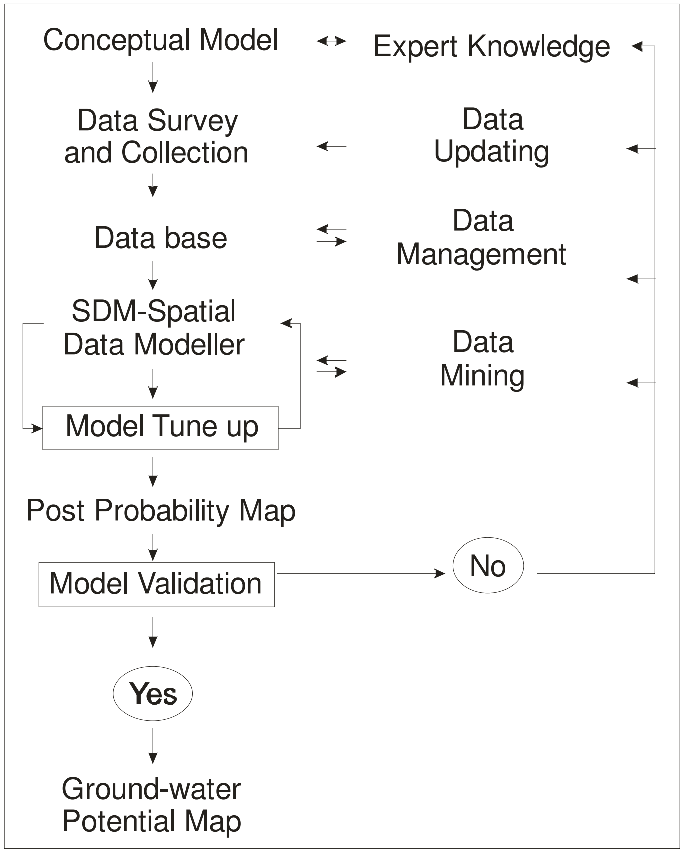

Figure 5.2 - Sequential procedures adopted in Weights-of-Evidence modeling (Modified from Masetti *et al.*, 2007).

The prior of a yield class is its natural chance to occur within the study area, and it is expressed by the area occupied by the yield class divided by the total area of study. The posterior of the yield class (*S*) is the probability of a yield class to occur given the presence or absence of a pattern (Bi or $\overline{Bi}$) as described by Bonham-Carter *et al.* (1989) and Mathew *et al.* (2007):

$$O(S|B_i) = O(S)[Pr(B_i|S)/Pr(B_i|\overline{S})] \quad \text{and} \quad O(S|\overline{B_i}) = O(S)[Pr(\overline{B_i}|S)/Pr(\overline{B_i}|\overline{S})],$$

where $O(S)$ is the prior odds of the yield class, $[Pr(B_i|S)/Pr(B_i|\overline{S})]$ is called the sufficiency ratio (LS), and $[Pr(\overline{B_i}|S)/Pr(\overline{B_i}|\overline{S})]$ is called the necessity ratio (LN).

Bonham-Carter (1994, in Mathew, *et al.*, 2007) defined the positive and negative weights (w^+_i and w^-_i) that combine these conditional probabilities as follows:

$$w^+_i = \log_e [Pr(B_i|S)/Pr(B_i|\overline{S})] \quad \text{and} \quad w^-_i = \log_e [Pr(\overline{B_i}|S)/Pr(\overline{B_i}|\overline{S})]$$

The positive and negative weights (w^+ and w^-) are calculated using the Spatial Data Modeler (SDM) and Spatial Analyst extensions in Geographic Information Systems (GIS) environment (Sawatzky *et al.,* 2008). The SDM utilize spatial cross-tabulation between locations of well yield classes and generalized evidential themes (such as a variable being present or absent) according to the combinations provided in Table 5.1. A positive weight indicates areas where training points are likely to occur, while negative weight refers to areas where training points and not likely to occur.

Table 5.1 - Cross-tabulation of training points and binary evidential theme (present or absent). N_{pix} indicates the number of pixels (Mathew *et al.*, 2007).

	Evidential theme, binary pattern	
Yield classes	Present	Absent
Present	N_{pix1}	N_{pix2}
Absent	N_{pix3}	N_{pix4}

Mathew *et al* (2007 and references there in) describes how positive and negative weights are calculated using GIS software:

$$w_{+i} = \log_e [(N_{pix1}/(N_{pix1} + N_{pix2}))/(N_{pix3}/(N_{pix3} + N_{pix4}))]$$

$$w_{-i} = \log_e[(N_{pix2}/(N\text{pix}1 + N_{pix2}))/(N_{pix4}/(N_{pix3} + N_{pix4}))]$$

Existing any *N* binary patterns, then the weights are added to find the natural logarithm of posterior odds of the yield classes as given by:

$$\log_e O_{\text{posterior}}(S) = \sum_{i=1}^{n} w_i + \log_e O_{\text{prior}}(S)$$

The prior odds of the yield classes ($O_{\text{prior}}(S)$) can be calculated from the prior probability of the yield classes. If any map pattern is absent, w^+ will be replaced by w^-. If data are absent or missing for any position, then the weight is assigned a value of zero. Combining predictor maps result in unique conditions, which are pixels or groups of pixels with the same combination of spatial evidence. For the *k*th ($k = 1, 2, \ldots, m$) unique condition, posterior odds of the yield classes are converted to posterior probability (P_k) as

$$P_k = \frac{e^{\sum_{i=1}^{n} w_i^k + \log_e O_{\text{prior}}(S)}}{1 + e^{\sum_{i=1}^{n} w_i^k + \log_e O_{\text{prior}}(S)}},$$

where w^k_i denotes the weights (w^+_i or w^-_i) contributed by binary pattern B_i in the *k*th unique condition.

The variance of posterior probability can be estimated based on variance of the weights (s^2) (Carranza, 2004 in Mathew *et al*, 2007):

$$s^2(P_k) = \left[\frac{1}{N_{\text{pix}}(S)} + \sum_{i=1}^{n} s^2(w_i^k)\right] \times P_k^2,$$

where $s^2(w^+_i) = [1/N_{\text{pix}}(B_i \cap S)][1/N_{\text{pix}}(B_i \cap \overline{S})]$, and $s^2(w^-_i) = [1/N_{\text{pix}}(\overline{B_i} \cap S)][1/N_{\text{pix}}(\overline{B_i} \cap \overline{S})]$.

The difference between w^+ and w^- defines the contrast (C), an overall measure of how well the generalized evidential themes predict training points (Bonham-Carter *et al.*, 1989). Contrast is as a measure of the spatial association between each class of the evidences and the response variable as yield classes.

Two uncertainty components of the posterior probability can be estimated: one due to the variances of the weights (described by the last equations), and a second due to the absence of one or more of the predictor maps (evidential theme).

The uncertainty due to the absence of predictor maps is measured by a confidence level, a ratio of the contrast-C to its standard deviation. It is also called the confidence level test (Sawatzky *et al.,* 2008), approximated using a Studentized-T (a ratio of C by its standard deviation) to test if the hypothesis that the contrast is not zero. The user selects the confidence level appropriate to the problem being considered. For this work, after several tentative trials, the confidence level of 1.5 (equivalent to 92% of confidence, as calculated in Raines, 1999) was chosen to constrain the use of evidence themes that are the least likely to be associated with high-yield wells, without being so restrictive to model building at the same time. To model low-yield favorability areas, a confidence level of 2 was chosen to represent the 98% confidence limit.

Following this process, the evidential themes were generalized into binary-classes to assess areas of the evidence that share a greater association with locations of training points. The break point or threshold for a binary-class generalization is the confidence level equal to, or greater than, a stipulated confidence level.

5.1.3 - Data Set Preparation

The preparation of the data sets that were used in this study is summarized below:

a) Using Phillips (1997) and Phillips *et al.* (2003) algorithms, the magnetic data were reduced to the magnetic north pole and high-pass filtered to emphasize shallow magnetic sources estimated to be located within 60 m of the topographic surface. The filtered magnetic and electromagnetic data were transformed to physical property maps of magnetization and electrical conductivity (Cordell and McCafferty, 1989). Positive and negative linear gradients were interpreted from geophysical data and extended to 50 m wide as proximity zones;

b) The Electromagnetic data were leveled to produce maps of apparent conductive from coaxial coil HEM-4500 Hz, coplanar HEM-900 Hz and coplanar HEM-33,000 Hz frequencies and a map of the difference between the HEM-4500 and HEM-900 data;

c) Flight-line data from the regional surveys of radiometric uranium (U), thorium (Th), and potassium (K) data were leveled, filtered, and gridded;

d) The ETM+/Landsat-7 data were interpreted using the Principal Components Analysis (PCA) (Loughlin, 1991) and Band Ratio RGB-Compositions (e.g. Sabins, 1999) to provide relative concentrations of weathering minerals, basically Fe-oxide (goethite, limonite), hydroxyl minerals/clay minerals (e.g.: Kaolinite, smectite and montmorillonite) and vegetation. Each image was low-pass filtered to smooth the high-frequency data and eliminate outliers then classified into high, medium, and low Fe-oxide content, hydroxyl minerals, and both. The processed images resulted by band ratio technique were then used in the probability ratio modeling, and the images generated by PCA were used in the weights of evidences modeling;

e) Digitized interpreted lineaments from aerial photos, ETM+/Landsat7 and SRTM data were classed in to azimuth ranges and extended by proximity zones with 100 m width then, converted to raster grids;

f) Directions of the downslope (aspect) were calculated from the elevation model provided by the SRTM data using the ArcGis 9.2 Aspect algorithm;

g) Hydrogeological information included the water-well yield data compiled from Souza Filho *et al*. (2003) and Veríssimo and Feitosa (2002), and our own field campaign in 2005.

All raster data layers were interpolated to a grid of 25-m cell size to comply with the same unit area and to facilitate comparisons between the models. They are displayed in the next sections according to their utility to the different data-driven modeling techniques.

5.2. - Predictive Groundwater Models based on Probability Ratio Technique

This section describes the training sites, raster layers and the results of predictive groundwater modeling using the Probability Ratio mapping technique (Lee et al. 2000, Silva 1999).

5.2.1 – Training sites

The training sites represent locations where water yields were determined from 20 drilled wells at depths between 7 and 80 m. The yields (Q m^3/h) were grouped into 4 classes, based on yield ranges defined according to their pump system commonly installed, and therefore their importance to community water supply:

a) Yield class 1 comprises unproductive wells or wells with very restricted exploration, where the manual pump is the only possible system otherwise the well run out of water;

b) Yield class 2 is the low productive class, usually installed with wind-mill, air-compressor or injection pump of low efficiency. Nowadays, submersible pumps are available for low-yield wells;

c) Yield class 3 represents the good production wells which supply a conglomerate of less than 10 houses with water for domestic uses (no irrigation) in the study area. The recommended pump system is the submersible pump to achieve the best efficiency;

d) Yield class 4 characterizes the exceptional yield wells. They can supply water for domestic use to a small village (tens of houses).

One-hundred-meter proximity zones were established around the wells and then transformed into a raster image characterized by 25 m wide pixels (Table 5.2a,b, Figure 5.3).

Table 5.2a – Well data used in Probability Ratio modeling.

Well	**Yield (m^3/h)**	**Yield Class**
MAN_6	0.10	1
UB_4	0.03	1
J_1	0.03	1
SP_4	0.30	2
SL_1	0.30	2
SP_2	0.30	2
UB_1	0.30	2
MAN_2	0.30	2
JC_1	0.70	2
BR_2	0.70	2
CB_1_p	0.70	2
RM_1	1.00	2
CAIB_1	1.10	3
CAI_3	1.20	3
ST_1	1.25	3
CD_1	2.00	4
CAIB_2	4.50	4
J_67	5.00	4
J_65	6.00	4
J-66	6.00	4

Table 5.2b - Yield classes for Juá area.

Yield Class (Q) and Range (m^3/h)	Water Wells within Class	Pixels within Class (25 m size)
Class 1 ($Q < 0.3$)	3	154
Class 2 ($0.3 < Q < 1$)	9	426
Class 3 ($1 < Q < 2$)	3	149
Class 4 ($Q > 2$)	5	232

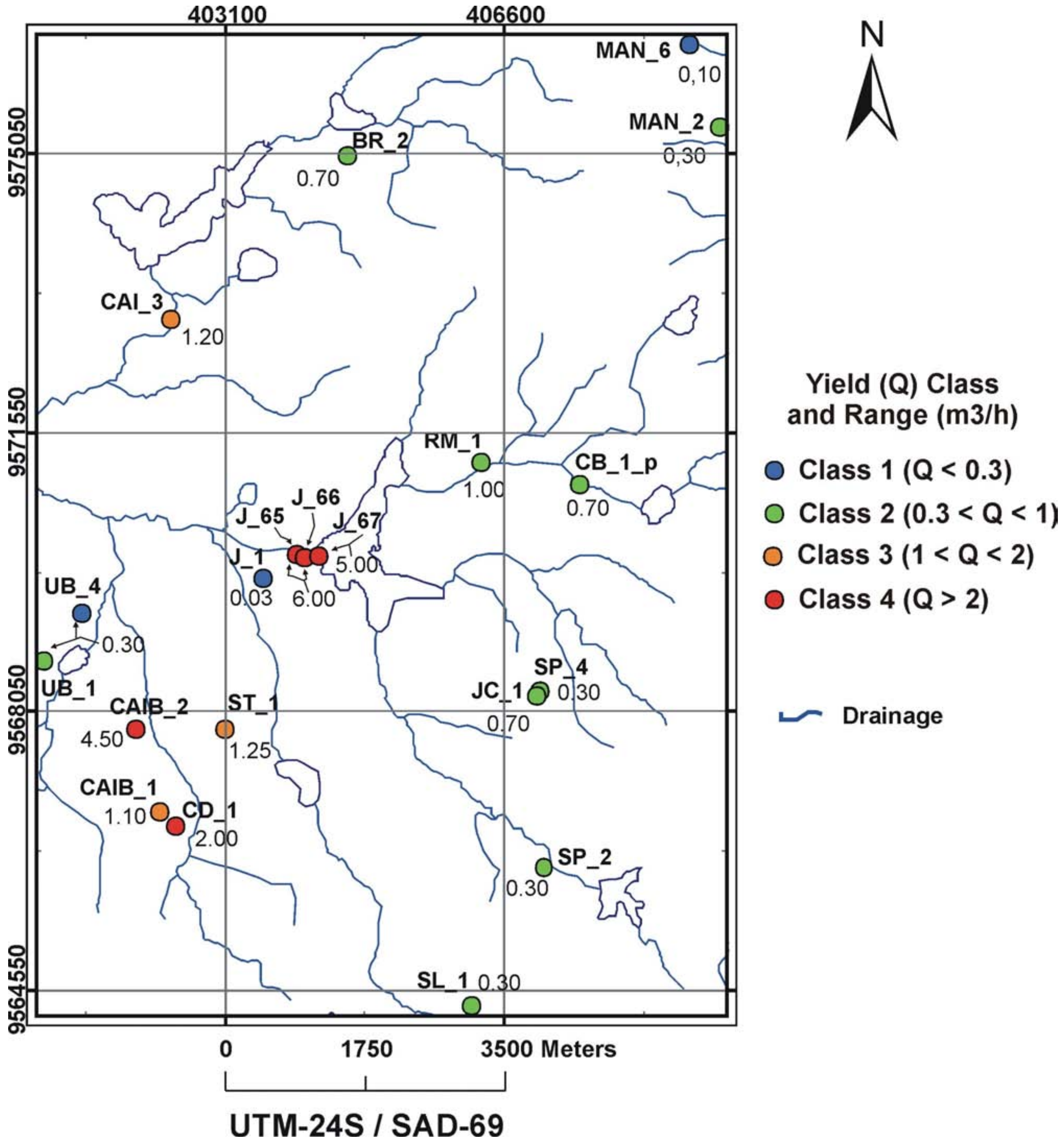

Figure 5.3 – Location of wells classified by water yield in the Juá area. The information was used in predictive groundwater modeling using the probability ratio mapping technique.

5.2.2 – Evidential Themes in Probability Ratio Modeling

The evidential themes used in the probability ratio modeling were described in Section 5.1.3. All data were converted to an integer file type for use with the method.

In order to have a better representation of the overlap area between the evidence theme and the training classes, different data transformation were required for some evidence themes. The linear geophysical gradients were classified into 36 equal azimuth classes. The difference HEM 4500-900 Hz, the terrace-magnetization, the terrace-conductivity and the magnetic layer at 60m depth were reclassified after adding a constant or changed their pixel depth (16 bits to 8 bits) to avoid negative values. The HEM-33000 Hz and HEM-900 Hz were used as 8-bit and 16-bit data to analyze the implications in the probability ratio values. The band ratios image was low-pass filtered to smooth the image and eliminate outliers. The evidences are presented together with their associations with yield class 4 and yield class 2 in Table 5.3.

The trends of geophysical and structural lineaments were mapped with following pattern:

a) Magnetic anomalies associated with negative gradient (non-magnetic gradients) between 290-320 azimuth degrees (Az) and 50-70 Az may be related to brittle tectonics. Positive magnetic gradients (magnetic gradients) occur between 10 to 50 Az, and are correlated with foliation and lithologic contacts;

b) Electrically conducive anomalies of positive gradients (conductive gradients) are mainly oriented along 350, 020 and 040 Az. Negative electrically conductive gradients (non conductive gradients) have primary orientations to NE-SW and minor orientations to N-S directions;

c) Structural lineaments are oriented from 311 to 330 Az and less to 65 Az;

Table 5.3 - Data sets used in Probability Ratio modeling and their association with water wells productivity. Fe(OH) = iron-oxide or iron–hydroxide mineral.

Evidence Theme	**Range / Classes**	**Class Associated with Yield class 2 (original values)**	**Class Associated with Yield class 4 (original values)**
Structural Lineament (Azimuth)	36 classes	61 – 110; 211-220; 161-170;	351-360; 311-320
Band Ratio - Fe(OH) oxide minerals + clay-minerals + Vegetation	18 classes combined	-------	Fe(OH)oxide = medium Clay minerals = low Vegetation = medium
HEM33000 Hz (0 – 505 mS/m)	Reclassified 0- 255	44-52; 56; 60	93 – 171; 64 – 91
HEM 900 Hz (mS/m)	0 – 116	------	15 – 41
HEM 4500 Hz (mS/m)	0 – 145	12 – 15	15 – 32
Potassium (cps)	22 – 108	36 – 43; 74 – 80	67 – 72
Thorium (cps)	9 – 53	38 – 42	27 – 29
Uranium (cps)	8 – 29	11 e 21	21
Magnetic gradients at 60 m depth (azimuth)	36 classes	61 – 70; 21 – 30	101 – 110; 11 – 20
Non magnetic gradients at 60 m depth (azimuth)	36 classes	81-90; 31- 40	101 - 110
Difference HEM 4500 - 900 (-38 to 56 mS/m)	Reclassified to (2 – 97)	6	5 – 12
Electromagnetic gradients	36 classes (azimuth)	51 – 60; 11-20	111 – 120; 11 – 20
Non electromagnetic gradients	36 classes (azimuth)	31 – 40; 61 - 70	-
Terracing of HEM-4500 Hz	(0 – 145)	14 – 19	19 – 28
Magnetic map down to 60 m depth (-38 to 98 nT)	Reclassified to 525 - 1893	-17 - -4; 3 – 23	-7 – 6
Terracing of Magnetization (-0.0054 – 0.0072)	Reclassified to 9946 – 10072	[-2.4 - -0.6; 1.2 - 1.5] x (10^{-3})	[-3.2 - -2.8; -2.1] x (10^{-3})
Aspect (0 - 360 Az)	36 classes	171 – 200	350 – 360; 11-20; 31 – 50; 60 – 90

5.2.3 – High-Yield Groundwater Favorability Models

High-yield favorability was modeled relative to the association among raster evidence and the yield class 4. Modeling results are presented in two ways: a) in the form of charts showing probability weight values against each evidential layer class, and b) as predictive maps related to their association with yield class 4 (Annex 2.1 to 2.16).

To create predictive maps, firstly the probability ratio-PR weights that characterize each physical property and structure with yield classes were transformed in to a raster image. Next, the corresponding weights that were greater than 2 of all evidential classes were added together to create a raster image that represents the ranked potential of the yield class 4 to be present in the study area. This corresponding potential is displayed in colors from the least-blue to greatest-red according to natural breaks defined in the ArcMap v.9.2 software (Figure 5.4a).

High-yield favorability areas modeled using probability ratio technique were found to have the following characteristics:

1) Negative magnetization values were positively associated with the highest yield classes 3 and 4 (Annexes 2.1 and 2.2);

2) Strong positive correlation exists between yield class 4 and high conductivity HEM values and, negative association with less-conductive units is common (Annexes 2.3 to 2.7);

3) All the yield classes show strong positive correlation with soils and rocks containing medium amounts of Fe-oxide and medium-to-high amounts of clay minerals. Yield class 4 showed the highest probability to be associated with these minerals (Annex 2.8);

4) High potassium-K, medium-to-high uranium-U and medium thorium-Th contents are most likely to occur in association with high-yield wells. High U and low Th content were not found in any yield classes (Annexes 2.9, 2.10 and 2.11);

5) Positive association with E-W and NE-SW trend of non-magnetic gradients and to magnetic gradients oriented to N-S to NNE-SSW directions (Annexes 2.12 and 2.13);

6) Undefined association with non-conductive gradients but strong positive association with N-S, E-Wand NE-SSW trends of electrically conductive gradients (Annexes 2.14 and 2.15);

7) Structural lineaments with N-S direction are positively associated with the highest yield classes (Annex 2.16);

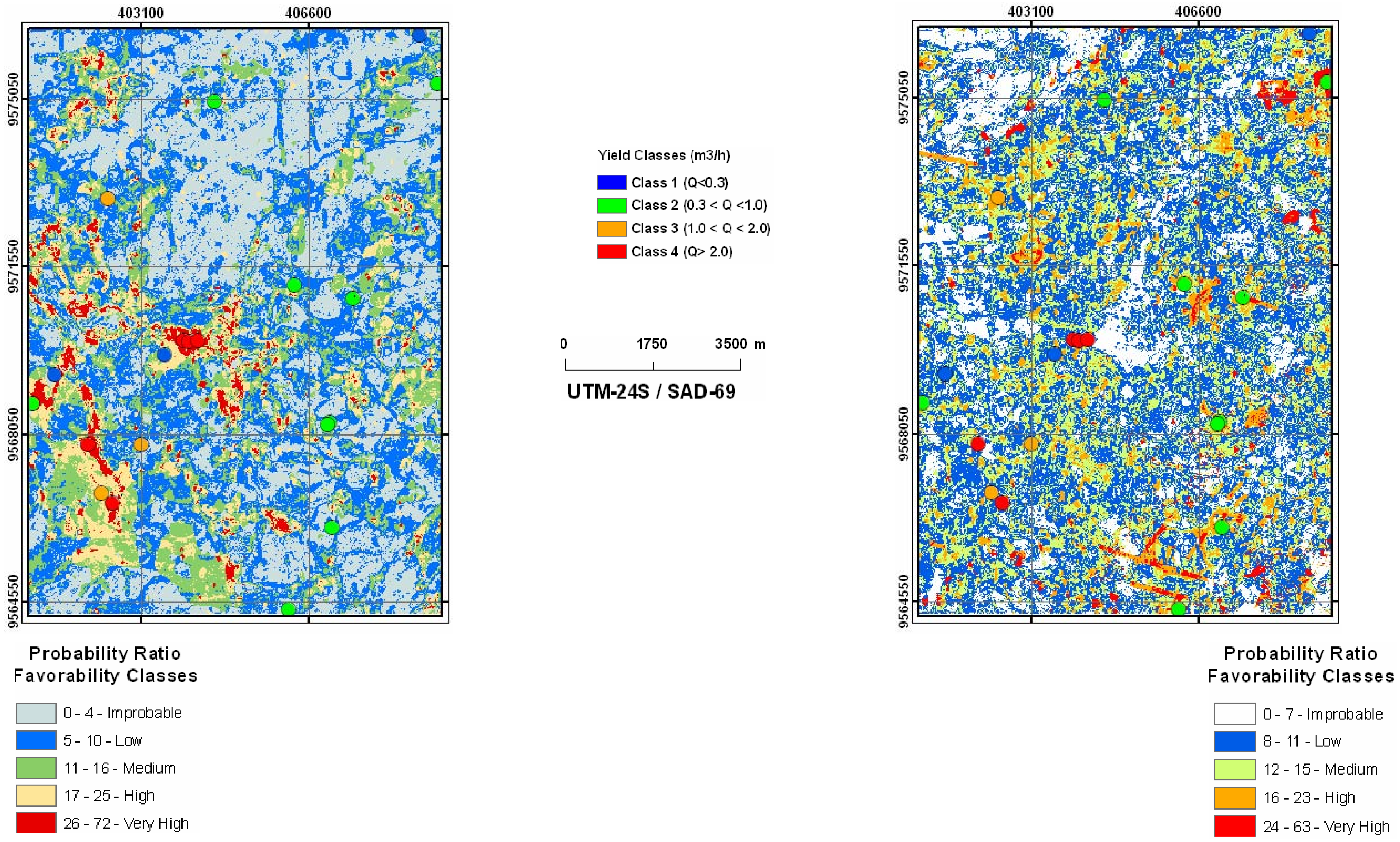

a)

b)

Figures 5.4 – Predictive groundwater models calculated from the sum of positive values for all data probability ratios: a) high yield favorability model; b) low-yield favorability model.

The model is considered reasonable in which the high-yield wells predominate in the most favorable classes and the low-yield wells predominate in the less favorable areas. Although both yield-well classes are found in the end-classes of the model (Figure 5.5) as it is expected, regarding the high variability of yield in the study-area.

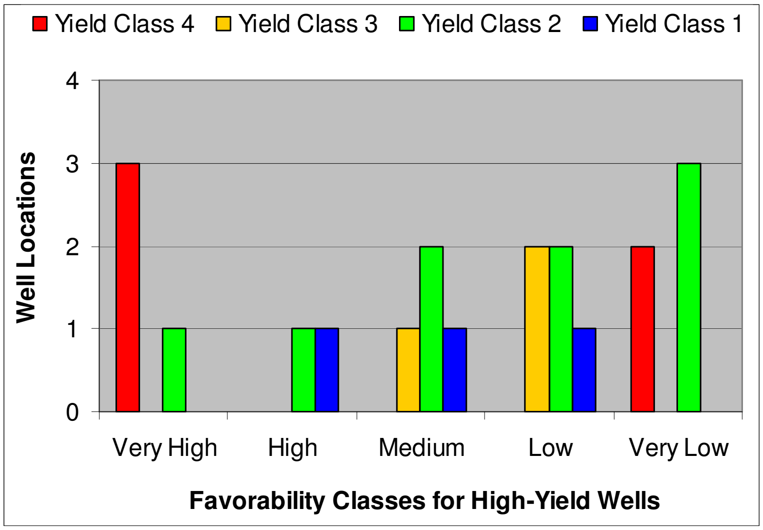

Figure 5.5 – Locations of yield-well classes in relation to classes of high-yield groundwater favorability model. The success of the model is determined by the clear separation between locations of low- and high-yield wells in the least favorable and most favorable model classes.

5.2.4 – Low-Yield Groundwater Favorability Models

Low-yield favorability areas modeled by probability ratio (Figure 5.4b) were found to have the characteristics of:

1) Positive association with positive magnetic anomalies and negative association with non-magnetic rocks (Annexes 2.1 and 2.2);

2) Positive association with moderate-to-low apparent conductivities (Annexes 2.3 to 2.7);

3) Undefined association with Fe(OH)oxide minerals and hydroxyl minerals, because they are equally present in soil, which becomes to a strongly negative association when relative the amount of Fe(OH)oxide minerals increase (Annex 2.8);

4) Soil and rocks containing extreme low or high K, low U with high Th values (Annexes 2.9 to 2.11);

5) Remarkable negative spatial associations exist with N-S non-magnetic gradients an positive association with E-W magnetic gradients. (Annexes 2.12 and 2.13);

6) Structural lineaments oriented between E-W to NE-SW are exclusively related to these low-yield classes (Annex 2. 16);

According to this model, the high-yield wells predominate in the medium to less favorable classes but the low-yield wells does not have a defined association. Both yield-well classes are found in the end-classes of the model (Figure 5.6). The model does not reasonably separated high- and low-favorability for groundwater. Nevertheless, the area comprised by the three wells of yield-class-2 located in low-favorability zones comprise restricted areas (pixel scale) surrounded by areas of high favorability. In this case, the high variability of yield is not the only explanation and the model is not successful to characterize low-yield groundwater domains.

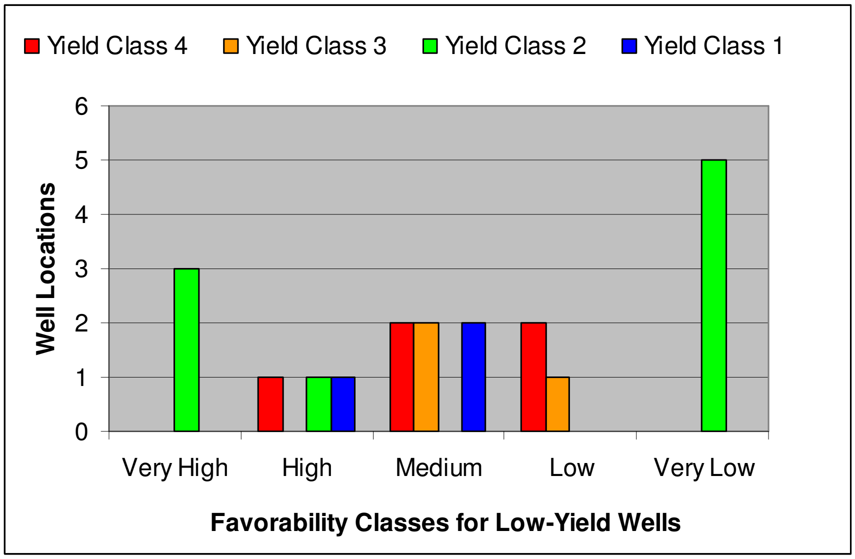

Figure 5.6 – Locations of yield-well classes in relation to classes of low-yield groundwater favorability model. The predominance of low-yield wells in the least favorable class is an indication the model was not successful to low-groundwater favorability. Yet high-yield wells predominated in non-expected classes of medium favorability.

5.3 – Predictive Groundwater Models Based on Weights of Evidences Technique

This section refers to groundwater potential models based on the spatial association of high-yield wells and low-yield wells but differently from probability ratio technique, two yield classes were used as training sites and, more raster data sets were incorporated as evidential themes.

5.3.1 - Training Sites

Within the Juá area, there are 20 water wells where yield was the most frequent information about water productivity (Table 5.4a,b). Yield in crystalline rocks is particularly variable, generally with an asymmetric distribution and wells from Juá area follow this pattern. Therefore, the wells were grouped into two classes in order to account for the best characterization of well locations: 12 wells as low-yield class (0 to 1 m^3/h); and 8 wells as high-yield class (1 to 6 m^3/h). The first yield class is equivalent to classes 1 and 2 in relation to the training sites used in probability ratio models and the second class is the combination of classes 3 and 4.

High-yield class wells have a greater range of values and therefore, they have more dispersed yield values, (see standard deviation and mean parameters in Table 5.4a). Also they are positioned on the western part of the study-area, whereas, low-yield wells, with a lower range and less variability, occur all over the area.

Characteristics of wells with these separate yield classes are reflected in physical parameters, as well as morpho-structural context and they are the main object of our study. Therefore, these high- and low- yield wells were used as training data for high- and low- yield groundwater favorability.

5.3.2 - Evidential Themes

Table 5.5 comprises all data sets used to modeling high-yield favorability and Tables 5.6 shows the data sets used to modeling low-yield favorability in Juá area. The tables contain also the original values, the reclassified ranges and the applied generalization for each evidence layer. Annexes 3.1 to 3.16 display each evidential theme used in the modeling.

In this work, an algorithm by Sawatzky *et al.* (2008) was used to build three models for high-yield favorability and two models for low-yield favorability in ArcMap v. 9.2/ESRI®, with the following specific goals: i) to test the importance of HEM data, the only geophysical theme directly related to ground-water occurrence due to the positive effect of water on bedrock conductivity; ii) to cross-validate favorable areas by comparing high- and low- yield favorability models; and iii) to test whether reclassification of themes helps the weights calculation.

Table 5.4 – Juá well data: Yield (m^3/h); EC = electrical conductivity (mS/m): a) high-yield wells class; b) low-yield wells class. (Adapted from Veríssimo and Feitosa, 2002 and own data).

a) High-yield wells class. Statistics: mean yield: 3.38 m^3/h; median: 3.25; standard deviation: 2.06

High-Yield Well	Drilled Rock	EC (mS/m)	Yield (m^3/m)	Depth (m)
CAIB_1	Biotite-gneiss with quartz lens	415.0	1.10	60
CAIB_2	Biotite-gneiss with quartz lens	558.2	4.50	60
ST_1	Biotite-gneiss	360.0	1.25	78
CD_1	Biotite-gneiss, calc-silicate	1050.0	2.00	72
CAI_3	Biotite-gneiss, granite sheet	203.0	1.20	60
J_65	Biotite-gneiss, granite-gneiss	274.4	6.0	48
J_66	Biotite-gneiss, granite-gneiss	603.0	6.0	54
J_67	Biotite-gneiss, granite-gneiss	117.0	5.0	42

b) Low-yield wells class. Statistics: mean: 0.36 m^3/h; median: 0.30; standard deviation: 0.24

Low-Yield Well	Drilled Rock	EC (mS/m)	Yield (m^3/m)	Depth (m)
SL_1	Biotite-gneiss marble lens	200.0	0.3	60
SP_2	Biotite-gneiss, amphibolite	234.0	0.3	7
SP_4	Biotite-gneiss with quartz lens	-----	0.3	-----
JC_1	Biotite-gneiss	150.0	0.7	75
BR_2	Biotite-gneiss, cataclasite	-----	0.7	72
RM_1	Garnet-biotite-gneiss	-----	0.5	-----
CB_1_P	Biotite-gneiss, granite-gneiss	1104.1	0.7	60
UB_1	Biotite-gneiss, granite-gneiss	-----	0.3	-----
UB_4	Biotite-gneiss, marble	-----	0.03	-----
J_1	Biotite-gneiss	-----	0.03	-----
MAN_2	Biotite-gneiss, marble	416.5	0.3	80
MAN_6	Biotite-gneiss	750.0	0.1	60

Table 5.5 - Themes used for modeling high-yield groundwater favorability. SD = standard deviation

Evidence Theme	**Reclassified theme**	**Generalization threshold and confidence level**	**Class with positive association**	**Class with negative association**
Structural gradients trends (0 – 360 Azimuth)	9 Equal classes	Categorical > 2	100 – 120 Azimuth	Region with no gradients
Fe(OH) oxide + clay-minerals abundance: Low-L; Medium-M; High-H	3 classes 0< L < mean; M < mean+1SD; H > mean+1 SD	Cumulative ascending > 2	Lower class	Medium and higher classes
Clay-minerals abundance Low-L; Medium-M; High-H	3 classes 0< L < mean; M < mean+1SD; H > mean+1 SD	Cumulative ascending > 2	Lower class	Medium and higher classes
HEM33000 (0 – 550 mS/m)	Not reclassified	Cumulative descending > 2	Values > 171 (mS/m)	Values < 30 mS/m
HEM33000 (0 – 550 mS/m)	10 Jenks, natural breaks	Cumulative descending > 2	Values > 153 mS/m	Values < 43 mS/m
HEM 900 (0 – 116 mS/m)	Not reclassified	Cumulative descending > 2	Values > 29 mS/m	-----
HEM 900 (0 – 116 mS/m)	10 Jenks, natural breaks	Cumulative descending >2	Class > 20 mS/m	-----
Potassium (22 – 108 cps)	5 quantile classes	Cumulative descending > 1.5	Values 60 to 72 cps	-----
Magnetic gradients 60 m depth	36 equal classes 0 – 360 Azimuth	Categorical > 2	Gradients 10 – 20 Azimuth	Region with no gradients
HEM 4500 - 900 (-2 – 56 mS/m)	13 Jenks, natural breaks	Cumulative descending > 2	Positive diference from 49 - 52 mS/m	Positive difference. from 41 - 43 mS/m
Terracing Magnetization	30 Natural jenks classes	Cumulative ascending >2	Low values	----
Topographic aspect (0 - 360 Azimuth)	10 equal classes	Categorical >2	60 – 100 Azimuth	280 – 320 Azimuth

Table 5.6 - Themes and parameters used to model low-yield groundwater favorability.

Evidence Theme	**Reclassified theme**	**Generalization threshold and confidence level**	**Class with positive association**	**Class with negative association**
Structural lineaments trend, 0 – 360 Azimuth	9 equal classes	Categorical > 2	60 – 80 Azimuth	100 – 120 Azimuth
Proximity to structural lineaments (m)	4 classes 0 - 50; 51 - 100; 101 - 200; 201 -300; >300 m	Cumulative descending > 2	> 300m	-
Clay-minerals abundance Low-L; Medium-M; High-H	3 classes 0< L < mean; M < mean+1SD; H > mean+1 SD	Cumulative ascending > 2	Lower class	-
HEM 4500 (0 – 140 mS/m)	10 Jenks natural breaks	Cumulative ascending > 1.7	Values 11 - 18 mS/m	-
Potassium (22 – 108 cps)	Not reclassified	Cumulative descending > 1.6	Values < 39 cps	Values > 54 cps
Thorium (9 – 53 cps)	Not reclassified	Cumulative descending > 2	Values > 39 cps	-
Magnetic gradient trends - 60 m depth	36 equal Classes 0 –360 Azimuth	Categorical > 2	Gradients 60 – 70 Azimuth	Region with no gradients
Terracing magnetization map	30 Jenks, natural breaks	Categorical >2	Medium to high values	Low values
60 m-depth magnetic field (-90 – 132 nT)	15 jenks, natural breaks	Cumulative descending >2	Values 9 – 13 nT	Negative values
Electrically conductive gradient	36 classes 0 – 360 Azimuth	Categorical > 2	Gradients 0 – 10 Azimuth	Region with no gradients
Electrically non-conductive gradient trends	36 classes 0 – 360 Azimuth	Categorical > 2	Gradients. 200 - 210	Region with no gradients

5.3.3 – High-Yield Groundwater Favorability Models

Model A1 includes not reclassified HEM data to later compare with model results from using reclassified data. Multiple-proximity zones of structural lineaments helped to define that the most associated distance to high-yield wells was 100 m. All evidence themes with confidence level higher than 1.5 were eligible to participate.

The calculated post-probability weights (Figure 5.7a) were classified according arbitrary divisions as presented in Table 5.7 and that representation as a favorability map is showed in Figure 5.7b. These divisions will be approximately the same for all models presented in this Thesis to make easier the comparisons among them. Therefore, the changing in each model will be due to the area occupied by each favorability class.

Model A1 indicates that the most potential region is concentrated on the WNW-ESE structure that captures the main drainage stream in the central area.

As for validation, low-yield wells, not used in the formulation of the model, were compared with the favorability classes and their locations were limited to not-probable areas or with low favorability. Seventy-five percent of the high-yield well locations were concentrated in areas of medium to highly favorable classes, despite two wells have been placed in non-probable areas.

Table 5.7 - Posterior-probability values for model A1, classified according to arbitrary divisions. The presence of high- and low- yield wells was quantified for each class.

Probability classes	Pprb Weight Intervals	Cumul. Area (%)	High-yield wells n = 8	Low-yield wells n = 12
Improbable	0 - 0.05	86.10	2 (25%)	11 (91.7%)
Low	0.051 - 0.50	95.99	-	1 (8.3%)
Medium	0.51 - 0.80	98.24	2 (25%)	-
High	0.81 - 0.95	99.26	-	-
Very High	0.96 – 1.00	100	4 (50 %)	-

Pprb = posterior probability; Cumul. area = cumulative area

Conditional independence (CI) tests did not indicate dependencies among the evidence themes that were used (Table 5.8). The tests followed the CI-ratio calculation from Bonham-Carter (1994) and the Agterberg and Cheng (2002) CI-test. These tests are necessary because WofE is an additive Bayesian method, so conditional independence of the evidences regarding training points is mandatory, otherwise the model is overestimated. Expected points are derived from the model and indicate the minimum number of training points to provide that model. Therefore, if T-n = 0 the hypothesis of independence fails.

Table 5.8 - Tests of conditional independence (CI) among two or more evidences calculated for model A1. Training points n = 8; Expected Points, T = 5.8; Difference T-n = -2.2; Standard Deviation of T, Tsd = 2.73.

CI tests	Formula	Result	Observation
CI-ratio	n/T	1.37	Dependence if CI-r < 0.85
CI-test	(T-n)/Tsd	-0.91 (18.2 %)	Dependence if CI-t > 50%

Model A2 differs from *Model A1* by using reclassified HEM data instead of original range values. All other model themes and constraints of model A2 are identical to those of A1. Highly favorable areas remain along the WNW-ESE structure/drainage and in minor areas to the south. Intermediate favorability areas are more restricted (Figure 5.8a,b). Table 5.9 shows the favorability classes with the same range of intervals as *Model A1*. Numbers of wells of both yield categories that are found within the model class areas are also shown in Table 5.9.

Table 5.9 - Post-probability values for *Model A2*, classified according to arbitrary divisions. The presence of high- and low- yield wells was quantified for each class.

Probability Classes	Pprb Weight Intervals	Cumul. Area (%)	High-yield wells n = 8	Low-yield wells n= 12
Improbable	0 - 0.05	85.68	2 (25%)	11 (91.7%)
Low	0.051 - 0.50	96.34	-	1 (8.3%)
Medium	0.51 - 0.80	98.70	2 (25%)	-
High	0.81 - 0.95	99.23	1 (12.5%)	-
Very high	0.96 – 1.00	100	3 (37.5)	-

Pprb = posterior probability; Cumul. area = cumulative area

Conditional independence-CI tests using CI-ratio from Bonham-Carter (1994) and the Agterberg e Cheng (2002) CI-test did not indicate dependencies among evidences themes used (Table 5.10).

Table 5.10 - Conditional independence tests calculated for model model A2. Training points n = 8; Expected points T = 6,0; Difference T-n = -2,0; Standard deviation of T, TSD = 2,622.

CI tests	Formula	Result	Observation
CI ratio	n/T	1.33	Dependence if CI-r < 0.85
CI test	(T-n)/TSD	-0.76 (22.3 %)	Dependence if CI-t > 50 %

Model A3 was calculated using only the HEM-900 Hz data to check if there is overestimation of weights in comparison with model A2. From the two HEM frequencies that have confidence level > 2 in relation to high-yield wells, the lower 900 Hz frequency was chosen because it measures conductivity from sources deeper than HEM-33000 Hz frequency is capable to measure (which is constrained to the first meters of soil, Section 3.4).

Probability classes for high yield according to model A3 is shown in Table 5.11 and in Figure 5.9a,b. Highly probable areas remain the same as previous models, but intermediate probability areas are enhanced relative to low probability areas. Again, conditional independence-CI tests did not indicate dependencies among used evidences themes (Table 12).

Table 5.11 - Probability classes for model A3, regarding high-yield wells. The presence of high- and low- yield wells was quantified for each class.

Probability Classes	Pprb Weights Intervals	Cumul. area	High-yield wells n = 8	Low-yield wells n = 12
Improbable	0 - 0.05	85.76	2 (25%)	11 (91.7%)
Low	0.051 - 0.50	96.55	-	1 (8.3%)
Médium	0.51 - 0.84	98.87	2 (25%)	-
High	0.85 - 0.93	99.48	1 (12.5%)	-
Very high	0.96 – 1.00	100	3 (37.5)	-

Pprb = posterior probability; Cumul. area = cumulative area

Table 5.12 - Conditional independence tests calculated for model model A3. Training points n = 8; Expected points T = 6.1; Difference T-n = -1.9; Standard deviation of T, TSD = 2.733.

CI tests	Formula	Result	Observation
CI ratio	n/T	1.30	Dependence if CI-r < 0.85
CI test	(T-n)/TSD	-0.68 (24.8 %)	Dependence if CI-t > 50 %

5.3.4 –Low-Yield Groundwater Favorability Models

Model B1 was built taking in to account reclassified HEM-4500 Hz data and multiple proximity zones, beside other themes. All the evidence themes achieved a confidence level higher than 2 (or 98 % of confidende - Sawatzky *et al.,* 2004). Through the evidence of multiple proximity zones it was found that distances greater than 300 m are most likely to be associated with low-yield wells. All other evidences that were included in the model were described in Table 5.6.

The model is shown in Figure 5.10a,b and the posterior probability classes are detailed in Table 5.13. Regions more favorable for low-yield wells are located along NE-SW structures that coincide with regional foliation, rock contact and electrically non-conductive gradients. This model is less restrictive than expected and, therefore, favorable areas are more widespread, not being restricted to a particular lithology.

Table 5.13 - Probability classes for model B1, regarding low-yield wells. The presence of high- and low- yield wells was quantified for each class.

Probability Classes	Pprb Weight Intervals	Cumul. Area	High-yield wells n= 8	Low-yield wells n = 12
Improbable	0 - 0.08	83.11	6 (75%)	2 (16.7%)
Low	0.81 - 0.40	96.53	1 (12.5%)	4 (33.3%)
Medium	0.41 - 0.79	99.57	1 (12.5%)	2 (16.7%)
High	0.80 - 0.94	99.88	-	1 (8.3%)
Very high	0.0941 – 1.00	100	-	3 (25%)

Pprb = posterior probability; Cumul. Area = cumulative area

Tests favor independence among evidence themes and training points, as shown by Table 5.14.

Table 5.14 - Conditional independence tests applied to model B1 regarding low-yield favorability, according to Bonham-Carter (1994) CI-ratio and the Agterberg and Cheng (2002) CI-test. Training points n = 12; Expected points T = 6.7; Difference T-n = -53; Standard Deviation of T, TSD = 1.612.

CI tests	Formula	Results	Observation
CI-ratio	n/T	1.80	Dependence if CI-r < 0.85
CI-test	(T-n)/TSD	-3.31 (0.0 %)	Dependence if CI-t > 50 %

Model B2 was built without using HEM data in order to verify the importance of this kind of data in modeling ground-water favorability. All other evidence themes were used as shown in Table 5.6. This model is more restricted than *Model B1*. Most likely associated areas with low-yield wells overlap ENE-WSW structures and NE-SW lithologic contacts and small regions in the southeast of the study-area (Figure 5.11a,b).

In Table 5.15 the probability intervals and yield-classes of wells located in each favorability domain of the *Model B2* are presented. None of the high-yield wells were located on favorable areas of the low-yield model. However, low-yield training points were almost equally distributed between favorable and non-favorable areas of the model. Yet, tests show no conditional dependence among the used evidence themes (Table 5.16).

Table 5.15 - Probability classes for model B2, regarding low-yield wells. The presence of high- and low- yield wells was quantified for each class.

Probability classes	Pprb Weight Intervals	Cumul. Area	High-yield wells n = 8	Low-yield wells n = 12
Improbable	0 - 0.04	81.75	6 (75%)	3 (25%)
Low	0.041 – 0.50	97.32	2 (25%)	4 (33.3%)
Medium	0.51 - 0.80	99.48		1 (8.3%)
High	0.81 - 0.96	99.88		1 (8.3%)
Very high	0.96 - 1.00	100		3 (25%)

Pprb = post probability; Cumul. Area = cumulative area

Table 5.16 - Conditional independence tests according Bonham-Carter (1994) CI-ratio and the Agterberg e Cheng (2002) CI-test applied to model B2 regarding low-yield favorability. Training points n = 12; Expected training points T = 6.8; Difference, T-n = -5.2; TSD = 2.102.

CI tests	Formula	Results	Observation
CI-ratio	n/T	1.77	Dependence if CI-r < 0.85
CI-test	(T-n)/TSD	-2.48 (0.7 %)	Dependence if CI-t > 50 %

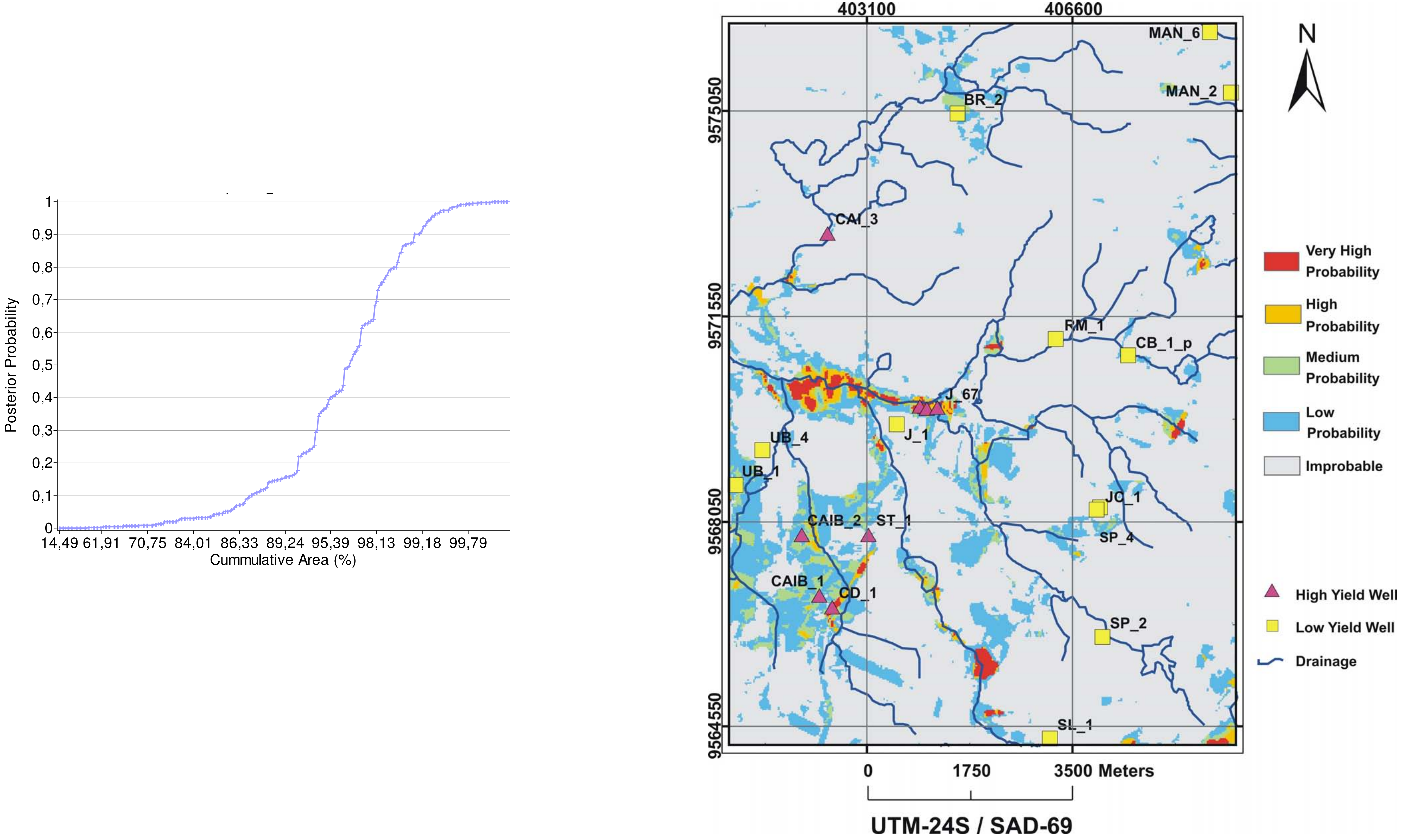

Figure 5.7 - High-yield groundwater *Model A1* for Juá area: a) Cumulative distribution of the posterior probabilities; b) Map representation of the posterior probabilities. Post-probability ranges: 0 – 0.05 –Gray; 0.051 – 0.5 –Blue; 0.51 – 0.8 –Green; 0.81 – 0.95 –Orange; 0.951 – 1.0 –Red.

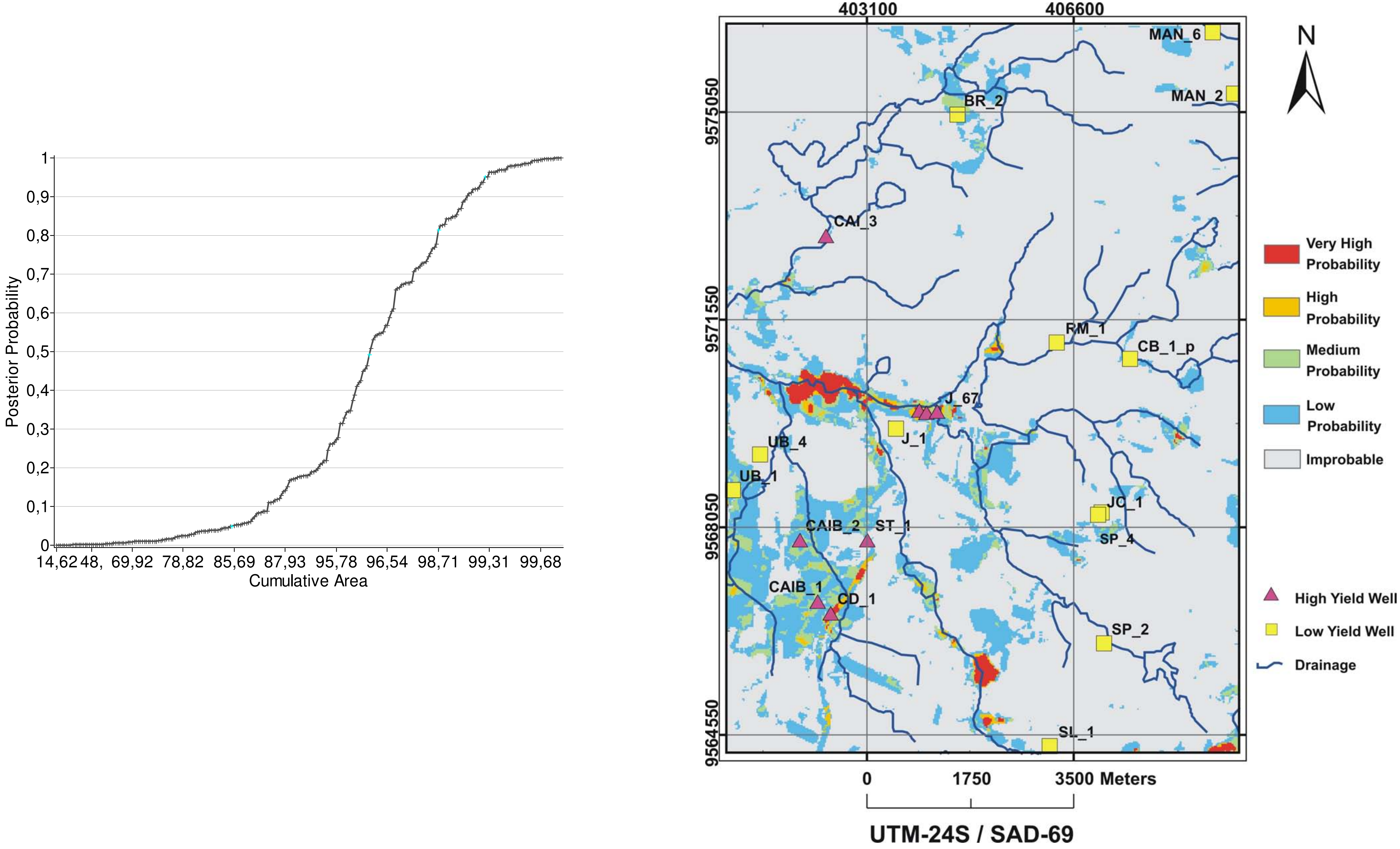

Figure 5.8 - High-yield groundwater *Model A2* for Juá area: a) Cumulative distribution of the posterior probabilities; b) Map representation of the posterior probabilities. Post-probability ranges: 0 – 0.05 –Gray; 0.051 – 0.5 –Blue; 0.51 – 0.8 –Green; 0.81 – 0.95 –Orange; 0.951 – 1.0 –Red.

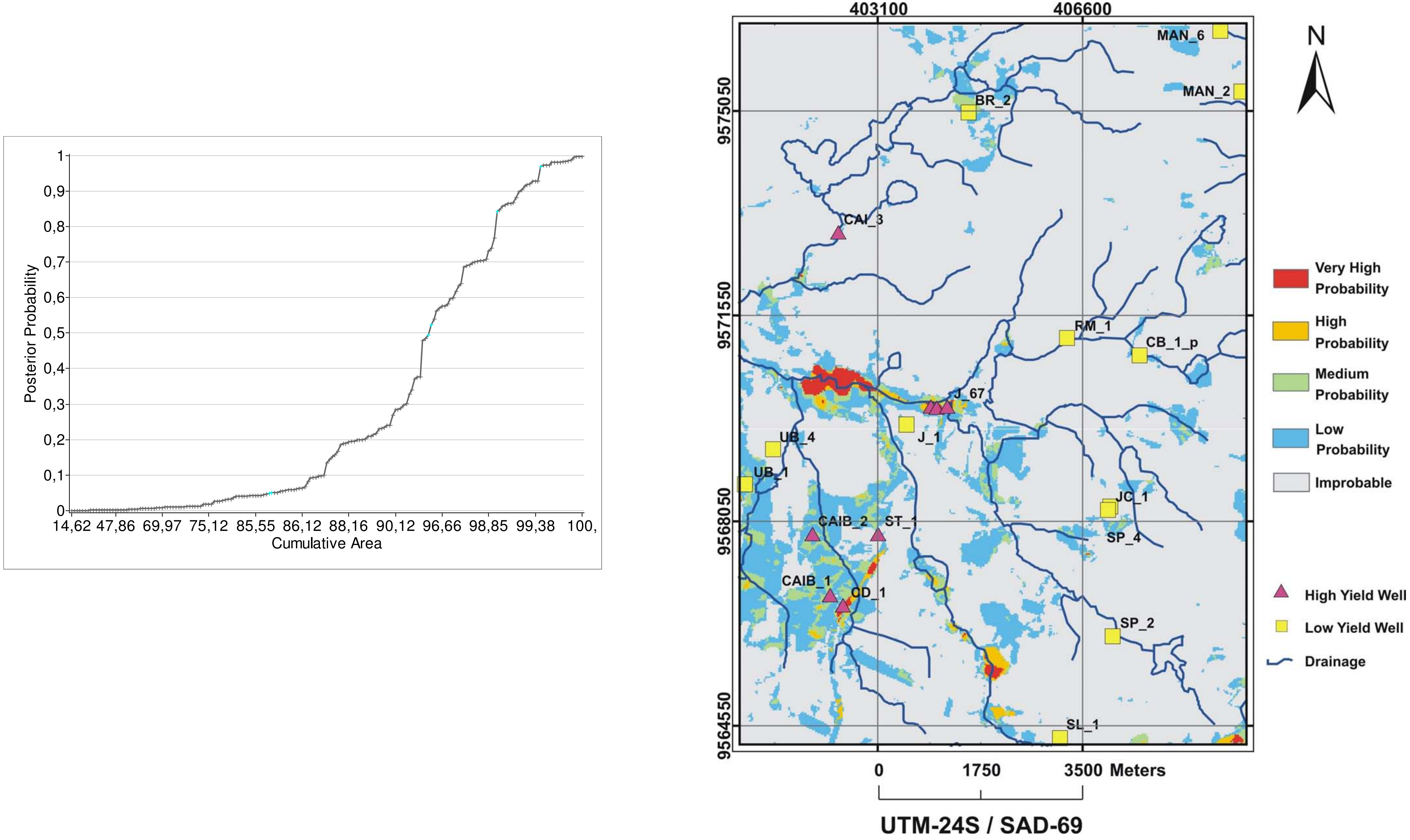

Figure 5.9 - High-yield groundwater *Model A3* for Juá area: a) Cumulative distribution of the posterior probabilities; b) Map representation of the posterior probabilities. Post-probability ranges: 0 – 0.05 –Gray; 0.051 – 0.5 – Blue; 0.51 – 0.8 –Green; 0.81 – 0.95 –Orange; 0.951 – 1.0 –Red.

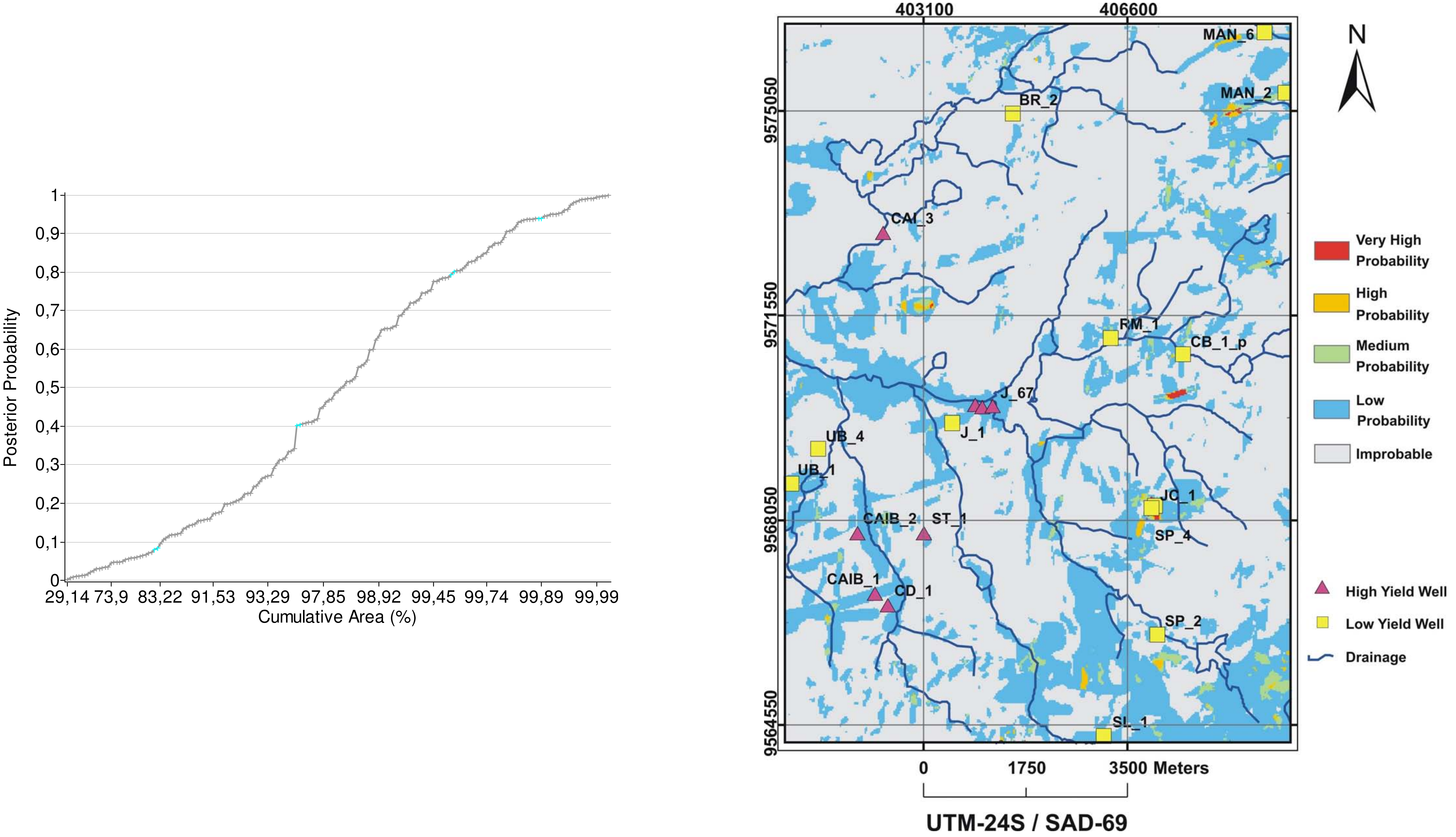

Figure 5.10 - Low-yield groundwater *Model B1* for Juá area: a) Cumulative distribution of the posterior probabilities; b) Map representation of the posterior probabilities. Post-probability ranges: 0 – 0.05 –Gray; 0.051 – 0.5 – Blue; 0.51 – 0.8 –Green; 0.81 – 0.95 –Orange; 0.951 – 1.0 –Red.

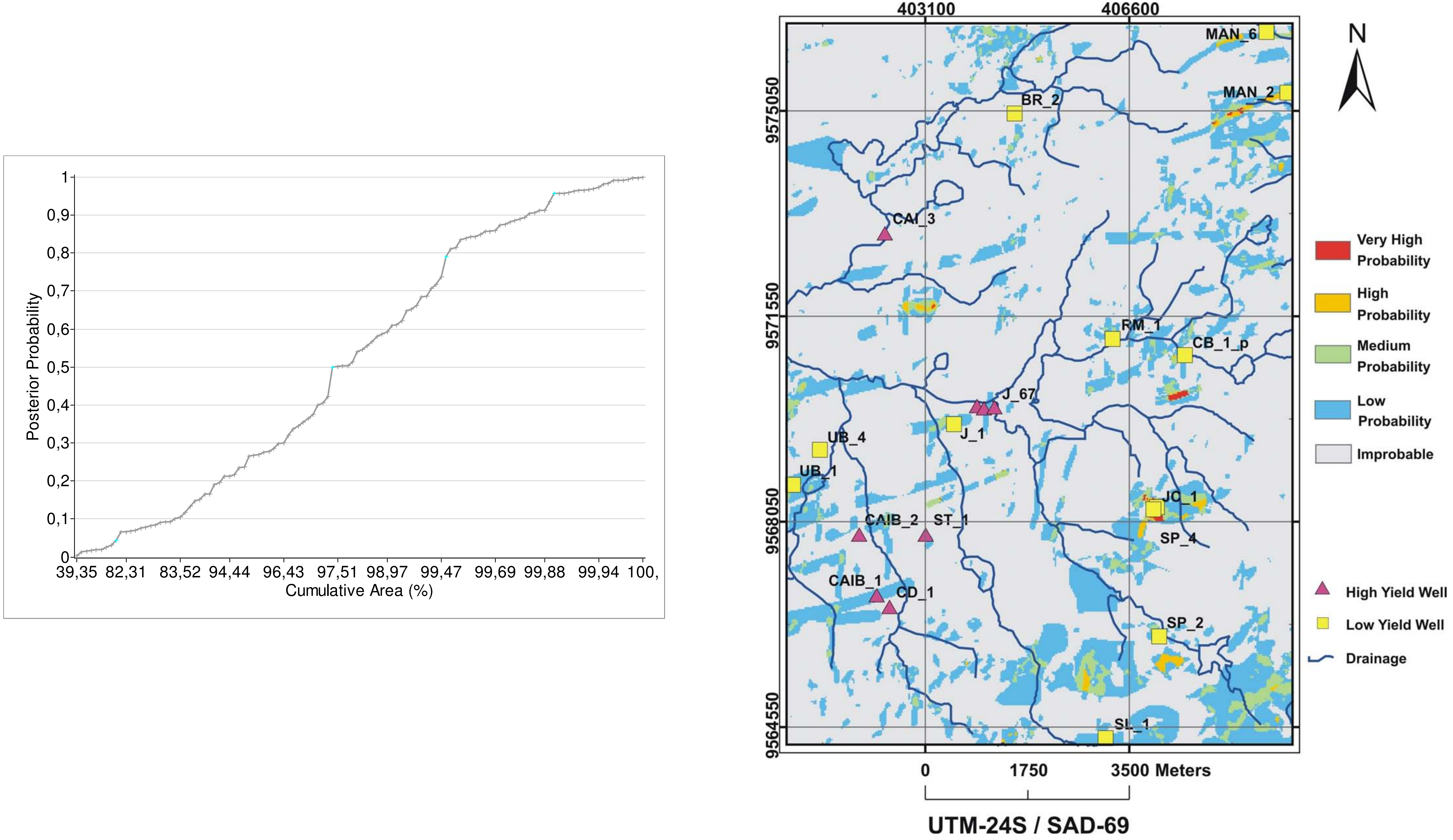

Figure 5.11 - Low-yield groundwater *Model B2* for Juá area: a) Cumulative distribution of the posterior probabilities; b) Map representation of the posterior probabilities. Post-probability ranges: 0 – 0.05 –Gray; 0.051 – 0.5 – Blue; 0.51 – 0.8 –Green; 0.81 – 0.95 –Orange; 0.951 – 1.0 –Red.

5.3.5 – Validity of Weights of Evidence Groundwater Favorability Models

According to the available conditional independence tests, weights-of-evidence models where more than one HEM data set was used did not indicated dependencies among the evidence themes. This is indicative that weights were not overestimated. That can be explained due to the fact that different HEM data investigate at different depths therefore, measures are dissimilar if geologic features exist on the surface and underground with distinct electrical properties.

The almost equal distribution of low-yield training points regarding favorability classes for low-yield models (B1 and B2) reflects the high variability of this productivity class. Because high-yield wells were not located in favorable areas for models B1 and B2, and low-yield wells were not find in favorable areas for models A1, A2 and A3 it is assumed that these models successfully separated physical properties associated with groundwater favorability.

Validity of the high and low groundwater favorability models will be fully accomplished when comparing with yield of new drilled-wells, which will happen with time, depending on the necessities of Juá inhabitants.

5.4 – Comparisons between Probability Ratio and Weights of Evidences Predictive Models

All high-yield groundwater models identified an elongated WNW-ESE region on the central-west part of the study area as the most favorable, and part of it is overlain by the alluvium cover of São Gabriel creek (page 32, section 2.3.1). Previous work (Souza Filho *et al.* 2007) suggests that this region comprises an extensional structure which is non-magnetic down to 600 m but electrically conductive up to 20 m from the ground surface. In the field, outcrops were much fractured (100 fractures/m^2) which resulted in intense weathering and generation of the main water stream in the study-area. Secondary favorable areas are restricted to the southwestern part of the study-area.

Weights-of-evidences-WofE based models are more restrictive to groundwater highly-favorable regions, and the northwestern portion of the area was only modeled as favorable by the probability ratio technique-PR. About the lithologic control over groundwater occurrence, both models still does not provide much information. The clearest evidences are that groundwater favorable areas are most likely to occur where alluvium overlays the bedrock and next to lithologic contacts between hornblende-gneiss and calc-silicate gneiss with biotite-gneiss located in the southwestern sector of the area (Figure 5.44a,b).

Regarding the initial conceptual model (Figure 2.7, Section 2.3) the geophysical and spectral characteristics associated with high-yield wells by the applied modeling techniques may be interpreted as follows:

i) Negative magnetic anomalies as linear features may correlate with ruptil zones, where water and weathering are channeled that disturb magnetic properties of rocks inside this zone (as found in Speed, 2002, Street *et al.*, 2002);

ii) Conductive zones may represent both cover veneer and developed regolith over resistive fractured bedrock that favor groundwater infiltration to underneath fractures;

iii) The relative high content of potassium and medium content of thorium and uranium may represent coarse-grained soil with few concentration of silt or clay particles, as understood by Street *et al.* (2002, and references there in);

iv) High-yield wells were found to be associated with medium content of Fe-oxide and high-to-medium content of clay mineral, according the PR method and low contents of Fe-oxide and clay mineral regarding the WofE method. This ambiguity implies in uncertainties regarding the true association of this theme. Nevertheless, preliminary spectral analysis of soil sampling was done with field-spectrometer favor clay-minerals (kaolinite-smectite and montmorilonite) as the principal weathering product.

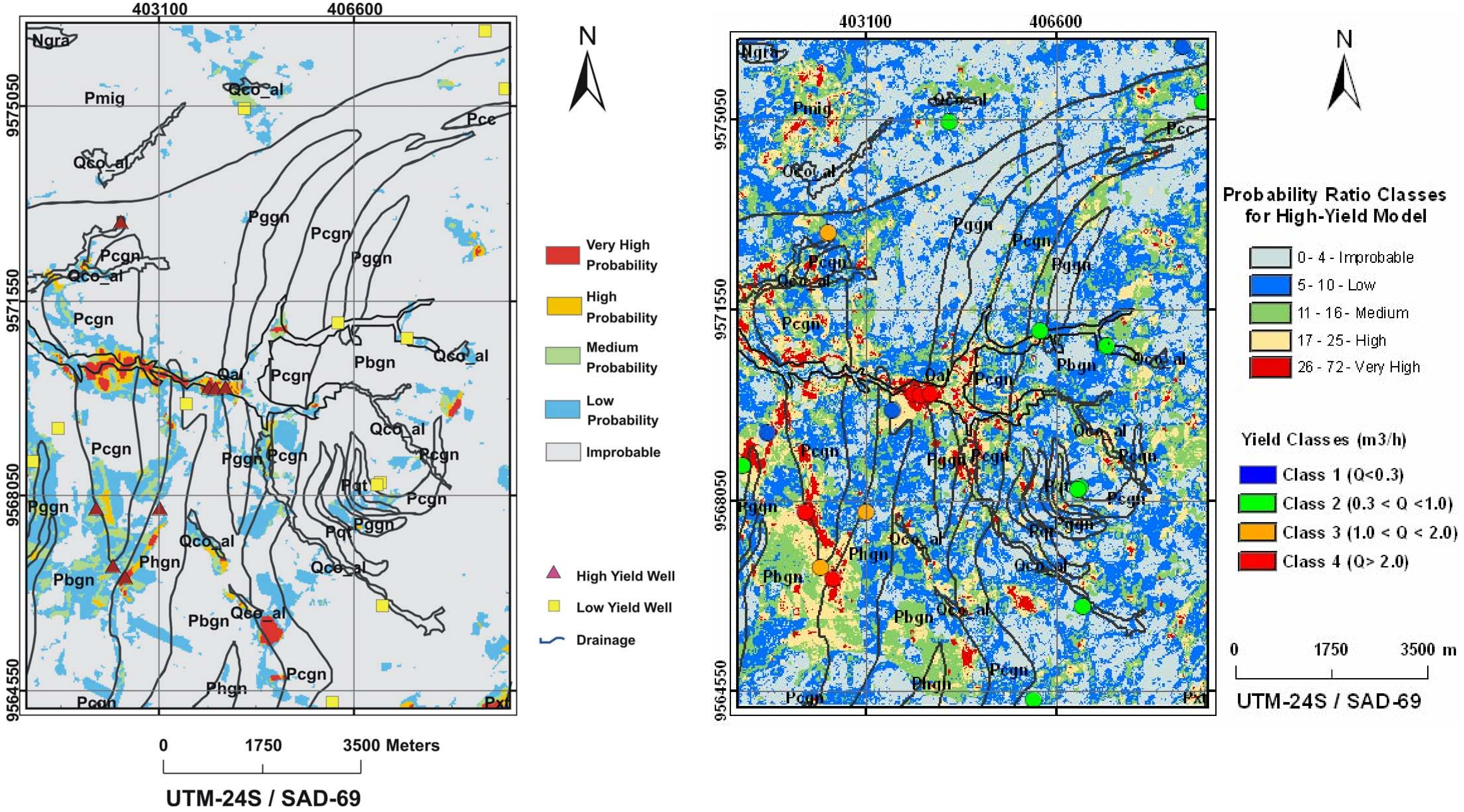

a)

b)

Figure 5.12 – Representation of lithologic units and the groundwater favorability models: a) Groundwater model A1 based on the weights-of-evidence technique; b) Groundwater model based on the probability ratio technique.

5.4.1 – What Is The Final Groundwater Predictive Model to Follow?

This section's title is the most expected to be answered at the end of any technical report or academic work about prospection of any economic goods. The methodology applied in this Thesis' theme enabled two predictive groundwater models for favorability.

It is presented the combinations of high-yield and low-yield groundwater favorability models, provided by the WofE technique, respectively models A1, A2 and A3 and models B1 and B2 (Figure 5.13). This combined WofE model was built based on the following steps:

1) Transformations of the models from raster to shape file to be processed in ArcMap v. 9.2 software;
2) Application of conditional operators to the 5 classes of favorability of the high-yield groundwater models (see Tables 5.7, 5.9 and 5.11, referring to A1, A2 and A3 models' classes). The favorability classes of the combined model will be as follow bellow:

Very high Class 5:

IF A1=A2=A3 = 5 THEN Class 5
IF A1=A2 = 5 <>A3 THEN Class 5
IF A1=A3 = 5 <>A2 THEN Class 5
IF A2=A3 = 5 <>A1 THEN Class 5

High Class 4:

IF A1=A2=A3 = 4 THEN Class 4
IF A1=A2 = 4 <>A3 THEN Class 4
IF A1=A3 = 4 <>A2 THEN Class 4
IF A2=A3 = 4 <>A1 THEN Class 4

Medium Class 3:

IF A1=A2=A3 = 3
IF A1=A2 = 3 <>A3
IF A1=A3 = 3 <>A2
IF A2=A3 = 3 <>A1
IF A1<>A2<>A3 AND minimum = 3

Low Class 2:

IF A1=A2=A3 = 2

IF A1=A2 = 2 <>A3

IF A1=A3 = 2 <>A2

IF A2=A3 = 2 <>A1

IF A1<>A2<>A3 AND minimum = 2

Improbable Class 1

IF A1=A2=A3 = 1

IF A1=A2 = 1 <>A3

IF A1=A3 = 1 <>A2

IF A2=A3 = 1 <>A1

IF A1<>A2<>A3 AND minimum = 1

3) Application of conditional operators to the 5 classes of favorability of the low-yield groundwater models (see Tables 5.13 and 5.15, referring to B1, B2 models' classes). The favorability classes of the combined model will be as follow bellow:

Exclusion of low class and Improbable Class:

Nodata = IF B1=B2 = Improbable OR Nodata = IF B1=B2 =1 (Low Class)

Low-Yield Class 0

IF: B1<>B2 AND minimum = 5

IF B1<>B2 AND minimum = 4

IF B1<>B2 AND minimum = 3

4) Final combination between reclassified models A and B

Class 0 = class 1 of combined model B

Class 1 = class 1 of combined model A, without class 1 from combined model B

Class 2 = class 2 of combined model A, without class 1 from combined model B

Class 3 = class 3 of combined model A, without class 1 from combined model B

Class 4 = class 4 of combined model A, without class 1 from combined model B

Class 5 = class 5 of combined model A, without class 1 from combined model B

The resulted combined model has the advantage to displays where are the favorable areas (red, orange and green color at the central and southwestern area), regions to be very cautious (blue and gray tonality, dispersed all over the area).

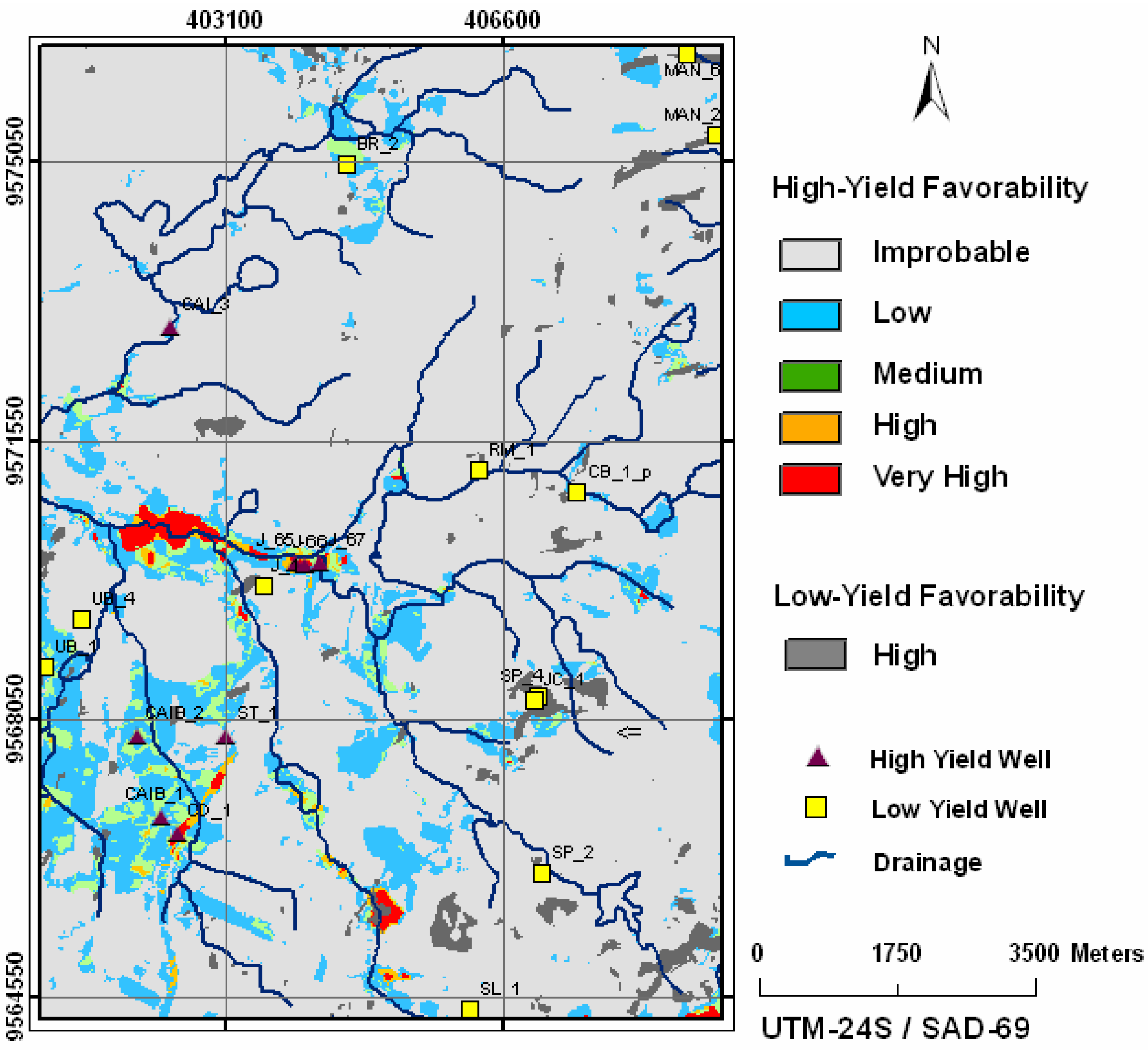

Figure 5.13 - Combinations of high-yield and low-yield groundwater favorability models, provided by the WofE technique, respectively models A1, A2 and A3 and models B1 and B2.

Regarding high-yield groundwater favorability, the models obtained by the techniques of Probability Ratio-Pr and Weights of Evidences-WofE are very similar relative to the highest favorable areas but they differ on medium to lowest favorable areas. The reader should consider both models when choosing for a prospective area. So it was generated a combination map between the five favorability classes of WofE model A2 and the PR model for yield class 4 using a conditional operator that subtracts PR from WofE classes if PR are greater than WofE classes, otherwhise let WofE classes. That combined WofE-Pr map (Figure 5.14) favors WofE model because is more restrictive, and has the advantage to map more regions with low to intermediate groundwater favorability than WofE model, without maximizing areas already highly-favorable.

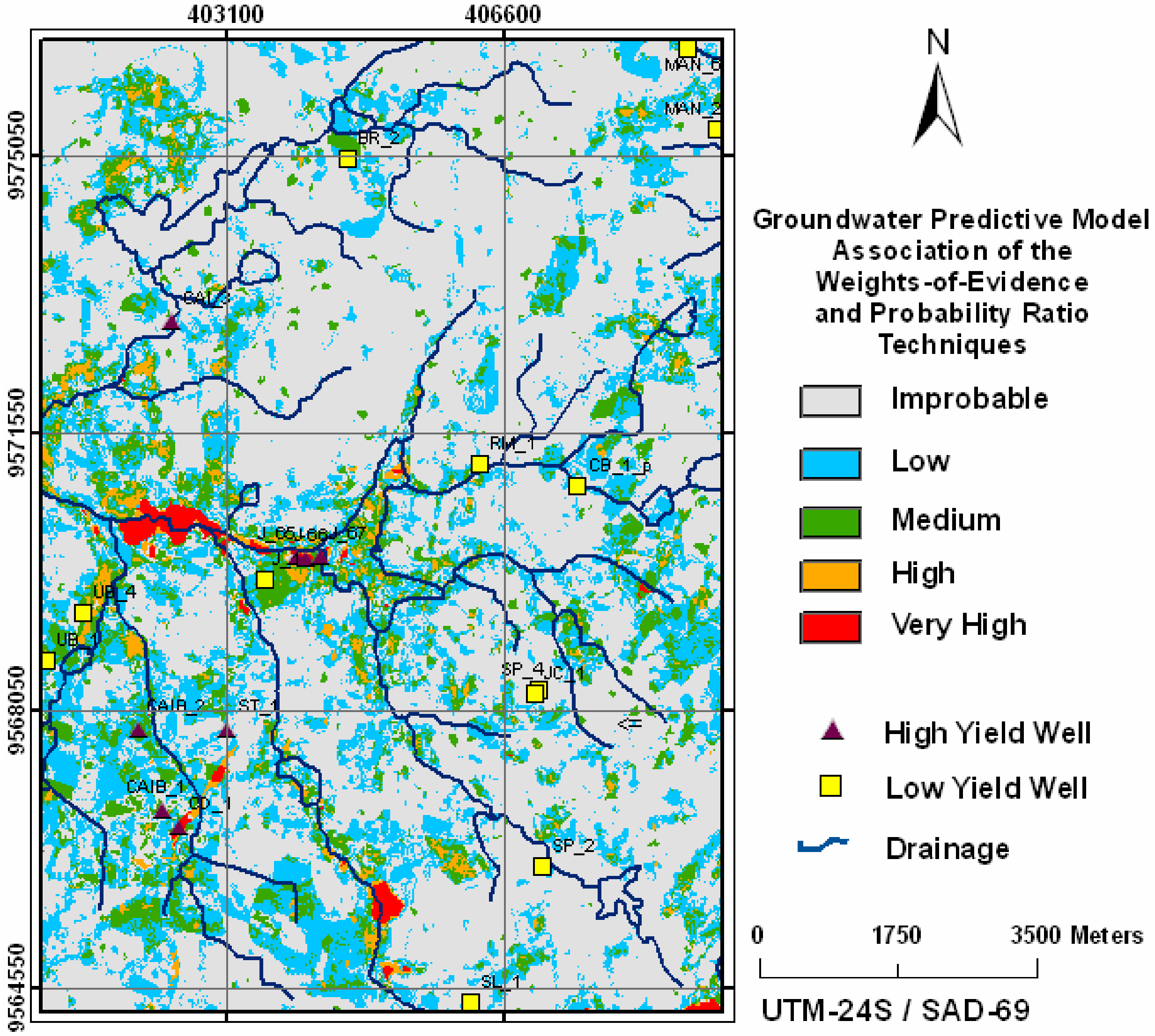

Figure 5.14 - Combined map between the five favorability classes of WofE model A2 and the yield class 4-Pr model, according to the conditional operator of Either Pr-WofE IF Pr>WofE ELSE WofE. Regions not mapped as favorable in WofE model (e.g. northwestern area) were better ranked.

6 – DISCUSSÕES E CONCLUSÕES

O enfoque no processamento de dados aerogeofísicos, em geostatística e na modelagem espacial através da utilização de modelagem espacial, marca o diferencial desta tese no que tange a pesquisa hidrogeológica. A disponibilidade de dados aerogeofísicos eletromagnéticos e magnéticos de alta resolução espacial permitiu a escolha de células de trabalho com tamanho pequeno o suficiente para se adequar às condições da área de influência de poços para água subterrânea.

No processamento dos dados aerogeofísicos magnéticos, foram utilizadas técnicas não convencionais de filtragem tais como o *matched filtering* e terraceamento, que em conjunto com a aplicação de derivadas verticais e gradientes horizontais, realçam anomalias magnéticas rasas (a 60 m) de anomalias com continuidade a profundidades abaixo de 400 m. Os resultados obtidos com as filtragens efetuadas nos dados magnéticos ampliaram a profundidade de investigação hidrogeológica e o realce de estruturas permissivas para água subterrânea. A disponibilidade de informação geofísica em profundidade e de dados de maior resolução expande a pesquisa hidrogeológica para profundidades superiores aos tradicionais 60 - 80 m de perfuração de poços no Nordeste do Brasil.

As informações eletromagnéticas-EM caracterizaram anomalias condutivas rasas, não superiores a 40 m de profundidade e a distinção entre limites condutivos associados a unidades geológicas e a descontinuidades rúpteis.

Os valores de condutividade elétrica aparente são compatíveis com valores, disponíveis na literatura específica (e.g. Telford e*t al.*, 1984), medidos em rocha cristalina com presença de água em fraturas, muito embora outros materiais também forneçam medições similares, tais como a presença de argilas, pouco expansivas ou solos muitos salinos. A forma em mapa da anomalia eletromagnética pode definir o tipo de material. Se a anomalia é linear, associa-se a fraturas, caso contrário pode ser regiões de regolito ou solo condutivo.

As inversões para profundidade dos dados eletromagnéticos, calculados através dos modelos de camada condutiva sobre semi-espaço resistivo, identificaram que a camada condutiva varia de 9 a 38 m de espessura, com condutividades variando entre 200 e 7 mS/m, sobreposta ao embasamento resistivo, com condutividade abaixo de 1 mS/m. Os valores mais freqüentes de espessura da camada condutiva variam entre 7 e 15 m. Tais resultados corroboram trabalhos anteriores sobre estimativa de profundidade de camadas condutivas (< 10 m da superfície) ou de anomalias tabulares verticais (24 m), correspondentes às fraturas na rocha cristalina (Pineo, 2005; Lasa, 2001).

Estimativas da profundidade de investigação dos dados eletromagnéticos mostram que o sistema EM utilizado, que trabalha no domínio da freqüência, possui grandes limitações para detectar anomalias condutivas no embasamento muito resistivo abaixo de 25 m de profundidade ou de penetração do sinal na ocorrência de coberturas superficiais muito condutivas, contendo argila ou excesso de sais e umidade no solo. A freqüência de aquisição 33000 Hz foi muito prejudicada nesse sentido, por outro lado ela pode ser útil na correlação entre as propriedades elétricas, a porosidade e salinidade da cobertura de solo.

Geralmente a possibilidade dessas limitações é verificada anteriormente ao aerolevantamento, por meio de sondagens eletrorresistivas ou eletromagnéticas no terreno ou em poços disponíveis. O sensor deve ser adequado às condições do terreno, em termos de freqüências de trabalho, configuração das bobinas, entre outros. Tais levantamentos prévios servirão posteriormente para efeito de calibração e análise de incertezas de qualquer modelagem, seja de inversão ou de cálculo da condutividade elétrica aparente.

Por outro lado, a utilização dos dados de condutividade elétrica aparente na freqüência de 4500 Hz foi fundamental na caracterização da condutividade elétrica da água subterrânea. O dado HEM serviu como variável externa permitindo a construção de cenários de qualidade da água subterrânea, por meio das técnicas de interpolação por krigagem e de simulação estocástica aplicadas aos dados de condutividade elétrica dos poços. Apesar da maioria dos poços da área estudada possuir água com salinidade muito acima do limite de potabilidade humana, a análise geoestatística identificou a região central com probabilidade acima de 70% de se encontrar águas menos salgadas. Tais regiões coincidem com áreas destacadas nos modelos de favorabilidade de água subterrânea.

Na profundidade de investigação dos dados HEM-4500 Hz, os gradientes que possuem razão Ip/Q constante são interpretados como estruturas que mantêm suas características elétricas, podendo ser bons alvos para detalhamento da geofísica de locação de poço.

Através das técnicas razões de probabilidade e pesos de evidências foi calculada a associação espacial entre as propriedades geológicas, geofísicas, estruturais e as classes de vazão de poços na área do Juá. Tais associações resultaram em modelos semelhantes de favorabilidade para água subterrânea, ao mesmo tempo em que são adequados em discriminar as características relacionadas às classes de alta e baixa vazão de poços. Foram produzidos mapas de combinação entre os modelos que auxiliam nas locações de novos poços para água na região de Juá.

A região centro-oeste da área foi identificada como a mais favorável para altas vazões. O modelo hidrogeológico mais favorável presume a existência de lineamentos estruturais E-W com propriedades não-magnéticas estendendo-se a profundidades superiores a 200 m e condutivos. Esses lineamentos podem ser cortados por estruturas N-S condutivas e pouco profundas. Regiões condutivas alcançam 15 m de profundidade, segundo os modelos de inversões dos dados eletromagnéticos. O solo ou regolito possui granulação mais arenosa do que fina e está associada a relativa alta contagem de potássio, média contagem de urânio e de tório. Como produtos do intemperismo, os minerais com hidroxila (argilo-minerais) predominam sobre minerais com óxido de ferro.

Os gradientes geofísicos magnéticos ou condutivos com direções W-E e N-S possuem grande importância hidrogeológica definida não somente por sua associação espacial com poços de alta vazão, bem como pela associação em campo com as direções de fraturas e falhas rúpteis extensionais (Souza Filho, 1998 e Santos, 2002).

Uma abordagem hidrogeológica tradicional, que compara produtividade de poços e litologia não foi realizada nessa tese porquê há pouca representatividade de poços e os mesmos ocorrem em poucas litologias. Esta comparação é mais adequada em estudos regionais, como fizeram Manoel Filho (1996) e Neves e Albuquerque (2004). Embora seja de pouca utilidade para os programas governamentais de perfuração de poços, porquê os critérios que norteiam a solicitação de obras hídricas no Nordeste privilegiam as condições sócio-econômicas, de infra-estrutura do município e sua inserção no polígono das secas.

Destacamos também que são raros os poços no cristalino do semi-árido brasileiro com vazão superior a 30 m^3/h, que é uma vazão normal para poços em ambiente sedimentar, notoriamente mais produtivo (vide Tabela 1.2). Em ambiente sedimentar, as vazões superiores a 30 m^3/h justificam sua perfuração em áreas remotas, com elevados custos de acesso das máquinas, da perfuração e posterior canalização da água até as vilas ou sedes de municípios. Assim sendo, as produtividades características de poços no cristalino não justificariam tais custos, independente da litologia perfurada.

Por isso consideramos mais coerente correlacionar os poços às propriedades físicas eletromagnéticas ou magnéticas, pois estão melhor representadas na área de estudo, em termos de freqüências de valores e a ocorrência de poços. Para áreas maiores, e na ausência de dados de maior resolução, uma alternativa seria construir mapas de unidades geomagnéticas e associá-las espacialmente às classes de produtividade de poços. O Brasil possui vasto aerolevantamento magnético e radiométrico com potencial pouco explorado em pesquisas hidrogeológicas. Essa alternativa será testada em novo projeto de pesquisa a ser executado pelo autor e orientadoras.

O aerolevantamento do PROASNE não efetuou uma verificação prévia em campo das características eletromagnéticas do subsolo. Algumas linhas de produção possuem dados inconsistentes com as linhas vizinhas, portanto alguns produtos não apresentam boa qualidade após a interpolação de dados. A ausência de dados de campo interfere na precisão das inversões de dados eletromagnéticos, de modo que quaisquer dos valores encontrados sejam de profundidade de anomalias, como de condutividade elétrica aparente, devem ser considerados como aproximados.

A escolha do método de aquisição eletromagnético no domínio da freqüência também está sujeita a críticas devido aos poucas freqüências de aquisição. No domínio do tempo, o maior número de canais de aquisição ampliaria a profundidade de investigação na pesquisa hidrogeológica.

REFERÊNCIAS BIBLIOGRÁFICAS

Agterberg, F. P.; Bonham-Carter, G. F.; Wright, D. F., 1990, Statistical Pattern Integration for Mineral Exploration. In: Gaal, G. & Merriam, D. F. (Eds.), Computer Applications in Resource Estimation, Prediction and Assessment for Metal and Petroleum. Pergamon Press, Oxford, UK.

Agterberg, F. P.; Cheng, Q. 2002. Conditional Independence Test for Weights-of-Evidence Modeling. Natural Resources Research v.11, n.4, p. 249-255.

Almeida, F. F. M.; Hasui, Y.; Neves, B. B. de B.; Fuck, R. A., 1977, Províncias Estruturais Brasileiras. In: VIII Simpósio de Geologia do Nordeste. Boletim. v. 6, p. 363-391.

Arthaud, M. H.; Vasconcelos, A. M.; Oliveira, F. V. C. de., 1998, As Seqüências Metassedimentares do Ceará Central. XL Congresso Brasileiro de Geologia. Belo Horizonte. Anais, p.16.

Baronov, V., 1957, A new method for interpretation of aeromagnetic maps: pseudo-gravimetric anomalies: geophysics, v. 22, p. 359-383.

Becker, A.; Barringer, A. R.; Annan, A. P. 1987, Airborne Electromagnetics 1978-1988. In: Developments and Applications of Modern Airborne Electromagnetic Surveys. Ed. by Fitterman, D. V., U.S. Geological Survey Bulletin n. 1925. p. 9-20.

Blakely, R. J., 1995. Gravity & Magnetic Applications. Cambridge University Press, 441p.

Blakely, R.J., and Simpson, R.W., 1986, Locating edges of source bodies for magnetic or gravity anomalies: Geophysics, v. 51, p. 1494-1498.

Bleines, C., Perseval, S., Rambert, F., Renard, D., Touffait, Y., 2000, ISATIS Software Manual. Geovariances & Ecole des Mines de Paris.

Blum, M.L.B. 1999. Processamento e Interpretação de Dados de Geofísica Aérea no Brasil Central e sua Aplicação à Geologia Regional e à Prospecção Mineral. Instituto de Geociências, Universidade de Brasília, Brasília, Tese de Doutoramento, 229p.

Bonham-Carter, G. F. 1994, Geographic Information Systems for Geoscientists: Modelling with GIS. Ed. Pergamon Press, Oxford.

Bonham-Carter, G. F.; Agterberg, F. P.; Wright D. F. 1989, Weights of Evidence modeling: a new approach to mapping mineral potential. In Agterberg, F. P., and Bonham-Carter, G. F., eds., Statistical Applications in the Earth Sciences: Geol. Survey Canada, Paper 89-9, p. 171–183.

Bonham-Carter, G. F., 1994, Tools for Map Analysis: Multiple Maps. In: Bonham-Carter, G. F., Geographic Information Systems for Geoscientists, ch. 9. Ed. Pergamon, Oxford, 398 p.

Brandão, R de L., 2003a, Zoneamento Geoambiental da Região de Irauçuba – CE. Texto explicativo. Carta Geoambienta. Fortaleza: CPRM, 2003. 67 p. il.

Brandão, R. L.; Gomes, F. E. M., 2003, Técnicas de Geoprocessamento e Sensoriamento Remoto Aplicadas na Avaliação do Potencial Hidrogeológico – Capítulo 6. In: Souza Filho, O. A. de; Ribeiro, J. A.; Veríssimo, L. S.; Oliveira, R. G. de; Gomes, F. E. M.; Brandão, R. de L.; Frizzo, S. J.; Oliveira, J. F. de. 2003, Projeto Otimização de Metodologias para Prospecção de Águas Subterrâneas em Rochas Cristalinas. Relatório Integrado De Atividades 1999 – 2002. CPRM/REFO. Fortaleza. p. 106-124.

Carranza, E. J. M., 2004. Weights of evidence modelling of mineral potential: A case study using small number of prospects, Abra, Philippines. Natural Resources Research, v. 13, p. 173–187. In:

Ceará, Secretaria de Planejamento e Coordenação – SEPLAN. Fundação Instituto de Planejamento do Ceará – IPLANCE, 1997, Atlas do Ceará. Fortaleza.

Cichon, J, R.; Baker, A. E.; Wood, A. R.; Arthur, J. D. 2005. Wekiva Aquifer Vulnerability Assessment. Report of investigation 104. Florida Geological Survey, Tallahasse. ISSN 0160-0931. 36 p.

Clark, I., 1979, Practical geostatistics. Ed. Applied Science Publishers, London. 129p.

Constable, S. C.; Parker, R. L.; Constable, C. G., 1987, Occam's Inversion: a practical algorithm for generating smooth models from electromagnetic sounding data. Geophysics, v. 52, n. 3, p.289-300.

Coppa, I.; Woodgate, P.; Webb, A., 1998, Improving the Management of Dryland Salinity In Australia Through The National Airborne Geophysics Project. In: AEM98, The international Conference on Airborne Electromagnetics. Ed. by Brian S.; Fitterman, D; Holladay, S. Guimin, L. Sydney, Australia. Exploration Geophysics, v. 29, n. 1 and 2 p.230-233.

Cordell, L.; McCafferty, A. E., 1989, A terracing Operator for Physical Property Mapping with Potential Field Data. Geophysics, v. 54, n. 17, p.621-634.

Coriolano, A. C. F., 2002, Reavaliação de Critérios Estruturais na Hidrogeologia de Terrenos Cristalinos, com Ênfase na Neotectônica e Sensoriamento Remoto. Tese de Doutorado, número 02 / PPGG. Centro de Ciências Exatas e da Terra, Universidade Federal do Rio Grande do Norte.

CPRM, 2003, Atlas de Geologia e Recursos Minerais do Ceará: Sistema de Informações Geográficas SIG e Mapas na escala 1: 500.000 / CPRM Serviço Geológico do Ceará; Secretaria de Recursos Hídricos do Estado do Ceará. Coord. Téc. José Carvalho Cavalcante, Antônio Maurílio Vasconcelos e Francisco Edson Mendonça Gomes. Fortaleza. 1 CD-Rom.

CPRM, 2007a, Programa Águas Subterrâneas para a Região Nordeste - Programa Anual de Trabalho – 2001. ftp://ftp.cprm.gov.br/pub/pdf/dehid/prgaguaregne.pdf , acessado em 02 de julho de 2007.

CPRM, 2007b, Geofísica em http://www.cprm.gov.br/aero/2000/aero2000.htm, acessado em 25 de junho de 2007.

Crósta, A. P.; Moore, J. McM., 1989, Enhancement of Landsat Thematic Mapper Imagery for Residual Soil Mapping in SW Minas Gerais State, Brazil: A prospecting case history inGreenstone Belt Terrain. In: Thematic Conference on Remote Sensing for Exploration Geology, Calgary, p.1173-1187.

Deutsch C. V., 1993, Kriging in a Finite Domain. Math. Geol., 25 (1): 41-52.

Deutsch, C. V.; Journel, A. G., 1992, Annealing Techniques Applied to the Integration of Geological and Engineering Data, Stanford Center for Reservoir Forecasting. Stanford, USA: Stanford University, Report 5. In: Oliveira, M. L. de, 1997, Análise das incertezas envolvidas na modelagem de reservatórios no contexto geoestatístico. Dissertação de Mestrado. UNICAMP, Campinas, São Paulo.

EMIGMA v. 7.8, Copyright Petros Eikon Inc, Canada. http://www.petroseikon.com/emigma/.

Engineering and Environmental Society-EEGS, 2007, Available at http://www.eegs.org/sageep/index.html.

Everett, M. E.; Meju, M. A., 2005, Near-Surface Controlled-Source Electromagnetic Induction: background and recent advances. In: In: Hydrogeophysics, Edited by Rubin Y. and Hubbard, S. S. Ed. Springer. The Netherlands. p. 157-183.

Feitosa, E. C., 2000, Pesquisa de Água Subterrânea. In: Feitosa, F. A. C. & Manoel Filho, J. (ed) Hidrogeologia – Conceitos e Aplicações. 2ª. ed. CPRM/REFO, LABHID-UFPE, Fortaleza, Brazil.p. 53-80

Feitosa, F. A. C., 1999, Carta Hidrogeológica – Folha Irauçuba-SA.24-Y-D-V In: Souza Filho, O. A. de, 1999, Programa Levantamentos Geológicos Básicos do Brasil. Irauçuba, Folha SA.24-Y-D-V, Escala 1: 100.000. Estado do Ceará. Organizado por Oderson Antônio de Souza Filho. Brasília. CPRM, 1 CD-Rom.

Feitosa FAC, Manoel Filho J (2000) Hidrogeologia - Conceitos e Aplicações (Hydrogeology – Concepts and Applications) (Coordinators). Fortaleza. CPRM/REFO, LABHIH-UFPE, 2ª. Edição

Feitosa, F. A. C.; Ribeiro J. A. R.; Veríssimo, L. S.; Souza Filho, O. A. de. 2000. Apresentações do Projeto PROASNE. CPRM, Fortaleza.

Fernandes, A. J.; Perrotta, M. M.; Salvador, E. D.; Azevedo, S. G, Gimenez Filho, A., Stefani, F. L, Paulon, N., 2005, Aqüíferos Fraturados In: Mapa de Águas Subterrâneas do Estado de São Paulo: escala 1: 1.000.000: Nota Explicativa. ed. São Paulo: Governo do Estado de São Paulo, p. 66-84.

Fetter, A. H.; Santos, T. J. S. dos; Van Schmus, W. R.; Hackspacker, P. C.; Neves, B. B. de B.; Arthaud, M. H.; Nogueira Neto, J. A.; Wernick, E. 2003, Evidence for Neoproterozoic Continental Arc Magmatism in the Santa Quitéria

Batholith of Ceará State, NW Borborema Province, NE Brazil: implications for the Assembly of West Gondwana. Gondwana Research, v. 6, no. 2, p. 265-273.

Fountain, D., 1998, Airborne Electromagnetic Systems – 50 years of development. In: International Conference on Airborne Electromagnetics (AEM 98). Ed. by Spies, B; Fitterman, D.; Holladay, S.; Liu, Guimin. Exploration Geophysics, v. 29, no. 1 e 2, p. 1-11.

Fraser, D. C., 1978 – Resistivity Mapping with an Airborne Multicoil Electromagnetic System: Geophysics, v 43, p. 144-172. In: Lasa, 2001, Projeto Aerogeofísico Água Subterrânea no Nordeste do Brasil, Blocos Juá (CE). Relatório final do levantamento e processamento dos dados magnetométricos e eletromagnetométricos e seleção das anomalias eletromagnéticas. Texto técnico. Cooperação Canadá-Brasil / PROASNE. Brasília.

Fuck, R. F., 2000, Interpretação de Dados Magnetométricos, Eletromagnetométricos e Gamaespectrométricos da Região de Carajás-Pa. Dissertação de Mestrado no. 147, Instituto de Geociências, Universidade de Brasília. Brasília, p.

Fugro S.A., 2005, Métodos Eletromagnéticos, Notas de Curso de Processamento Aerogeofísico, Convênio ADIMB-FUGRO, UERJ, Rio de Janeiro. Arquivos digitais diversos.

GLCF – Global Landcover Facility, 2003, Landsat sensor ETM, scene WRS-2 path 217, row 63, October/07/1999, orthorectified, GeoCover registered. University if Maryland, Earth Science Data Interface (ESDI) at the Global Land Cover Facility (GLCF). U.S. Geological Survey, December/22/2003. Sioux Falls, South Dakota: USGS. Available in http://glcfapp.umiacs.umd.edu:8080/esdi/index.jsp, accessed in April, 22th 2007.

Gomes, F. E. M.; Brandão, R. de L.; Péloquim, S.; Gwyn, H.; Melo, A. C. R. de; Veríssimo, L. S.; Forgiarini, L. L.; Souza Filho, O. A. de; Frizzo, S. J., 2004, Comparação entre Modelos de Ocorrência de Água Subterrânea em Rochas Cristalinas na Região de Irauçuba-Ce. In: I Simpósio De GPR, I Simpósio de Hidrogeofísica, Fortaleza, organizado por LGPSR/UFC e ABAS-CE. 1CD-Rom.

Gómez-Hernández, J. J., 2005, Geostatistics. In: Rubin, Y; Hubbard, S. S. (eds.), Hydrogephysics, Springler Ed., The Netherlands, 2005. p 59-83.

Hageman, L. P., 2005, A Simple Field Leach Test to Assess Potential Leaching of Soluble Constituents from Mine Wastes, Soils, and Other Geologic Materials. USGS Fact Sheet 2005-3100. Accessed on July, 18th 2007 on http://pubs.usgs.gov/fs/2005/3100/pdf/FS-3100_508.pdf , 4 p. il.

Hildenbrand, T. G.; Raines, G. L.; Fitterman, D. V. 1997, National Airborne Geophysic Program. In: Developments and Applications of Modern Airborne Electromagnetic Surveys. Ed. by Fitterman, D. V., U.S. Geological Survey Bulletin n. 1925. p. 3-5.

Hydrogeology Journal, 2007, Special Series: Remote Sensing and GIS in Hydrogeology. Ed. Springler Berlin / Heidelberg, v.15, n.1, 200 p. il.

Kruse, F. A.; Lefkoff, A. B.; Boardman, J. B.; Heidebrecht, K. B.; Shapiro, A. T.; Barloon, P. J.; Goetz, A. F. H., 1993, The Spectral Image Processing System (SIPS) - Interactive Visualization and Analysis of Imaging spectrometer Data. Remote Sensing of Environment, v. 44, p. 145 - 163.

LASA Engenharia e Prospecções S/A, 1978, Projeto Aerogeofísico Itatira, Empresas Nucleares Brasileiras S/A - NUCLEBRÁS, 3 volumes (Subáreas A, B e C), texto e anexos, Rio de Janeiro.

LASA Engenharia e Prospecções S/A, 2001, Projeto Aerogeofísico Água Subterrânea no Nordeste do Brasil, Blocos Juá (CE). Relatório final do levantamento e processamento dos dados magnetométricos e eletromagnetométricos e seleção das anomalias eletromagnéticas. Texto técnico. Cooperação Canadá-Brasil / PROASNE. Brasília.

Lee, G. K; McCafferty, A. E.; Alminas, H. V.; Bankey, V.; Frishman, D.; Knepper, D. H. Jr.; Kulik, D. M.; Marsh, S. P.; Phillips, J. D.; Pitkin, J. A.; Smith, S. M.; Stoeser, D. B. Tysdal, R. G.; Van gosen, B. S., 2001, Montana geoenvironmental explorer: U.S. Geological Survey Digital Data Release DDS-65, Denver, 2001. Volume original de 1999, USGS Digital Data Series-XX.

Loughlin, W. P., 1991, Principal Components Analysis for Alteration Mapping. Photogrammetric Engineerring and Remote Sensing, 57(9): 1163-1169.

Lubczynski, M.; Roy, J., 2004, Magnetic resonance sounding: new method for ground water assessment. Ground-Water, 42(2):291-303.

Mandrucci, V.; Araújo, C. C. de; Taioli, F., 2003, Sensoriamento Remoto, Aerogeofísica e Geoprocessmanto Aplicados ao Estudo de Aquífero Fraturado em Terreno Cristalino, Leste do Estado de São Paulo. In: Revista Brasileira de Geociências, v. 33 (suplemento), p. 43-52.

Manoel Filho, J., 1996, Modelo de dimensão Fractal para Avaliação de Parâmetros Hidráulicos em Meio Fissural. Tese de Doutoramento. Instituto de Geociências, Universidade de São Paulo, São Paulo. 197 p.

Marquadrt, D. W., 1963, An Algorithm for Least-Squares estimation of non-linear parameters. J. Soc. Ind. Appl. Math., n.11, p.431-441.

Masetti, M.; Poli, S.; Sterlacchini, S. 2007. The Use of the Weights-of-Evidence Modeling Technique to Estimate the Vulnerability of Groundwater to Nitrate Contamination. Natural Resources Research, v. 16, n. 2, p.109-119.

Mathew J.; Jha, V. K.; Rawat, G. S. 2007. Weights of evidence modelling for landslide hazard zonation mapping in part of Bhagirathi valley, Uttarakhand. Current Science, v. 92, n. 5, p.628-638.

Mccafferty, A.E.; Smith, B.D.; Sole, T.C.; Karl, S.; Taylor, C.D., 1999, Predictive Geophysical Models for Select Geologic Units and Mineralized Environments, Kuprenof and Zarembo Islands, Southeast Alaska: U.S.G.S. Open-File Report 99-X, Digital Web Release.

McDougal, R. R.; McCafferty, A. E.; Smith, B. D.; Yager, D. B., *in press*, Topographic, Geophysical, and Mineralogical Characterization of Geologic Structures Using a Statistical Modeling Approach. In: Integrated Investigations of Environmental Effects of Historical Mining in the Animas River Watershed, San Juan County, Colorado - Chapter E13. Ed. Church, S. E., von Guerard P., Finger, S. E., U.S. Geological Survey Professional Paper 1651-E13. CD-Rom.

McNeill, J. D. 1991. Use of electromagnetic methods for groundwater studies. *In*: Geothecnical and Environmental Geophysics, Ed. Ward, S. H. Society of Exploration Geophysicists. Series Investigations in Geophysics no. 5 v.1 Review and Tutorial. p. 191-218.

Meng, O.; Hu, H.; Yu, Q., 2006, The Application of an Airborne Electromagnetic System in Groundwater Resource and Salinization Studies in Jilin, China. Journal of Environmental and Engineering Geophysics-JEEG, v. 11, issue 2, pp. 103–109.

Millingan, P. R.; Gunn, P. J., 1997, Enhancements and Presentation of Airborne Geophysical Data. ASGO Journal of Australian Geology and Geophysics, 17(2):31-38.

Miranda, E. E. de; (Cord.), 2005, Brasil em Relevo. Campinas: EMBRAPA Monitoramento por Satélite, 2005. Disponível em: http://www.relevobr.cnpm.embrapa.br. Acesso em 12 de julho de 2007.

Ministério da Saúde, 2005, Portaria MS n.º 518/2004/Ministério da Saúde, Secretaria de Vigilância em Saúde, Coordenação Geral de Vigilância em Saúde Ambiental, Série E. Legislação em Saúde, Brasília. Editora do Ministério da Saúde.

Nabighian, M.N., 1991a, Eletromagnetic Methods in Applied Geophysics. *In*: Investigations in Geophysics, No. 3, Vol. 1 – Theory. Ed. Misac N. Nabighian, SEG, Tulsa, U.S., 505 p. il.

Nabighian, M.N., 1991b, Eletromagnetic Methods in Applied Geophysics, Volume 2, Applications, parts A and B. *In:* Investigations in Geophysics, No. 3. Ed. Misac N. Nabighian, SEG, Tulsa, U.S., Chapters 1, 3, 5, 7 and 10.p.1-877.

Neves, M. A. 2005, Análise Integrada Aplicada à Exploração de Água Subterrânea na Bacia do Rio Jundiaí. Tese de Doutoramento. Universidade Estadual Paulista, Rio Claro. 200 p. e apêndices.

Neves, B. B. de B.; Albuquerque, J. do P. T., 2004, Tectônica e Água Subterrânea em Rochas Pré-Cambrianas do Nordeste do Brasil - A Diversidade do Sistema Aqüífero. Revista do Instituto de Geociências – USP - 71 - Geol. USP, Sér. Cient., São Paulo, v. 4, n. 2, p. 71-90.

Oliveira, M. L. de, 1997, Análise das Incertezas Envolvidas na Modelagem de Reservatórios no Contexto Geoestatístico. Dissertação de Mestrado. UNICAMP, Campinas, São Paulo. 116 p.

Oliveira, R. G. de;.Souza Filho, O. A de; Ribeiro, J. A; Oliveira, J. F. de; Veríssimo, L. S., 2002, Área-Piloto do Juá - Interpretação e correlação geológica dos dados geofísicos. CPRM/ Projeto Água Subterrânea no Nordeste do Brasil – PROASNE. Relatório Interno. Fortaleza. 35 p. il.

Olofson B., 1994, Flow of Groundwater from soil to Crystalline Rocks. Applied Hydrogeology, v. 2, n. 3, p. 71-83.

Palacky, G. J., 1991, Resisitivity Characteristics of Geologic Targets. *In*: Electromagnetic Methods in Applied Geophysics. Vol. 1 – Theory. Ed. Nabighian. M. N. Society of Exploration Geophysicists. Series: Investigations in Geophysics, No. 3. Tulsa, U.S., p. 53-129.

Paterson, N. R.; Reford, W.W., 1986, Inversion of airborne electromagnetic data for overburden mapping and groundwater exploration. In: Palacky, G. J., ed., Airborne resistivity mapping: Geological Survey of Canada Paper, p. 39-48.

Perrotta, M. M., 1996, Potencial Aurífero de uma Região no Vale do Ribeira, São Paulo, Estimado por Modelagem de Dados Geológicos, Geoquímicos, Geofísicos e de Sensores Remotos num Sistema de Informações Geográficas. Tese de Doutoramento, Universidade de São Paulo, São Paulo, 156 p. il.

Perrotta, M. M.; Salvador, E. D., 2006, Avaliação regional do potencial de produtividade de aqüíferos cristalinos em um sistema de informações geográficas (SIG) In: FRANCA-ROCHA, W. et al. (ed): Geotecnologias: trilhando novos caminhos nas geociências. 1 ed. Salvador : SBG-Núcleo Bahia-Sergipe, 2006, p.123-135.

Phillips, J.D., 1997, Potential-Field geophysical software for the PC, version 2.2: U.S. Geological Survey Open-File Report 97-725, 34 p.

Phillips, J.D., 2007, Geosoft eXecutables (GX's) developed by the U.S. Geological Survey, version 2.0, with notes on GX development from Fortran code: U.S. Geological Survey Open-File Report 2007-1355.

Phillips, J.D., Duval, J.S.; Saltus, R.W., 2003, Geosoft eXecutables (GXs) developed by the U.S. Geological Survey, version 1.0, with a viewgraph tutorial on GX development: U.S. Geological Survey Open-File Report 03-101, 22 p. Available in http://pubs.usgs.gov/products/books/openfile/2003.html.

Pine, J. G.; Minty, B. R. S., 2005, Airborne Hydrogeophysics. In: Hydrogeophysics, Edited by Rubin Y. and Hubbard, S. S. Ed. Springer. The Netherlands. p. 333-360.

Pinéo, T. R. G., 2005, Integração de Dados Geofísicos, Geológicos e de Sensores Remotos Aplicados à Prospecção de Água Subterrânea em Meio Fissural (Distrito de Juá, Irauçuba/CE). Dissertação de Mestrado. Universidade Federal do Ceará. Fortaleza, Brasil. 126 p. il.

PROASNE – Projeto Água Subterrânea no Nordeste do Brasil, http://proasne.net , acessado em julho/2007.

Rabus B.; Eineder, M.; Roth, A.; Bamler R., 2003, The Shuttle Radar Topography Mission – a new class of digital elevation models acquired by spaceborne radar. ISPRS journal of Photogrammetry & Remote Sensing. Elsevier Ed., n. 57, p. 241-262.

Raines, G.L., 1999, Evaluation of weights of evidence to predict epithermal-gold deposits in the Great Basin of the western United States: Natural Resources Research, v. 8, no. 4, p. 257-276.

Remacre, A. Z., 1999, Introdução a Funções Aleatórias. Instituto de Geociências/UNICAMP. Campinas, 23 p. il.

Ribeiro, J. A., Feitosa. F. A. C., Oliveira, J. F. de, Souza Filho, O. A., Feitosa, E. C., 2003, Zonas (eixos) Condutivas em Rochas Cristalinas na Região de Irauçuba, Norte do Estado do Ceará, Brasil. Revista Águas Subterrâneas. N.17. Curitiba. ABAS. 113-124.

Rubin, Y; Hubbard, S. S., 2005 (eds.), Hydrogephysics, Springler Ed., The Netherlands, 2005. 523 p. il.

Sabine, C., 1999, Remote Sensing Strategies for Mineral Exploration, Chapter 8. In: Rencz, A.N. (ed.) Remote Sensing for the Earth Sciences. Manual of Remote Sensing, 3rd edition, ASPRS/John Wiley & Sons, volume 3, p. 375-448

Sabins, F. F., 1997, Remote Sensing: Principles and interpretation. 3rd edition, W. H. Freeman and Company, New York, 494 p. il.

Santos, A. C., 2000, Noções de Hidroquímica. In Feitosa, F. A. C. & Manoel Filho, J. (ed) Hidrogeologia – Conceitos e Aplicações. 2ª. ed. CPRM/REFO, LABHID-UFPE, Fortaleza, Brazil. p.81-107.

Santos, T. J. S. dos. 2002. Tectônica frágil da região de Irauçuba, Ceará . Relatório Interno de Consultoria. CPRM. Fortaleza. 7 p. il.

Sattel, D.; Kgotlhand, L., 2003, Modelling Aquifer Structures with Airborne EM in the Boteti Area, Botswana. Proceedings of Symposium on the Application of Geophysics to Engineering and Environmental Problems, San Antonio, Tx, U.S.A.

Sawatzky, D. L.; Raines, G. L.; Bonham-Carter, G. F.; Looney, C. G., 2008, Spatial Data Modeler (SDM): ArcMAP geoprocessing tools for spatial data modelling using weights of evidence, logistic regression, fuzzy logic and neural network. Available in http://www.ige.unicamp.br/sdm/default_e.htm.

SGU- Sveriges geologiska undersökning, 2007, available at http://www.sgu.se/sgu/en/.

Silva, A. M., 1999, Integração de Dados Geológicos e Geofísicos utilizando-se uma nova técnica estatística para a seleção de alvos para exploração mineral, aplicada ao Greenstone Belt Rio das Velhas, Quadrilátero Ferrífero. Tese de Doutoramento. Universidade de Brasília, Brasília. 195 p.

Silva, C. M.S. V., Vasconcelos, M. B., Santiago, M. M. F., 2001, Recarga e datação de poços no cristalino. In: IV Simpósio de Hidrogeologia do Nordeste, 2001, Recife. Anais do IV Simpósio de Hidrogeologia do Nordeste. : ABAS (ed). São Paulo. pp 8-14.

Silva, C. M. S.V.; Demétrio, J. G. A.; Santiago, M. M. F.; Vasconcelos, M. B.; Feitosa, F. A. C., 2003, Perfis verticais de temperatura no estudo de conexões entre açude e poços no cristalino (temperature bore log in the study of conections between reservoirs and drilled wells in the crystalline domain). In: XV Simpósio Brasileiro de Recursos Hídricos, 2003, Curitiba. Anais do XV Simpósio Brasileiro de Recursos Hídricos. CD-Rom.

Smith, B. D.; Bisdorf, R.; Slack, L. J.; Mazella, A. T., 1997, Evaluation of Electromagnetic Mapping Methods to Delineate Subsurface Saline Waters in the Brookhaven Oil Field, Mississipi. Proceedings of the Symposium on the Application of Geophysics to Engineering and Environmental Problems, Reno, Nevada, U.S.A., pp 685-693.

Smith, B.D.; McCafferty, A.E.; McDougal, R. R., 2000, Utilization of airborne magnetic, electromagnetic, and radiometric data in abandoned mine land investigations: Reston, VA, U.S.A., U.S. Geological Survey Open-File Report OFR-00-0034, p. 86-91.

Souza Filho, O. A. de., 1998, Geologia e Mapa de Previsão de Ocorrência de Água Subterrânea. Folha SA.24-Y-D-V Irauçuba, Ceará. Dissertação de Mestrado. Universidade Federal de Ouro Preto, Brasil. Ouro Preto 99 p. il. e mapas.

Souza Filho, O. A. de, 2000, Programa Levantamentos Geológicos Básicos do Brasil – Projeto Mapa de Previsão de Recursos Hídricos Subterrâneos, Folha SA.24-Y-D-V – Irauçuba. CPRM - Serviço Geológico do Brasil, Residência de Fortaleza. Fortaleza. 50 p. il.

Souza Filho, O. A. de., 2002, Integração de Geologia Estrutural, Geotecnia e Geoprocessamento em Aquíferos Fissurais. Irauçuba – CE, Nordeste do Brasil. XXXII Congresso da Associação Internacional de Hidrogeologia e VI Congresso da Associação Latino-Americana de Hidrologia Subterrânea. Mar Del Plata, Argentina. CD-Rom, p. 1080-1089.

Souza Filho, O. A. de; Veríssimo, L. S; Feitosa, F. A. C., 2002, Dados lito-estruturais e hidrogeológicos da área de detalhe de Juá - Município de Irauçuba - Estado do Ceará, Brasil . In: Xii Congresso Brasileiro de Águas Subterrâneas, 2002, Florianópolis. Aquíferos Transfronteiriços. Santo Amaro: Novo. Disc, Brasil Indústria Fonográfico.

Souza Filho, O. A. de; Ribeiro, J. A.; Veríssimo, L. S.; Oliveira, R. G. de; Gomes, F. E. M.; Brandão, R. de L.; Frizzo, S. J.; Oliveira, J. F. de, 2003, Projeto Otimização de Metodologias para Prospecção de Águas Subterrâneas em Rochas Cristalinas. Relatório Integrado De Atividades 1999 – 2002 - Bases para avaliação do projeto. CPRM/REFO. Fortaleza. 160 p. il. Anexos.

Souza Filho, O. A. de; Veríssimo, L. S.; Silva, C. M. S. V.; Santiago, M. M. F. 2004, Medidas Hidroquímicas nas Águas Subterrâneas da Região de Irauçuba, Norte do Ceará. In XIII Congresso Brasileiro de Águas Subterrâneas.Cuiabá. Anais, 1 CD-Rom.

Souza Filho, O. A. de; Oliveira, R. G.; Ribeiro, J. A.; Veríssimo, L. S.; Sá, J. U., 2006a, Interpretação e Modelagens de Dados de Eletrorresistividade para Locações de Poços Tubulares no Aqüífero Fissural da Área-Piloto Juá, Irauçuba-Ceará. In: Revista de Geologia, v. 19, n. 1, DEGEO/UFC, p. 7-21.

Souza Filho, O. A. de; Remacre, A. Z.; Silva, A. M.; Sancevero, S. S.; McCafferty, A. E.; Perrotta, M. M. 2006b. Airborne Electromagnetic Data as External Variable to Predict Groundwater Electrical Conductivity in the Crystalline Domain of Irauçuba Region – Ceará, Brazil. 2006b Hydrogeophysics Symposium, Vancouver. Society of Exploration Geophysicists, Tulsa, abstracts.

Souza Filho, O. A. de; McCafferty, A. E.; Silva, A. M.; Perrotta, M. M., 2007a, Groundwater Potential: A Predictive Model from Airborne Geophysical, Radiometric and Remote Sensing Data, Ceará, Brazil. In: Simpósio Brasileiro de Sensoriamento Remoto (SBSR), 13., Florianópolis. Anais... São José dos Campos: INPE, 2007a, p. 3593-3595. CD-ROM. ISBN 978-85-17-00031-7.

Souza Filho, O. A. fe; Silva, A. M.; Mccafferty, A. E.; Perrotta, M. M.; Deszczpan, M.; Fitterman, D., 2007b, Geophysical properties associated to Juá District geology, Ceará, Brazil. 10o Congresso Internacional da Sociedade Brasileira de Geofísica, SBGf, Rio de Janeiro, RJ, Brasil.CD-Rom.

Speed, R., 2002, Airborne Geophysics for Catchment Management – Why and Where. Exploration Geophysics, v.33, p. 51-56.

Steensma, G.; Kellett, R. Short course: applications of geophysics in groundwater studies. Komex International Ltd.; Geological Survey of Canada, Natal-RN, Brasil, 2000.

Street, G. J.; Pracillio, G.; Anderson-Mayes, A., 2002, Interpretation of geophysical data for salt hazard identification and catchment management in Southwest Western Australia. Exploration Geophysics, v.33, p. 65-72.

Syberg, F.J.R., 1972, A Fourier method for the regional-residual problem of potential fields: Geophysical Prospecting, v.20, p.47-75. In: Phillips, J.D., 1997, Potential-Field geophysical software for the PC, version 2.2: U.S. Geological Survey Open-File Report 97-725, 34 p.

Taylor, M. J.; Smettem, K.; Pracillio, G.; Verboom, W., 2002, Relationships between soil properties and high-resolution radiometrics, Central Eastern Wheatbelt, Western Australia. Exploration Geophysics, v.33, p. 95-102.

Teixeira, A. de A, 2003, Integração de Dados Multifontes para Exploração de Ouro no *Greenstone Belt* Rio das Velhas, Quadrilátero Ferrífero, Mg. Dissertação de Mestrado. Universidade de Brasília, Brasília. 195 p.

Telford, W. M., Geldart, L. P., Sheriff, R.E., and Keys, D.A., 1984, Applied Geophysics, Cambridge University Press. New York, U. S. Chapters 7 and 8, p. 500-700.

United States Salinity Laboratory Staff. 1954. Diagnosis and improvement of saline and alkai soils. USDA Handbook. 60. U.S. Gov. Print. Office, Washington, D.C. In: Souza Filho, O. A. de *et al.*, 2003, Projeto Otimização de Metodologias para Prospecção de Águas Subterrâneas em Rochas Cristalinas. Relatório Integrado De Atividades 1999 – 2002 - Bases para avaliação do projeto. CPRM/REFO. Fortaleza. 160 p. il. Anexos.

Veríssimo, L. S.; Feitosa, F. A. C., 2000, Cooperação Técnica Canadá–Brasil, 1a Missão de Geofísica do Estado do Ceará. Relatório de Atividades - Programa de Água Subterrânea para a Região Nordeste. Org. por Veríssimo, L. S.; Feitosa, F. A. C., CPRM-Serviço Geológico do Brasil, Fortaleza. 24 p. il.

Veríssimo, L. S.; Feitosa, F., A.. C. 2002, As Águas Subterrâneas no Nordeste do Brasil. Região de Irauçuba - Estado do Ceará, Brasil. XXXII Congresso da Associação Internacional de Hidrogeologia e VI Congresso da Associação Latino-Americana de Hidrologia Subterrânea. Mar Del Plata, Argentina. CD-Rom, p. 889-896.

Wackernagel, H., 1995, External Drift. In: Multivariate Geostatistics - An Itroduction with Applications. Springer-Verlag Editora, Berlin. p. 190-200.

Wilkinson, K.; Chamberlain, T.; Grundy, M. 2005 – The Role of Geophysics in Understanding Salinisation in Southwestern Queensland. Exploration Geophysics, v. 36, p. 78-85.

Won, I. J.; Huang H., 2004, Magnetometers and electro-magnetometers. The Leading Edge, 2004. Geophex Tutorial available in http://www.geophex.com/Publications/mag%20emag.pdf. Acessado em Junho de 2007.

Wright, D.F.; Bonham-Carter, G.F., 1996, VHMS Favourability Mapping with GIS-based Integration Models, Chisel Lake-Anderson Lake area: In EXTECH I: A Multidisciplinary Approach to Massive Sulphide Research in the Rusty Lake-Snow Lake Greenstone Belts, Manitoba, Eds. G.F. Bonham-Carter, A.G. Galley and G.E.M. Hall, Geological Survey of Canada, Bulletin 426, p. 339-376, 387-401.

ANEXO 1 - Conceitos Teóricos

Mapa Pseudo-Gravimétrico = transformação por transformada de Fourier do dado magnético (componente vertical) em propriedades gravimétricas (densidade) partindo do teorema de Poisson que relaciona os campos potenciais magnéticos e gravimétricos aplicados sobre um ponto (p). Segue o princípio de que as anomalias magnéticas sobre as fontes causadoras podem ser transformadas em anomalias gravimétricas que seriam esperadas, caso a distribuição de magnetização e densidade sejam iguais (Baranov, 1957 in Phillips *et al,* 2002). Ou seja, admite-se um modelo de camada semi-infinita homogênea, localizada no pólo magnético de forma que a anomalia magnética esteja sobre a fonte causadora que possui anomalia gravimétrica equivalente. (Modificado de Ward, 1992; Blum, 1999).

$$V_{(p)} = (J / G\sigma)^{*} (\partial U_{(p)} / \partial m)\text{, onde:}$$

$V_{(p)}$ = potencial magnético, J = magnetização, m = direção de magnetização
$U_{(p)}$ = potencial gravimétrico, G = constante gravitacional, σ = densidade no ponto

Nessa equação apenas corpos magnéticos contribuem para o cálculo. Os resultados não são propriedades verdadeiramente gravimétricas, pois corpos não magnéticos também influenciam no campo gravimétrico, por isso os valores resultantes são chamadas de pseudo-gravimétricos. Por causa desse aspecto, alguns autores preferem a denominação de Unidades de Potencial Magnético (Anne McCafferty, comunicação pessoal). Essa técnica é preparatória para o cálculo do gradiente horizontal da anomalia magnética que delimita as extremidades de corpos anômalos.

Técnica de Terraceamento em Geofísica (Cordell e McCafferty, 1989) = operador matemático aplicado sobre dados de campos potenciais gravimétricos e magnéticos que transforma uma função de uma curva em terraço (patamares). Parte do princípio de que a curvatura do campo potencial local pode ser representada por domínios uniformes, separados por domínios abruptos.

Uma janela de operação nos valores, incrementando ou diminuindo, tentando aproximar cada anomalia a forma de terraço verificando o sinal da curvatura do campo local da função através da segunda derivada vertical avaliada no ponto central. São feitos ajustes sucessivos até que seja alcançado o efeito de terraço (Cordell e McCafferty, 1989; Blum,1999). Os resultados não são valores gravimétricos ou de magnetização, mas deve ser entendido como um modelo de propriedades físicas equivalentes. Auxiliam na interpretação, pois se assemelham a mapas geológicos com contatos bruscos.

$$C_i = \frac{f_{i+1} + f_{i-1} - 2f_i}{\Delta x^2}$$

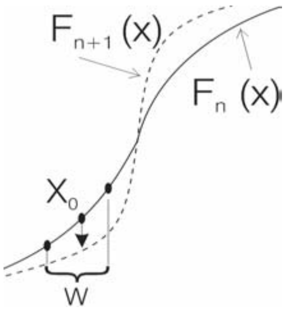

, onde: Ci = curvatura do campo; Δx é o intervalo de amostragem; f_{i+1} e f_{i-1} são os valores anterior e posterior ao valor central fi .

Os dados magnéticos devem ser reduzidos ao pólo e transformados para mapa mapas de potencial magnético previamente ao terraceamento para posicionar matematicamente as anomalias sobre as fontes causadoras.

Aquisição pelo Método Eletromagnético-EM

O método presume que um corpo condutivo ao ser induzido por um campo eletromagnético externo (primário - Hp) produz um campo eletromagnético secundário (Hs), cuja intensidade é proporcional as suas propriedades (condutividade elétrica, permissividade dielétrica e permeabilidade magnética) e ao campo primário. Tanto a altura de vôo como a freqüência influenciam no sinal recebido, porém admite-se que sejam constantes durante o levantamento.

O sistema EM aeroportado ou terrestre possui uma bobina transmissora que emite um campo primário e uma receptora que recebe tanto o campo magnético primário e o campo resultante da indução do corpo condutor em subsuperfície. As bobinas podem ter várias configurações, as mais comuns são com posicionamentos horizontais (coplanares) e verticais (coaxiais). Os dados EM provêm das razões entre as leituras de Hp e Hs na bobina receptora e é expressa pela fórmula (Ward e Hohmann, 1988, in Won e Huang, 2004):

$$T \equiv \frac{H_s}{H_p} = c\int_0^{\infty} \frac{u-\lambda}{u+\lambda}\lambda^n e^{-2\lambda h} J_k(\lambda r)\,d\lambda\,; \quad u = \frac{\mu_0}{\mu}\sqrt{\lambda^2 + i\omega\mu\sigma}$$

onde,

h = altura do sensor ; ω = freqüência angular (2π *f*); J_k função de Bessel de ordem K (K = 1, para configurações de bobinas coplanares); μ_0 = permeabilidade magnética no ar ($4\pi 10^{-7}$ N*A^{-2} e $\mu = \mu_0 (1 + k)$ a permeabilidade magnética do corpo; k = susceptibilidade magnética do corpo-desprezível para corpos pouco ou não magnéticos); $c = r^3$; n = 1 e r = espaçamento entre as bobinas

T = número complexo que multiplicado por 10^6 corresponde às leituras em ppm dos canais de fase e quadratura do banco de dados do levantamento fornecidos pela empresa executora do levantamento.

A aquisição geofísica por helicóptero com os sistemas EM estão mostradas na figura (Steensma e Kellet, 2000 *in* Oliveira, 2002).

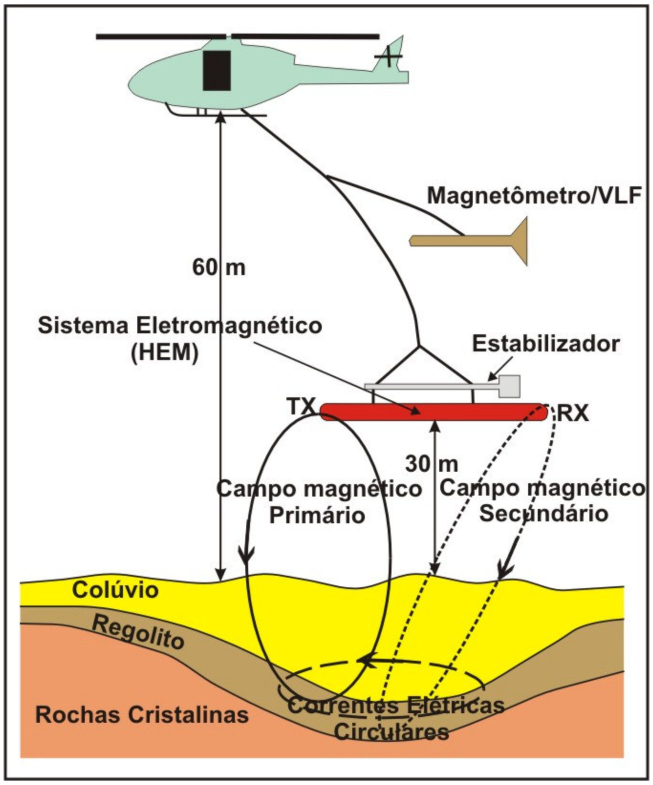

Desenho do levantamento por helicóptero, com aquisição simultânea de dados geofísicos com os sistemas eletromagnéico, magnético e Very Low Frequence.

Condutividade Elétrica Aparente

Corresponde aos valores de condutividade camada semi-infinita homogênea (hipotética) produziria se fosse induzida pelo mesmo campo eletromagnético e freqüência. É uma medida referencial a um intervalo de camada rochosa ou solo, não sendo necessariamente a média das condutividades em cada posição resultante da passagem do campo primário e desconsidera qualquer anisotropia nessa camada (estruturas, fácies, etc.). Os valores de condutividade aparente são freqüentemente apresentados na forma de mapas. Pine e Minty (2005) apresentam a fórmula para o cálculo:

$$\sigma_{app} = 4\,[Hs / Hp]^{Q} / (\omega\,\mu_0\,r^2) \text{ onde, } \sigma_{app} = \text{condutividade aparente (mS/m)}$$

$[\ ]^Q$ refere-se ao valor da componente de quadratura; ω = freqüência angular ($2\pi f$); f = cada uma das freqüências de aquisição; μ_0 = permeabilidade magnética no ar; r = espaçamento entre as bobinas horizontais

A figura abaixo apresenta os intervalos de condutividade elétrica para materiais rochosos e sedimentos. (Palacky, 1991; Fugro, 2005).

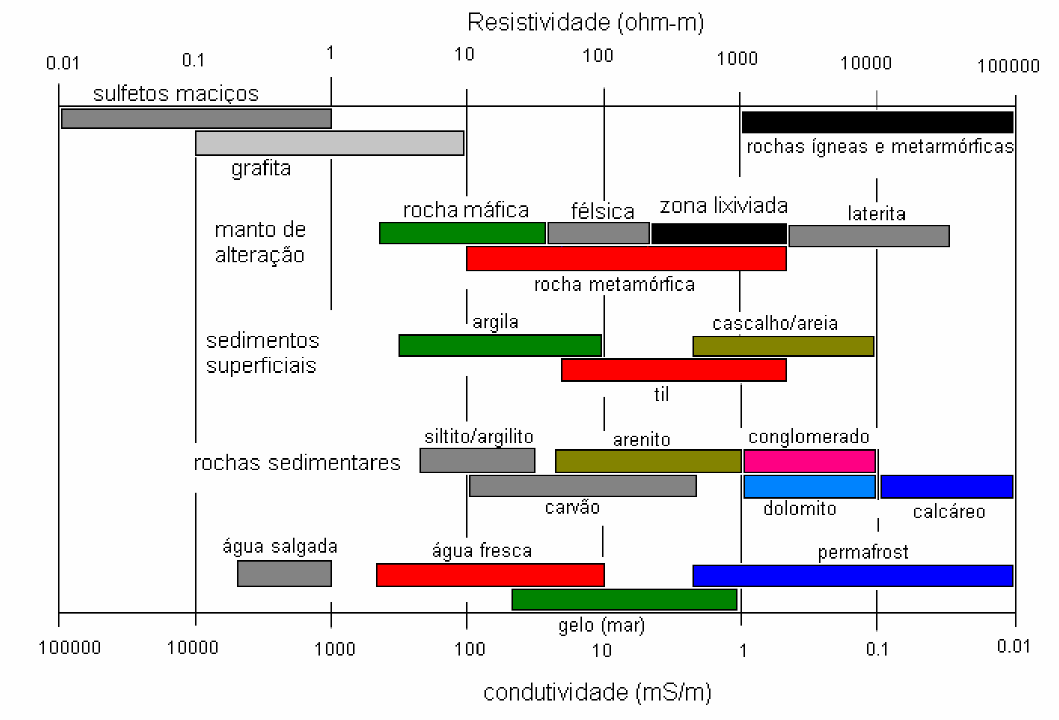

Intervalos de condutividade elétrica para materiais rochosos e sedimentos (Palacky, 1991)

Profundidade de Investigação dos Sensores Eletromagnéticos = A profundidade de investigação diminui tanto com o aumento da freqüência transmitida pelo sensor, bem como pela condutividade do terreno. Ela é aproximada pelo *skin depth,* que é a profundidade em que a força gerada pelo campo primário é reduzida a 1/e vezes ou 37% do seu valor original, de acordo com a equação (Telford *et al.*, 1984):

$\delta = 503\sqrt{\rho / f}$ ou $15.681\sqrt{1/\sigma f}$, onde δ = profundidade de investigação; ρ = resistividade elétrica (ohm-m); σ = condutividade elétrica (mS/m); f = freqüência do sensor EM (hertz)

Para o levantamento do Juá, o executor do levantamento (Lasa, 2001) estimou em 40 m o alcance do sensor EM utilizando a freqüência nominal de 4500 Hz. Todavia pode variar entre 10 m para locais extremamente condutivos (400 mS/m), como leitos argilosos no riacho principal São Gabriel e até 70 m em sobre rochas sãs e provavelmente não fraturadas (10 mS/m).

Deriva Externa na Geoestatística = O conceito de deriva externa pressupõe uma ou mais variáveis secundárias cujas medidas relacionam-se ao mesmo fenômeno natural da variável principal a ser estudada (existe uma relação física entre elas). Os parâmetros espaciais estatísticos da variável secundária (com maior taxa de amostragem) são usados para auxiliar na modelagem da variabilidade da variável principal, tornando-se mais importante nos locais não amostradas por essa.

O conceito de deriva externa é definido em Deutsch e Journel (1992) e Wackernagel (1995). Oliveira (1997) estudou a aplicabilidade e limitações dessa modalidade na análise de reservatórios petrolíferos no Brasil.

A **krigagem com Deriva Externa** é uma extensão da krigagem universal, onde a informação de uma ou mais funções de variáveis externas são integradas ao processo de krigagem da variável primária. O domínio espacial de ambas as variáveis deve ser o mesmo.

Em Oliveira (1997), "...Admitindo a existência de apenas uma variável secundária e assumindo o modelo de deriva do tipo E (Z (x)) = $a_o + a_1 s(x)$, o sistema da KDE pode ser escrito como:

$$\left\{\begin{array}{ll} n & \\ \sum \quad \lambda j (x0)CY(xi - xj) + \mu 0 (x0) + \mu 1 (x0)s(xi) = CY(xi - x0) \ \ j=1 & \\ \forall i = 1,2,...,n & \textbf{eq. (1)} \\ n & \\ \sum \lambda j (x0) = 1 & \textbf{eq. (2)} \\ j=1 & \\ n & \\ \sum \lambda j (x0)s(x j) = s(x0).... & \textbf{eq. (3)} \\ j=1 & \end{array}\right.$$

Sendo:
λ = peso para cada ponto j estimado em relação a i; μ, multiplicador de Lagrange;
eq.(1) - função aleatória de segunda ordem da variável primária,
eq.(2) – função que atesta a somatória dos pesos igual à unidade,
eq.(3) -função da variável secundária que descreve uma forma/superfície média para a variável primária,

Tendo a variância de estimativa para a situação do sistema **eqs**. **(1)** escrita na **eq**. **(4)**

$$\sigma^2_{KDE}(x_0) = C_\gamma(0) - \sum_{i=1}^{n} \lambda_i(x_0)C_\gamma(x_i - x_0) - \mu_0(x_0) - \mu_1(x_0)s(x_0) \quad \textbf{eq.(4)}...".$$

A **simulação estocástica** que gera parâmetros de campo que simulam padrões naturais de variabilidade espacial. No processo estocástico são apresentadas várias realizações da distribuição espacial do atributo (condutividade elétrica) num comportamento consistente com o dado amostrado. O processo envolve o conceito de função aleatória e permite também o uso de deriva externa para auxiliar na caracterização de variáveis de comportamento não-estacionário.

Aplica-se muito bem aos estudos em geociências (Gómez-Hernández, 2005; Remacre 1999), principalmente quando a variabilidade de um fenômeno não puder ser estimada em posições não amostradas, através de interpolação tradicional com poucos pontos amostrados (krigagem universal, razão do inverso do quadrado da distância...), a exemplo de meios não contínuos como no cristalino fraturado.

Os parâmetros não-estacionários como a deriva externa foi aplicada aos métodos de interpolação porquê a extrema variabilidade da condutividade elétrica da água, tão comum no domínio cristalino do Nordeste do Brasil - ver Manoel Filho (1996), não pode ser determinada em locais sem amostragem e tão pouco é exclusivamente aleatória. Para acessar essa heterogeneidade, assumimos como premissa que os dados HEM estavam relacionados à condutividade elétrica da água, pois a presença de água é um dos principais fatores da condutividade do solo ou rocha. Por possuir maior amostragem que os valores obtidos nos quinze poços da área do Juá, os dados HEM enfatizariam a variabilidade da condutividade elétrica da água subterrânea.

ANNEX 2 – Probability Ratio Maps of Geophysical, Structural and Alteration Mineral Evidences Associated with Groundwater Potential

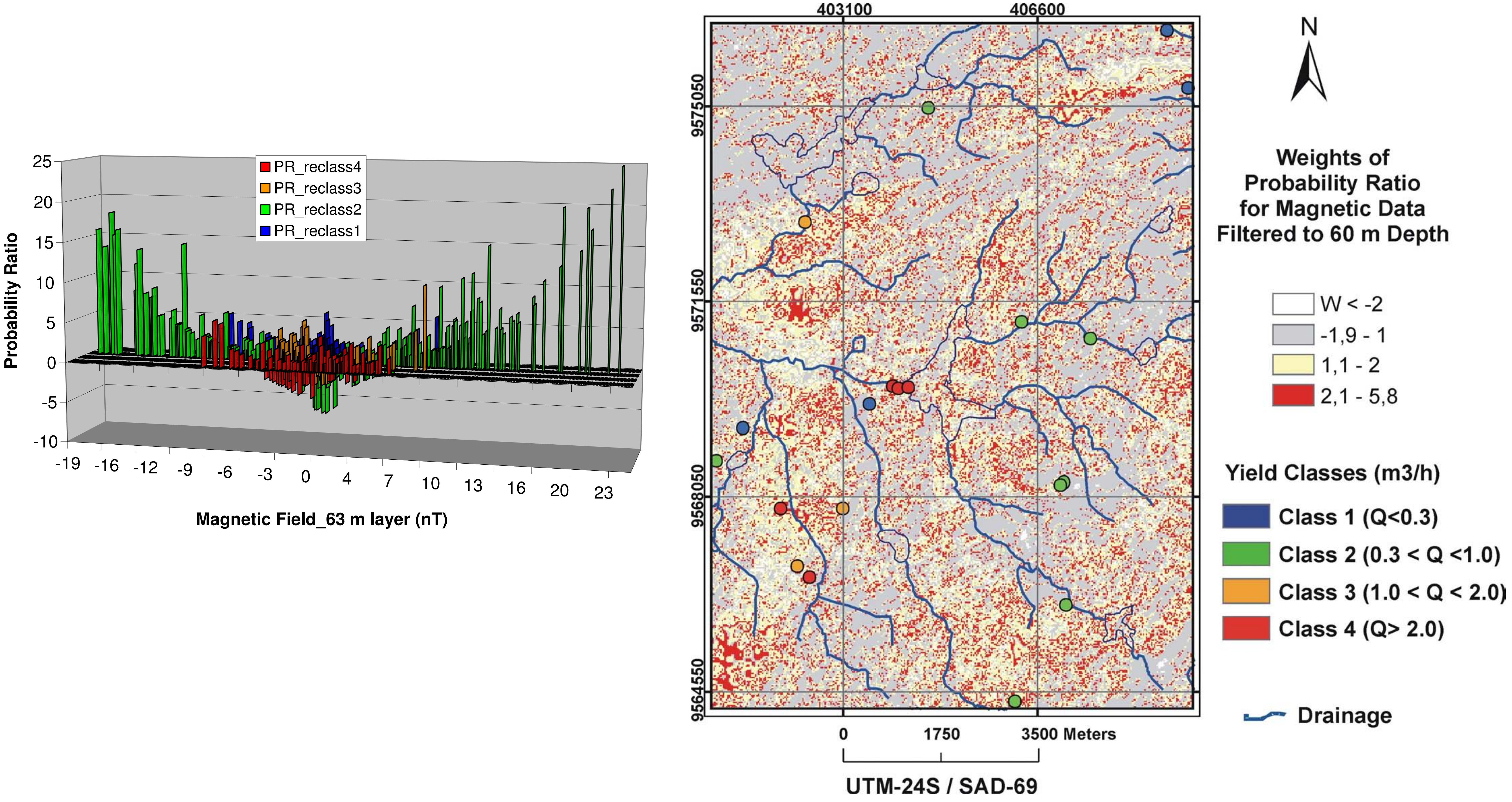

Annex 2.1 – Weights of probability ratio referred to the spatial association between magnetic the field down to 60 m –depth and well yield classes for the Juá area: a) Full-range values of probability ratio as a chart representation; b) Map representation of reclassified values of probability ratio relative to the yield class 4. Negative values are the reciprocal negative of original values range from 0 to 0.99.

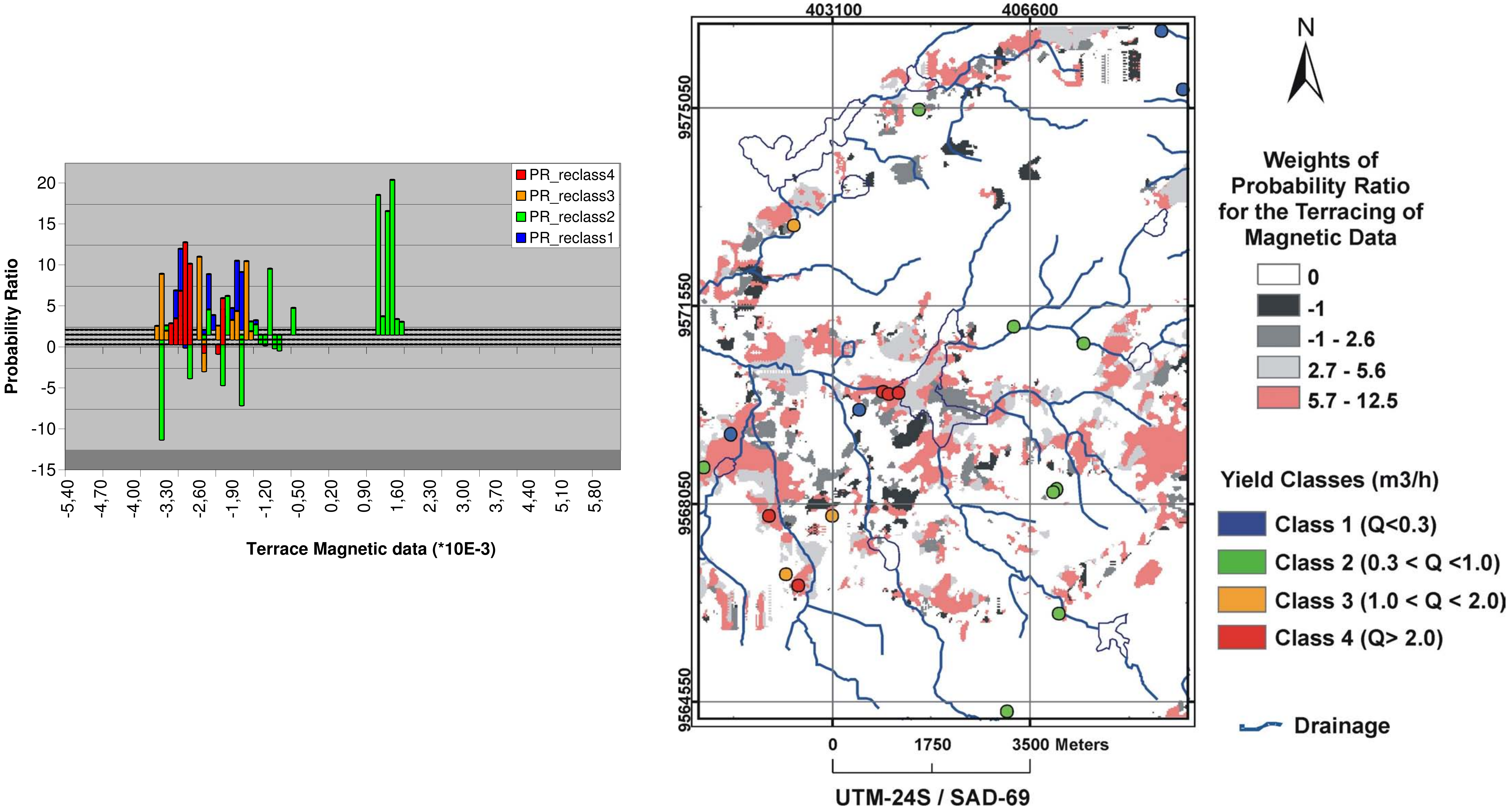

Annex 2.2 – Weights of probability ratio referred to the spatial association between the terracing of magnetic data and well yield classes for the Juá area: a) Full-range values of probability ratio as a chart representation; b) Map representation of reclassified values of probability ratio relative to the yield class 4. Negative values are the reciprocal negative of original values range from 0 to 0.99.

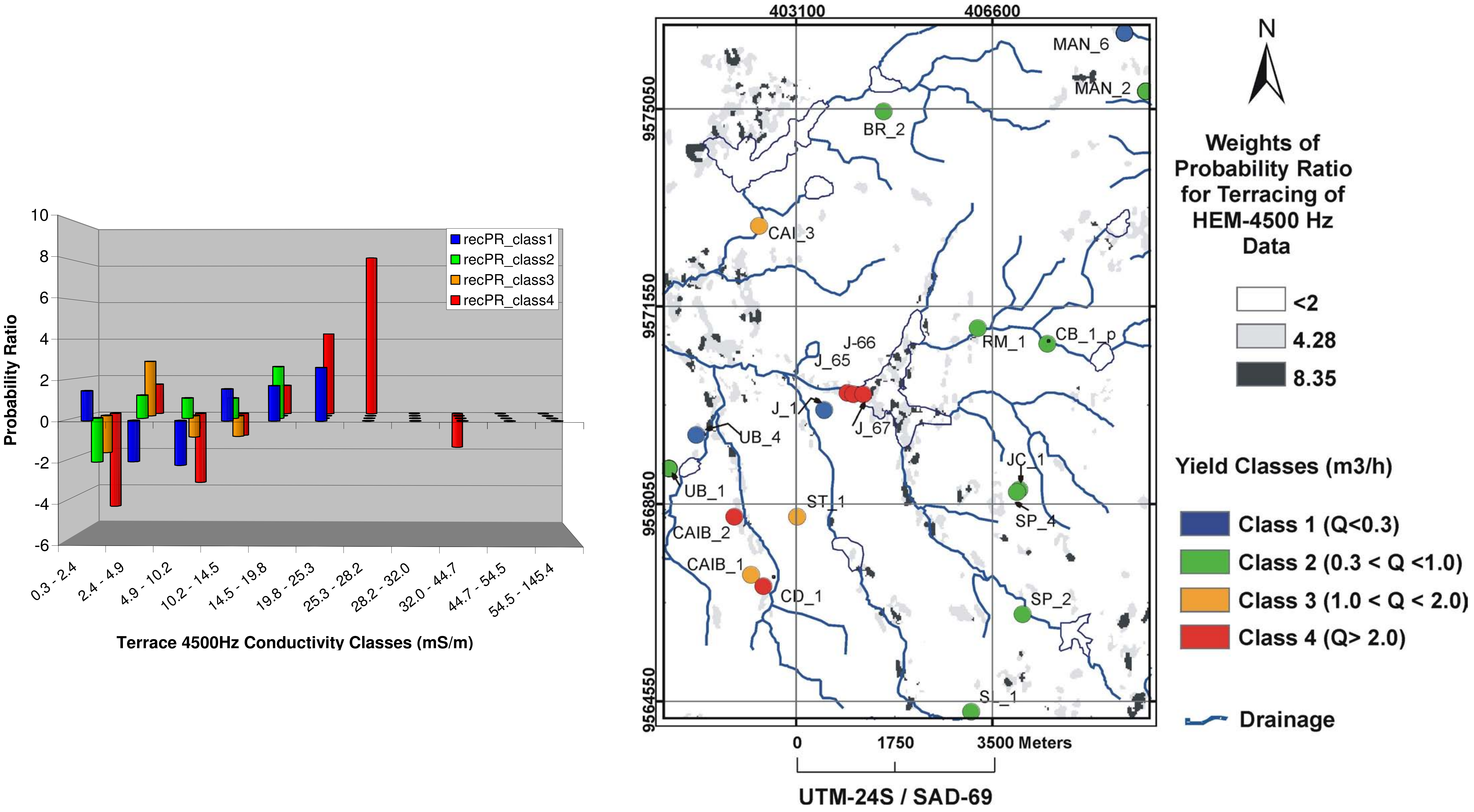

Annex 2.3 – Weights of probability ratio referred to the spatial association between the terracing of electrical conductivity and well yield classes for the Juá area: a) Full-range values of probability ratio as a chart representation; b) Map representation of reclassified values of probability ratio relative to the yield class 4. Negative values are the reciprocal negative of original values range from 0 to 0.99.

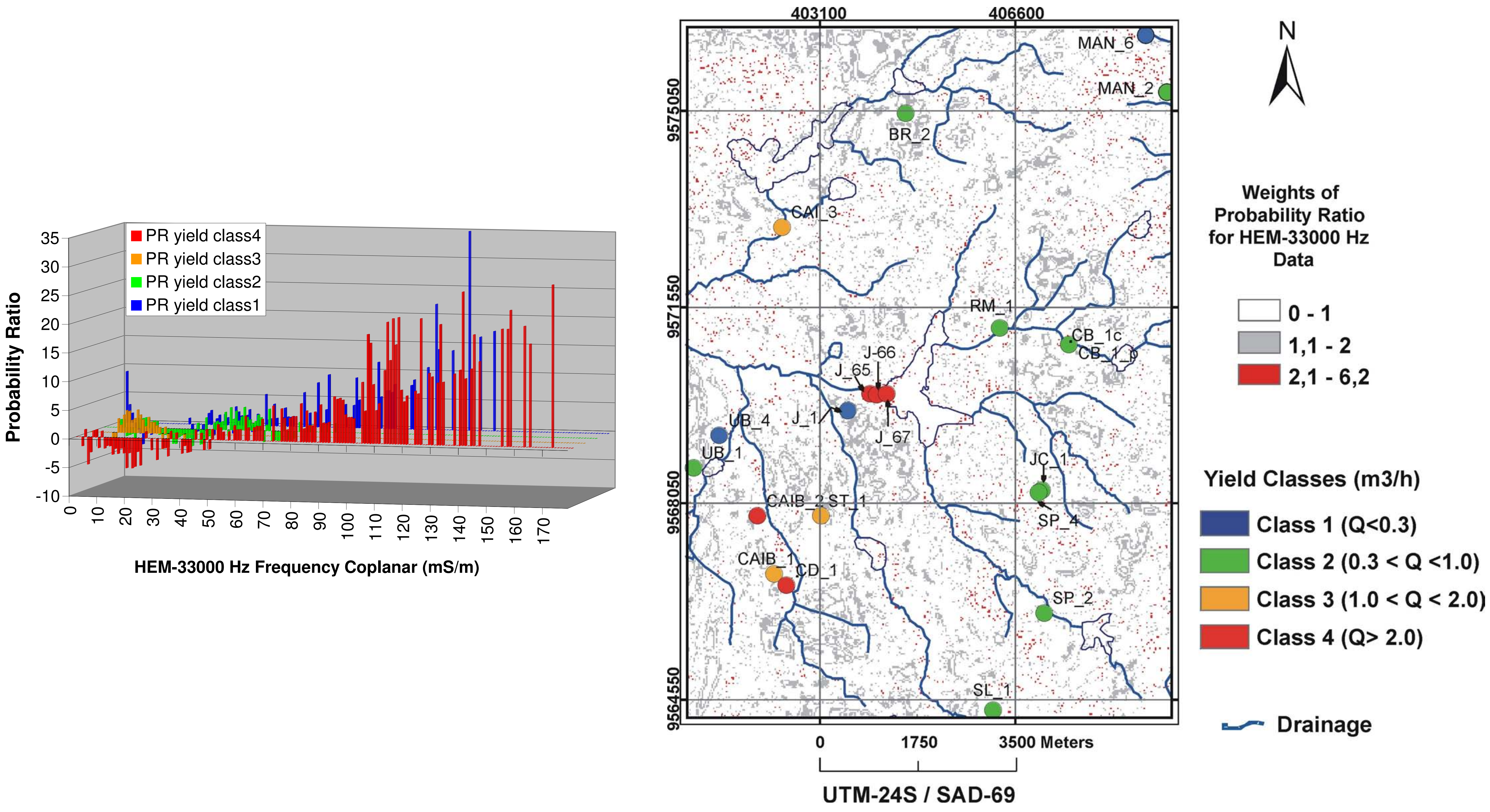

Annex 2.4 – Weights of probability ratio referred to the spatial association between the electrical conductivity from HEM-33000 HZ data and well yield classes for the Juá area: a) Full-range values of probability ratio as a chart representation; b) Map representation of reclassified values of probability ratio relative to the yield class 4. Negative values are the reciprocal negative of original values range from 0 to 0.99.

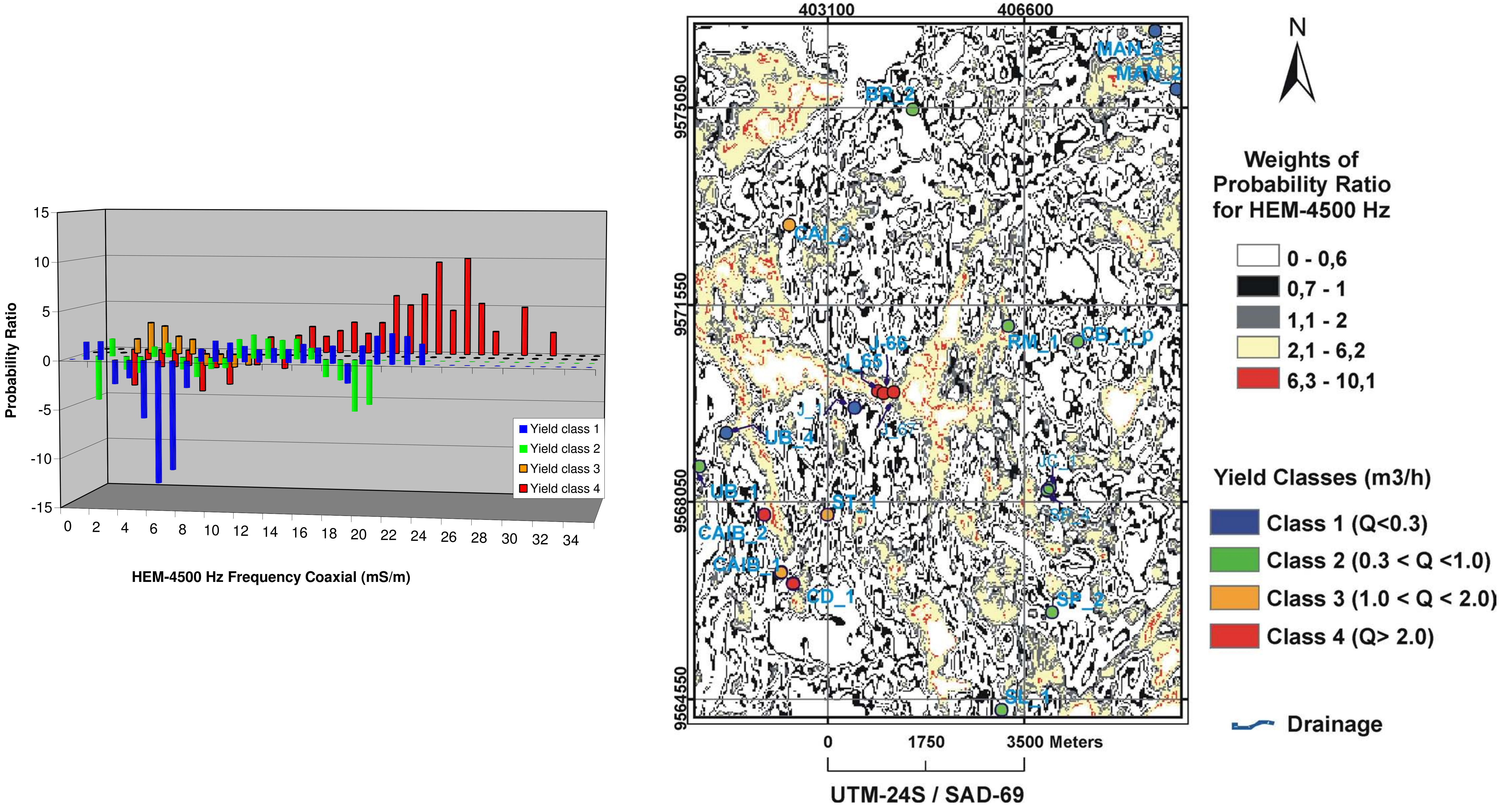

Annex 2.5 – Weights of probability ratio referred to the spatial association between the electrical conductivity from HEM-4500 HZ data and well yield classes for the Juá area: a) Full-range values of probability ratio as a chart representation; b) Map representation of reclassified values of probability ratio relative to the yield class 4. Negative values are the reciprocal negative of original values range from 0 to 0.99.

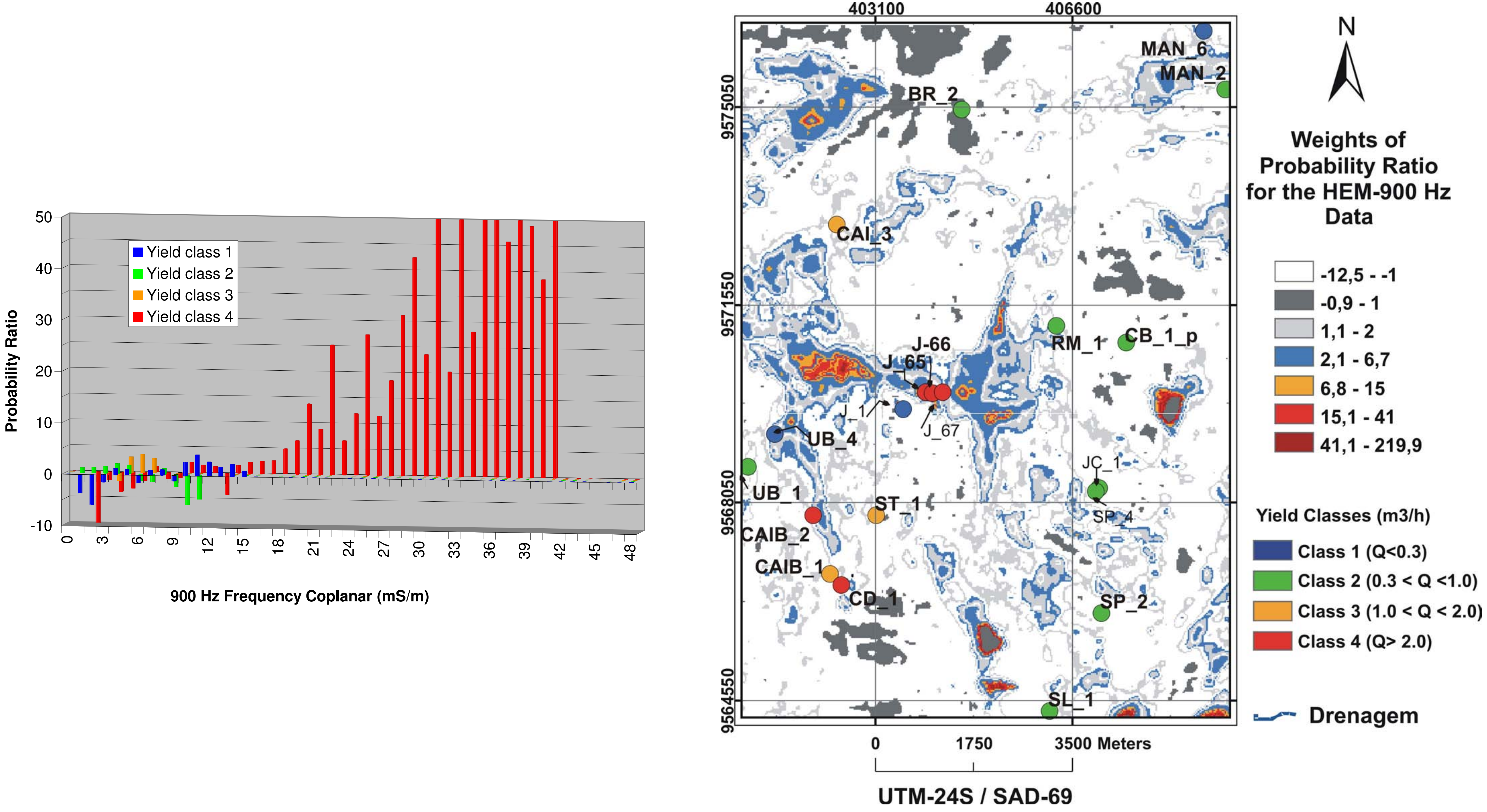

Annex 2.6 – Weights of probability ratio referred to the spatial association between the electrical conductivity from HEM-900 HZ data and well yields classes for the Juá area: a) Full-range values of probability ratio as a chart representation; b) Map representation of reclassified values of probability ratio relative to the yield class 4. Negative values are the reciprocal negative of original values range from 0 to 0.99.

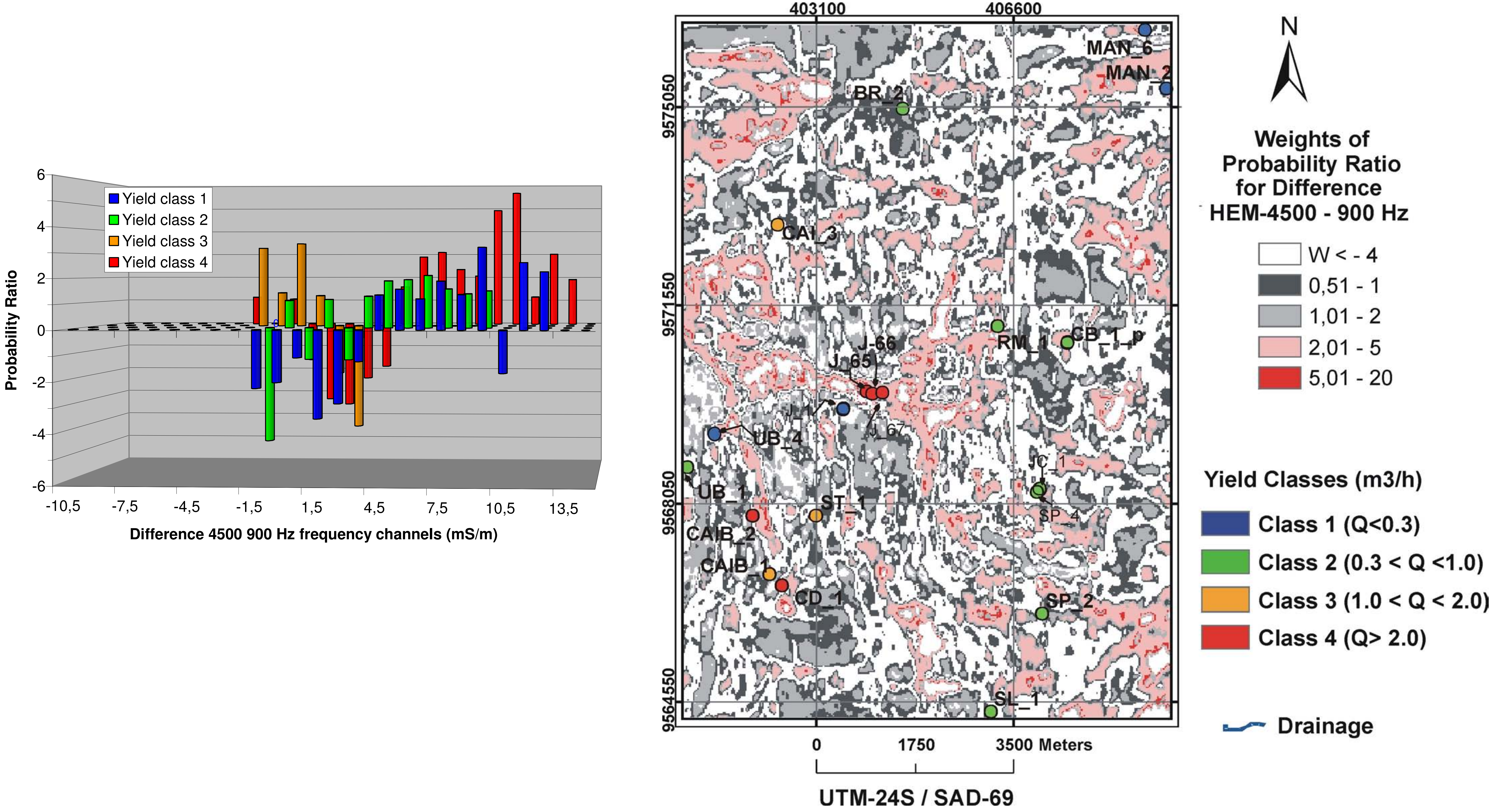

Annex 2.7 – Weights of probability ratio referred to the spatial association between the electrical conductivity from the subtraction of HEM-4500 – HEM-900 HZ data and well yield classes for the Juá area: a) Full-range values of probability ratio as a chart representation; b) Map representation of reclassified values of probability ratio relative to the yield class 4. Negative values are the reciprocal negative of original values range from 0 to 0.99.

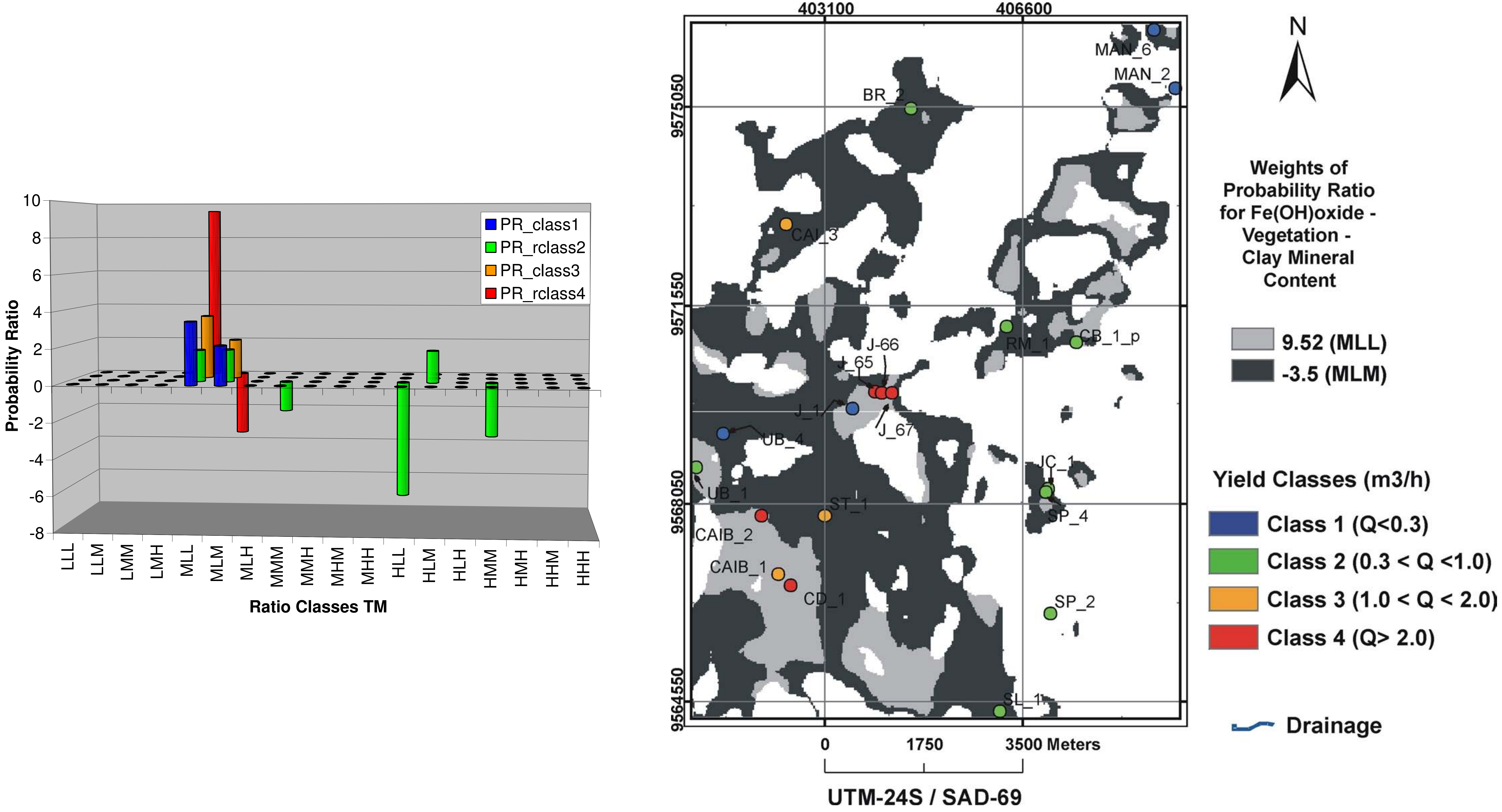

Annex 2.8 – Weights of probability ratio referred to the spatial association between the map of relative contents of Fe-(OH) oxide minerals, vegetation and clay-minerals (a composite-band ratio product of ETM+/Landsat-7 data) and well yield classes for the Juá area. The composite relative content classes are ordered as cited in this caption and in the text and, the letters refer to their relative content: H = high; M = medium; B = low: a) Full-range values of probability ratio as a chart representation; b) Map representation of reclassified values of probability ratio relative to the yield class 4. Negative values are the reciprocal negative of original values range from 0 to 0.99.

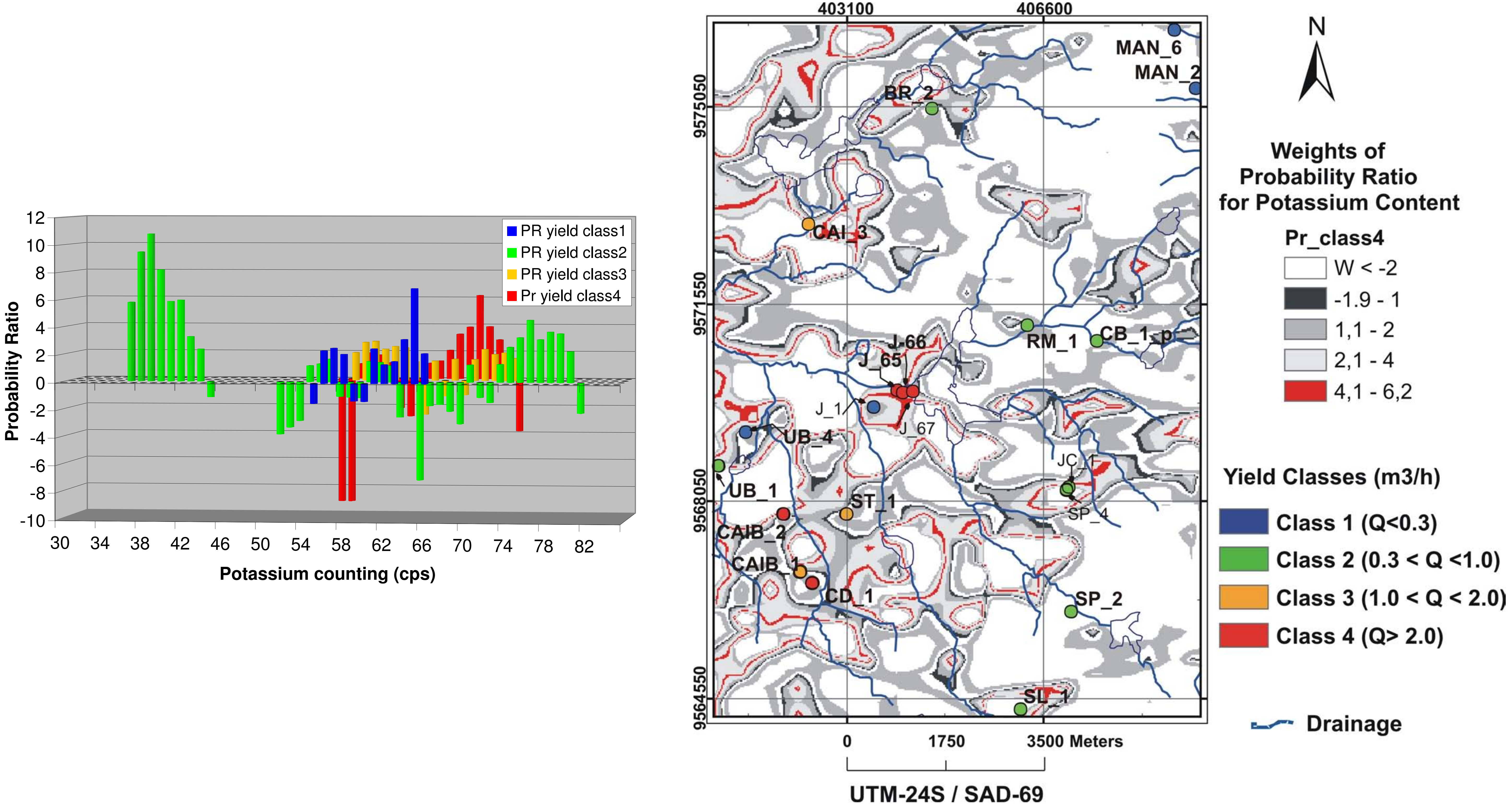

Annex 2.9 – Weights of probability ratio referred to the spatial association between potassium content and well yield classes for the Juá area: a) Full-range values of probability ratio as a chart representation; b) Map representation of reclassified values of probability ratio relative to the yield class 4. Negative values are the reciprocal negative of original values range from 0 to 0.99.

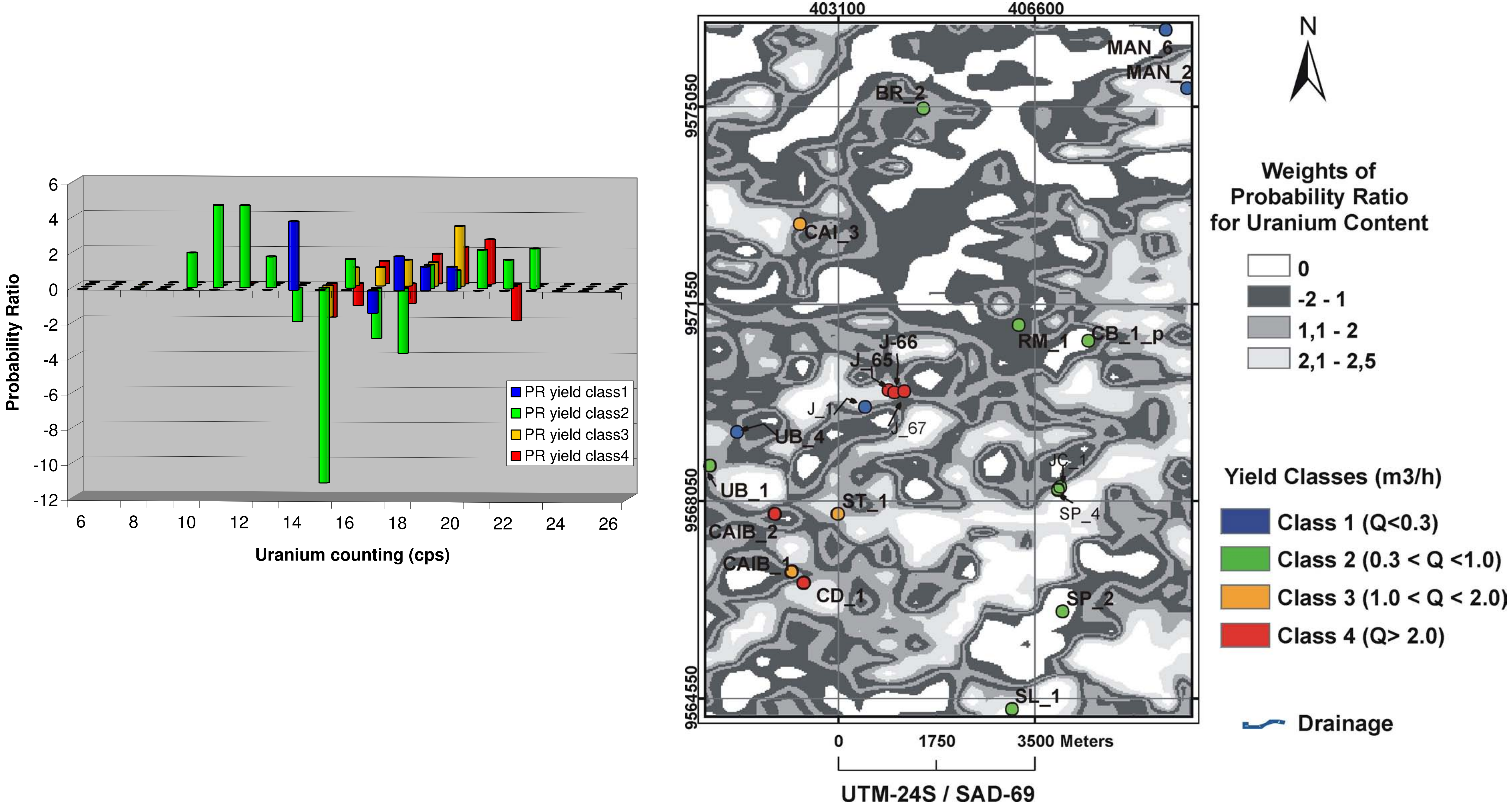

Annex 2.10 – Weights of probability ratio referred to the spatial association between uranium content and well yield classes for the Juá area: a) Full-range values of probability ratio as a chart representation; b) Map representation of reclassified values of probability ratio relative to the yield class 4. Negative values are the reciprocal negative of original values range from 0 to 0.99.

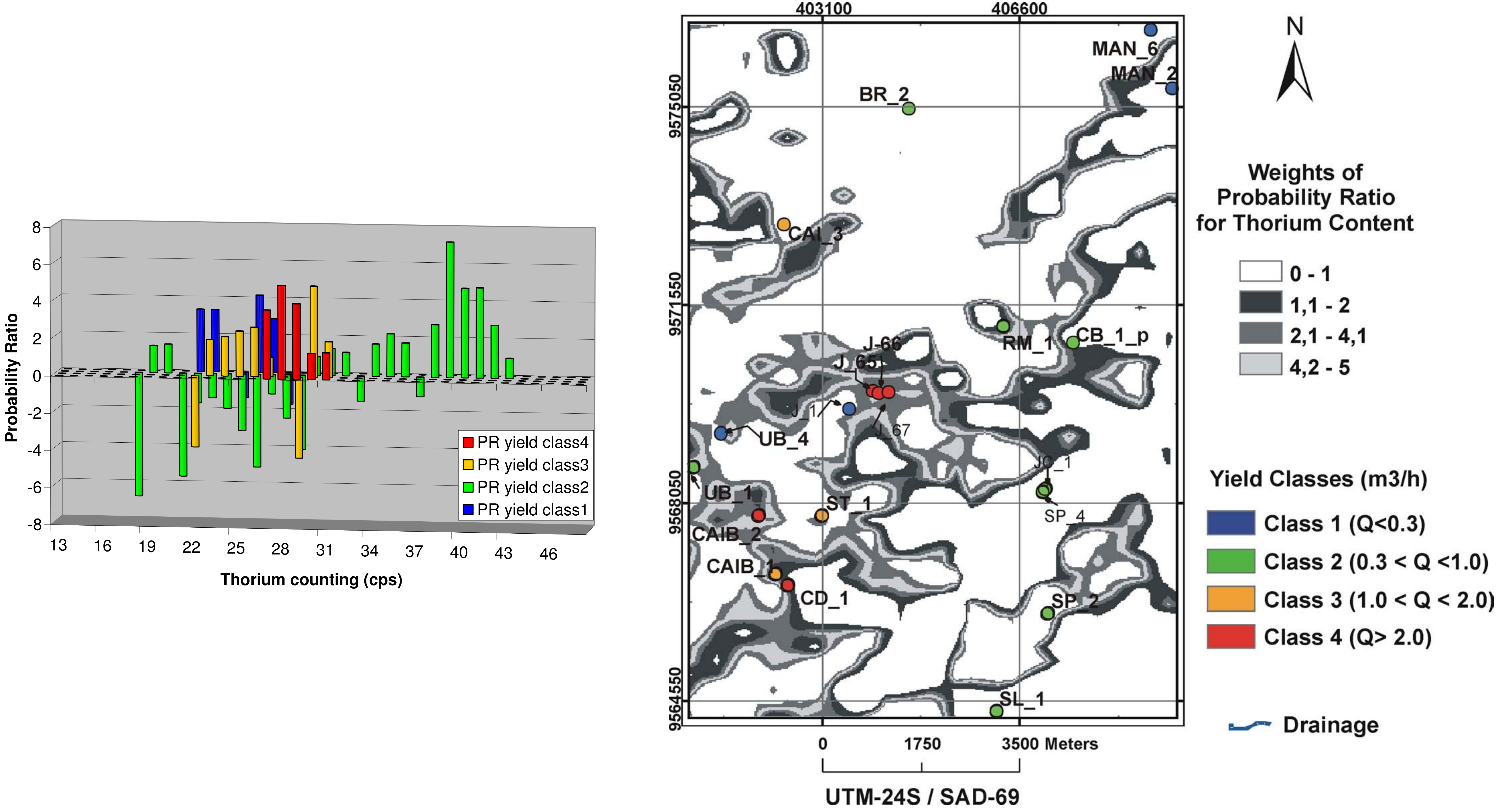

Annex 2.11 – Weights of probability ratio referred to the spatial association between thorium content and well yield classes for the Juá area: a) Full-range values of probability ratio as a chart representation; b) Map representation of reclassified values of probability ratio relative to the yield class 4. Negative values are the reciprocal negative of original values range from 0 to 0.99.

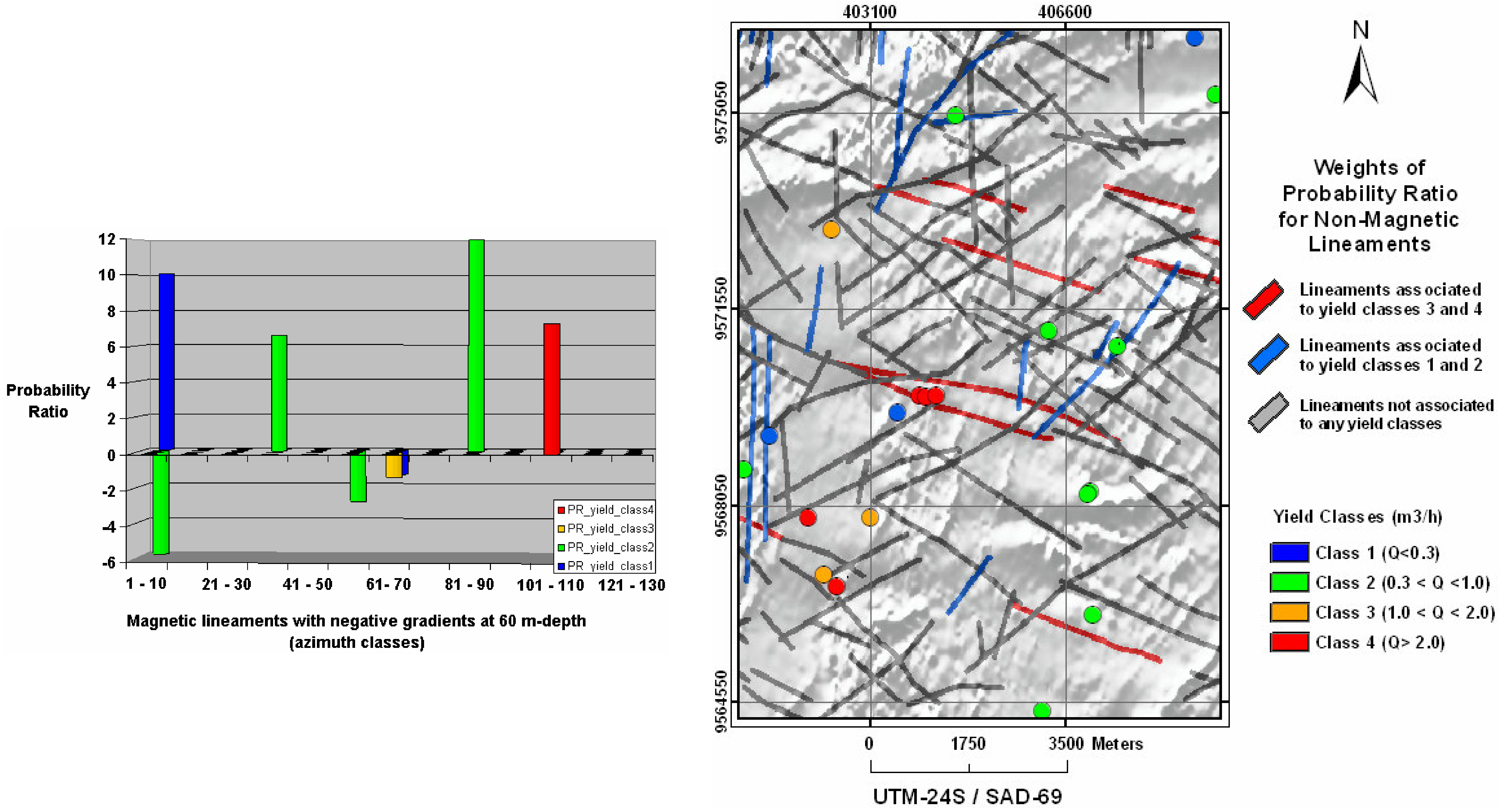

Annex 2.12 – Weights of probability ratio referred to the spatial association between non-magnetic gradients and well yields classes for the Juá area: a) Full-range values of probability ratio as a chart representation; b) Map representation of reclassified values of probability ratio-PR relative to the lowest and highest yield classes. Negative values are the reciprocal negative of original PR values range from 0 to 0.99.

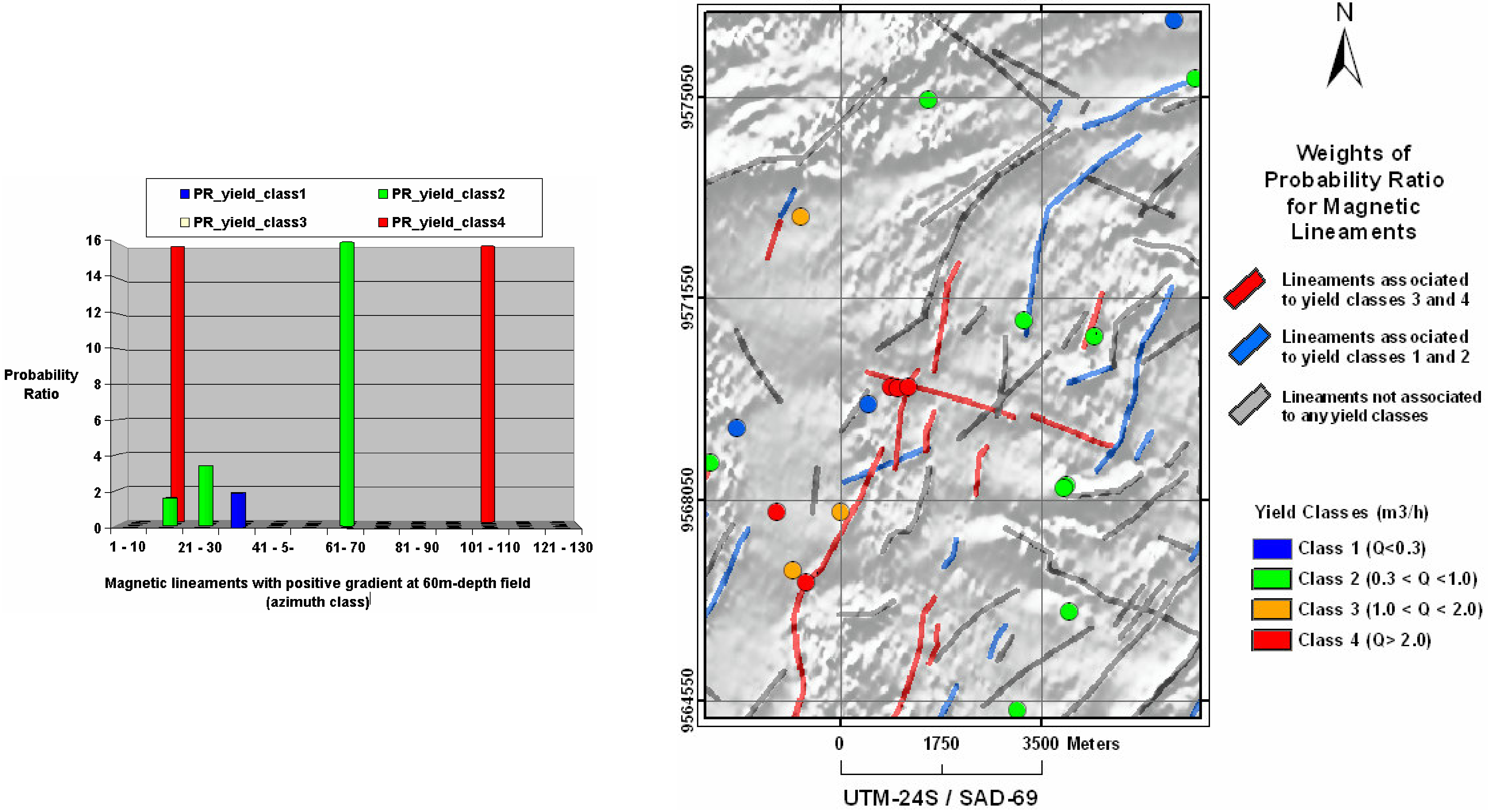

Annex 2.13 – Weights of probability ratio referred to the spatial association between magnetic gradients and well yields classes for the Juá area: a) Full-range values of probability ratio as a chart representation; b) Map representation of reclassified values of probability ratio-PR relative to the lowest and highest yield classes. Negative values are the reciprocal negative of original PR values range from 0 to 0.99.

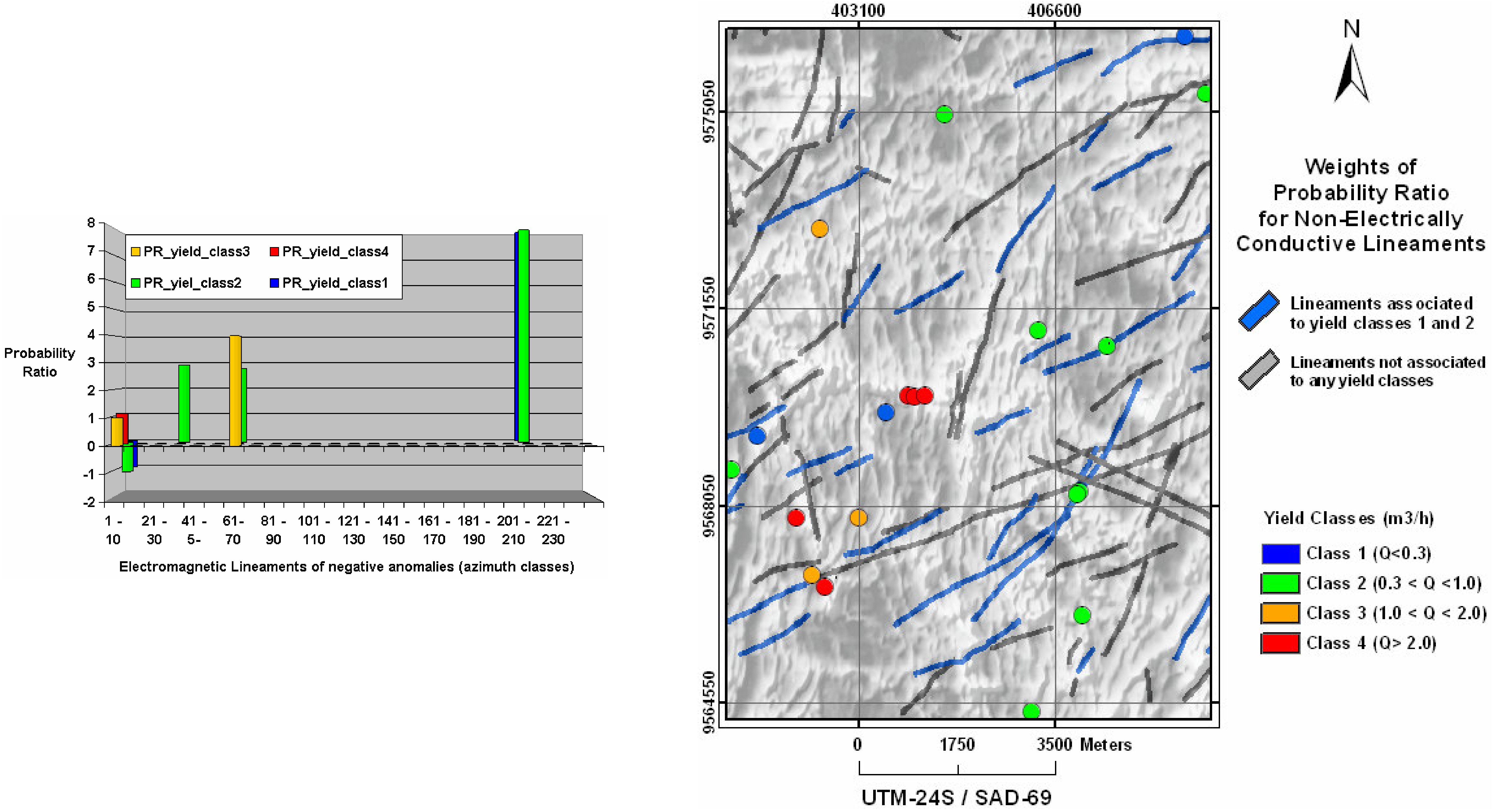

Annex 2.14 – Weights of probability ratio referred to the spatial association between non-electrically conductive gradients and well yield classes for the Juá area: a) Full-range values of probability ratio as a chart representation; b) Map representation of reclassified values of probability ratio-PR relative to the lowest and highest yield classes. Negative values are the reciprocal negative of original PR values range from 0 to 0.99.

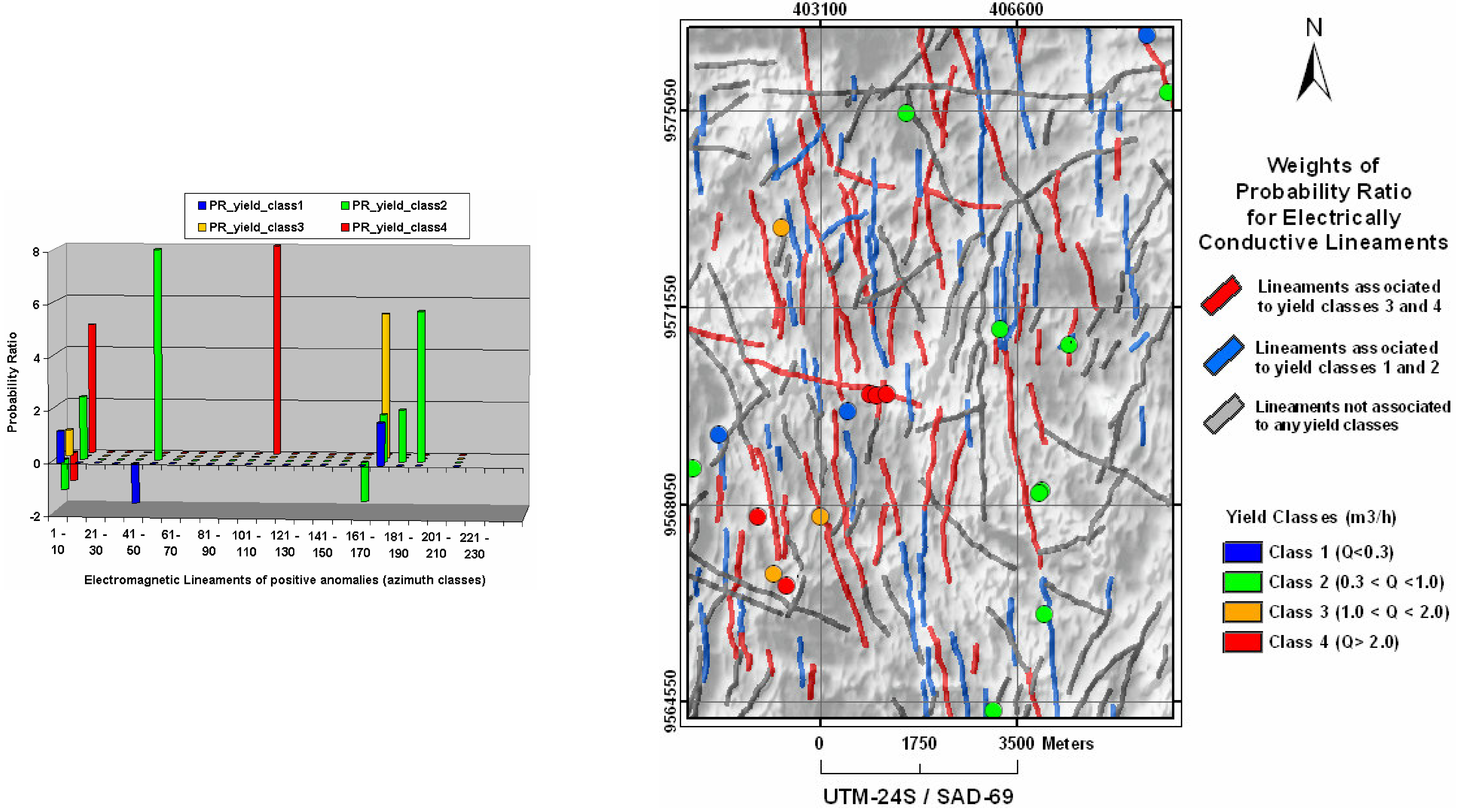

Annex 2.15 – Weights of probability ratio referred to the spatial association between electrically conductive gradients and well yield classes for the Juá area: a) Full-range values of probability ratio as a chart representation; b) Map representation of reclassified values of probability ratio-PR relative to the lowest and highest yield classes. Negative values are the reciprocal negative of original PR values range from 0 to 0.99.

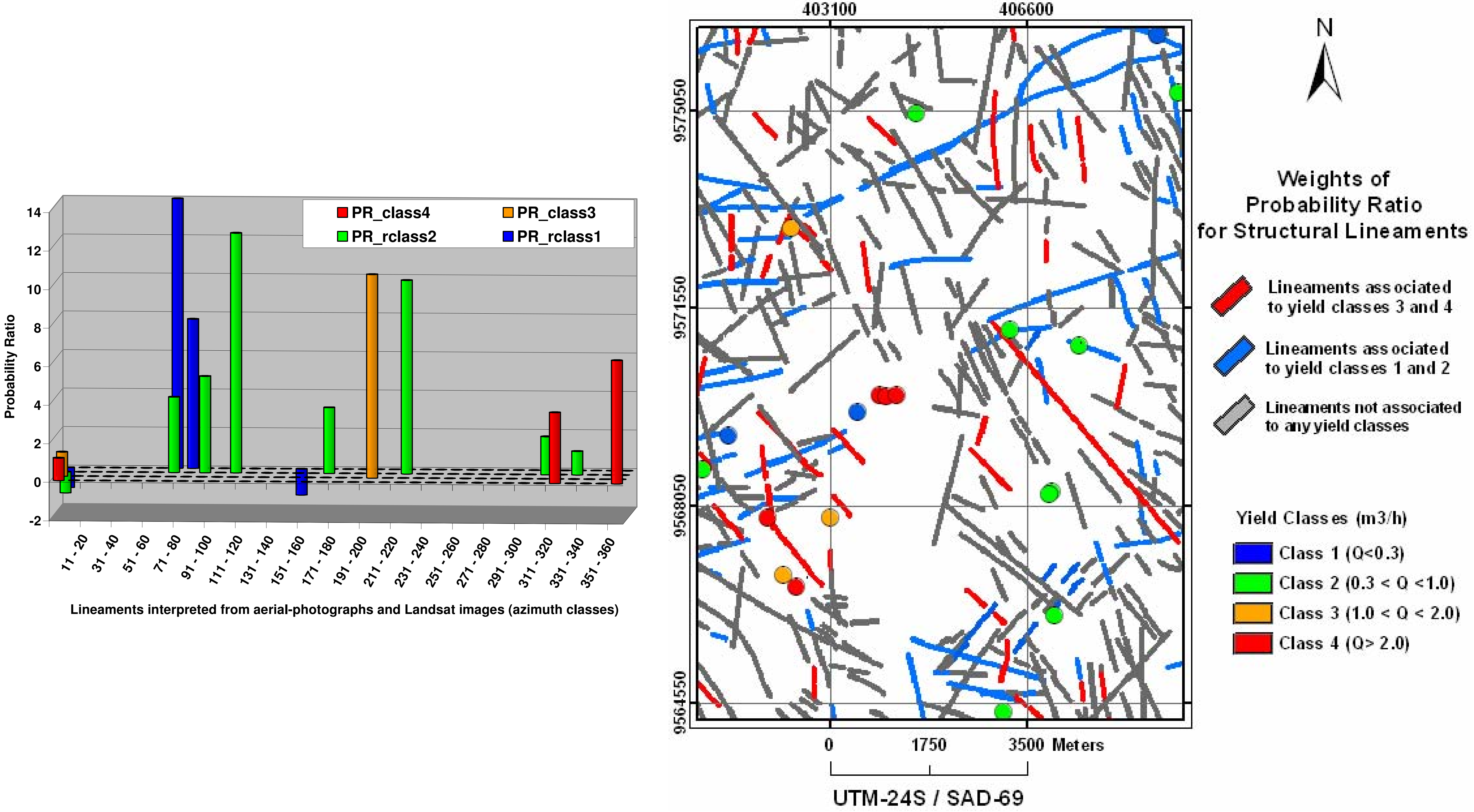

Annex 2.16 – Weights of probability ratio referred to the spatial association between structural lineaments and well yield classes for the Juá area: a) Full-range values of probability ratio as a chart representation; b) Map representation of reclassified values of probability ratio-PR relative to the lowest and highest yield classes. Negative values are the reciprocal negative of original PR values range from 0 to 0.99. Lineaments interpreted from ETM+/Landsat-7 images and aerial photographs at 1:70.000 scale.

ANNEX 3 – Geophysical, Structural and Alteration Mineral Evidences used for Groundwater Modeling with Weights of Evidences Technique

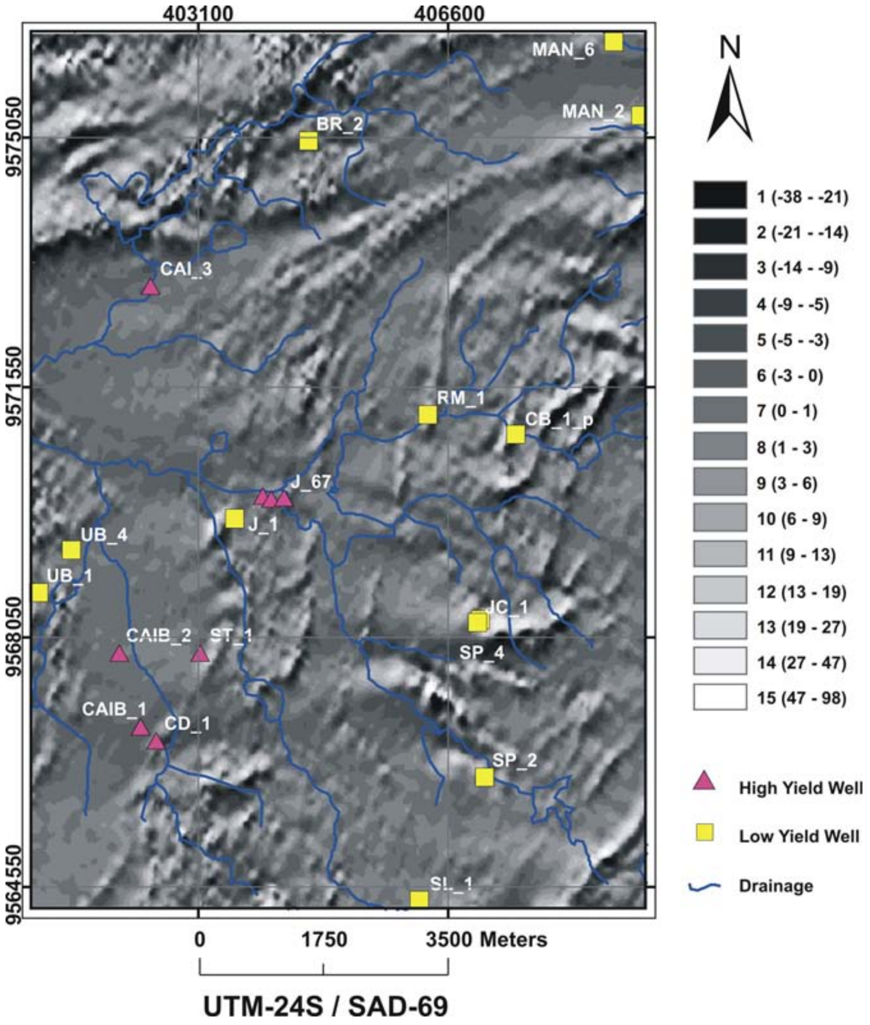

Annex 3.1 - Map of the magnetic residual field at 60 m depth of Juá study area.

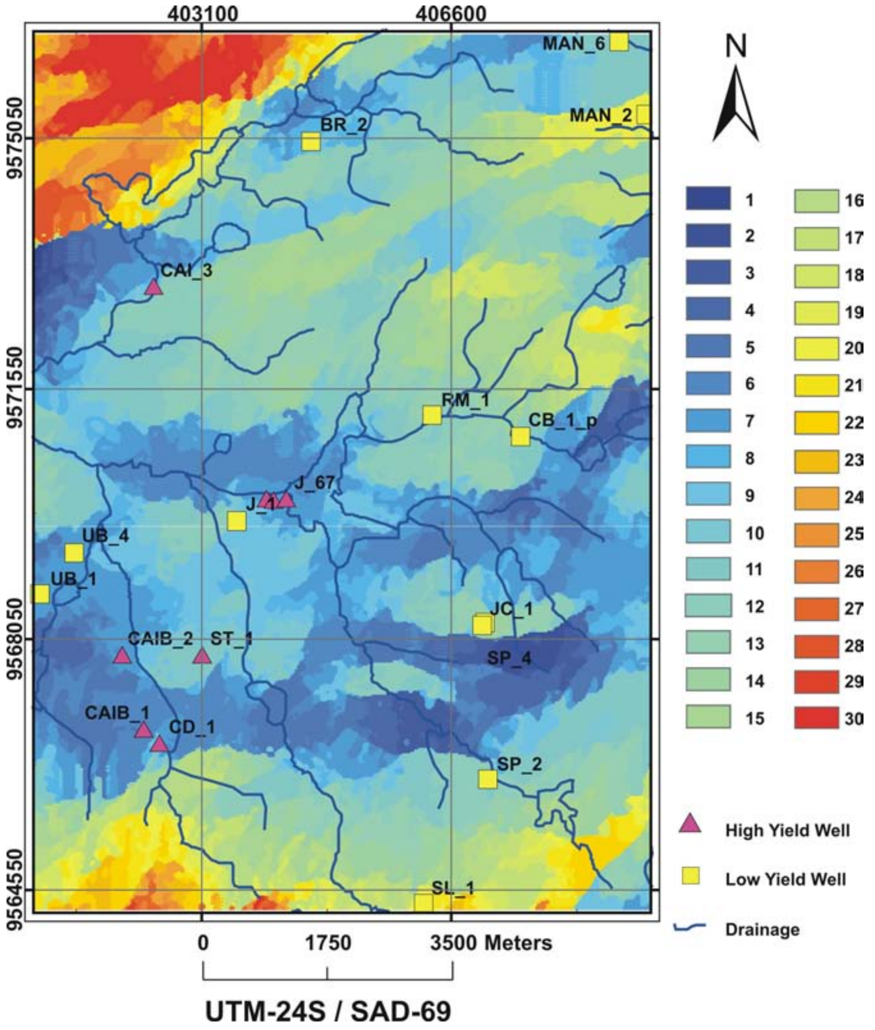

Annex 3.2 - Terracing from magnetic field (nT) filtered down to 270 m depth of Juá study area.

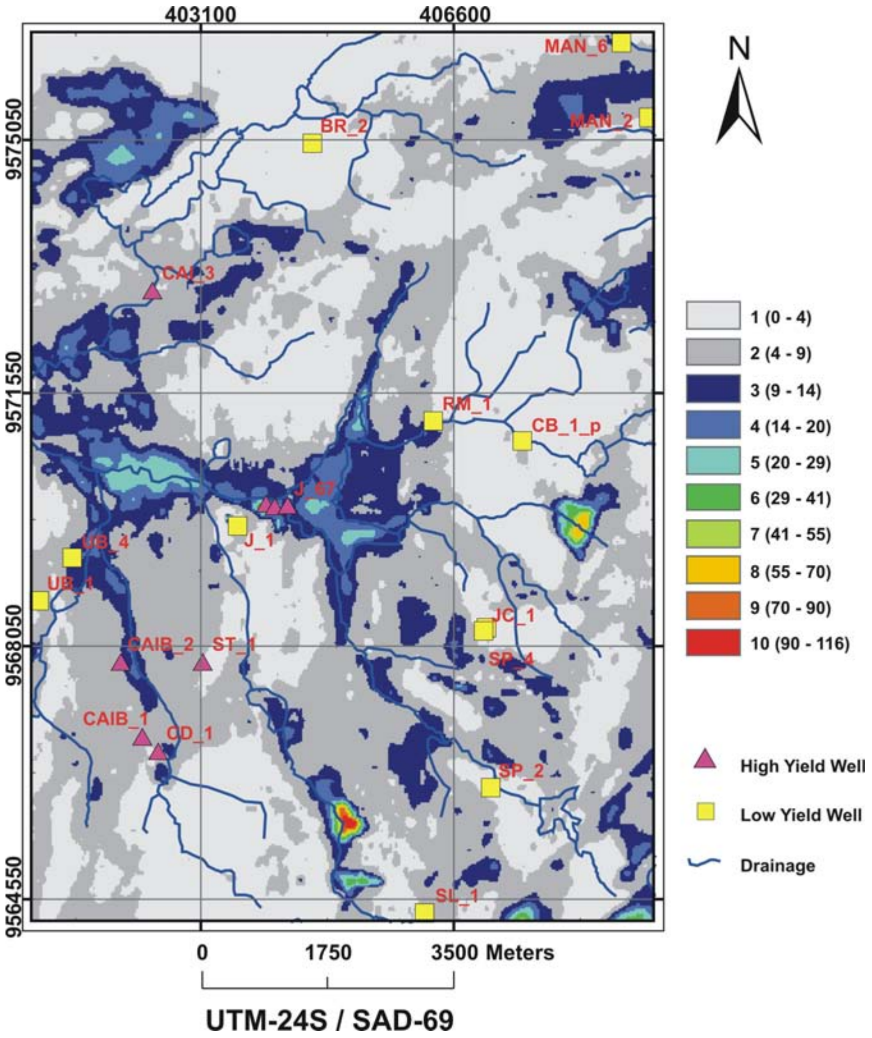

Annex 3.3 - Apparent electrical conductivity map from HEM 900 Hz data (mS/m) of Juá study area.

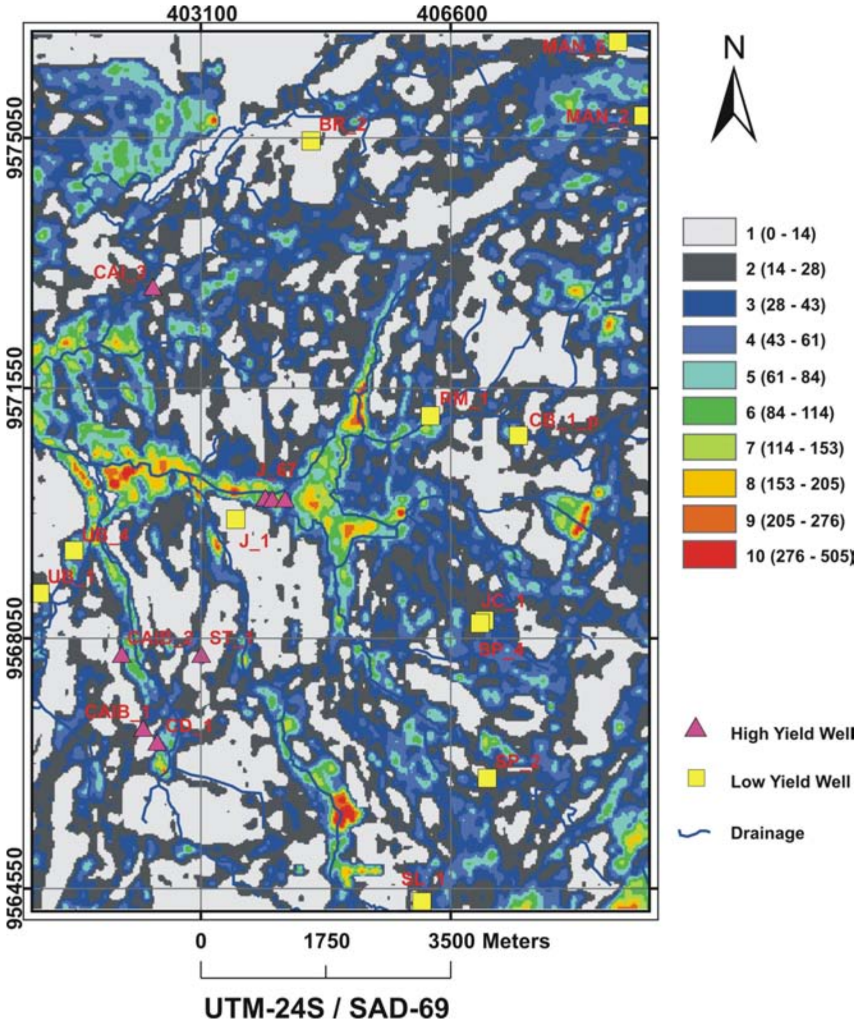

Annex 3.4 - Apparent electrical conductivity map from HEM 33000 Hz data (mS/m) of Juá study area.

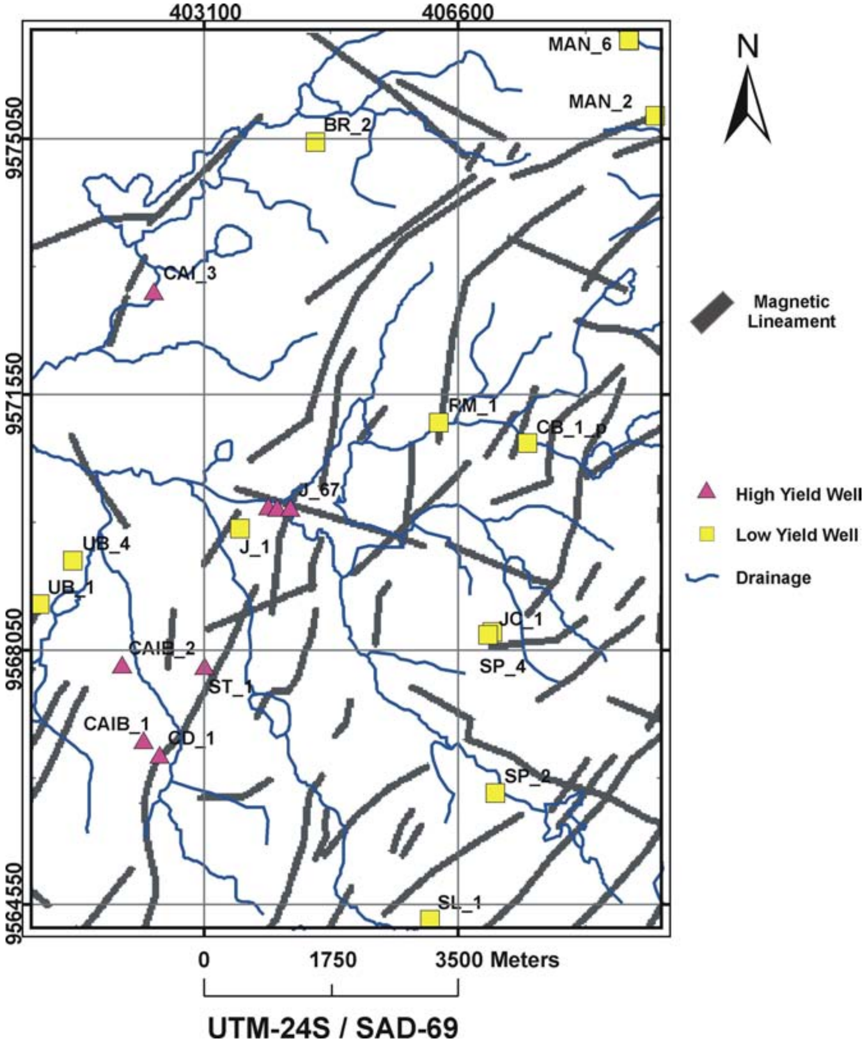

Annex 3.5 - Map of interpreted magnetic gradients at 60 m depth of Juá study area.

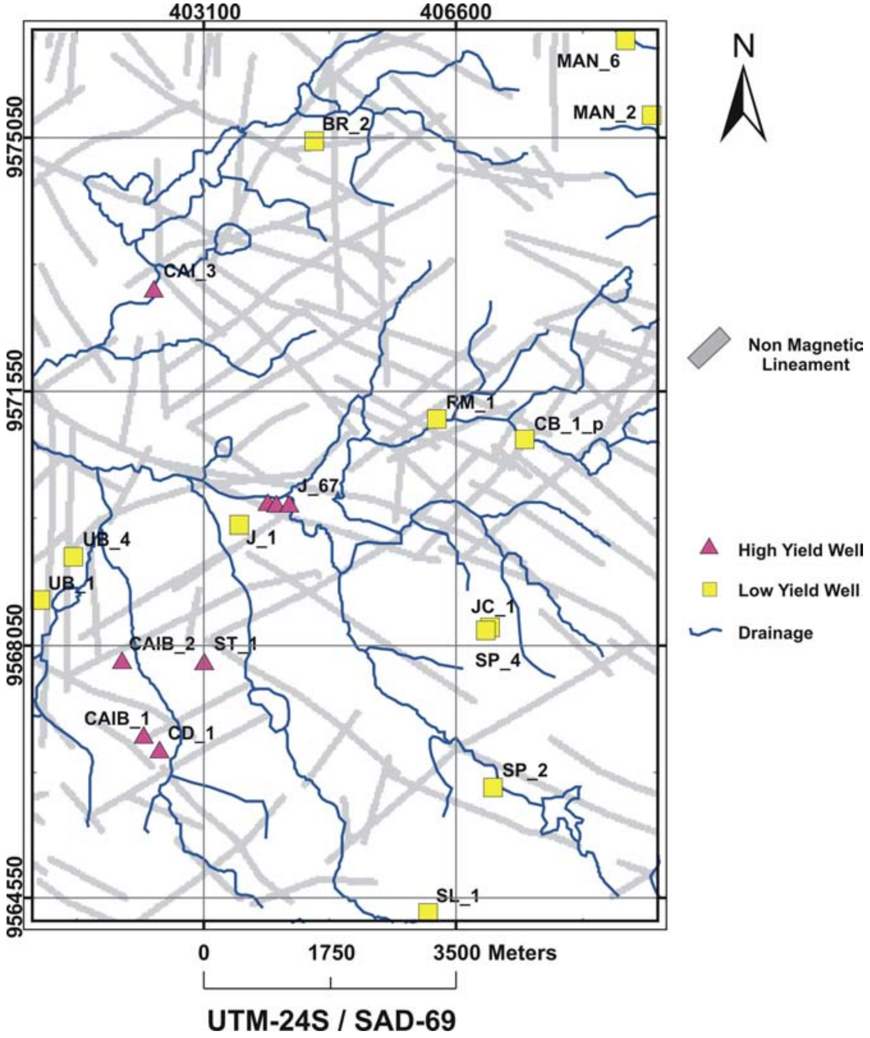

Annex 3.6 - Map of non-magnetic gradients at 60 m depth of Juá study area.

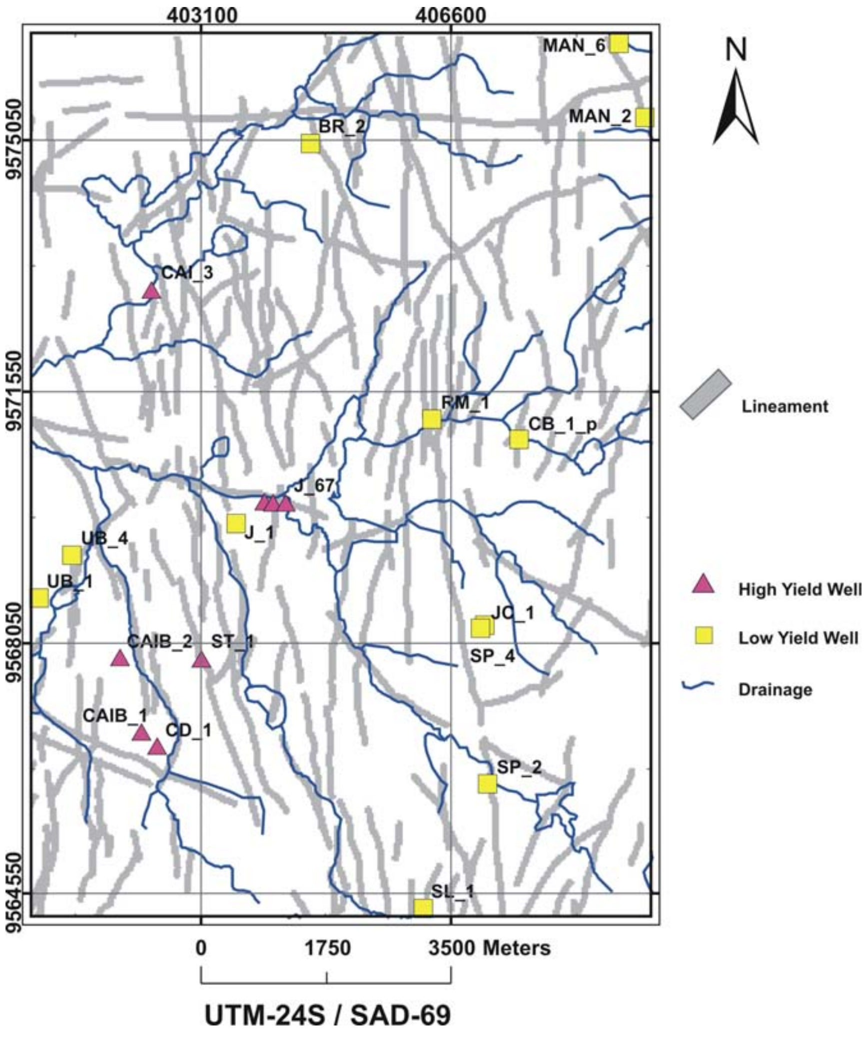

Annex 3.7 - Map of electrically conductive gradients of Juá study area.

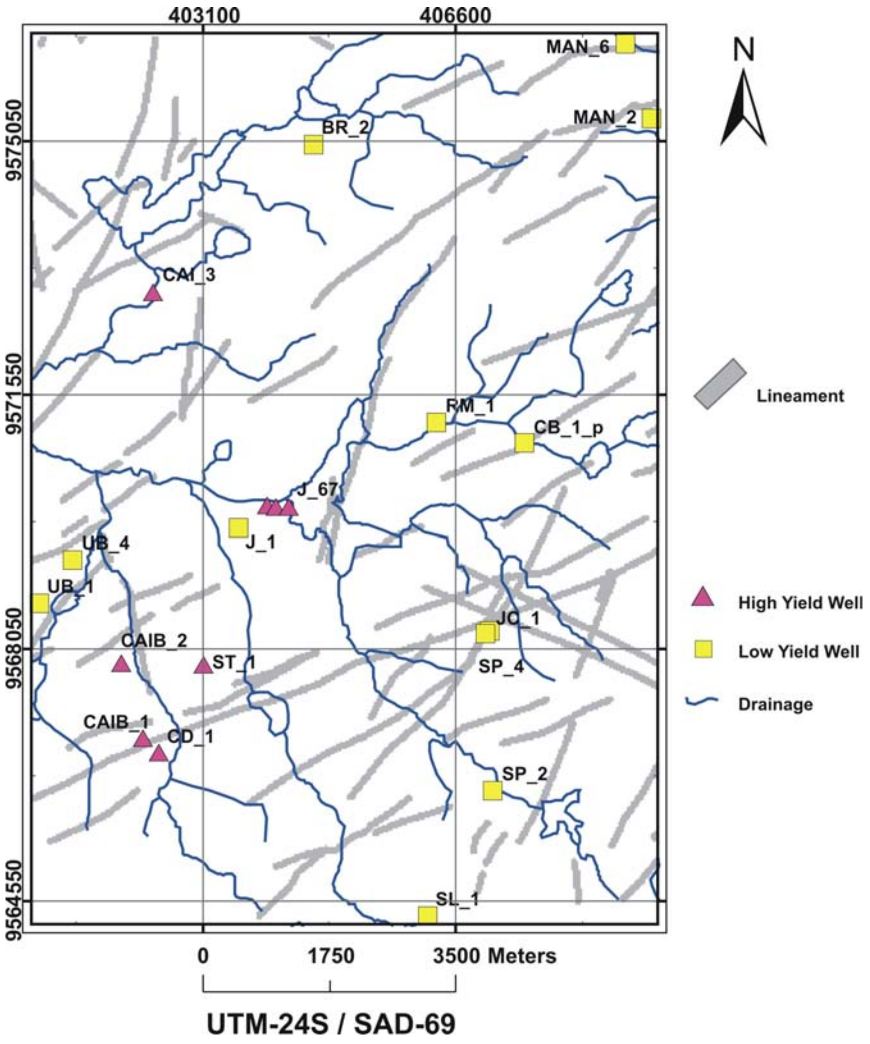

Annex 3.8 - Map of electrically non-conductive gradients of Juá study area.

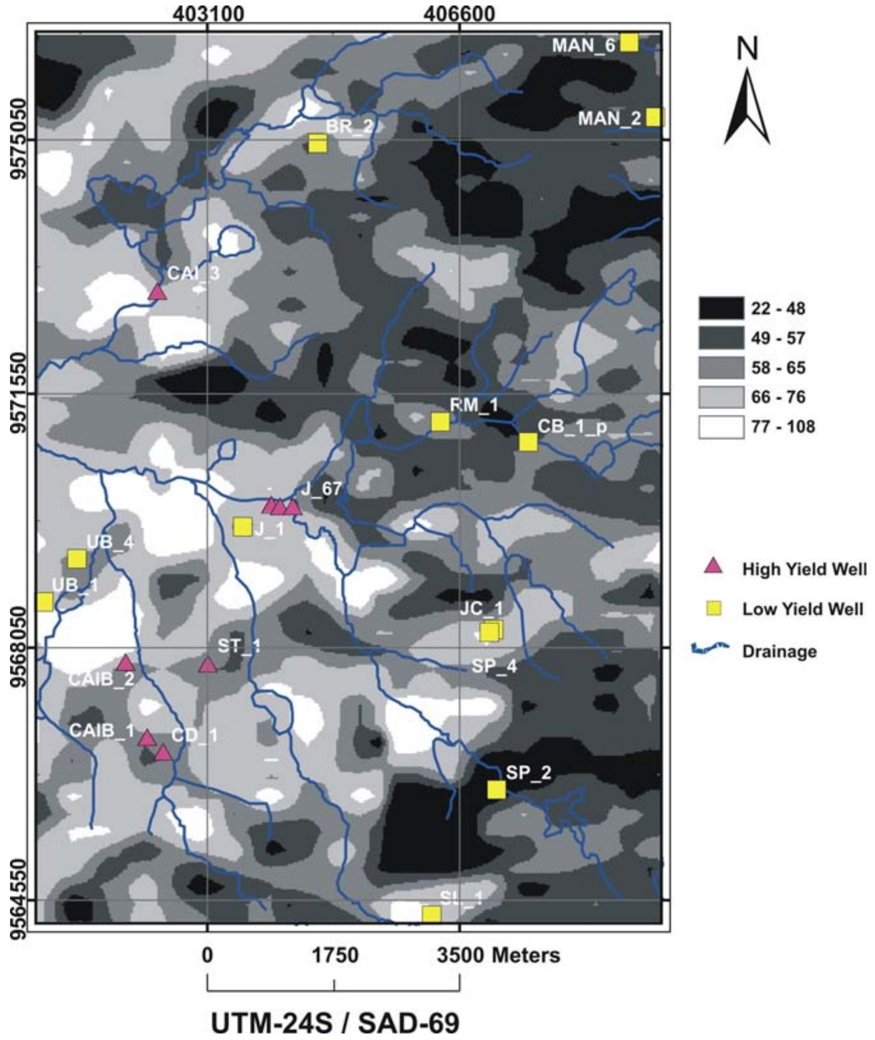

Annex 3.9 - Map of potassium content (counting per second-CPS) of Juá study area.

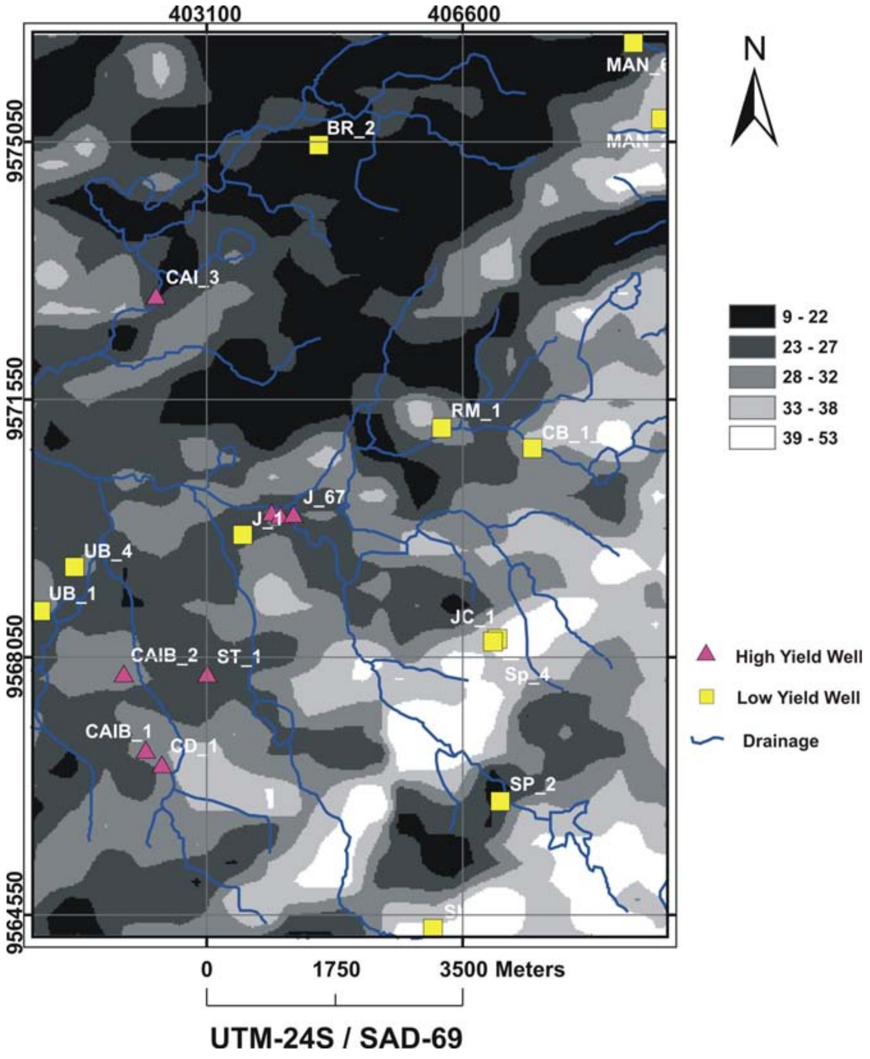

Annex 3.10 - Map of thorium content (counting per second-CPS) of Juá study area.

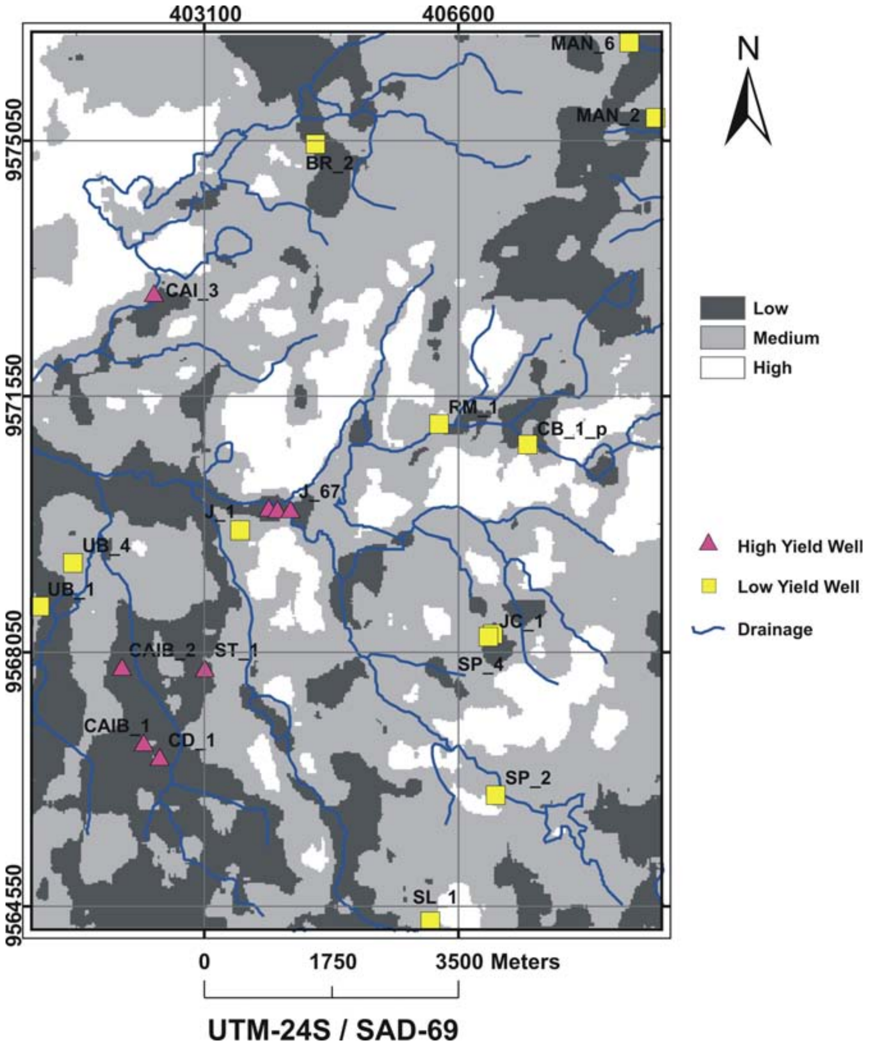

Annex 3.11 - Map of Fe-oxide (goethite) mineral content, plus Al-hydroxide mineral (kaolinite-smectite) content of Juá study area.

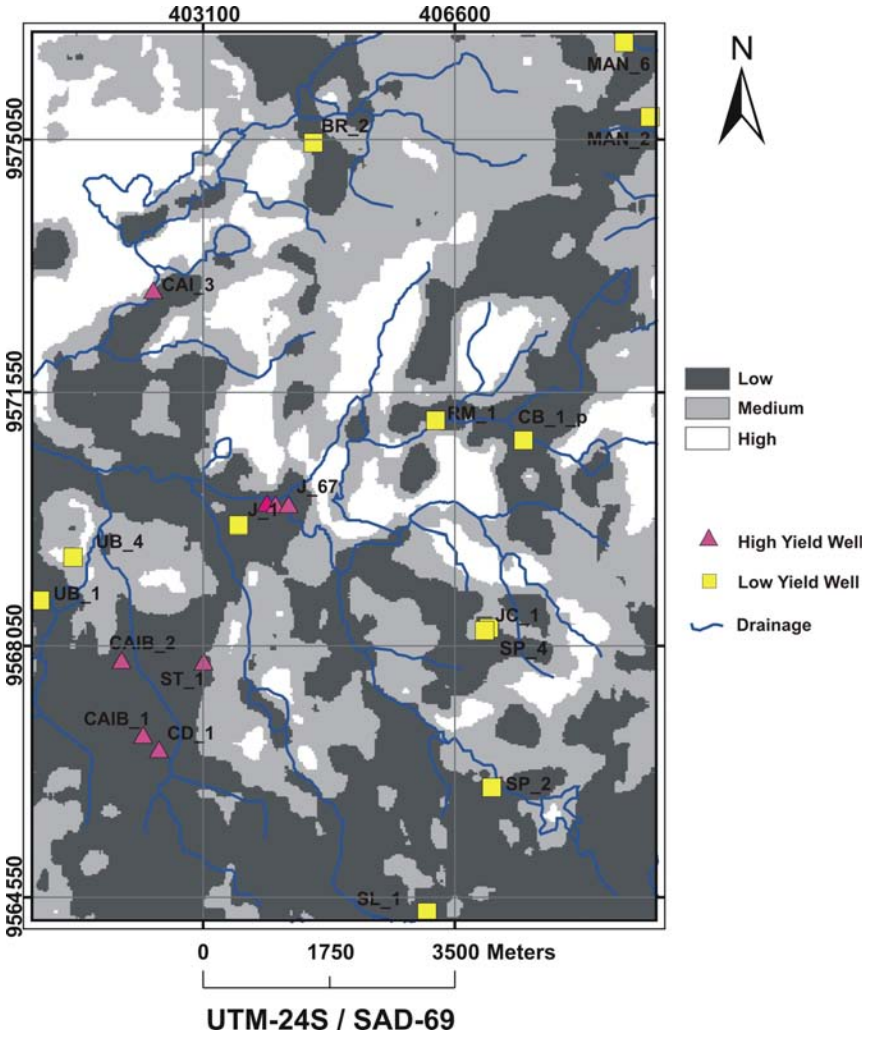

Annex 3.12 - Map of Al-hydroxide mineral (kaolinite-smectite) content of Juá study area.

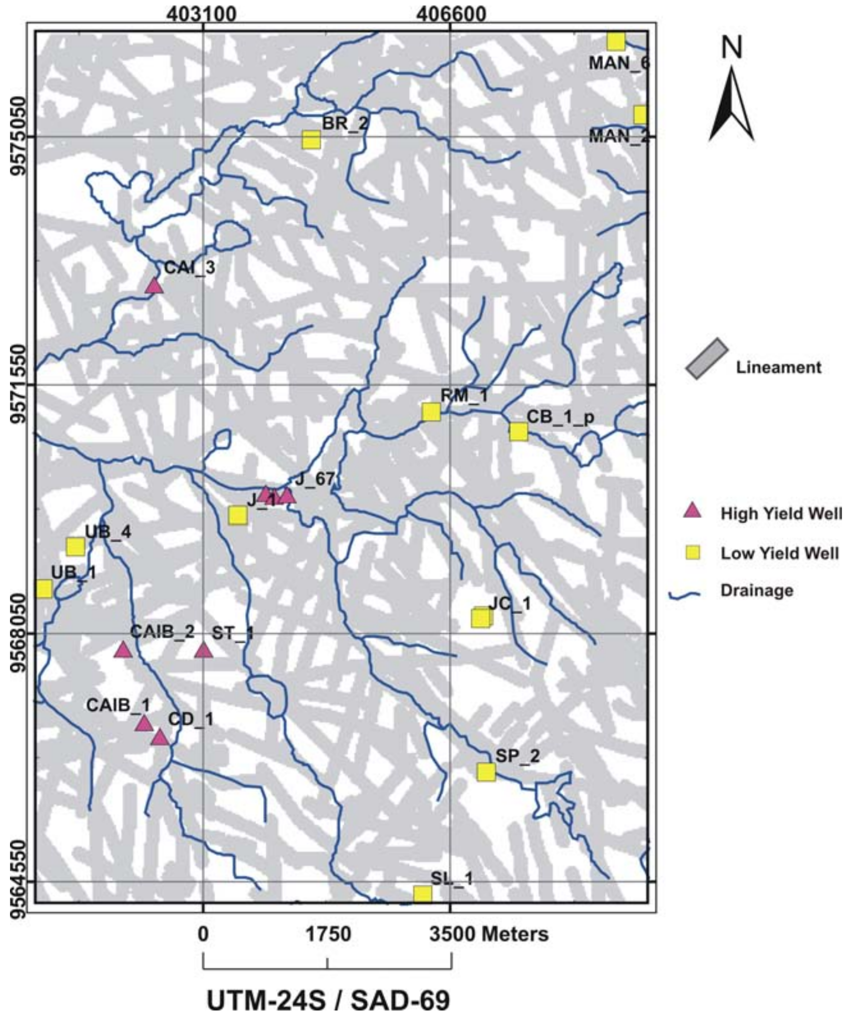

Annex 3.13 - Map of proximity zones of 100 m from structural lineaments depicted from the digital elevation model of SRTM, ETM+/Landsat images and aerial-photographs of Juá study area.

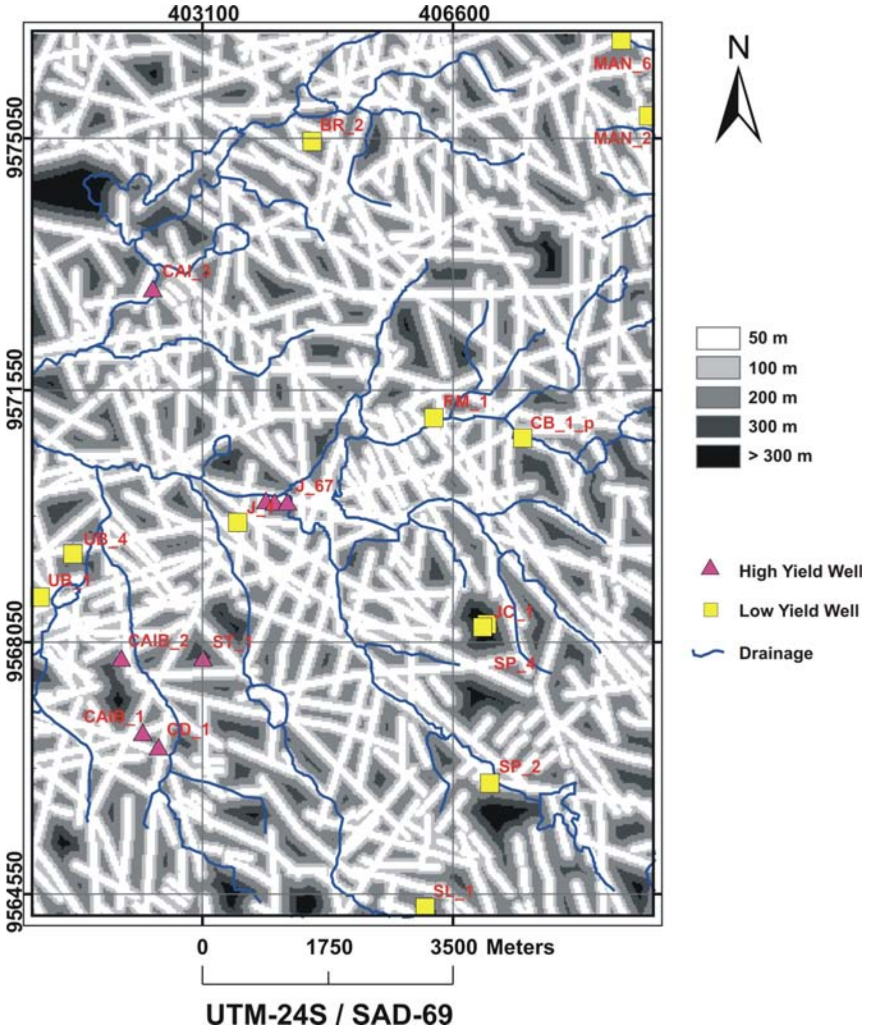

Annex 3.14 - Map of multiple proximity zones from structural lineaments depicted from Landsat images and aerial-photographs for Juá study area.

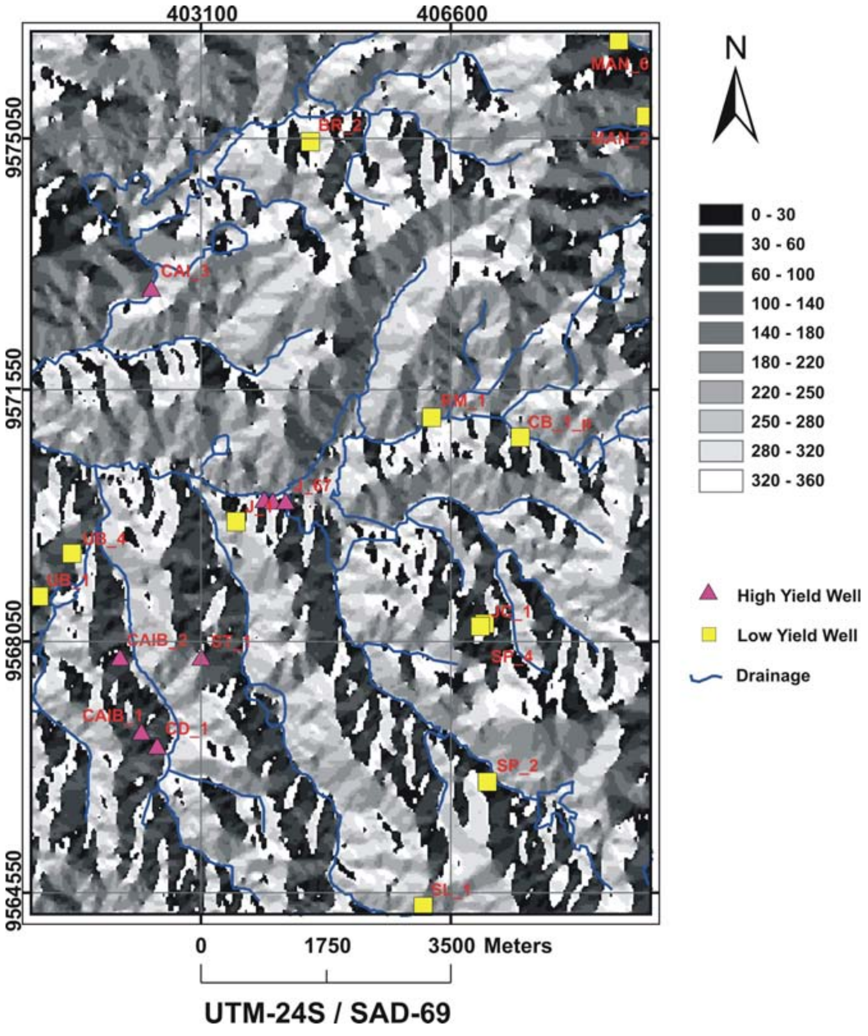

Annex 3.15 - Map of slope aspect (Azimuth) depicted from the digital elevation model of SRTM images for Juá study area.

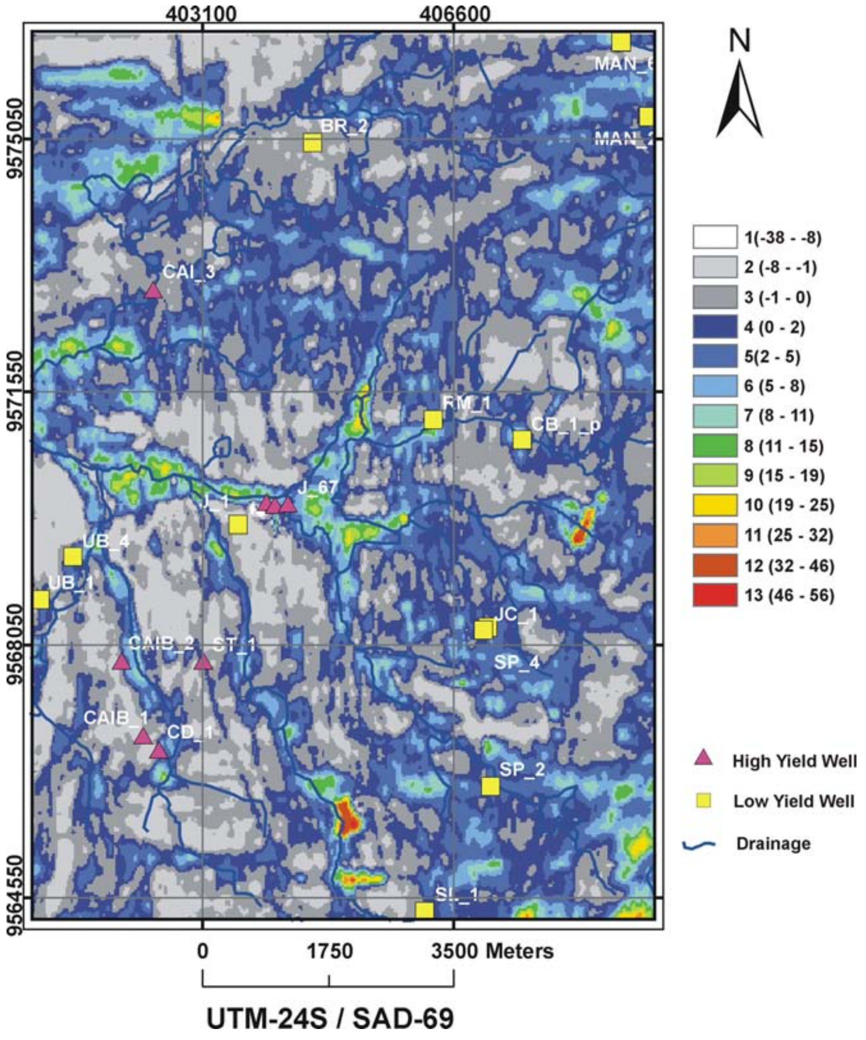

Annex 3.16 - Map of apparent electrical conductivity (mS/m) from the difference between HEM 4500 Hz and HEM 900 Hz data of Juá study area.